INTERMEDIATE FILAMENT MECHANICS ACROSS SCALES

From single filaments to single interactions and networks in cells

DISSERTATION

for the award of the degree
"DOCTOR RERUM NATURALIUM" (DR. RER. NAT.)

of the
Georg-August-Universität Göttingen

within the doctoral programme
Physics of Biological and Complex Systems
in the Göttingen Graduate School
of Neuroscience, Biophysics and Molecular Bioscience (GGNB)
of the Georg-August University School of Science (GAUSS)

submitted by

ANNA VERONIKA SCHEPERS

from Munich, Germany

Göttingen, August 2021

THESIS COMMITTEE:

Sarah Köster, Physics / Institute for X-Ray Physics

Andreas Janshoff, Chemistry / Institute for Biophysical Chemistry

Jörg Enderlein, Physics / III. Physical Institute – Biophysics

MEMBERS OF THE EXAMINATION BOARD:

Reviewer: Sarah Köster, Physics / Institute for X-Ray Physics

Second Reviewer: Andreas Janshoff, Chemistry / Institute for Biophysical Chemistry

Further members of the Examination Board:

Jörg Enderlein, Physics / III. Physical Institute – Biophysics

Stefan Klumpp, Physics / Institute for the Dynamics of Complex Systems

Timo Betz, Physics / III. Physical Institute – Biophysics

Michael Meinecke, University Medical Center / Department of Cellular Biochemistry

DATE OF THE ORAL EXAMINATION:

October 12th, 2021

CONTENTS

1 INTRODUCTION 3
REFERENCES . . . 5

2 INTERMEDIATE FILAMENTS – FROM PROTEINS TO NETWORKS 9
2.1 Structure and assembly of intermediate filament proteins . . . 10
2.2 Mechanical properties of single intermediate filaments . . . 12
2.2.1 Persistence length . . . 12
2.2.2 Stretching response . . . 13
2.3 Networks of reconstituted intermediate filaments . . . 15
2.4 Intermediate filament networks in cells . . . 16
2.4.1 Structure and function of intermediate filament networks in cells . . . 16
2.4.2 Intermediate filament networks and cell mechanics . . . 16
2.4.3 Keratin networks in cells under load . . . 17
REFERENCES . . . 17

3 BIOPOLYMER MECHANICS – THEORETICAL AND EXPERIMENTAL PRINCIPLES 29
3.1 Optical tweezers . . . 29
3.1.1 Particle trapping . . . 30
3.1.2 Force detection . . . 31
3.2 Microrheology . . . 34
3.2.1 Rheology of viscoelastic materials . . . 34
3.2.2 Passive microrheology: microparticle tracking . . . 34
3.2.3 Active microrheology: optical trapping . . . 36
3.3 Polymer mechanics . . . 38
3.3.1 Entropic stretching of worm-like chains . . . 38
3.3.2 Worm-like bundles . . . 39
3.3.3 Networks of semiflexible polymers . . . 39
3.4 Molecular reactions . . . 43
3.4.1 Step-growth polymerization . . . 43
3.4.2 Molecular reaction kinetics – two state models . . . 43
REFERENCES . . . 44

4 MATERIALS AND METHODS 51
4.1 Vimentin preparation . . . 51
4.2 Maleimide functionalization of polystyrene beads . . . 52
4.3 Stretching single filaments by optical trapping . . . 53
4.4 Analysis of single filament mechanics . . . 54
4.5 Force-strain Monte-Carlo simulations . . . 56
4.6 Optical trap measurements of individual filament–filament interactions . . . 56
4.7 Analysis of the interaction data . . . 58

4.8 Microrhelogy of reconstituted vimentin networks . . . 60
4.9 Analysis of microrheology experiments . . . 61
4.10 Imaging filament networks . . . 63
4.11 Imaging single filaments . . . 63
4.12 Analysis of filament lengths . . . 64
4.13 Finite element simulation of the microfluidic flowcell . . . 64
4.14 Stretching MDCK II cells on elastic substrates . . . 65
4.15 Analysis of images of stretched cells . . . 68
REFERENCES . . . 70

5 TUNING INTERMEDIATE FILAMENT MECHANICS BY VARIATION OF PH AND ION CHARGES 75
5.1 Introduction . . . 76
5.2 Results and discussion . . . 77
5.2.1 Cations stiffen single vimentin IFs . . . 77
5.2.2 Stretching vimentin filament bundles . . . 81
5.2.3 IF mechanics adapt to pH changes . . . 82
5.2.4 IF stiffening saturates at low pH . . . 83
5.2.5 Variations in the free energy landscapes influence filament mechanics . . . 85
5.3 Conclusions . . . 90
REFERENCES . . . 91

6 MULTISCALE MECHANICS AND TEMPORAL EVOLUTION OF VIMENTIN INTERMEDIATE FILAMENT NETWORKS 97
6.1 Introduction . . . 98
6.2 Results and discussion . . . 98
6.2.1 Vimentin filament networks mature and stiffen on time scales of days . . . 98
6.2.2 The filament length depends on elongation and lateral association . . . 100
6.2.3 Electrostatic and hydrophobic interactions lead to mechanically distinct networks . . . 101
6.2.4 Maturation of networks is concentration dependent . . . 104
6.2.5 Surface effects modify network structures . . . 105
6.2.6 Single filament mechanics are unaffected by detergents or divalent ions . . . 107
6.2.7 Electrostatics increase single filament–filament interactions 108
6.2.8 Interactions are independent of binding-site encounter rate 112
6.2.9 A two-state model accurately describes network mechanics 112
6.3 Conclusions . . . 113
6.4 Outlook . . . 115
6.4.1 Entropic and elastic stretching of single vimentin filaments 115
6.4.2 Single interactions of pre-strained filaments . . . 117
REFERENCES . . . 119

7 RESPONSE OF ACTIN AND KERATIN STRUCTURES TO ISOTROPIC CELL STRETCHING 125
7.1 Introduction . . . 125
7.2 Results and Discussion . . . 126
7.2.1 Equibiaxial stretching of PDMS devices . . . 126
7.2.2 The cell area increases during isotropic stretching . . . 128
7.2.3 Actin stress fibers disassemble at increasing cell extension 129
7.2.4 The keratin structure adapts to increasing strains . . . 131
7.3 Conclusion . . . 133
REFERENCES . . . 133

8 DISCUSSION AND CONCLUSION 137
REFERENCES . . . 140

APPENDIX 145

A SUPPORTING INFORMATION: TUNING INTERMEDIATE FILAMENT MECHANICS BY VARIATION OF PH AND ION CHARGES 145
A.1 Flow simulations . . . 145
A.2 Single force-strain curves . . . 147

B SUPPORTING INFORMATION: MULTISCALE MECHANICS AND TEMPORAL EVOLUTION OF VIMENTIN INTERMEDIATE FILAMENT NETWORKS 149
B.1 Additional information for elongation measurements . . . 149
B.2 Data analysis of microrheology measurements . . . 152
B.3 Modeling single interactions . . . 161

C SUPPORTING INFORMATION: RESPONSE OF ACTIN AND KERATIN STRUCTURES TO ISOTROPIC CELL STRETCHING 167
REFERENCES . . . 169

Acknowledgments 172

List of acronyms 174

Publications 176

ABSTRACT

The mechanical properties of cells are largely determined by the cytoskeleton. The cytoskeleton is an intricate and complex structure formed by protein filaments, motor proteins, and crosslinkers. The three main types of protein filaments are microtubules, actin filaments, and intermediate filaments (IFs). Whereas the proteins that form microtubules and actin filaments are exceptionally conserved throughout cell types and organisms, the family of IFs is diverse. For example, the IF protein vimentin is expressed in relatively motile fibroblasts, and keratin IFs are found in epithelial cells. This variety of IF proteins might therefore be linked to the various mechanical properties of different cell types.

In the scope of this thesis, I combine studies of IF mechanics on different time scales and in systems of increasing complexity, from single filaments to networks in cells. This multiscale approach allows for the simplification necessary to interpret observations while adding increasing physiological context in subsequent experiments. We especially focus on the tunability of the IF mechanics by environmental cues in these increasingly complex systems. In a series of experiments, including single filament elongation studies, single filament stretching measurements with optical tweezers, filament-filament interaction measurements with four optical tweezers, microrheology, and isotropic cell stretching, we characterize how electrostatic (pH and ion concentration) and hydrophobic interactions (detergent) provide various mechanisms by which the mechanics of the IF cytoskeleton can be tuned. These studies reveal how small changes, such as charge shifts, influence IF mechanics on multiple scales. In combination with simulations, we determine the mechanisms by which charge shifts alter single vimentin filament mechanics and we extract energy landscapes for interactions between single filaments. Such insights will provide a deeper understanding of the mechanisms by which cells can maintain their integrity and adapt to the mechanical requirements set by their environment.

1 INTRODUCTION

The various cell types found in metazoan organisms are highly specialized. By performing vastly different tasks, the different cell types allow organisms to perform a remarkable variety of complex processes [1]. With their distinct roles come completely different requirements to their mechanical properties [2]. For example, muscle cells have to reliably and repeatedly exert contractile forces, the endothelial cells that line blood vessels experience shear stresses, and skin tissue has to create a stretchable, though tear-proof barrier between the body and the environment. The mechanical properties of cells are largely determined by the cytoskeleton [3]. The cytoskeleton is an intricate and complex structure formed by protein filaments, motor proteins, and crosslinkers [4]. The three main types of protein filaments are microtubules, actin filaments, and IFs [3]. The electron microscopy image shown in Fig. 1.1 illustrates the complexity of the cytoskeleton with the three coexisting filament groups.

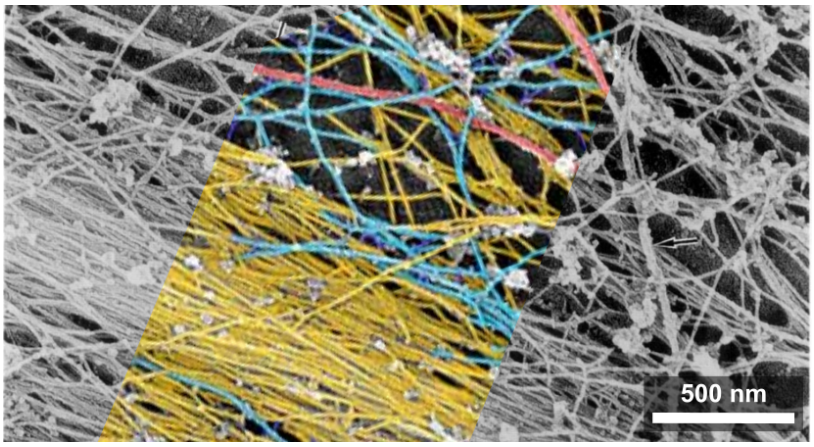

Fig. 1.1: **Three types of filaments of the cytoskeleton.** Scanning electron microscopy image of cytoskeletal filaments in a rat embryonic fibroblast. Actin filaments (yellow) are densely packed in a bundle in the bottom left. Few microtubules (red) span the depicted region. IFs (blue) are found throughout the image. Black/white image reprinted from Ref. [5], © 1995 with permission from Elsevier. Pseudo colored image from Tatyana Svitkina, University of Pennsylvania.

Each of the filament types fulfills specific functions in cells. The roles of microtubules for directed transport and during cell division are well studied [3]. Actin filaments are known to be one of the main players in cellular force generation, in separating cells during mitosis, and they are important for cell shape [3]. Whereas the proteins that form microtubules and actin filaments are exceptionally conserved throughout cell types and organisms [3], the family of IFs is diverse [6], and specific IF proteins are expressed in different cell types. This variety of IF proteins might therefore be linked to the various mechanical properties of different cell types.

When cells are mechanically stressed, IFs become load bearing, while the actin filament network disassembles and fluidizes [7, 8]. It is the remarkable stability and extensibility of the IF cytoskeleton that enables IFs to effectively act as cellular 'seat belts' and 'shock absorbers' [9, 10]. Studies of reconstituted IF networks have revealed the exceptional extensibility and mechanical stability of these structures [11–14], which are in contrast to the properties displayed by actin filament and microtubule networks. For this reason, understanding the origin and properties of IFs mechanics attracts more and more attention [9–16]. In recent years, some of the characteristic mechanical properties of IF networks, including their extensibility and ability to dissipate energy, have been observed at the single filament level [9, 10, 15].
When studying the properties of a complex material such as the IF cytoskeleton, it is helpful to drastically simplify the system to disentangle different processes or contributions. However, each single experimental observation is bound to disregard some important aspects. Multiscale approaches hence allow for the simplification necessary to interpret observations while adding increasing physiological context in subsequent experiments. In the scope of this thesis, I therefore combine studies of IF mechanics on different time scales and in systems of increasing complexities, from single filaments to networks in cells. I especially focus on the tunability of the IF mechanics by environmental cues in these increasingly complex systems.

OUTLINE OF THE THESIS

In chapter 2, I give an overview over IFs. I summarize published results on their extraordinary mechanical properties, the origin of these mechanics, and their role in cell mechanics. Chapter 3 introduces the physical principles of the measurement techniques and the models used to describe IF assembly, mechanics, binding kinetics, and network properties. The methods and materials used during this thesis are described in chapter 4.
In chapter 5, I present the results published in Ref. [17], where we study the effect of pH and ionic charge shifts on the mechanical response of single vimentin IFs to stretching by optical tweezers (OTs). We show how some indirect and direct charge shifts soften and destabilize the IFs whereas other charge shifts stiffen and stabilize the filaments. Chapter 6 includes results published in Ref. [18]. Based on the results of single-filament experiments, we study how hydrophobic and electrostatic interactions within and between filaments influence the elongation of vimentin filaments and the mechanical properties of single filaments. By employing four OTs, we directly measure interactions between single filaments to determine the interaction kinetics and interaction forces. We supplement the experimental results with simulations to disentangle which of the three processes – elongation, single filament mechanics, and interactions – dominate the changes in vimentin network mechanics observed in microrheology measurements. For both chapters 5 and 6, I extend the published manuscripts by additional data and analysis. As IFs are known to be especially important in cells under mechanical stress, I present the development and characterization of an isotropic cell stretching device and preliminary observations of the response

of cellular actin filament and IF networks to stretching in chapter 7. I focus on how different structures of the same cytoskeletal filament type in single cells respond to cell stretching. In chapter 8, I conclude the thesis by bringing the results from chapters 5 to 7 into context, discussing the physiological relevance of the observed effects, and exploring possible future directions.

[1] J. W. Valentine, A. G. Collins, and C. P. Meyer. "Morphological Complexity Increase in Metazoans." *Paleobiology* 20 (1994). DOI: 10.1017/S0094837300012641.

[2] D. L. Silver F. H.and Christiansen. "Mechanical Properties of Tissues." *Biomaterials Science and Biocompatibility*. Springer New York, 1999, pp. 187–212. DOI: 10.1007/978-1-4612-0557-9_7.

[3] B. Alberts et al. *Molecular biology of the cell*. Vol. 6. W. W. Norton & Company, 2014.

[4] D. A. Fletcher and R. D. Mullins. "Cell Mechanics and the Cytoskeleton." *Nature* 463 (2010), pp. 485–92. DOI: 10.1038/nature08908.

[5] T. M. Svitkina, A. B. Verkhovsky, and G. G. Borisy. "Improved procedures for electron microscopic visualization of the cytoskeleton of cultured cells." *J. Struct. Biol.* 155 (1995), 290–303. DOI: 10.1006/jsbi.1995.1054.

[6] S. A. Eldirany et al. "Recent insight into intermediate filament structure." *Curr. Opin. Cell Biol.* 68 (2021), pp. 132–143. DOI: 10.1016/J.CEB.2020.10.001.

[7] E. Latorre et al. "Active superelasticity in three-dimensional epithelia of controlled shape." *Nature* 7730 (2018), pp. 6481–6487. DOI: 10.1021/ac8009643.

[8] H. Wu et al. "Vimentin Intermediate Filaments and Filamentous Actin Form Unexpected Interpenetrating Networks That Redefine the Cell Cortex." *BioRxiv* (2021). (visited on 08/04/2021). DOI: 10.1101/2021.07.29.454155.

[9] J. Block et al. "Nonlinear Loading-Rate-Dependent Force Response of Individual Vimentin Intermediate Filaments to Applied Strain." *Phys. Rev. Lett.* 118 (2017), p. 048101. DOI: 10.1103/PhysRevLett.118.048101.

[10] J. Block et al. "Viscoelastic Properties of Vimentin Originate from Nonequilibrium Conformational Changes." *Sci. Adv.* 4 (2018), eaat1161. DOI: 10.1126/sciadv.aat1161.

[11] P. A. Janmey et al. "Viscoelastic Properties of Vimentin Compared with Other Filamentous Biopolymer Networks." *J. Cell Biol.* 113 (1991), pp. 155–160. DOI: 10.1083/jcb.113.1.155.

[12] M. Schopferer et al. "Desmin and Vimentin Intermediate Filament Networks: Their Viscoelastic Properties Investigated by Mechanical Rheometry." *J. Mol. Biol.* 388 (2009), pp. 133–143. DOI: 10.1016/j.jmb.2009.03.005.

[13] P. Pawelzyk et al. “Attractive Interactions Among Intermediate Filaments Determine Network Mechanics In Vitro.” *PLoS ONE* 9 (2014), e93194. DOI: 10.1371/journal.pone.0093194.

[14] A. Aufderhorst-Roberts and G. H. Koenderink. “Stiffening and Inelastic Fluidization in Vimentin Intermediate Filament Networks.” *Soft Matter* 15 (2019), pp. 7127–7136. DOI: 10.1039/C9SM00590K.

[15] J. Forsting et al. “Vimentin Intermediate Filaments Undergo Irreversible Conformational Changes During Cyclic Loading.” *Nano Lett.* 19 (2019), pp. 7349–7356. DOI: 10.1021/acs.nanolett.9b02972.

[16] K. T. Sapra et al. “Nonlinear mechanics of lamin filaments and the meshwork topology build an emergent nuclear lamina.” *Nat. Commun.* 11 (2020), p. 6205. DOI: 10.1038/s41467-020-20049-8.

[17] A. V. Schepers, C. Lorenz, and S. Köster. “Tuning Intermediate Filament Mechanics by Variation of pH and Ion Charges.” *Nanoscale* 12 (2020), pp. 15236–15245. DOI: 10.1039/D0NR02778B.

[18] A. V. Schepers et al. “Multiscale mechanics and temporal evolution of vimentin intermediate filament networks.” *Proc. Natl. Acad. Sci.* 118 (2021), e2102026118. DOI: 10.1073/pnas.2102026118.

2 INTERMEDIATE FILAMENTS – FROM PROTEINS TO NETWORKS

After the first observations of IFs were reported, it took decades until it was discovered that IFs constitute a class of cytoskeletal filaments [1]. These first reports of bundles of keratin IFs in epithelial tissue, at the time termed "tonosils", were published in 1928, years before the two other main types of filaments of the cytoskeleton, actin (1942 [2, 3]) filaments and microtubules (late 1950's [4]) were identified. During the early years of IF research, many different names were used, *e.g.*, 10-nm filaments, square filaments, round filaments, neurofilaments and beta filaments [1]. However, as the diameter of IFs is between the values found for actin filaments, also called F-actin, (7 nm) and microtubules (25 nm) [5], the intermediate sized filaments became known as "intermediate filaments". One main difference between IF proteins, actin monomers, and tubulin is that the IF protein family comprises many different proteins that are expressed in a cell-type-specific manner [6]. In humans, more than 70 genes encode for IF proteins [6, 7]. The class of IFs proteins is typically divided into subclasses, which are grouped by their primary structure, function, and tissue of origin [6, 7]: type 1 and type 2 IF proteins are keratin proteins where type 1 keratin proteins are acidic and type 2 keratin proteins are basic. Keratin proteins are further divided into cytokeratin proteins which, for example, form the cytoskeleton of epithelial cells, schematically shown in blue in Fig. 2.1, and hard/structural keratin proteins that are, for example, found in hair or nails. For example, vimentin, which is found in cells of mesynchymal origin, desmin (green in Fig. 2.1), which is expressed in muscle cells, or glial fibrillary acidic protein, found in astrocyes and glial cells, belong to type 3 IFs. Type 4 IFs, for example the three types of neurofilaments, are mostly found in nerve cells, as sketched in orange in Fig. 2.1. Type 5 IFs, the lamins, form the nuclear lamina of all cells, as shown in red in Fig. 2.1. Type 6 IFs, phakinin and filensin, are expressed in the eye lens. Since actin and tubulin are highly conserved throughout different cell types [5], the large variety of IFs proteins indicates that IF protein expression might be a tool for cells to tune their properties.

Fig. 2.1: Examples for the types of IFs in different cells. Type 1 & 2 keratins co-assemble in skin cells. The type 3 IF desmin is expressed in muscle cells. Type 4 neurofilaments are expressed in neurons. The type 5 lamins form the nuclear lamina.

2.1 STRUCTURE AND ASSEMBLY OF INTERMEDIATE FILAMENT PROTEINS

Analysis of the amino acid sequence of IF proteins revealed a highly conserved tripartite structure, consisting of an α-helical rod region that is flanked by disordered N-terminal *head* and C-terminal *tail* domains [8, 9], as sketched in Fig. 2.2 (left). The rod is further subdivided into three helices, coil 1A, coil 1B, and coil 2 [8], see Fig. 2.2. Whereas details of the amino acid sequence, such as the length of the head and tail domains, the overall charge, *etc.*, vary between IF proteins, this structure is the basis of all IF proteins [10]. A comparison of the structures of all known IF proteins and an overview of the currently available structural data with atomic resolution are presented in Ref. [7].
Experiments with reconstituted IF proteins have revealed that the rod-like monomers self-assemble into mature IFs in a hierarchical manner:

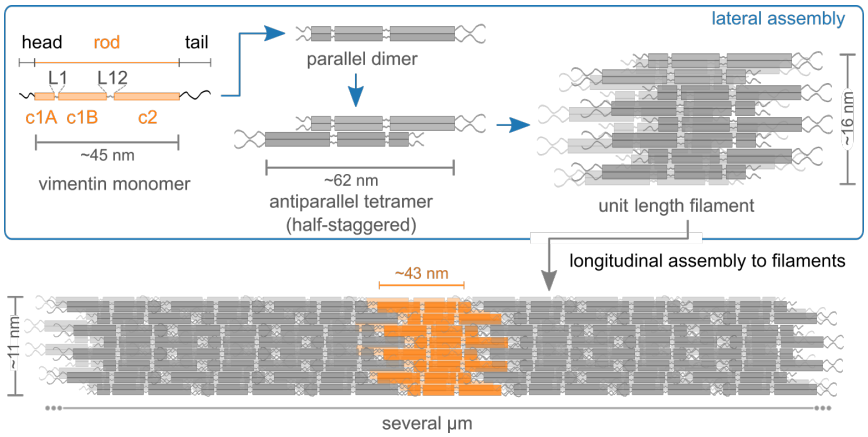

Fig. 2.2: **The hierarchical assembly:** lateral arrangement of monomers leads to dimers, tetramers, and finally ULFs, subsequent longitudinal elongation yields long filaments.

Two monomers align in parallel to form a dimeric, left-handed coiled-coil [8]. The coiled-coil formation is caused by the heptad repeat pattern in the primary structure $(abcdefg)_n$ in the rod domain [8]. Most IF proteins form homodimers with only one type of protein, whereas keratins form heterodimers, and some studies also show assemblies of several different IF proteins [11].
The dimerization is the first step of the hierarchical assembly of IFs. In the next step, two dimers align in an antiparallel, half-staggered manner to form tetramers, in the case of vimentin, of ∼62 nm length [12–14]. Due to this arrangement, the tetramer is a symmetric unit with "overhanging" C-terminal ends, *i.e.*, the tails [15]. Tetramers are remarkably stable even in low ionic strength buffers, and to obtain the monomer or dimer state, denaturing agents have to be added. From the stable tetramer state, further assembly into filaments can be induced by changing the pH or increasing the cation concentration of the buffer. Tetramers align in parallel to form unit length filaments (ULFs), the last stage of the lateral assembly [16]. The exact number of tetramers per ULF varies for different IF proteins, reconstituted vimentin ULFs consist of, on average, 8 tetramers, keratin ULFs typically of 4 tetramers [17]. Vimentin ULFs have an average diameter of 16 nm and are of the same length as the tetramer

[13]. Longitudinal assembly of ULFs by end-to-end annealing [18–20] results in highly periodic filaments [21] of several µm length. In the mature vimentin IF, interlacing of the overhanging ends of the ULFs leads to a repetition of the structure every 43 nm [22]. Vimentin filaments further undergo a radial compaction step where the diameter reduces to ∼11 nm [13, 23, 24], for example shown in Fig. 2.3. It has to be noted that the diameter of the filaments can vary, not only between IF types but also within one filament. Depending on the assembly conditions, filaments exhibit a significant degree of polymorphism in their mass-per-length [13, 17, 25].

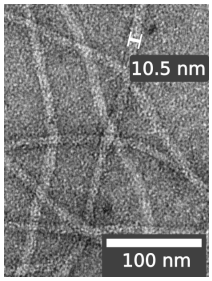

Fig. 2.3: Negative staining electron micrograph of reconstituted vimentin filaments. Imaged by Wiebke Möbius.

The longitudinal assembly continues over hours and days [18, 19, 26–28] and is significantly slower than the lateral assembly, which occurs on time scales of 100 ms [29–31]. During this elongation step, filaments grow simultaneously at both ends, and filaments can fuse with each other. The end-to-end annealing was shown nicely by mixing of short, pre-assembled filaments that were labeled with two different colors that make "striped" filaments, where the previous pre-assembled sections are visible [19, 20]. This assembly pattern is typical for polymer step-growth [32], which is in contrast to actin and tubulin polymerization, where the monomers are globular and subunits are successively added to the polar polymer [5]. Moreover, IFs form without the consumption of nucleoside triphosphates [5].

The assembly kinetics of IFs are influenced by the protein concentration, and filament formation slows down at low concentrations [16, 27, 30]. The assembly speed as well as the resulting filament structure are highly sensitive to temperature, variation of ionic species and ion concentration, and pH [17, 33–38]. The assembly process is reversible: By simply reducing the ionic strength of the buffer, filaments disassemble [30] into tetramers from which they can, once again, reassemble into filaments [30]. In cells, disassembly of the IF networks and filaments, for example during cell division, is induced by phosphorylation [39].

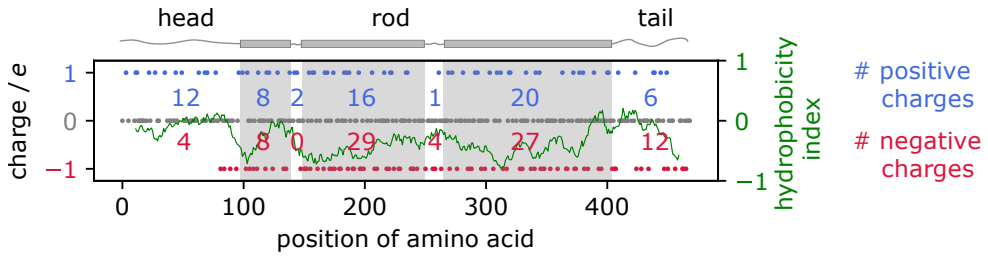

Fig. 2.4: **Charge and hydrophobicity patterns in human vimentin.** Comparison of the total number of positive to negative charges at pH 7.4 results in a net positive charge of the head domain and a net negative charge of the tail domain. The overall monomer has a negative net charge. The hydrophobicity based on Ref. [40], calculated with a moving mean over 21 amino acids [41]. Figure based on Ref. [42].

The self-assembly of IFs depends on the distribution of charges and hydrophobic residues along the sequence [43, 44]. As shown in Fig. 2.4, the head domain is mostly positively charged, and the tail has a negative net charge. Regions that are in close proximity in the tetramer have "patches" of opposing charges, for

example, the positive net charge of L1 and the negatively charged last segment of coil 1B [43]. The overall negative charge of -19 e gives an indication as of why vimentin assembly beyond the tetramer stage is induced by cation addition; in typical assembly conditions, 100 mM KCl [45] are used, but some assembly already occurs at concentrations as low as 10 mM [34, 38], and 50 mM KCl are sufficient for the formation of filaments [35].
Studies of mutants with deletions of the head or tail domains have shown that the head domain is crucial for assembly beyond the dimer and tetramer stage [46–48], whereas vimentin proteins lacking the tail domain form filaments [13]. In the current understanding, the tail domains protrude from the core of the filament [9] like a negatively charged brush [34, 36] and are heavily involved in filament-to-filament interactions [49–52].
Whereas atomistic models of parts of the monomer, dimer, and tetramer have allowed for a better understanding of the tetramer structure of vimentin [43, 44, 53, 54], the exact arrangements of the substructures within the filament are still mostly unknown [24, 44, 55]. Very recently, cryo electron tomography of vimentin filaments in cells has revealed the organization of octameric subunits within the filaments, where parallel subunits are linked by the head and coil 1A domains [56]. A study where a dimer of coil 2 segments was "unzipped" by pulling the monomers apart with OTs, revealed high, structure-stabilizing, internal forces in some areas and weaker inter-dimer interactions in other parts of the sequence [57]. These findings indicate that specific intra-filament interactions are the key to the structural and mechanical integrity of the filament.

2.2 MECHANICAL PROPERTIES OF SINGLE INTERMEDIATE FILAMENTS

Different properties are relevant to describing the mechanical characteristics of a filament. Two questions are investigated in the following: How does a filament respond to bending and how does it behave during stretching?

2.2.1 Persistence length

As described in section 3.3.3, the length scale where thermal energy leads to bending deformations of a filament is the persistence length l_p. While it is accepted that the persistence length of IFs is lower than for actin filaments (17.7 ± 1.1 µm) and microtubules (5200 ± 200 µm) [58], the exact values which were determined for vimentin IFs with various methods range from 0.4 - 2.1 µm [45, 49, 59–62], see Fig. 2.5. In general, methods where the flexibility was determined for filaments adsorbed to a surface, for example, negative staining electron microscopy or imaging with atomic force microscopy (AFM) [45], Fig. 2.5a, yield lower values for the persistence length than measurements without support [61, 62], Fig. 2.5b,c. This is caused by interactions with the support that lead to non-equilibrium conformations of the filaments and likely also additional unraveling of parts of the filaments. Such unraveled structures were observed in various negative staining electron micrographs and AFM images [62]. In measurements of vitrified IFs with cryo-electron tomography, Fig. 2.5c, long, straight sections of IFs were interrupted by more flexible, unraveled "hinges"

[62]. The persistence length of vimentin filaments as determined from rheology experiments is lower than the values discussed so far, see Fig. 2.5d. The discrepancy between the results of the different experimental methods may, besides the effect of interactions with the support or other filaments [63], be caused by the superposition of the bending and stretching responses of filaments in the network measurements.

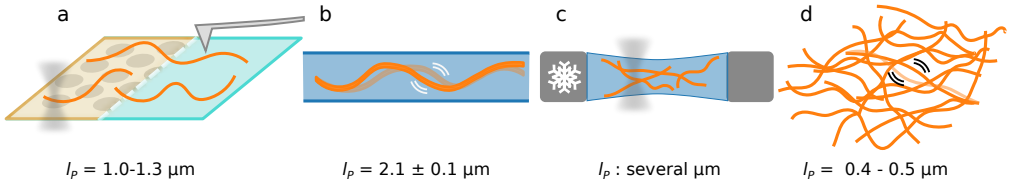

Fig. 2.5: **Experiments determining the persistence length of vimentin:** a) Tracing filaments, adsorbed to different solid supports, in electron microscopy (left) or AFM images (right) [45]; b) Fluctuations of a filament, confined in a microchannel [61]; c) Cryo-electron tomography [62]; d) Calculation of l_P from network mechanics [49, 59, 60].

2.2.2 Stretching response

The first single molecule stretching experiments with IFs revealed a huge potential for elongation: By dragging an AFM cantilever laterally through a filament that was adsorbed to a surface, a desmin filament was elongated up to 3.6-fold [64]. A sketch of the experiment is shown in Fig. 2.6a. The average extension before rupture measured for desmin with this setup was 2.8-fold, for keratin K5/K14 2.3-fold, and for neurofilaments 2.6-fold [64]. However, in these measurements, filaments were in direct contact with the surface throughout. By reducing the influence of the surface and pulling the IF away from the surface, as sketched in Fig. 2.6b, vimentin filaments were extended up to 4.5-fold [65]. The high extensibility has since been observed in multiple experiments [64–68], for example, by indenting single filaments in an IF network, supported by nuclear pore complexes, as shown in Fig. 2.6c [69].

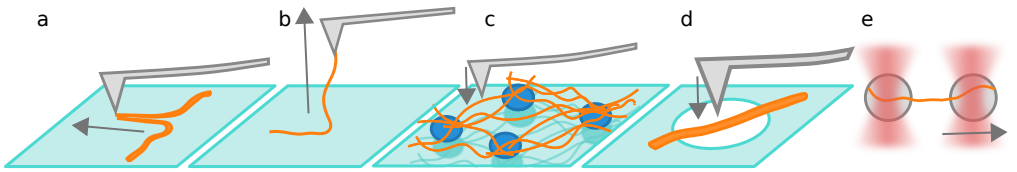

Fig. 2.6: **Experiments determining the stretching behavior of IFs.** a) Stretching IFs on a solid support by dragging an AFM cantilever across the IF [64, 66]. b) Stretching a single IF away from the support [65]. c) Indenting a single IF in a network, supported by nuclear pore complexes (blue) [69]. d) Indenting a pore-spanning IF with an AFM cantilever [70]. e) Stretching of a single IF using OTs and beads as handles [65, 67, 68, 71].

During the extension of single IFs, for example by indenting a pore-spanning filament with an AFM cantilever as shown in Fig. 2.6d, the force-extension response is linear, as for a Hookian spring [65, 66, 70]. This linear force-extension

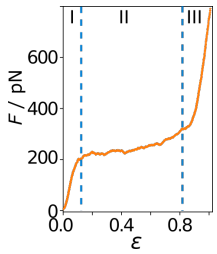

Fig. 2.7: Typical force (F)-strain (ε) curve of a single vimentin filament, stretched by OTs. The three regimes I) linear extension, II) plateau-like, and III) subsequent, stiff response are indicated.

behavior has also been observed for IF-based and IF-like structures such as hair, wool, and hagfish slime threads [72–75]. At higher extensions, however, the force-strain curve shows a characteristic, non-linear shape which was revealed, for example, by AFM stretching of desmin, vimentin, and lamin A [65, 66, 69], and has been extensively studied by stretching single vimentin filaments with OTs as shown in Fig. 2.6e [65, 67, 68, 71]. For forces up to ∼1 nN, the three regimes shown in Fig. 2.7 are observed: At small extensions (I), the previously described, linear regime is observed. The slope then drastically decreases and the filament extends further with only little additional pulling force, resulting in a plateau-like regime (II). At high extensions, the slope is increased with respect to the plateau regime (III). This three-regime stretching is reminiscent of the response of α helices and coiled-coils to stretching [76–79], which indicates that the shape of the force-strain curve originates from structural changes in the filament. Early studies of the extension behavior of wool and hair with wide-angle X-ray scattering (WAXS) already revealed that the coiled-coil and α-helical contributions reduce upon stretching, and a new feature appears in the diffraction pattern that is characteristic of β sheets [74, 80–82]. This conformational change has since also been detected for stretched vimentin hydrogels by WAXS [83] and vimentin bundles by Raman scattering [84]. However, in all of these methods, gels and bundles of IFs were stretched. Simulations have been useful to understand which conformational changes accompany which regime in the force-strain curves. Molecular dynamics simulations of the stretching of vimentin dimers and tetramers [69, 85, 86] have shown the unfolding of α helices upon stretching and the formation of β sheets at high strains. Descriptions of the force-strain curves, obtained by stretching vimentin filaments with OTs, by a two state model where each α helix consists of a spring, attached to an equivalent-freely-jointed-chain, reproduce the pronounced plateau region by the subsequent unfolding of the α helices in the filament [65]. More sophisticated Monte-Carlo simulations of extension and retraction curves for vimentin reveal that β sheet formation is most likely irreversible [67, 68]. The structural changes by the unfolding of the α helices are not sufficient to explain the stretching response and enormous elongation potential of the filaments and are, most likely, accompanied by subunit sliding [45, 67, 70, 82, 85].

The extension-retraction curves used for these models reveal other remarkable properties of IFs: The filaments show a pronounced hysteresis during retraction, which allows them to dissipate large amounts of energy [66, 67]. This property allows IFs to act as "shock absorbers" in cells [67]. Moreover, repeated extension-retraction cycles show a softening of re-stretched filaments [67, 68]. This softening upon re-stretching was also previously observed for wool and hair [74], hagfish slime threads [75], and is most likely caused by irreversible structural changes [68].

Another characteristic of IFs is their loading-rate dependent response to stretching. A filament that is stretched at a high speed shows a steeper force-extension curve and is less extensible at the same force than a filament stretched at a low speed [65, 76, 85–87]. This loading-rate dependent force response matches, again, observations reported for the stretching of wool fibers [73] and is typical for the strain response of α helices [79]. Such a loading-rate dependent stiffening

could allow cells to be protected against fast impact but to retain flexibility when slowly migrating through small spaces where they need to deform [65].

2.3 NETWORKS OF RECONSTITUTED INTERMEDIATE FILAMENTS

IF networks are soft and flexible; they can easily withstand large strains ε at which networks of actin filaments or microtubules rupture, see Fig. 2.8 [88, 89]. During deformation, IF networks display a highly nonlinear force response, a property that is reminiscent of the single filament mechanics. Whereas the response at low forces is mostly elastic, IF networks show a pronounced nonlinear strain stiffening [49, 51, 52, 60, 88, 89]. Strain stiffening is typical for many biopolymer networks [90], and often described by the deformation of a network of inextensible chains [91]. For vimentin networks, this description is sufficient at low strains where the response is dominated by entropic stretching. At intermediate strains, still in the strain stiffening regime, however, the filaments are extended and the model fails [49]. The strain stiffening is followed by a softening, which is attributed to structural reorganization within the network – an adaptation to the applied stress. The capability to adapt has been shown to depend on the interactions between filaments in the network: If the filaments are covalently connected to each other, no reorganization occurs and the softening is not observed [52]. By contrast, crosslinkers that bind transiently allow the network to maintain the structure on short time scales, this leads to the strain stiffening, but to rearrange on longer time scales.

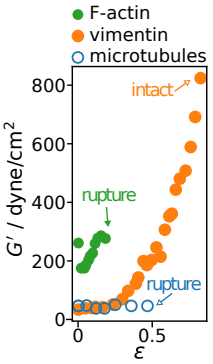

Fig. 2.8: Shear moduli of cytoskeletal filament networks. Vimentin remains undamaged, while actin filament (F-actin) and microtubule networks rupture. Data from Ref. [88].

For IF networks, no crosslinking proteins are necessary. IFs are polyelectrolytes, vimentin, for example, has an approximate surface charge density of $0.5\,e/\mathrm{nm}^2$ [92]. Because of the polyelectrolyte nature of the filaments, multivalent ions act as transient crosslinks [49, 52, 60, 93–95]. Through counter ion condensation of monovalent and multivalent cations on the surface of the filament, repulsions are screened. The accumulation of multivalent counter ions leads to attraction between filaments [96]. The addition of multivalent ions, typically divalent ions, thereby leads to an ion-concentration dependent stiffening which has been observed for keratins [94], neurofilaments [60], and vimentin [49, 60, 93, 95]. The multivalent ions therefore lead to point-like interactions and also promote bundle formation through multiple interaction sites [94, 95]. Studies of the structure of vimentin networks with fluorescence microscopy and electron microscopy at increasing concentrations of divalent ions show that low concentrations of divalent ions promote interactions. Increased interactions were observed as spontaneous parallel alignment of two filaments in solution, "zipping" [96], which causes bundling. At high concentrations of multivalent ions, the networks collapse into a dense, bundled structure [97, 98] where mechanical measurements become unreliable, for example, due to a drastic change of the mesh size [95, 99]. This so called "bundling concentration" varies for different ions and does not solely depend on the valency of the cation [38, 92, 95, 100]. The multivalent-ion sensitivity decreases for networks of tail-truncated or tail-mutated IFs [49, 52, 101], indicating that the tails are highly involved in inter-filament interactions. The tails have also been speculated to mediate direct interactions between actin filaments and vimentin [50].

The structure and the mechanical properties of IF networks not only depend on the concentration of multivalent ions but also on the protein concentration itself [51, 99], the temperature [99], and the assembly duration [50, 59]. Moreover, different measurement techniques, especially macroscopic shear rheology *vs.* microrheology, lead to different results. This discrepancy has been shown to decrease if amphiphilic molecules, which decrease the interfacial tension, are added to the air-liquid interface in shear rheology measurements. It is, however, possible that the amphiphilic molecules not only decrease the interfacial tension but also reduce hydrophobic interactions between filaments [51, 102].

2.4 INTERMEDIATE FILAMENT NETWORKS IN CELLS

2.4.1 Structure and function of intermediate filament networks in cells

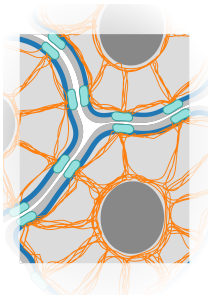

Fig. 2.9: Rim-and-spoke structure of keratin networks. Keratin filaments (orange) form a layer below the actin cortex (blue), and bundles in a radial arrangement. Keratin filaments are connected to desmosomes (light blue). Based on Ref. [109].

IF networks perform various functions in the cell and are, for example, involved in mechanical sensing processes, the organization of cell organelles [103–105], and provide cells with mechanical integrity and stability. Networks of keratins or vimentin form protective cages around the nucleus to prevent damage [106], and are highly involved in mechano transduction, see Refs. [104, 105, 107] for reviews.
The structures formed by the different IFs vary: Vimentin typically forms a dense perinuclear network and the density decreases towards the periphery [108]. The large variety of keratins comes with a large variety in their network structures. One remarkable keratin network structure that has, for example, been observed in blastocysts [110] and Madin-Darby Canine Kidney (MDCK) cells [109], manifests as a dense mesh work close to the nucleus with bundles of keratin radiating outwards to a layer of keratin beneath the actin cortex at the cell membrane, sketched in Fig. 2.9. The resemblance to a wagon wheel has given this structure the name "rim-and-spokes" [109]. At the cortex, the keratin bundles are attached to desmosomes and hemidesmosomes and lead to a seemingly continuous bundle structure in the neighboring cell. This connectivity provides high mechanical and structural integrity for tissues [111].

2.4.2 Intermediate filament networks and cell mechanics

Studies comparing cells with and without vimentin networks by employing active microrheology with OTs have found that the cytoplasm is stiffer if the vimentin network is intact [112, 113]. These measurements further reveal that more energy is dissipated in cells with vimentin networks, compared to the vimentin knock-out (KO) cells. Cell stiffness measurements with AFM have shown that cells expressing vimentin are stiffer than KO cells [108, 114, 115] and that vimentin contributes to the cortical [116] and cytoplasmic stiffness [115]. However, the results of these measurements are strongly dependent on the shape of the AFM tip [115] and the region of the cell that is probed [117]. Another factor that influences the outcome of such cell mechanics measurements is how much the cells are spread. Some studies, for example magnetic bead twisting assays, report a higher contribution of the vimentin network in cells that have

spread to a large area [118, 119]. Vimentin limits the deformation of the nucleus and thereby protects the nucleus against rupture at strong cellular deformations [108, 114] and has been shown to be crucial for cell viability in deformed cells [113].
The mechanical contribution of keratin IFs to cell mechanics has been studied by comparing cells expressing wild-type (wt) keratins to keratin KO cells. Force-indentation measurements with AFM and experiments with magnetic tweezers showed that keratin KO cells are softer and have a larger viscous contribution to their mechanical response than cells with wt keratin networks. Interestingly, the loss of keratin does not affect the structure of the microtubule or F-actin networks [120]. A similar comparison employing an optical stretcher, *i.e.*, the deformation of single cells by a laser beam, showed that keratin KO cells are more deformable. The higher deformability is accompanied by more invasive behavior [121]. The loss of keratin further decreases the mechano coupling between cells, which impedes the collective behavior of cultured cells [106].

2.4.3 **Keratin networks in cells under load**

The keratin network in cells is remarkably resilient, even at high strains. In cells stretched up to 133% uniaxial strain, sketched in Fig. 2.10a, the keratin network remains undamaged and cell viability high [122, 123]. The bundles become straight at high strains when stretched on a support, see Fig. 2.10b, as well as in stretched, free-standing cell monolayers [124] indicating that they become load bearing and play a crucial role for cell integrity [122, 123]. After the strain is released, the bundles buckle and look wavy [111, 122, 125]. Cells that are subjected to equibiaxial strain, sketched in Fig. 2.10c, show a similar response: The bundles become load bearing at high strains [111, 126]. This response was observed in alveolar cells that were stretched equibiaxially on an elastic support, Fig. 2.10c,d, with an area increase of up to 30% [111], as well as in kidney epithelial cells that were stretched by inducing the formation of expanding, freestanding "domes", see Fig. 2.10e,f [126]. Laser cutting of taut keratin bundles in highly stretched cells proved that these bundles are crucial for maintaining the cell shape at high strains [126]. Phosphorylation of keratin has been shown to increase in stretched cells [111], where the network in the periphery of the cells is phosphorylated the most [125].

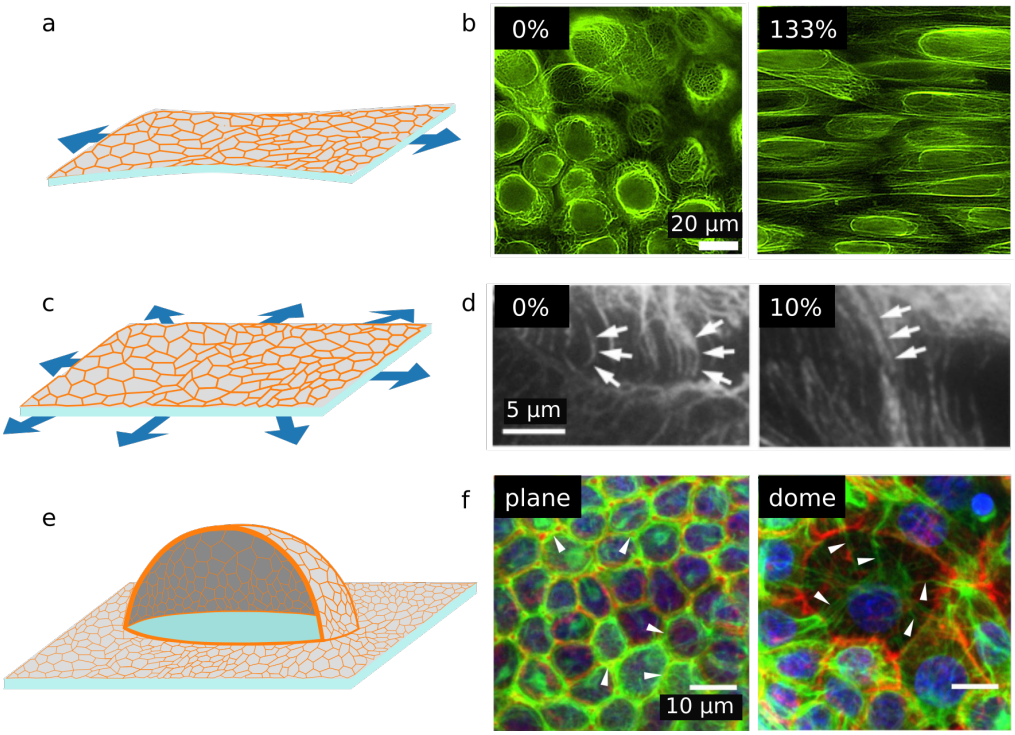

Fig. 2.10: **Keratin networks in cells under load.** a) Uniaxial deformation of a cell layer (cell outline in orange) on an elastic support. b) The keratin network in alveolar cells before straining and at 133% uniaxial strain. Reproduced with permission from Beriault *et al.*, 2012, Ref. [123]. c) Equibiaxial deformation of a cell layer on an elastic support. d) Keratin bundles in two alveolar cells, connected to the desmosomes. The cells are imaged before straining and at 10% area increase from equibiaxial strain. Curved bundles in relaxed cells (left), and straight bundles in stretched cells (right) are indicated by white arrows. Reproduced with permission from Felder *et al.*, 2008, Ref. [111]. e) Deformation of cells by formation of a free-standing "dome". f) Left: Unstretched cells on the support. The keratin network is stained in green, F-actin in red, and the nucleus in blue . Right: Stretched cells at the apex of the dome. Keratin bundles are indicated by white arrows. Reprinted with permission ©Springer, Nature, 2018, Latorre *et al.* Ref [126].

REFERENCES

[1] J. E. Eriksson et al. "Introducing Intermediate Filaments : From Discovery to Disease." *J. Clin. Invest.* 119 (2009), pp. 1763–1771. DOI: 10.1172/JCI38339.cells.

[2] A. Szent-Györgyi. "Das kontraktile Element des Muskels." *Ber. Dtsch. Chem. Ges.* 75 (1942), pp. 1868–1870. DOI: 10.1002/cber.19420751264.

[3] B. Bugyi and M. Kellermayer. "The discovery of actin: "to see what everyone else has seen, and to think what nobody has thought"." *J. Muscle Res. Cell Motil.* 41 (2020), pp. 3–9. DOI: 10.1007/s10974-019-09515-z.

[4] G. Borisy et al. "Microtubules: 50 years on from the discovery of tubulin." *Nat. Rev. Mol. Cell Biol.* 17 (2016), pp. 322–328. DOI: 10.1038/nrm.2016.45.

[5] B. Alberts et al. *Molecular biology of the cell*. Vol. 6. W. W. Norton & Company, 2014.

[6] I. Szeverenyi et al. "The Human Intermediate Filament Database: Comprehensive Information on a Gene Family Involved in Many Human Diseases." *Hum. Mutat.* 29 (2008), pp. 351–360. DOI: 10.1002/humu.20652.

[7] S. A. Eldirany et al. "Recent insight into intermediate filament structure." *Curr. Opin. Cell Biol.* 68 (2021), pp. 132–143. DOI: 10.1016/J.CEB.2020.10.001.

[8] N. Geisler and K. Weber. "The amino acid sequence of chicken muscle desmin provides a common structural model for intermediate filament proteins." *EMBO J.* 1 (1982), pp. 1649–1656. DOI: 10.1002/j.1460-2075.1982.tb01368.x.

[9] P. M. Steinert et al. "Complete amino acid sequence of a mouse epidermal keratin subunit and implications for the structure of intermediate filaments." *Nature* 302 (1983), pp. 794–800. DOI: 10.1038/302794a0.

[10] H. Herrmann and U. Aebi. "Intermediate Filaments : Structure and Assembly." *Cold Spring Harbor Perspect. Biol.* 8 (2016), a018242. DOI: 10.1101/cshperspect.a018242.

[11] H. Herrmann, L. Kreplak, and U. Aebi. "Isolation, Characterization, and In Vitro Assembly of Intermediate Filaments." *Methods in Cell Biology*. Vol. 78. Academic Press, 2004, pp. 3–24. DOI: 10.1016/S0091-679X(04)78001-2.

[12] R. A. Quinlan et al. "Characterization of dimer subunits of intermediate filament proteins." *J. Mol. Biol.* 192 (1986), pp. 337–349. DOI: 10.1016/0022-2836(86)90369-4.

[13] H. Herrmann et al. “Structure and Assembly Properties of the Intermediate Filament Protein Vimentin: The Role of its Head, Rod and Tail Domains.” *J. Mol. Biol.* 264 (1996), pp. 933–953. DOI: 10.1006/jmbi.1996.0688.

[14] A. A. Chernyatina, D. Guzenko, and S. V. Strelkov. “Intermediate Filament Structure: The Bottom-Up Approach.” *Curr. Opin. Cell Biol.* 32 (2015), pp. 65–72. DOI: 10.1016/j.ceb.2014.12.007.

[15] A. Aziz et al. “Site-directed spin labeling and electron paramagnetic resonance determination of vimentin head domain structure.” *J. Biol. Chem.* 285 (2010), pp. 15278–15285. DOI: 10.1074/jbc.M109.075598.

[16] N. Mücke et al. “Molecular and biophysical characterization of assembly-starter units of human vimentin.” *J. Mol. Biol.* 340 (2004), pp. 97–114. DOI: 10.1016/j.jmb.2004.04.039.

[17] H. Herrmann et al. “Characterization of distinct early assembly units of different intermediate filament proteins.” *J. Mol. Biol.* 286 (1999), pp. 1403–1420. DOI: 10.1006/jmbi.1999.2528.

[18] R. Kirmse et al. “A quantitative kinetic model for the in vitro assembly of intermediate filaments from tetrameric vimentin.” *J. Biol. Chem.* 282 (2007), pp. 18563–18572. DOI: 10.1074/jbc.M701063200.

[19] S. Winheim et al. “Deconstructing the Late Phase of Vimentin Assembly by Total Internal Reflection Fluorescence Microscopy (TIRFM).” *PLoS ONE* 6 (2011), e19202. DOI: 10.1371/journal.pone.0019202.

[20] B. Nöding, H. Herrmann, and S. Köster. “Direct Observation of Subunit Exchange Along Mature Vimentin Intermediate Filaments.” *Biophys. J.* 107 (2014), pp. 2923–2931. DOI: 10.1016/j.bpj.2014.09.050.

[21] D. Henderson, N. Geisler, and K. Weber. “A periodic ultrastructure in intermediate filaments.” *J. Mol. Biol.* 155 (1982), pp. 173–176. DOI: 10.1016/0022-2836(82)90444-2.

[22] P. M. Steinert, L. N. Marekov, and D. A. D. Parry. “Diversity of intermediate filament structure. Evidence that the alignment of coiled-coil molecules in vimentin is different from that in keratin intermediate filaments.” *J. Biol. Chem.* 268 (1993), pp. 24916–24925. DOI: 10.1016/S0021-9258(19)74552-9.

[23] H. Herrmann and U. Aebi. “Intermediate filament assembly: fibrillogenesis is driven by decisive dimer-dimer interactions.” *Curr. Opin. Struc. Biol.* 8 (1998), pp. 177–185. DOI: 10.1016/S0959-440X(98)80035-3.

[24] S. V. Strelkov, H. Herrmann, and U. Aebi. “Molecular architecture of intermediate filaments.” *BioEssays* 25 (2003), pp. 243–251. DOI: 10.1002/bies.10246.

[25] M.S. Weber et al. “Structural heterogeneity of cellular K5/K14 filaments as revealed by cryo-electron microscopy.” *eLife* 10 (2021). DOI: 10.7554/elife.70307.

[26] S. Portet et al. "Vimentin Intermediate Filament Formation: In Vitro Measurement and Mathematical Modeling of the Filament Length Distribution during Assembly." *Langmuir* 25 (2009), pp. 8817–8823. DOI: 10.1021/la900509r.

[27] C. G. Lopez et al. "Lateral association and elongation of vimentin intermediate filament proteins: A time-resolved light-scattering study." *Proc. Natl. Acad. Sci.* 113 (2016), pp. 11152–11157. DOI: 10.1073/pnas.1606372113.

[28] N. Mücke et al. "In Vitro Assembly Kinetics of Cytoplasmic Intermediate Filaments: A Correlative Monte Carlo Simulation Study." *PLoS ONE* 11 (2016), e0157451. DOI: 10.1371/journal.pone.0157451.

[29] M. E. Brennich et al. "Dynamics of Intermediate Filament Assembly Followed in Micro-Flow by Small Angle X-Ray Scattering." *Lab Chip* 11 (2011), pp. 8708–716. DOI: 10.1039/C0LC00319K.

[30] N. Mücke et al. "Assembly Kinetics of Vimentin Tetramers to Unit-Length Filaments: A Stopped-Flow Study." *Biophys. J.* 114 (2018), pp. 2408–2418. DOI: 10.1016/j.bpj.2018.04.032.

[31] E. Perego and S. Köster. "Exploring early time points of vimentin assembly in flow by fluorescence fluctuation spectroscopy." *Lab Chip* 21 (2021), pp. 735–745. DOI: 10.1039/D0LC00985G.

[32] P. J. Flory. "Molecular Size Distribution in Linear Condensation Polymers." *J. Am. Chem. Soc.* 58 (1936), pp. 1877–1885. DOI: 10.1021/ja01301a016.

[33] R. Kirmse et al. "Plasticity of Intermediate Filament Subunits." *PLoS ONE* 5 (2010), e12115. DOI: 10.1371/journal.pone.0012115.

[34] M. E. Brennich et al. "Impact of ion valency on the assembly of vimentin studied by quantitative small angle X-ray scattering." *Soft Matter* 10 (2014), pp. 2059–2068. DOI: 10.1039/C3SM52532E.

[35] C. G. Lopez et al. "Effect of ionic strength on the structure and elongational kinetics of vimentin filaments." *Soft Matter* 14 (2018), pp. 8445–8454. DOI: 10.1039/C8SM01007B.

[36] M. E. Brennich et al. "Mutation-induced alterations of intra-filament subunit organization in vimentin filaments revealed by SAXS." *Soft Matter* 15 (2019), pp. 1999–2008. DOI: 10.1039/c8sm02281j.

[37] A. Mónico et al. "Zinc Differentially Modulates the Assembly of Soluble and Polymerized Vimentin." *Int. J. Mol. Sci.* 21 (2020), pp. 1–20. DOI: 10.3390/ijms21072426.

[38] M. Denz et al. "Ion type and valency differentially drive vimentin tetramers into intermediate filaments or higher order assemblies." *Soft Matter* 17 (2021), pp. 870–878. DOI: 10.1039/d0sm01659d.

[39] J. E. Eriksson et al. "Specific In Vivo Phosphorylation Sites Determine the Assembly Dynamics of Vimentin Intermediate Filaments." *J. Cell Sci.* 117 (2004), pp. 919–932.

[40] R. Cowan and R. G. Whittaker. "Hydrophobicity indices for amino acid residues as determined by high-performance liquid chromatography." *Pept. Res.* 3 (1990), pp. 75–80.

[41] E. Gasteiger et al. "Protein Identification and Analysis Tools on the ExPASy Server." *The Proteomics Protocols Handbook*. Humana Press, 2005, pp. 571–607. DOI: 10.1385/1-59259-890-0:571.

[42] A. V. Schepers, C. Lorenz, and S. Köster. "Tuning Intermediate Filament Mechanics by Variation of pH and Ion Charges." *Nanoscale* 12 (2020), pp. 15236–15245. DOI: 10.1039/D0NR02778B.

[43] A. A. Chernyatina et al. "Atomic structure of the vimentin central -helical domain and its implications for intermediate filament assembly." *Proc. Natl. Acad. Sci.* 109 (2012), pp. 13620–13625. DOI: 10.1073/pnas.1206836109.

[44] A. Premchandar et al. "Structural dynamics of the vimentin coiled-coil contact regions involved in filament assembly as revealed by hydrogen-deuterium exchange." *J. Biol. Chem.* 291 (2016), pp. 24931–24950. DOI: 10.1074/jbc.M116.748145.

[45] N. Mücke et al. "Assessing the Flexibility of Intermediate Filaments by Atomic Force Microscopy." *J. Mol. Biol.* 335 (2004), pp. 1241–1250. DOI: 10.1016/j.jmb.2003.11.038.

[46] P. Traub and C. E. Vorgias. "Involvement of the N-terminal polypeptide of vimentin in the formation of intermediate filaments." *J. Cell Sci.* 63 (1983), pp. 43–67. DOI: 10.1242/JCS.63.1.43.

[47] H. Herrmann, I. Hofmann, and W. W. Franke. "Identification of a non-apeptide motif in the vimentin head domain involved in intermediate filament assembly." *J. Mol. Biol.* 223 (1992), pp. 637–650. DOI: 10.1016/0022-2836(92)90980-X.

[48] X. Zhou et al. "Transiently structured head domains control intermediate filament assembly." *Proc. Natl. Acad. Sci.* 118 (2021), e2022121118. DOI: 10.1073/pnas.2022121118.

[49] Y.-C. Lin et al. "Divalent Cations Crosslink Vimentin Intermediate Filament Tail Domains to Regulate Network Mechanics." *J. Mol. Biol.* 399 (2010), pp. 637–644. DOI: 10.1016/j.jmb.2010.04.054.

[50] O. Esue et al. "A direct interaction between actin and vimentin filaments mediated by the tail domain of vimentin." *J. Biol. Chem.* 281 (2006), pp. 30393–30399. DOI: 10.1074/jbc.M605452200.

[51] P. Pawelzyk et al. "Attractive Interactions Among Intermediate Filaments Determine Network Mechanics In Vitro." *PLoS ONE* 9 (2014), e93194. DOI: 10.1371/journal.pone.0093194.

[52] A. Aufderhorst-Roberts and G. H. Koenderink. "Stiffening and Inelastic Fluidization in Vimentin Intermediate Filament Networks." *Soft Matter* 15 (2019), pp. 7127–7136. DOI: 10.1039/C9SM00590K.

[53] S. V. Strelkov et al. "Conserved segments 1A and 2B of the intermediate filament dimer: Their atomic structures and role in filament assembly." *EMBO J.* 21 (2002), pp. 1255–1266. DOI: 10.1093/emboj/21.6.1255.

[54] M. Meier et al. "Vimentin Coil 1A-A Molecular Switch Involved in the Initiation of Filament Elongation." *J. Mol. Biol.* 390 (2009), pp. 245–261. DOI: 10.1016/j.jmb.2009.04.067.

[55] A. V. Sokolova et al. "Monitoring intermediate filament assembly by small-angle x-ray scattering reveals the molecular architecture of assembly intermediates." *Proc. Natl. Acad. Sci.* 103 (2006), pp. 16206–16211. DOI: 10.1073/pnas.0603629103.

[56] M. Eibauer et al. "The molecular architecture of vimentin filaments." *bioRxiv* (2021). accessed on 2021-07-31. DOI: 10.1101/2021.07.15.452584.

[57] B. Ramm et al. "Sequence-resolved free energy profiles of stress-bearing vimentin intermediate filaments." *Proc. Natl. Acad. Sci.* 111 (2014), pp. 11359–11364. DOI: 10.1073/pnas.1403122111.

[58] F. Gittes et al. "Flexural rigidity of microtubules and actin filaments measured from thermal fluctuations in shape." *J. Cell Biol.* 120 (1993), pp. 923–934. DOI: 10.1083/jcb.120.4.923.

[59] M. Schopferer et al. "Desmin and Vimentin Intermediate Filament Networks: Their Viscoelastic Properties Investigated by Mechanical Rheometry." *J. Mol. Biol.* 388 (2009), pp. 133–143. DOI: 10.1016/j.jmb.2009.03.005.

[60] Y.-C. Lin et al. "Origins of elasticity in intermediate filament networks." *Phys. Rev. Lett.* 104 (2010), p. 058101. DOI: 10.1103/PhysRevLett.104.058101.

[61] B. Nöding and S. Köster. "Intermediate Filaments in Small Configuration Spaces." *Phys. Rev. Lett.* 108 (2012), p. 088101. DOI: 10.1103/PhysRevLett.108.088101.

[62] K. N. Goldie et al. "Dissecting the 3-D structure of vimentin intermediate filaments by cryo-electron tomography." *J. Struct. Biol.* 158 (2007), pp. 378–385. DOI: 10.1016/j.jsb.2006.12.007.

[63] J. Block et al. "Physical Properties of Cytoplasmic Intermediate Filaments." *Biochim. Biophys. Acta, Mol. Cell Res.* 1853 (2015), pp. 3053–3064. DOI: 10.1016/j.bbamcr.2015.05.009.

[64] L. Kreplak et al. "Exploring the Mechanical Behavior of Single Intermediate Filaments." *J. Mol. Biol.* 354 (2005), pp. 569–577. DOI: 10.1016/j.jmb.2005.09.092.

[65] J. Block et al. "Nonlinear Loading-Rate-Dependent Force Response of Individual Vimentin Intermediate Filaments to Applied Strain." *Phys. Rev. Lett.* 118 (2017), p. 048101. DOI: 10.1103/PhysRevLett.118.048101.

[66] L. Kreplak, H. Herrmann, and U. Aebi. "Tensile Properties of Single Desmin Intermediate Filaments." *Biophys. J.* 94 (2008), pp. 2790–2799. DOI: 10.1529/biophysj.107.119826.

[67] J. Block et al. "Viscoelastic Properties of Vimentin Originate from Nonequilibrium Conformational Changes." *Sci. Adv.* 4 (2018), eaat1161. DOI: 10.1126/sciadv.aat1161.

[68] J. Forsting et al. "Vimentin Intermediate Filaments Undergo Irreversible Conformational Changes During Cyclic Loading." *Nano Lett.* 19 (2019), pp. 7349–7356. DOI: 10.1021/acs.nanolett.9b02972.

[69] K. T. Sapra et al. "Nonlinear mechanics of lamin filaments and the meshwork topology build an emergent nuclear lamina." *Nat. Commun.* 11 (2020), p. 6205. DOI: 10.1038/s41467-020-20049-8.

[70] C. Guzmán et al. "Exploring the Mechanical Properties of Single Vimentin Intermediate Filaments by Atomic Force Microscopy." *J. Mol. Biol.* 360 (2006), pp. 623–630. DOI: 10.1016/j.jmb.2006.05.030.

[71] J. Kraxner et al. "Post-translational modifications soften vimentin intermediate filaments." *Nanoscale* 13 (2021), pp. 380–387. DOI: 10.1039/d0nr07322a.

[72] S. A. Shorter. "An investigation of the nature of the elasticity of fibres." *J. Text. Inst., Trans.* 15 (1924), T207–T229. DOI: 10.1080/19447022408661298.

[73] J. B. Speakman. "The intracellular structure of the wool fibre." *J. Text. Inst., Trans.* 18 (1927), T431–T453. DOI: 10.1080/19447022708661427.

[74] W. T. Astbury and A. Street. "X-ray studies of the structure of hair, wool, and related fibres." *J. Philos. Trans. R. Soc., A* 230 (1931), pp. 75–101. DOI: 10.1098/rsta.1932.0003.

[75] D. S. Fudge et al. "The mechanical properties of hydrated intermediate filaments: insights from hagfish slime threads." *Biophys. J.* 85 (2003), pp. 2015–2027. DOI: 10.1016/S0006-3495(03)74629-3.

[76] T. Ackbarow and M. J. Buehler. "Superelasticity, Energy Dissipation and Strain Hardening of Vimentin Coiled-Coil Intermediate Filaments: Atomistic and Continuum Studies." *J. Mater. Sci.* 42 (2007), pp. 8771–8787. DOI: 10.1007/s10853-007-1719-2.

[77] M. Goktas et al. "Molecular Mechanics of Coiled Coils Loaded in the Shear Geometry." *Chem. Sci.* 9 (2018), pp. 4610–4621. DOI: 10.1039/c8sc01037d.

[78] P. López-García et al. "Structural Determinants of Coiled Coil Mechanics." *Phys. Chem. Chem. Phys.* 21 (2019), pp. 9145–9149. DOI: 10.1039/C9CP00665F.

[79] A. E. Bergues-Pupo, R. Lipowsky, and A. Vila Verde. "Unfolding mechanism and free energy landscape of single, stable, alpha helices at low pull speeds." *Soft Matter* 16 (2020), pp. 9917–9928. DOI: 10.1039/D0SM01166E.

[80] W. T. Astbury and H. J. Woods. "X-Ray Studies of the Structure of Hair, Wool, and Related Fibres. II.-The Molecular Structure and Elastic Properties of Hair Keratin." *J., Phil. Trans. Roy. Soc., A* 232 (1933), pp. 333–394. DOI: 10.1098/rsta.1934.0010.

[81] E. G. Bendit. "The α-β Transformation in keratin." *Nature* 179 (1957), p. 535. DOI: 10.1038/179535a0.

[82] L. Kreplak et al. "New aspects of the alpha-helix to beta-sheet transition in stretched hard alpha-keratin fibers." *Biophys. J.* 87 (2004), pp. 640–647. DOI: 10.1529/biophysj.103.036749.

[83] N. Pinto et al. "Self-Assembly Enhances the Strength of Fibers Made from Vimentin Intermediate Filament Proteins." *Biomacromolecules* 15 (2014), pp. 574–581. DOI: 10.1021/bm401600a.

[84] F. Fleissner et al. "Tension Causes Unfolding of Intracellular Vimentin Intermediate Filaments." *Adv. Biosyst.* 4 (2020), p. 2000111. DOI: 10.1002/adbi.202000111.

[85] Z. Qin, L. Kreplak, and M. J. Buehler. "Hierarchical Structure Controls Nanomechanical Properties of Vimentin Intermediate Filaments." *PLoS ONE* 4 (2009), e7249. DOI: 10.1371/journal.pone.0007294.

[86] Z. Qin, L. Kreplak, and M. J. Buehler. "Nanomechanical properties of vimentin intermediate filament dimers." *Nanotechnology* 20 (2009), p. 425101. DOI: 10.1088/0957-4484/20/42/425101.

[87] T. Ackbarow and M. J. Buehler. "Molecular mechanics of stutter defects in vimentin intermediate filaments." *Exp. Mech.* 49 (2009), pp. 79–89. DOI: 10.1007/s11340-007-9100-6.

[88] P. A. Janmey et al. "Viscoelastic Properties of Vimentin Compared with Other Filamentous Biopolymer Networks." *J. Cell Biol.* 113 (1991), pp. 155–160. DOI: 10.1083/jcb.113.1.155.

[89] T. Golde et al. "Glassy dynamics in composite biopolymer networks." *Soft Matter* 14 (2018), pp. 7970–7978. DOI: 10.1039/C8SM01061G.

[90] C. Storm et al. "Nonlinear elasticity in biological gels." *Nature* 435 (2005), pp. 191–194. DOI: 10.1038/nature03521.

[91] C. P. Broedersz and F. C. Mackintosh. "Modeling semiflexible polymer networks." *Rev. Mod. Phys.* 86 (2014), pp. 995–1036. DOI: 10.1103/RevModPhys.86.995.

[92] P. A. Janmey et al. "Polyelectrolyte properties of filamentous biopolymers and their consequences in biological fluids." *Soft Matter* 10 (2014), pp. 1439–1449. DOI: 10.1039/c3sm50854d.

[93] S. Köster et al. "Nanomechanics of vimentin intermediate filament networks." *Soft Matter* 6 (2010), p. 1910. DOI: 10.1039/c000113a.

[94] A. Leitner et al. "Properties of intermediate filament networks assembled from keratin 8 and 18 in the presence of Mg^{2+}." *Biophys. J.* 103 (2012), pp. 195–201. DOI: 10.1016/j.bpj.2012.06.014.

[95] H. Wu et al. "Effect of divalent cations on the structure and mechanics of vimentin intermediate filaments." *Biophys. J.* 119 (2020), pp. 55–64. DOI: 10.1016/j.bpj.2020.05.016.

[96] C. Dammann, H. Herrmann, and S. Köster. "Competitive Counterion Binding Regulates the Aggregation Onset of Vimentin Intermediate Filaments." *Isr. J. Chem.* 56 (2016), pp. 614–621. DOI: 10.1002/ijch.201400153.

[97] C. Dammann, B. Nöding, and S. Köster. "Vimentin networks at tunable ion-concentration in microfluidic drops." *Biomicrofluidics* 6 (2012), p. 022009. DOI: 10.1063/1.4705103.

[98] C. Dammann and S. Köster. "Dynamics of Counterion-Induced Attraction between Vimentin Filaments Followed in Microfluidic Drops." *Lab Chip* 14 (2014), pp. 2681–2687. DOI: 10.1039/c3lc51418h.

[99] J. Kayser et al. "Assembly Kinetics Determine the Structure of Keratin Networks." *Soft Matter* 8 (2012), p. 8873. DOI: 10.1039/C2SM26032H.

[100] K. Cruz et al. "Polyelectrolyte Gels Formed by Filamentous Biopolymers: Dependence of Crosslinking Efficiency on the Chemical Softness of Divalent Cations." *Gels* 7 (2021), p. 41. DOI: 10.3390/gels7020041.

[101] H. Bär et al. "Mutations in Desmin's Carboxy-Terminal "Tail" Domain Severely Modify Filament and Network Mechanics." *J. Mol. Biol.* 397 (2010), pp. 1188–1198. DOI: 10.1016/J.JMB.2010.02.024.

[102] S. Yamada, D. Wirtz, and P. A. Coulombe. "The Mechanical Properties of Simple Epithelial Keratins 8 and 18: Discriminating Between Interfacial and Bulk Elasticities." *J. Struct. Biol.* 143 (2003), pp. 45–55. DOI: 10.1016/S1047-8477(03)00101-1.

[103] E. E. Charrier and P. A. Janmey. "Mechanical Properties of Intermediate Filament Proteins." *Methods in Enzymology*. Vol. 568. 2016, pp. 35–57. DOI: 10.1016/bs.mie.2015.09.009.

[104] R. Sanghvi-Shah and G. F. Weber. "Intermediate Filaments at the Junction of Mechanotransduction, Migration, and Development." *Front. Cell Dev. Biol.* 5 (2017). DOI: 10.3389/fcell.2017.00081.

[105] G. Dutour-Provenzano and S. Etienne-Manneville. "Intermediate filaments." *Curr. Biol.* 31 (2021), R522–R529. DOI: 10.1016/j.cub.2021.04.011.

[106] S. Karsch et al. "An intact keratin network is crucial for mechanical integrity and barrier function in keratinocyte cell sheets." *Cell. Mol. Life Sci.* 77 (2020), pp. 4397–4411. DOI: 10.1007/s00018-019-03424-7.

[107] A. E. Patteson et al. "The vimentin cytoskeleton: when polymer physics meets cell biology." *Phys. Biol.* 18 (2021), p. 011001. DOI: 10.1088/1478-3975/abbcc2.

[108] A. E. Patteson et al. "Vimentin protects cells against nuclear rupture and DNA damage during migration." *J. Cell Biol.* 218 (2019), pp. 4079–4092. DOI: 10.1083/jcb.201902046.

[109] R. A. Quinlan et al. "A rim-and-spoke hypothesis to explain the biomechanical roles for cytoplasmic intermediate filament networks." *J. Cell Sci.* 130 (2017), pp. 3437–3445. DOI: 10.1242/jcs.202168.

[110] N. Schwarz et al. "Dissection of keratin network formation, turnover and reorganization in living murine embryos." *Sci. Rep.* 5 (2015), p. 9007. DOI: 10.1038/srep09007.

[111] E. Felder et al. "Mechanical strain of alveolar type II cells in culture: changes in the transcellular cytokeratin network and adaptations." *Am. J. Physiol. Lung Cell Mol. Physiol.* 295 (2008), pp. L849–L857. DOI: 10.1152/ajplung.00503.2007.

[112] M. Guo et al. "The role of vimentin intermediate filaments in cortical and cytoplasmic mechanics." *Biophys. J.* 105 (2013), pp. 1562–1568. DOI: 10.1016/j.bpj.2013.08.037.

[113] J. Hu et al. "High stretchability, strength, and toughness of living cells enabled by hyperelastic vimentin intermediate filaments." *Proc. Natl. Acad. Sci.* 116 (2019), pp. 17175–17180. DOI: 10.1073/pnas.1903890116.

[114] L. D. C. Stankevicins et al. "Vimentin provides the mechanical resilience required for amoeboid migration and protection of the nucleus." *bioRxiv* (2019). accessed on 2021-06-26. DOI: 10.1101/720946.

[115] A. Vahabikashi et al. "Probe Sensitivity to Cortical versus Intracellular Cytoskeletal Network Stiffness." *Biophys. J.* 116 (2019), pp. 518–529. DOI: 10.1016/j.bpj.2018.12.021.

[116] Y. Messica et al. "The role of Vimentin in Regulating Cell Invasive Migration in Dense Cultures of Breast Carcinoma Cells." *Nano Lett.* 17 (2017), pp. 6941–6948. DOI: 10.1021/acs.nanolett.7b03358.

[117] A. E. Patteson et al. "Loss of Vimentin Enhances Cell Motility through Small Confining Spaces." *Small* 15 (2019), p. 1903180. DOI: 10.1002/smll.201903180.

[118] N. Wang and D. Stamenović. "Contribution of intermediate filaments to cell stiffness, stiffening, and growth." *Am. J. Physiol. Cell Physiol.* 279 (2000), pp. C188–C194. DOI: 10.1152/ajpcell.2000.279.1.c188.

[119] M. G. Mendez, D. Restle, and P. A. Janmey. "Vimentin Enhances Cell Elastic Behavior and Protects against Compressive Stress." *Biophys. J.* 107 (2014), pp. 314–323. DOI: 10.1016/j.bpj.2014.04.050.

[120] L. Ramms et al. "Keratins as the main component for the mechanical integrity of keratinocytes." *Proc. Natl. Acad. Sci.* 110 (2013), pp. 18513–18518. DOI: 10.1073/pnas.1313491110.

[121] K. Seltmann et al. "Keratins significantly contribute to cell stiffness and impact invasive behavior." *Proc. Natl. Acad. Sci.* 110 (2013), pp. 18507–18512. DOI: 10.1073/pnas.1310493110.

[122] D. Fudge et al. "The intermediate filament network in cultured human keratinocytes is remarkably extensible and resilient." *PLoS ONE* 3 (2008), e2327. DOI: 10.1371/journal.pone.0002327.

[123] D. R. Beriault et al. "The mechanical behavior of mutant K14-R125P keratin bundles and networks in NEB-1 keratinocytes." *PLoS ONE* 7 (2012), e31320. DOI: 10.1371/journal.pone.0031320.

[124] A. R. Harris et al. "Characterizing the mechanics of cultured cell monolayers." *Proc. Natl. Acad. Sci.* 109 (2012), pp. 16449–16454. DOI: 10.1073/pnas.1213301109.

[125] G. Fois et al. “Effects of keratin phosphorylation on the mechanical properties of keratin filaments in living cells.” *FASEB J.* 27 (2013), pp. 1322–1329. DOI: 10.1096/fj.12-215632.

[126] E. Latorre et al. “Active superelasticity in three-dimensional epithelia of controlled shape.” *Nature* 7730 (2018), pp. 6481–6487. DOI: 10.1021/ac8009643.

3 BIOPOLYMER MECHANICS – THEORETICAL AND EXPERIMENTAL PRINCIPLES

3.1 OPTICAL TWEEZERS

Light carries momentum, and when light interacts with matter, this momentum can be transferred. However, the momentum that is transmitted by a single photon is very small, for the wavelength of 1064 nm the momentum is only $6 \cdot 10^{-28}$ Ns small. In 1970, Arthur Ashkin calculated and demonstrated experimentally that with the high intensity of a laser beam, micron sized particles can be manipulated purely by light [1]. In these first versions of optical traps or optical tweezers (OTs), which he called laser levitation beams, small particles were held in the laser beam in two dimensions only, and they were pushed along the beam axis. Based on these observations, Ashkin further improved his setup to achieve 3D levitation of small polystyrene particles, first with two counter propagation laser beams [1], and, in 1986, by employing one single, strongly focused laser beam [2]. OTs were soon applied to biological systems as they allowed for unprecedented control by micromanipulation and the study of the micromechanical properties of a sample. The first biological OT experiments were performed by Ashkin himself, trapping living cells and cell organelles [3]. However, the first application of OTs as a means of measuring forces, *i.e.*, the compliance of the flagella for different bacteria, was reported by Steven Block in 1989 [4]. Only one year later, Ashkin was able to trap mitochondria in living cells and measure the forces that dynein motors exert on mitochondria that are transported along microtubules [5].
Since these early studies, OTs have been used to study the mechanical properties of living cells [6], single components in living cells [3, 7], double stranded DNA [8–10], reconstituted networks of cytoskeletal filaments [11, 12], single filaments [13], and even the forces holding single proteins together [14].
One prominent example that illustrates the nm and sub-pN sensitivity of OTs is the measurement of kinesin "walking" on microtubules. OTs were used to first measure that kinesin motors take 8 nm steps [15]. Recently, by employing improved probe particles that increase the resolution of the OT, it was found that these motors actually take 4 nm sub steps [16]. The maximum forces OTs can exert depend on the laser power and can reach up to several hundred pN, for example in Ref. [13].
In the following, the basic physical principles that allow the trapping of dielectric particles and the detection of forces and their analysis are described.

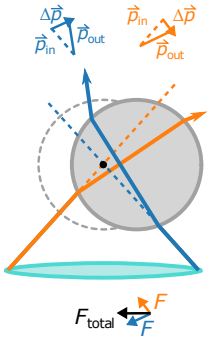

Fig. 3.1: Sketch of rays and momentum transfer for lateral deflection. The center of the trap is marked by a black dot.

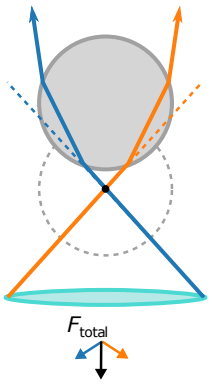

Fig. 3.2: Sketch of rays and momentum transfer for axial deflection in the beam direction.

3.1.1 Particle trapping

The trapping of dielectric particles with light is caused by the interaction of the focused laser light with the particle. It depends on the size of the particle relative to the wavelength λ of the trapping laser which physical principle is best suited to explain the trapping forces. The most intuitive picture is based on ray optics and is valid for large particles in the Mie size regime [17]. An incident ray is refracted when entering the particle. Momentum conservation leads to a momentum transfer from the ray to the particle, as described by Snell's law

$$n_m \, sin(\theta_{in}) = n_p \, sin(\theta_p) \,, \tag{3.1}$$

with the refractive indices n_m of the medium and n_p of the particle, and the incident angle θ_{in} and refracted angle in the particle θ_p. In Fig. 3.1, the refraction of two incoming rays by a particle that is laterally displaced from the beam focus is depicted. The momentum of each ray is changed by $\Delta\vec{p} = \vec{p}_{out} - \vec{p}_{in}$; $-\Delta\vec{p}$ is transferred to the particle and leads to a restoring movement towards the beam focus. Fig. 3.2 shows the refraction for axial displacement [1, 2]. While, in the description so far, all rays have the same intensity, the beams used for OTs typically have a Gaussian beam profile. Thus, in the ray description, the rays at the beam center carry a higher momentum than rays far away from the center. This intensity profile amplifies the restoring force for lateral displacement of the particle [17].
For particles with a diameter smaller than λ, *i.e.*, Rayleigh particles, the dielectric particles are approximated as point-like dipoles, with the dipole momentum $\vec{p}_d$. In the electromagnetic field $(\vec{E}, \vec{B})$ of the laser, the dipole experiences a Lorentz force [18–20].

$$\vec{F} = (\vec{p}_d \cdot \nabla)\vec{E} + \frac{\partial \vec{p}_d}{\partial t} \times \vec{B} \tag{3.2}$$

The dipole moment $\vec{p}_d$ of the particle with the polarizability α in the superimposed electric fields of the incident and refracted light $\vec{E}$ is

$$\vec{p}_d = \alpha \vec{E} \,. \tag{3.3}$$

By combining Eq. (3.2) and Eq. (3.3) and substituting the term $(\vec{E} \cdot \nabla)\vec{E} = \frac{1}{2}\vec{E}^2 - \vec{E} \times (\nabla \times \vec{E})$ and using $\nabla \times \vec{E} = -\frac{\partial}{\partial t}\vec{B}$, the force is expressed as

$$\vec{F} = \alpha \left(\frac{1}{2} \nabla \vec{E}^2 + \frac{\partial}{\partial t}(\vec{E} \times \vec{B}) \right) . \tag{3.4}$$

For a continuous wave with $\frac{\partial}{\partial t}(\vec{E} \times \vec{B}) = 0$, the force becomes

$$\vec{F} = \frac{\alpha}{2} \nabla \vec{E}^2 . \tag{3.5}$$

For a small, but not point-like, particles of volume V, Eq. (3.5) is given by [21]:

$$\vec{F} = \frac{\varepsilon_0 n_m^2 \mathrm{Re}(\alpha)}{4} \nabla \vec{E}^2 \,, \tag{3.6}$$

where ε_0 is the vacuum permittivity.
The particle experiences the superposition of the incident $\vec{E}_i$ and scattered field $\vec{E}_s$, leading to the total force, which is integrated over the volume of the spherical particle, being the sum of the gradient force $\vec{F}_{grad}$ and scattering force $\vec{F}_{scat}$.

$$\vec{F}_{tot} = \int_V \frac{\vec{F}}{V} \mathrm{d}V = \vec{F}_{grad} + \vec{F}_{scat} \tag{3.7}$$

$$\vec{F}_{grad} = \frac{\varepsilon_0 n_m^2 \mathrm{Re}(\alpha)}{4V} \int_V \nabla |\vec{E}_i|^2 \mathrm{d}V \tag{3.8}$$

$$\vec{F}_{scat} = \frac{\varepsilon_0 n_m^2 \mathrm{Re}(\alpha)}{4V} \int_V \nabla \left(|\vec{E}_s|^2 + \vec{E}_i \vec{E}_s^* + \vec{E}_i^* \vec{E}_s \right) \mathrm{d}V. \tag{3.9}$$

The scattering force $\vec{F}_{scat}$ points in the direction of the beam, causing the "resting" position of the particle to be slightly shifted along the axis of the beam. However, the exact calculation of $\vec{F}_{scat}$ is demanding and, as it only causes a small offset of the position, it is typically neglected [20]. The scattering force $\vec{F}_{scat}$ and the gradient force $\vec{F}_{grad}$ depend on α, which, in turn, depends on the relation of the refractive indices of the particle n_p and medium n_m [21]:

$$\alpha = 3V \frac{m^2 - 1}{m^2 + 2} \quad \text{with} \quad m = \frac{n_p}{n_m}. \tag{3.10}$$

For a particle with $n_p > n_m$, $\vec{F}_{grad}$ leads to a force directed towards the beam center. Particles with $n_p < n_m$, for example, air bubbles in a glycerol-water mixture [1], are pushed away from the beam center. The particles used for OT experiments are typically in an intermediate size range where neither of the two descriptions is fully correct. However both descriptions give a reasonable approximation of the forces and an explanation why small particles can be trapped and moved by a strongly focused laser beam.

3.1.2 Force detection

OTs can not only be used for trapping and micromanipulation but also allow for the quantitative analysis of the displacement of the particle from the beam focus and the forces that are exerted on the trapped particle. To determine these forces, several methods have been developed [15, 22, 23]. Most approaches rely on detecting changes of the laser beam after passing the sample, for example of the polarization [15], phase [24], or momentum [23]. Either the trapping laser itself or a designated detection laser is used for the detection. Fig. 3.3 shows a simplified sketch of a setup that uses the trapping laser for detection. In brief, the laser (bottom) is focused by the objective lens (blue) and interacts with the sample (gray sphere). The unscattered and forward scattered light is collected by a high numerical aperture condenser, and the light pattern at the back focal plane, indicated by BFP in Fig. 3.3, is projected onto the detector. Historically, quadrant photo diode (QPD) detectors were employed, however, the system used in this thesis is based on detection by a position sensitive detector (PSD). In the back focal plane, the unscattered and scattered light interfere. This method

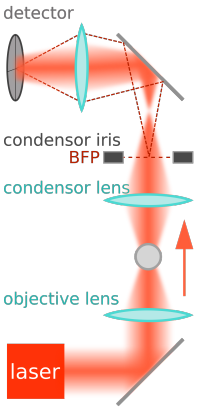

Fig. 3.3: Simplified schematic of an OT setup. The direction of the light is indicated.

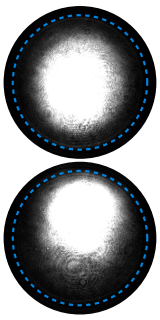

Fig. 3.4: Camera images of interference patterns in the back focal plane. The pattern is symmetric if the particle is in the trap center (top) and asymmetric if the particle is displaced (bottom).

is therefore referred to as back focal plane interferometry [25]. A sample that is centered in the beam leads to a symmetric interference pattern, see Fig. 3.4, top, while the displacement of the sample from the beam waist causes the pattern to shift, Fig. 3.4, bottom; the intensity pattern on the detector is consequently asymmetric. This shift of the intensity distribution is used for detection.
For a quantitative measurement of forces, the voltage signal from the detector has to be converted. For this conversion, the setup is calibrated. The most widely used calibration methods are based on the complete description of the gradient and scattering forces, see Fig. 3.5. For small displacements, the force-displacement curve is approximated by a linear relation so that it can be described by a Hookian spring with the spring constant k_{OT}, typically referred to as the trap stiffness.

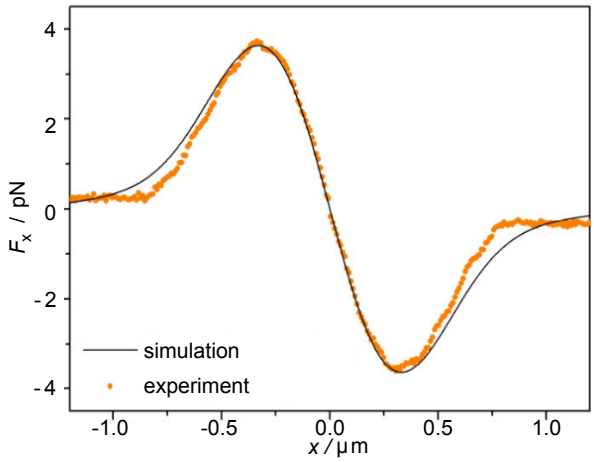

Fig. 3.5: **Complete force-displacement curve.** Experimental and simulated force-displacement curves for 610 nm particles and a laser power of 18 mW. Adapted from Ref. [23]. © 2012, Optical Society of America

There are different approaches to the calibration of the trap stiffness of OTs [23]. For example, the drag force acting on a bead which is moved or oscillated in a Newtonian fluid of known viscosity can be used to calculate k_{OT} [4]. In the setup used in this thesis, the trap stiffness is extracted from the power spectral density of the Brownian motion of a trapped particle [22]. The equation of motion for a particle is:

$$m\ddot{x}(t) + \gamma\dot{x}(t) + k_{OT}x(t) = F(t)\,, \tag{3.11}$$

where x is the position of the particle, the drag coefficient is $\gamma = 6\pi\eta\frac{a}{2}$, with the viscosity η of the medium, and the radius of the particle $\frac{a}{2}$. For Brownian motion, the thermal noise is given by

$$F(t) = \sqrt{2k_BT\gamma}\psi_n(t)\,, \tag{3.12}$$

where $\psi_n(t)$ is Gaussian white noise with unit variance and zero mean, *i.e.*, $\langle\psi_n(t)\rangle_t = 0$, and the amplitude of $F(t)$ is $\sqrt{2k_BT\gamma}$. The detector signal caused by Brownian motion of a trapped particle is shown in Fig. 3.6a. Analysis of the signal intensity in Fig. 3.6b shows the expected Gaussian distribution with the width σ.

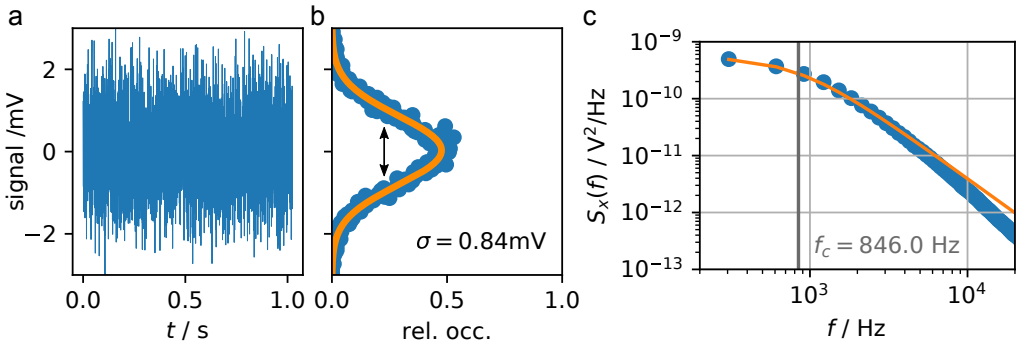

Fig. 3.6: **The power spectral density.** a) The signal of a PSD, recorded for a 4.4 µm polystyrene bead at 350 mW laser power of a 1064 nm laser at 78 kHz sampling rate shows a b) Gaussian distribution. c) The experimental power spectral density (blue dots) and the Lorentz function based on the fit parameters (orange line). The corner frequency results in $k_{OT} = 0.22$ pN/nm.

To determine the trap stiffness, inertial forces are neglected, as the particles are typically very small. By substituting the diffusion coefficient $D = {}^{k_B T}/_{\gamma}$ and the corner frequency $f_c = {}^{k_{OT}}/_{2\pi\gamma}$, Eq. (3.11) becomes

$$\dot{x}(t) + 2\pi f_c x(t) = \sqrt{2D}\psi_n(t)\,. \tag{3.13}$$

Fourier transformation of Eq. (3.13) results in

$$\tilde{x}(f) = \frac{\sqrt{2D}\tilde{\psi}_n(f)}{2\pi(f_c - if)}\,. \tag{3.14}$$

As $\psi_n(t)$ is an uncorrelated Gaussian process, *i.e.*, $\langle \psi_n(t)\psi_n(t+\tau)\rangle_t = \delta(\tau)$ where $\delta(\tau)$ is the delta function, the power spectral density $S_x(f)$ is calculated for the measurement duration t_m

$$S_x(f) = |\tilde{x}(f)|^2/t_m\,, \tag{3.15}$$

where $S_x(f)$ is a Lorentzian function

$$b^2 S_x(f) = \frac{k_B T}{2\gamma\pi^2}\frac{1}{(f_c^2 + f^2)}\,. \tag{3.16}$$

The conversion factor b translates the detector voltage into the bead displacement and is, together with the corner frequency f_c, determined by fitting the absolute values of the experimental power spectral density, blue in Fig. 3.6c, with the Lorentzian in Eq. (3.16), orange line in Fig. 3.6c. Finally, the trap stiffness is calculated for a known particle diameter and the viscosity of the medium from

$$k_{OT} = 2\pi\gamma f_c\,. \tag{3.17}$$

The fitting of the experimental power spectral density can be improved, especially at high frequencies, by extending Eq. (3.16), for example, by considering finite frequency effects [22].

3.2 MICRORHEOLOGY

3.2.1 Rheology of viscoelastic materials

With rheology, the elastic and viscous properties of a material are studied. They can range from a purely viscous fluid, where all the input energy is dissipated, to a purely elastic, rubber-like solid, where all the energy is stored [26, 27]. Many, especially biological, systems are viscoelastic. These systems can be described as complex fluids as their mechanical response combine elastic and viscous contributions. Complex fluids are, for example, colloidal dispersions, polymer solutions, or filament networks, and contain a hierarchy of structures ranging from length scales of single nanometers to several tens of micrometers. The mechanical properties of these systems are determined by the interactions within or between the largest of these structures, for example, IFs [27, 28].
With rheology, the relation of the elastic (storage, G') and dissipative (loss, G'') contributions to the shear modulus G^* of a complex fluid is characterized. The complex shear modulus G^* or, equivalently, the complex viscosity η^*

$$G^*(\omega) = G'(\omega) + iG''(\omega) = i\omega\eta^*(\omega) \tag{3.18}$$

$$\eta^*(\omega) = \eta'(\omega) - i\eta''(\omega) \tag{3.19}$$

$$\text{with} \quad G'(\omega) = \omega\eta'' \quad \text{and} \quad G''(\omega) = \omega\eta' \,, \tag{3.20}$$

depend on the frequency ω of a mechanical excitation [26, 29].
With conventional macrorheology, *i.e.*, typically shear rheometry, the bulk properties of a sample are determined, whereas microrheology probes the local properties of a complex fluid. This local probing is achieved by embedding micron-scale tracer particles in the sample, in our case, in the network. The particles can either be used in passive methods, where thermal fluctuations (Brownian motion) are observed, or to actively apply shear to the medium with an external force. Such active deformations can, for example, be achieved with magnetic or optical tweezers. All microrheology approaches are based on the assumption that the medium that the particles are embedded in is continuous, *i.e.*, that the probe size is larger than the structures within the sample [28, 29]. In the case of a network, this refers to the meshsize ξ [28, 29].

3.2.2 Passive microrheology: microparticle tracking

In passive microrheology, the response of the system to thermal fluctuations is probed by tracer particles. Thermal fluctuations only lead to small deformations of the sample, and the system relaxes back to its equilibrium state. Passive microrheology is a collective term for various experimental methods. One group of techniques measures the ensemble average of many tracer particles, typically with scattering based methods such as dynamic wave spectroscopy (DWS) or dynamic light scattering (DLS) [27]. Another group of techniques is based on the measurement of single particles, for example by using laser interferometry or low-power OTs [28, 30–32]. The most straight forward implementation of this second group of methods is to simply observe the 2D-positions of the particles

with a wide field microscope and record a time series with a camera. Several particles are recorded at once, and each single particle can be localized. This method is called microparticle tracking (MPT).
In MPT, the positions of the tracer particles in the field of view of the camera are tracked over the experiment time t. Examples of the resulting trajectories are shown in Fig. 3.7. The mean squared displacement (MSD) is calculated from the change in (x,y)-position over the lag-time tau. [28].

$$\text{MSD} = \langle \Delta r^2(\tau) \rangle = \langle (x(t+\tau) - x(t))^2 \rangle_t + \langle (y(t+\tau) - y(t))^2 \rangle_t \tag{3.21}$$

For elastic solids, the complex shear modulus is equal to the frequency independent elastic modulus $G^*(\omega) = G'$ and the 2D-MSD for a particle with diameter a is therefore independent of τ, see the red curve in Fig. 3.8 [29].

$$\langle \Delta r^2(\tau) \rangle = \frac{2k_B T}{3\pi \frac{a}{2} G'} \tag{3.22}$$

For a Newtonian fluid, the tracer motion is purely diffusive which leads to a linear MSD, as shown by the blue line in Fig. 3.8.

$$\langle \Delta r^2(\tau) \rangle = 4D\tau \tag{3.23}$$

The diffusion coefficient of the bead D is given by the Stokes-Einstein equation, with the bead diameter a, and the frequency independent viscosity η [33]

$$D = \frac{k_B T}{6\pi\eta \frac{a}{2}}. \tag{3.24}$$

For complex fluids that lead to subdiffusive behavior, the MSD includes the diffusive exponent n [34].

$$\langle \Delta r^2(\tau) \rangle = 4D\tau^n \tag{3.25}$$

The diffusive exponent $0 < n < 1$ describes whether the elastic ($n < 0.5$) or viscous ($n > 0.5$) properties dominate the material response. For example, for the orange curve in Fig. 3.8, the subdiffusive behavior is dominated by the viscous contribution.
In more complex samples, such as filament networks, several different relaxation processes, each with their respective time scales, become relevant, see Fig. 3.8 green curve. This hierarchy of relaxation times leads to viscous or subdiffusive motion on short time scales while approaching an elastic-solid-like MSD for longer lag-times [29]. For viscoelastic samples, the MSD is translated into the complex shear modulus by a generalized Langevin equation that comprises a term describing the stochastic forces acting on the particleand a term for the viscous damping. By assuming that the microscopic memory function is proportional to the bulk memory function, the shear modulus becomes

$$\tilde{G}(s) = \frac{s}{6\pi\frac{a}{2}} \left[\frac{6k_B T}{s^2 \langle \Delta \tilde{r}^2(s) \rangle} - ms \right] \overset{m \to 0}{\approx} \frac{k_B T}{\pi \frac{a}{2} s \langle \Delta \tilde{r}^2(s) \rangle} \tag{3.26}$$

with the Laplace transformed shear modulus $\tilde{G}(s)$, the Laplace transformed MSD $\langle \Delta \tilde{r}^2(s) \rangle$, the frequency in the Laplace domain s, and the particle mass m.

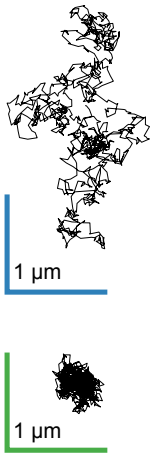

Fig. 3.7: Representative trajectories of a freely diffusing particle (top) and a confined particle (bottom). Both particles are tracked for the same duration.

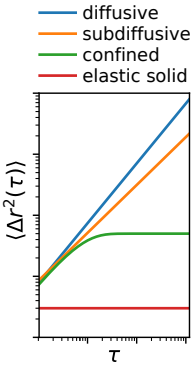

Fig. 3.8: Theoretical MSDs for diffusive, subdiffusive and confined motion in a fluid, and time independent motion in an elastic solid.

After neglecting the influence of inertia (ms), Eq. (3.26) results in a generalized Stokes-Einstein equation [27, 28].
Numerical calculation of the Laplace transform leads to truncation errors at the extremes of the recorded frequencies [35]. Instead, the complex shear modulus is typically derived from Eq. (3.26) by fitting a local power law to the MSD at each time τ_0

$$\langle \Delta r^2(\tau) \rangle \approx \langle \Delta r^2(\tau_0) \rangle (\tau/\tau_0)^{\alpha(1/\tau_0)} \tag{3.27}$$

where the local power-law exponent $\alpha(1/\tau_0)$ is the logarithmic slope of the MSD at $1/\tau_0$

$$\alpha(1/\tau_0) = \frac{d \ln \langle \Delta r^2(\tau) \rangle}{d \ln \tau}\Big|_{\tau=\tau_0}. \tag{3.28}$$

For MPT data from a passive system, this logarithmic slope has to be $0 \leq \alpha(1/\tau_0) \leq 1$. The case $\alpha(1/\tau_0) = 1$ describes viscous diffusion, and $\alpha(1/\tau_0) = 0$ describes confinement in an elastic solid [35].
G^* is now determined analytically by identifying $G^*(\omega) = \tilde{G}(s = i\omega)$ and taking the Fourier transform of Eq. (3.26).

$$G^*(\omega) = \frac{k_B T}{\pi \frac{a}{2} i\omega \mathcal{F}\{\langle \Delta r^2(\tau) \rangle\}} \tag{3.29}$$

Eq. (3.29) is approximated from the local power law fit to the MSD to yield

$$\left|G^*(\omega_0)\right| \approx \frac{k_B T}{\pi \frac{a}{2} \langle \Delta r^2(\tau_0) \rangle \Gamma[1 + \alpha(\tau_0)]}\Big|_{\tau_0 = 1/\omega_0}, \tag{3.30}$$

where Γ is the gamma function [35]. The storage and loss moduli are now determined from Eq. (3.30) with Euler's equation, giving

$$G'(\omega) = \left|G^*(\omega)\right| \cos(\pi\alpha(\omega)/2), \tag{3.31}$$
$$G''(\omega) = \left|G^*(\omega)\right| \sin(\pi\alpha(\omega)/2). \tag{3.32}$$

The power law fitting analysis is constantly being improved, for example, for MSDs with stronger curvature [36], and other approaches that are not based on the Fourier transform have been proposed [37]. The Fourier approach is widely used and accessible, as codes for analysis have been published [38].

3.2.3 Active microrheology: optical trapping

In active microrheology measurements, an external force drives the local deformation of the sample. In contrast to passive microrheology methods, this allows for a larger displacement of the tracer particles, and the non-linear properties of materials can also be studied. However, at small displacements, equivalent results to passive methods are achieved. Different techniques have been employed to control the particle motion. The most frequently used methods are based on magnetic fields and OTs [29]. Both techniques have been applied to measurements inside living cells, which is only possible because of the non-invasive

nature of microrheology methods [11]. As we, in this thesis, only employ active microrheology in the same frequency and amplitude range as observed in MPT, the description here will focus on the theory applicable to the linear response of the sample. A comprehensive overview of active microrheology with OTs can be found in Ref. [11]. For the active microrheology experiments presented in this work, the probe particle is oscillated by a single OT. The amplitude $D(\omega)$ and phase shift $\delta(\omega)$ of the particle movement, blue in Fig. 3.9, with respect to the OT movement with amplitude A (orange) are analyzed. A particle that is oscillated by an OT in a complex fluid at the frequency ω with the amplitude of the trap movement A experiences a complex interaction with the medium ($-6\pi\frac{a}{2}\eta^*(\omega)\dot{x}$), an elastic, restoring force by the OT ($-\kappa_{OT}x$), the driving force of the OT ($\kappa_{OT}A\exp(i\omega t)$), and inertial forces ($m\ddot{x}$)

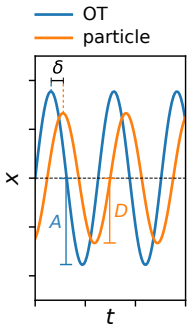

Fig. 3.9: Phase shift and amplitudes for oscillation of a particle in a viscoelastic medium at one particular frequency ω.

$$m\ddot{x}(t) = -6\pi\frac{a}{2}\eta^*(\omega)\dot{x}(t) - \kappa_{OT}x(t) + \kappa_{OT}A\exp(i\omega t) \tag{3.33}$$

where m is the particle mass, $a/2$ the particle radius, $\eta^*(\omega)$ the complex viscosity, and κ_{OT} the spring constant of the OT. The solution for the equation of motion

$$x(t) = D(\omega)\exp\Big(i\big(\omega t - \delta(\omega)\big)\Big), \tag{3.34}$$

depends on the amplitude $D(\omega)$ of the particle moment and the phase lag $\delta(\omega)$ between OT and particle movement. As microrheology experiments are in the low-Reynolds number regime, inertial effects are negligible. By re-writing Eq. (3.33) with Eq. (3.34), the equation of motion leads to the complex shear modulus

$$G^*(\omega) = i\omega\eta^*(\omega) = \frac{\kappa_{OT}}{6\pi\frac{a}{2}}\left[\frac{A}{D(\omega)}\Big(\exp\big(i\delta(\omega)\big)\Big) - 1\right], \tag{3.35}$$

which is now expressed in terms of the measurement parameters, A, $D(\omega)$, $\delta(\omega)$, and the trap stiffness κ_{OT}. Separating the real and imaginary parts provides the storage and loss modulus [29, 39, 40]:

$$G'(\omega) = \frac{\kappa}{6\pi\frac{a}{2}}\left[\frac{A}{D(\omega)}\Big(\cos\big(\delta(\omega)\big)\Big) - 1\right] \tag{3.36}$$

$$G''(\omega) = \frac{\kappa}{6\pi\frac{a}{2}}\left[\frac{A}{D(\omega)}\Big(\sin\big(\delta(\omega)\big)\Big)\right]. \tag{3.37}$$

3.3 POLYMER MECHANICS

The biopolymers in the cytoskeleton can reach lengths of several micrometers, while the radius is only a few nm small [41]. Despite their small diameter, these filaments have a considerable resistance to bending, which is typical for *semiflexible polymers*. One widely applied model for semiflexible polymers is the worm-like chain (WLC), which was originally introduced in 1949 by Otto Kratky and Günther Porod [42]. In brief, the WLC consist, of infinitely short, rigid, and inextensible sections. The angle between a segment and the previous segment is not random, which is in contrast to the freely-jointed chain model. However, if the chain is observed sufficiently far away from the first segment, the correlation of the angle is lost. The distance along the chain where this loss of correlation occurs is called the persistence length l_P. The persistence length thereby describes the length scale on which thermal forces lead to bending of these filaments with the bending stiffness κ [43].

$$l_P = \frac{\kappa}{k_B T} \tag{3.38}$$

3.3.1 Entropic stretching of worm-like chains

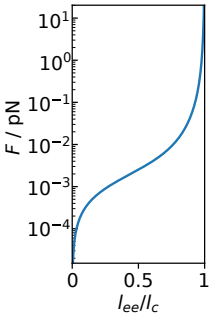

Fig. 3.10: Theoretical, interpolated force-extension curve for a WLC with $l_P = 2\,\mu m$.

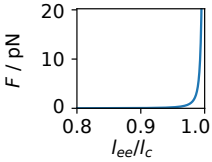

Fig. 3.11: The high extension regime of Fig. 3.10.

A filament in a randomly coiled conformation is subject to thermal fluctuations. By stretching the filament, *i.e.*, increasing the end-to-end distance, the number of degrees of freedom is reduced. This loss of entropy causes a restoring force. The exact force-extension behavior of the "straightening" of an inextensible WLC can be calculated numerically [44].
For the purpose of describing the stretching of filaments in an OT, it is sufficient to use an interpolated, simple calculation, originally derived for the stretching of DNA [44, 45]. This interpolation is only valid for semiflexible filaments where $l_c > l_P$ with the contour length l_c, and it is a good description of the force-extension behavior of WLCs in the low and high force regimes. In the high force regime, the end-to-end distance l_{ee} is close to the contour length l_c, which is fulfilled in the OT experiments, as the filaments are already relatively straight before l_{ee} is increased further. The interpolated equation, shown in Fig. 3.10 and Fig. 3.11, depends on the contour length, the end-to-end distance, the persistence length, the applied force, and thermal energy [44]:

$$\frac{l_P F}{k_B T} = \frac{l_{ee}}{l_c} + \frac{1}{4\left(1 - {}^{l_{ee}}/_{l_c}\right)^2} - \frac{1}{4} \tag{3.39}$$

Fig. 3.11 shows that, while the force is small for most extensions, F increases strongly close to the contour length.
For extensible filaments, both, entropic and elastic stretching contributions, are relevant. Which process dominates depends on the length of the observed segment l and the filament diameter a. When $l^3 \gtrsim (\frac{a}{2})^2 l_P$, the entropic contribution dominates, while at $l^3 \lesssim (\frac{a}{2})^2 l_P$, the enthalpic, mechanical properties are relevant [43]. In chapter 6, a model that combines the entropic and enthalpic stretching of vimentin filaments is provided.

3.3.2 Worm-like bundles

A worm-like bundle (WLB) is a bundle of length l which is comprised of N parallel filaments, each with the bending stiffness κ_f, that can be connected by some type of crosslinker. The mechanical response of a WLB depends on the coupling strength between the single filaments. In the case of tight coupling, the filaments do not slide along each other during the bending of the bundle, and the crosslinkers are not deformed, as indicated in blue in Fig. 3.12. The bending stiffness κ_b of the bundle and the persistence length of the bundle $l_{P,b}$ scale as

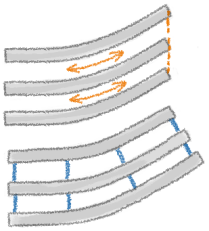

Fig. 3.12: Bending deformation of an uncoupled bundle with sliding (top) and a strongly coupled bundle (bottom). The rigid crosslinks are indicated in blue.

$$\kappa_b \sim N^2 \kappa_f \qquad \text{or alternatively} \qquad l_{P,b} \sim N^2 l_{P,f} \,, \tag{3.40}$$

with the persistence length of the single filament $l_{P,f}$. If the filaments in the bundle can freely slide along each other during bending, which is the uncoupled case, top in Fig. 3.12, the bundle properties scale as

$$\kappa_b \sim N \kappa_f \qquad \text{or alternatively} \qquad l_{P,b} \sim N l_{P,f} \,. \tag{3.41}$$

In the intermediate regime, κ_b strongly depends on the wavelength of the bending deformation $\kappa_b \sim N k_x q^{-2}$, where k_x is the stiffness of the crosslinker and q wave number of the bending mode [43, 46].

3.3.3 Networks of semiflexible polymers

In cells, the cytoskeletal filaments form complex networks and are not present as independent, single filaments or bundles. In this section, the properties that determine the mechanics of semiflexible polymer networks are discussed. These models are based on the assumption that the filaments in the network are inextensible, at least within the applied force regime, and that the elasticity of the network is caused by entropic stretching of the filaments.
Semiflexible polymer networks can be described as viscoelastic materials which are introduced in section 3.2. Their mechanical properties can therefore be expressed by the complex shear modulus G^*. A schematic of the storage modulus G' and loss modulus G'' for a semiflexible polymer network is shown in Fig. 3.13. The mechanical response is frequency dependent, and different processes occur on characteristic time scales. The terminal relaxation time, also called the reptation time or disentanglement time, τ_d, is the time it takes a filament to diffuse over a distance equal to l_c. At these low frequencies, the reptation, *i.e.*, Brownian motion of the filament along the filament axis, leads to flow of the network. The second characteristic time scale is the entanglement time τ_e, also called relaxation time, which depends on the relaxation of bending deformations of single filaments or bundles. τ_e is the relaxation time of the longest, unconstrained bending mode of the filament. The frequency spectrum can therefore be divided into three regions: i) for frequencies $\omega < \tau_d^{-1}$, the network flow dominates the mechanical response, ii) for intermediate frequencies, $\tau_e^{-1} > \omega > \tau_d^{-1}$, the network deformation is measured, and iii) at high frequencies $\omega > \tau_e^{-1}$, the mechanics of the single filaments or bundles become apparent [48].

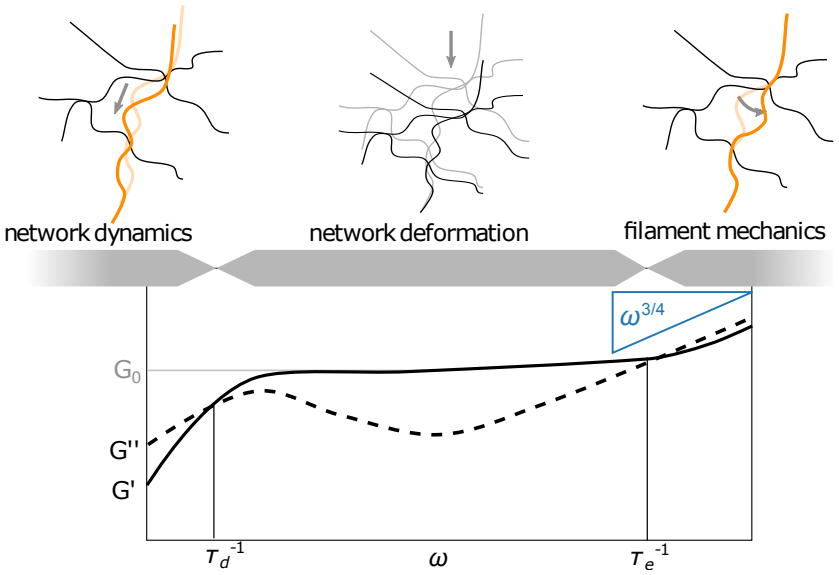

Fig. 3.13: **Three regimes in the viscoelastic properties of semiflexible polymer networks.** At low frequencies $\omega < \tau_d^{-1}$, the response is due to flow of the network by self-diffusion of the filaments. At intermediate frequencies, between the disentanglement time and the relaxation time, $\tau_e^{-1} > \omega > \tau_d^{-1}$, the network deformation is probed. The slope of the plateau depends on the entanglement or crosslinking of the network. At high frequencies $\omega > \tau_e^{-1}$, the mechanics, *i.e.*, bending, of single filaments or bundles dominate the response. The power law exponent of 3/4 in the high frequency regime is indicated. Figure reproduced from Ref. [47].

The mechanical properties of a network intuitively depend on the density of the filaments in the structure. At high filament concentrations, there is little unoccupied space between filaments. This free distance between the filaments is defined as the mesh size ξ, and depends on the protein mass concentration c in g/L and the mass-per-length ρ_m of the filament type. For a biopolymer, the mass-per-length is calculated from the number of monomers per chain N_m, where each monomer has the molecular weight M_m and the length l_m. N_A is Avogadro's constant. For a simple 3D network consisting of a cubic mesh, ξ_{cubic}, the amount of polymer per mesh in length per volume is given by

$$\xi_{cubic} = \sqrt{\frac{3\rho_m}{c}} = \sqrt{\frac{3N_m M_m}{l_m N_A c}}\,. \tag{3.42}$$

This simple model provides an approximation of the mesh sizes for "real", non-cubic networks.
Besides the mesh size, the interactions between filaments determine the network properties. Three types of interactions are presented in the following: i) Filaments interact purely sterically by entanglements, ii) fixed crosslinks define the network properties, or iii) transient crosslinks cause a time dependent interaction.

Entangled networks

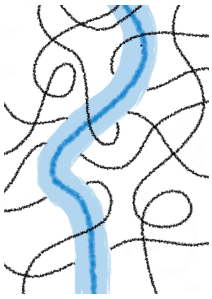

Fig. 3.14: Entangled network. The black filaments sterically limit the fluctuations of the blue filament to the shaded area.

An entanglement is a steric constraint of the fluctuations of filaments as sketched in Fig. 3.14 [49]. Such entanglements lead to a frequency dependent mechanical response of the network to deformations. On intermediate time scales, where the entanglements prohibit filaments from relaxing, the shear modulus has a considerable elastic contribution. In the intermediate frequency region in Fig. 3.13 this is evident, as $G' > G''$.
One important length scale in an entangled network is the distance between entanglements l_e. This entanglement length, measured along the filament backbone, can be larger than the mesh size ξ. The plateau modulus G_0 of the storage modulus G', which describes the rubber/solid like, elastic contribution, can be derived from these two lengths by [24, 50, 51]

$$G_0 \approx \frac{k_B T}{\xi^2 l_e} \,. \tag{3.43}$$

This expression already shows that the length scales of the network and filaments strongly influence the mechanical properties. Entanglements can only form when filaments are sufficiently long, *i.e.*, $l_c > l_e$. However, the filament length still affects the mechanical properties of the network at $l_c > l_e$, as more and more entanglements can form [51].
At low frequencies $\omega < \tau_d^{-1}$, reptation of the filaments becomes relevant and the response is mostly viscous. The timescale where reptation becomes dominant depends on the contour length of the semiflexible filament $\tau_d \propto l_c^3$ [52]. In contrast, in irreversibly crosslinked networks, reptation is inhibited and this regime is typically not observed [53].

Crosslinked networks

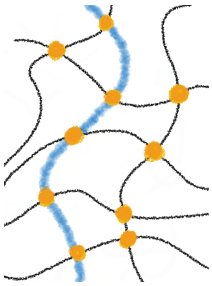

Fig. 3.15: Crosslinked network. Positions that can be crosslinked are marked in orange.

Crosslinks lead to site specific interactions between filaments, for example at positions of entanglements. In these networks, the crosslinks, instead of or in addition to entanglements, prevent the relaxation of filaments. These constraints lead to a pronounced plateau G_0 of the storage modulus. In the following, we assume that the interactions are affine, *i.e.*, the system deforms uniformly [54], in contrast to non-affine deformations, where the strains single filaments experience are not equal to the network strain [55]. In the limit of a densely crosslinked network where the distance between crosslinks l_{cl} is shorter than l_p, G_0 is given by the expression [24]:

$$G_0 = 6\rho_v \frac{\kappa^2}{k_B T l_{cl}^3} = 6\rho_v \frac{k_B T l_p^2}{l_{cl}^3} \,, \tag{3.44}$$

where ρ_v is the concentration of filaments in length per volume. In Eq. (3.44), we assume that the network is not fully crosslinked, *i.e.*, not every possible crosslinking position is occupied, and $l_{cl} \geq \xi$. The response of the network therefore depends on the amount of crosslinking.
In addition to the crosslinking density, the mechanical properties of the crosslinkers themselves also influence the network mechanics, which is especially relevant for actin networks where many crosslinking and motor proteins of varying lengths and stiffnesses are known [56].

Transiently crosslinked networks

Most biological interactions within networks are transient where the crosslinkers, including the previously mentioned motor proteins, bind and unbind on timescales that influence the network mechanics. In a transiently crosslinked network under shear, the unbinding of a crosslinker allows the filaments to relax and the network to flow. The unbinding kinetics typically become most apparent at low frequencies [53, 57], especially when several relaxation rates superimpose [57].
Transient crosslinks strongly affect the shape of G''. Permanent crosslinking leads to a nearly constant value of G'' at low and intermediate frequencies, as reptation is impeded by the crosslinks and the network cannot flow. However, for transiently crosslinked networks, the local minimum at intermediate frequencies and the local maximum at low frequencies are pronounced [53, 58], see Fig. 3.13. While the plateau of the storage modulus G_0 of tightly crosslinked networks is mostly frequency independent, in weakly or transiently crosslinked as well as entangled networks, the plateau can increase weakly with ω. This not fully constant plateau can, for example, be seen in Refs. [53, 59, 60] and is caused by the superposition of the elastic response of the network with multiple crosslink relaxation times and the onset of reptation [58].

High frequency mechanics

The mechanical response of semiflexible polymer networks at high frequencies is postulated to follow

$$G^*(\omega) \approx \frac{1}{15}\rho_v \kappa l_P \left(-2i\frac{\zeta}{\kappa}\right)^{3/4} \omega^{3/4} - i\omega\eta\,, \tag{3.45}$$

which depends on the filament length per volume ρ_v, the persistence length l_P, the lateral drag coefficient ζ, and the bending stiffness κ [24, 30, 61]. This response is independent of parameters such as l_e or l_c and therefore expected to be valid for both, entangled and crosslinked networks [24]. The lateral drag coefficient ζ is given by the solvent viscosity η, the diameter of the filament, and the characteristic length λ, which can, for example, be the mesh size ξ [62]:

$$\zeta = \frac{4\pi\eta}{\ln(0.6\,\lambda/d_f)}\,. \tag{3.46}$$

The power law dependence proposed in Eq. (3.45) has, among other systems, been observed for actin filament [35, 63] and IF networks [62].
For networks of semiflexible bundles, the high frequency behavior is linked to the coupling strength in the bundle. The two extremes, fully coupled and uncoupled bundles, lead to the strongest frequency dependence of the mechanical response with a power law exponent of 3/4. For fully coupled bundles that basically behave like a single, albeit stiffer and thicker filament, and uncoupled bundles, where the filaments can slide along each other, the high frequency power law exponent is therefore the same as calculated for networks of single semiflexible filaments in Eq. (3.45). For intermediate coupling strengths, the power law exponent decreases to 1/2 [64].

3.4 MOLECULAR REACTIONS

3.4.1 Step-growth polymerization

A short version of this section is published in the supporting information of Ref. [47].
The elongation reaction of intermediate filaments, as introduced in section 2.1, is a polymer step growth. In a step-growth polymerization, all reactive species are bi-functional and reactions occur equally at both chain ends, regardless of the size of the species. A monomer can therefore react with another monomer or a polymer in the same manner as polymers react with other polymers. This is in contrast to polymer chain growth where only monomers attach one-by-one at the reactive polymer chain end. Because of the simultaneous formation of many short polymers during step growth, the average length of the resulting polymers is short until a high conversion p, which is the extent of the reaction, is reached.
The weight of the resulting polymers, depending on the extent of the reaction p was calculated by Paul Flory in 1936 [65]. The probability that a single reaction, the end-to-end annealing, occurs is equal to p. To build a polymer from x monomers, $x-1$ reactions have to take place, which occurs with the probability p^{x-1}. The probability of finding an unreacted end group is $1-p$. The probability of finding a polymer of size x is therefore given by:

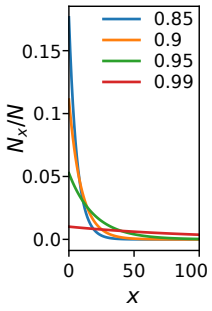

Fig. 3.16: Distribution of the number fraction at increasing p.

$$P_x = (1-p)p^{x-1} = \frac{N_x}{N}, \tag{3.47}$$

where N is the total number of molecules of all sizes, and N_x is the number of molecules of size x. The distribution of N_x for different conversions p is shown in Fig. 3.16. The average weight of the polymer is calculated from p and the monomer weight M_0. The number average M_N or weight average M_W can be calculated with the expressions [65]

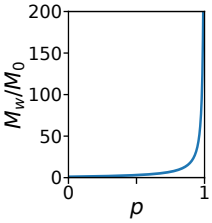

Fig. 3.17: M_w only increases for high p.

$$M_W = \frac{M_0(1+p)}{1-p} = M_N(1+p)\,, \tag{3.48}$$

and increase strongly at high p as shown in Fig. 3.17 .

3.4.2 Molecular reaction kinetics – two state models

Many dynamic processes can be described by a simple model that assumes that a system can be in one of two states. Such two-state models, with few parameters, describe many biophysical processes on various length scales remarkably well, and are, for example, used to calculate the kinetics of chemical reactions [66], the folding and unfolding of biopolymers under tension [67] or cell-cell adhesion [68].
In the model, two states b and u are separated by a high-energy transition state, sketched in Fig. 3.18. For a system in equilibrium that experiences a thermal

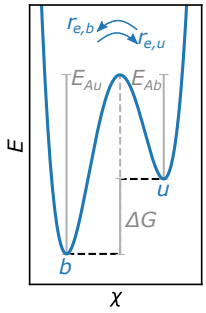

Fig. 3.18: Energy landscape of a two state system.

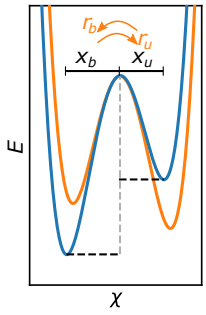

Fig. 3.19: Energy landscape of a two state system, without (blue) and with an applied, force (orange).

energy k_BT, the transition rates $r_{e,u}$ from state $b \rightarrow u$, and accordingly $r_{e,b}$ from $u \rightarrow b$ are described by the Arrhenius equation [66]

$$r_{e,u} = r_{0,u} \exp\left(\frac{-E_{Au}}{k_BT}\right), \tag{3.49}$$

$$r_{e,b} = r_{0,b} \exp\left(\frac{-E_{Ab}}{k_BT}\right), \tag{3.50}$$

where E_{Au} and E_{Ab} are the heights of the energy barrier. The rates $r_{0,u}$ and $r_{0,b}$ are the inverse of the characteristic time constants for diffusive escape from the minimum position, as described by H. A. Kramers [69]. These inverse time constants can be understood as the frequency of escape attempts [70].
When a force is applied to the system, the energy landscape changes, as for example in Fig. 3.19. In Bell's theory [68], also known as the Bell-Evans theory [70], an applied force F, for the example sketched in Fig. 3.19, reduces (for $b \rightarrow u$) or increases (for $u \rightarrow b$) the height of the energy barrier linearly and the transition rates are therefore given by the expressions:

$$r_u(t) = r_{0,u} \exp\left(\frac{-(E_{Au} - F(t)x_u)}{k_BT}\right) = r_{e,u} \exp\left(\frac{F(t)x_u}{k_BT}\right) \tag{3.51}$$

$$r_b(t) = r_{0,b} \exp\left(\frac{-(E_{Ab} + F(t)x_b)}{k_BT}\right) = r_{e,b} \exp\left(\frac{-F(t)x_b}{k_BT}\right) \tag{3.52}$$

The transition rates therefore now additionally depend on the force F, and distance of the respective state to the transition state x_u and x_b, as sketched in Fig. 3.19. The total distance of the states u and b, $x_u + x_b = x_c = const.$, is a characteristic length scale of the system.

[1] A. Ashkin. "Acceleration and Trapping of Particles by Radiation Pressure." *Phys. Rev. Lett.* 24 (1970), pp. 156–159. DOI: 10.1103/PhysRevLett.24.156.

[2] A. Ashkin et al. "Observation of a single-beam gradient force optical trap for dielectric particles." *Opt. Lett.* 11 (1986), p. 288. DOI: 10.1364/OL.11.000288.

[3] A. Ashkin, J. M. Dziedzic, and T. Yamane. "Optical trapping and manipulation of single cells using infrared laser beams." *Nature* 330 (1987), pp. 769–771. DOI: 10.1038/330769a0.

[4] S. M. Block, D. F. Blair, and H. C. Berg. "Compliance of bacterial flagella measured with optical tweezers." *Nature* 338 (1989), pp. 514–518. DOI: 10.1038/338514a0.

[5] A. Ashkin et al. "Force generation of organelle transport measured in vivo by an infrared laser trap." *Nature* 348 (1990), pp. 346–348. DOI: 10.1038/348346a0.

[6] L. Chaubet et al. "Dynamic actin cross-linking governs the cytoplasm's transition to fluid-like behavior." *Mol. Biol. Cell* 31 (2020), pp. 1744–1752. DOI: 10.1091/mbc.E19-09-0504.

[7] M. Guo et al. "The role of vimentin intermediate filaments in cortical and cytoplasmic mechanics." *Biophys. J.* 105 (2013), pp. 1562–1568. DOI: 10.1016/j.bpj.2013.08.037.

[8] T. T. Perkins et al. "Stretching of a single tethered polymer in a uniform flow." *Science* 268 (1995), pp. 83–87. DOI: 10.1126/science.7701345.

[9] S. B. Smith, Y. Cui, and C. Bustamante. "Overstretching B-DNA: The elastic response of individual double-stranded and single-stranded DNA molecules." *Science* 271 (1996), pp. 795–799. DOI: 10.1126/science.271.5250.795.

[10] J. Van Mameren et al. "Unraveling the structure of DNA during overstretching by using multicolor, single-molecule fluorescence imaging." *Proc. Natl. Acad. Sci.* 106 (2009), pp. 18231–18236. DOI: 10.1073/pnas.0904322106.

[11] R. M. Robertson-Anderson. "Optical Tweezers Microrheology: From the Basics to Advanced Techniques and Applications." *ACS Macro Lett.* 7 (2018), pp. 968–975. DOI: 10.1021/acsmacrolett.8b00498.

[12] B. Gurmessa et al. "Counterion Crossbridges Enable Robust Multiscale Elasticity in Actin Networks." *Phys. Rev. Res.* 1 (2019), p. 013016. DOI: 10.1103/PhysRevResearch.1.013016.

[13] J. Block et al. "Nonlinear Loading-Rate-Dependent Force Response of Individual Vimentin Intermediate Filaments to Applied Strain." *Phys. Rev. Lett.* 118 (2017), p. 048101. DOI: 10.1103/PhysRevLett.118.048101.

[14] T. Suren et al. "Single-molecule force spectroscopy reveals folding steps associated with hormone binding and activation of the glucocorticoid receptor." *Proc. Natl. Acad. Sci.* 115 (2018), pp. 11688–11693. DOI: 10.1073/pnas.1807618115.

[15] K. Svoboda et al. "Direct observation of kinesin stepping by optical trapping interferometry." *Nature* 365 (1993), pp. 721–727. DOI: 10.1038/365721a0.

[16] S. Sudhakar et al. "Germanium nanospheres for ultraresolution picotensiometry of kinesin motors." *Science* 371 (2021), eabd9944. DOI: 10.1126/science.abd9944.

[17] A. Ashkin. "Forces of a single-beam gradient laser trap on a dielectric sphere in the ray optics regime." *Biophys. J.* 61 (1992), pp. 569–582. DOI: 10.1016/S0006-3495(92)81860-X.

[18] Y. Harada and T. Asakura. "Radiation forces on a dielectric sphere in the Rayleigh scattering regime." *Opt. Commun.* 124 (1996), pp. 529–541. DOI: 10.1016/0030-4018(95)00753-9.

[19] J. W. Shaevitz. *A Practical Guide to Optical Trapping*. Tech. rep. 2006.

[20] M. D. Koch and J. W. Shaevitz. "Introduction to Optical Tweezers." *Optical Tweezers: Methods and Protocols, Methods in Molecular Biology*. Ed. by Arne Gernnerich. Springer Sciences, 2017, pp. 3–24. DOI: 10.1007/978-1-4939-6421-5_1.

[21] A. Rohrbach. "Stiffness of optical traps: Quantitative agreement between experiment and electromagnetic theory." *Phys. Rev. Lett.* 95 (2005), p. 168102. DOI: 10.1103/PhysRevLett.95.168102.

[22] K. Berg-Sørensen and H. Flyvbjerg. "Power spectrum analysis for optical tweezers." *Rev. Sci. Instrum.* 75 (2004), pp. 594–612. DOI: 10.1063/1.1645654.

[23] A. Farré, F. Marsà, and M. Montes-Usategui. "Optimized back-focal-plane interferometry directly measures forces of optically trapped particles." *Opt. Express* 20 (2012), p. 12270. DOI: 10.1364/OE.20.012270.

[24] F. Gittes and F. C. MacKintosh. "Dynamic Shear Modulus of a Semiflexible Polymer Network." *Phys. Rev. E* 58 (1998). DOI: 10.1103/PhysRevE.58.R1241.

[25] F. Gittes and C. F. Schmidt. "Interference model for back-focal-plane displacement detection in optical tweezers." *Opt. Lett.* 23 (1998), pp. 7–9. DOI: 10.1364/ol.23.000007.

[26] J. D. Ferry. *Viscoelastic properties of polymers*. John Wiley & Sons, 1980.

[27] T. G. Mason and D. A. Weitz. "Optical measurements of frequency-dependent linear viscoelastic moduli of complex fluids." *Phys. Rev. Lett.* 74 (1995), pp. 1250–1253. DOI: 10.1103/PhysRevLett.74.1250.

[28] T. G. Mason et al. "Particle Tracking Microrheology of Complex Fluids." *Phys. Rev. Lett.* 79 (1997), pp. 3282–3285. DOI: 10.1103/PhysRevLett.79.3282.

[29] E. M. Furst and T. M. Squires. *Microrheology*. Vol. 1. Oxford University Press, 2018. DOI: 10.1093/oso/9780199655205.001.0001.

[30] F. Gittes et al. "Microscopic viscoelasticity: Shear moduli of soft materials determined from thermal fluctuations." *Phys. Rev. Lett.* 79 (1997), pp. 3286–3289. DOI: 10.1103/PhysRevLett.79.3286.

[31] B. Schnurr et al. "Determining microscopic viscoelasticity in flexible and semiflexible polymer networks from thermal fluctuations." *Macromolecules* 30 (1997), pp. 7781–7792. DOI: 10.1021/ma970555n.

[32] S. Yamada, D. Wirtz, and S. C. Kuo. "Mechanics of living cells measured by laser tracking microrheology." *Biophys. J.* 78 (2000), pp. 1736–1747. DOI: 10.1016/S0006-3495(00)76725-7.

[33] A. Einstein. "Über die von der molekularkinetischen Theorie der Wärme geforderte Bewegung von in ruhenden Flüssigkeiten suspendierten Teilchen." *Ann. Phys.* 322 (1905), pp. 549–560. DOI: 10.1002/andp.19053220806.

[34] M. L. Gardel, M. T. Valentine, and D. A. Weitz. "Microrheology." *Microscale Diagnostic Techniques*. Springer, 2005, pp. 1–49. DOI: 10.1007/3-540-26449-3_1.

[35] T. G. Mason et al. "Rheology of F-actin solutions determined from thermally driven tracer motion." *J. Rheol.* 44 (2000), pp. 917–928. DOI: 10.1122/1.551113.

[36] B. R. Dasgupta et al. "Microrheology of Polyethylene Oxide Using Diffusing Wave Spectroscopy and Single Scattering." *Phys. Rev. E* 65 (2002), p. 051505. DOI: 10.1103/PhysRevE.65.051505.

[37] Q. Li et al. "The laplace approach in microrheology." *Soft Matter* 16 (2020), pp. 3378–3383. DOI: 10.1039/c9sm02242b.

[38] J. C. Crocker et al. "Two-Point Microrheology of Inhomogeneous Soft Materials." *Phys. Rev. Lett.* 85 (2000), pp. 888–891. DOI: 10.1103/PhysRevLett.85.888.

[39] M. T. Valentine, L. E. Dewalt, and H. D. Ou-Yang. "Forces on a colloidal particle in a polymer solution: A study using optical tweezers." *J. Phys.: Condens. Matter* 8 (1996), pp. 9477–9482. DOI: 10.1088/0953-8984/8/47/048.

[40] L. A. Hough and H. D. Ou-Yang. "A New Probe for Mechanical Testing of Nanostructures in Soft Materials." *J. Nanopart. Res.* 1 (1999), pp. 495–499. DOI: 10.1023/A:1010075223642.

[41] E. Fuchs and D. W. Cleveland. "A structural scaffolding of intermediate filaments in health and disease." *Science* 279 (1998), pp. 514–519. DOI: 10.1126/science.279.5350.514.

[42] O. Kratky and G. Porod. "Röntgenuntersuchung gelöster Fadenmoleküle." *Rec. Trav. Chim.* 68 (1949), pp. 1106–1122. DOI: 10.1002/recl.19490681203.

[43] C. P. Broedersz and F. C. Mackintosh. "Modeling semiflexible polymer networks." *Rev. Mod. Phys.* 86 (2014), pp. 995–1036. DOI: 10.1103/RevModPhys.86.995.

[44] J. F. Marko and E. D. Siggia. "Stretching DNA." *Macromolecules* 28 (1995), pp. 8759–8770. DOI: 10.1021/ma00130a008.

[45] C. Bustamante et al. "Entropic elasticity of lambda-phage DNA." *Science* 265 (1994), pp. 1599–1600. DOI: 10.1126/science.8079175.

[46] C. Heussinger, M. Bathe, and E. Frey. "Statistical mechanics of semiflexible bundles of wormlike polymer chains." *Phys. Rev. Lett.* 99 (2007), p. 048101. DOI: 10.1103/PhysRevLett.99.048101.

[47] A. V. Schepers et al. "Multiscale mechanics and temporal evolution of vimentin intermediate filament networks." *Proc. Natl. Acad. Sci.* 118 (2021), e2102026118. DOI: 10.1073/pnas.2102026118.

[48] M. Keller et al. "Slow Filament Dynamics and Viscoelasticity in Entangled and Active Actin Networks." *Philos. Trans. R. Soc. A* 361 (2003), pp. 699–712. DOI: 10.1098/rsta.2002.1158.

[49] J. D. Ferry. "Viscoelastic Properties of Polymer Solutions." *J. Res. Natl. Bur. Stand.* 41 (1948), pp. 53–62. DOI: 10.6028/jres.041.008.

[50] H. Isambert and A. C. Maggs. "Dynamics and rheology of actin solutions." *Macromolecules* 29 (1996), pp. 1036–1040. DOI: 10.1021/ma946418x.

[51] B. Hinner et al. "Entanglement, elasticity, and viscous relaxation of actin solutions." *Phys. Rev. Lett.* 81 (1998), pp. 2614–2617. DOI: 10.1103/PhysRevLett.81.2614.

[52] D. C. Morse. "Viscoelasticity of concentrated isotropic solutions of semiflexible polymers. 2. Linear response." *Macromolecules* 31 (1998), pp. 7044–7067. DOI: 10.1021/ma980304u.

[53] O. Lieleg et al. "Transient binding and dissipation in cross-linked actin networks." *Phys. Rev. Lett.* 101 (2008), p. 108101. DOI: 10.1103/PhysRevLett.101.108101.

[54] F. C. MacKintosh, J. Kas, and Paul A. Janmey. "Elasticity of biopolymer networks." *Phys. Rev. Lett.* 75 (1995), pp. 4425–4429. DOI: 10.1103/PhysRevLett.75.4425.

[55] C. Heussinger and E. Frey. "Floppy modes and nonaffine deformations in random fiber networks." *Phys. Rev. Lett.* 97 (2006), p. 105501. DOI: 10.1103/PhysRevLett.97.105501.

[56] K. E. Kasza et al. "Actin filament length tunes elasticity of flexibly cross-linked actin networks." *Biophys. J.* 99 (2010), pp. 1091–1100. DOI: 10.1016/j.bpj.2010.06.025.

[57] C. P. Broedersz et al. "Cross-link-governed dynamics of biopolymer networks." *Phys. Rev. Lett.* 105 (2010). DOI: 10.1103/PhysRevLett.105.238101.

[58] O. Lieleg et al. "Cytoskeletal polymer networks: Viscoelastic properties are determined by the microscopic interaction potential of cross-links." *Biophys. J.* 96 (2009), pp. 4725–4732. DOI: 10.1016/j.bpj.2009.03.038.

[59] Y.-C. Lin et al. "Divalent Cations Crosslink Vimentin Intermediate Filament Tail Domains to Regulate Network Mechanics." *J. Mol. Biol.* 399 (2010), pp. 637–644. DOI: 10.1016/j.jmb.2010.04.054.

[60] H. Wu et al. "Effect of divalent cations on the structure and mechanics of vimentin intermediate filaments." *Biophys. J.* 119 (2020), pp. 55–64. DOI: 10.1016/j.bpj.2020.05.016.

[61] D. C. Morse. "Viscoelasticity of tightly entangled solutions of semiflexible polymers." *Phys. Rev. E* 58 (1998), pp. 1237–1240. DOI: 10.1103/PhysRevE.58.R1237.

[62] M. Schopferer et al. "Desmin and Vimentin Intermediate Filament Networks: Their Viscoelastic Properties Investigated by Mechanical Rheometry." *J. Mol. Biol.* 388 (2009), pp. 133–143. DOI: 10.1016/j.jmb.2009.03.005.

[63] T. Gisler and D. A. Weitz. "Scaling of the microrheology of semidilute F-actin solutions." *Phys. Rev. Lett.* 82 (1999), pp. 1606–1609. DOI: 10.1103/PhysRevLett.82.1606.

[64] C. Heussinger, F. Schüller, and E. Frey. "Statics and Dynamics of the Wormlike Bundle Model." *Phys. Rev. E* 81 (2010), p. 021904. DOI: 10.1103/PhysRevE.81.021904.

[65] P. J. Flory. "Molecular Size Distribution in Linear Condensation Polymers." *J. Am. Chem. Soc.* 58 (1936), pp. 1877–1885. DOI: 10.1021/ja01301a016.

[66] S. Arrhenius. "Über die Dissociationswärme und den Einfluss der Temperatur auf den Dissociationsgrad der Elektrolyte." *Z. Phys. Chem.* (1889). DOI: 10.1515/zpch-1889-0408.

[67] M. Rief, J. M. Fernandez, and H. E. Gaub. "Elastically coupled two-level systems as a model for biopolymer extensibility." *Phys. Rev. Lett.* 81 (1998), pp. 4764–4767. DOI: 10.1103/PhysRevLett.81.4764.

[68] G. I. Bell. "Models for the Specific Adhesion of Cells to Cells." *Science* 200 (1978), pp. 618–627. DOI: 10.1126/science.347575.

[69] H. A. Kramers. "Brownian motion in a field of force and the diffusion model of chemical reactions." *Physica* 7 (1940), pp. 284–304. DOI: 10.1016/S0031-8914(40)90098-2.

[70] E. Evans and K. Ritchie. "Dynamic strength of molecular adhesion bonds." *Biophys. J.* 72 (1997), pp. 1541–1555. DOI: 10.1016/S0006-3495(97)78802-7.

MATERIALS AND METHODS

4

In this chapter, the experimental and analytical methods are described. The methods described in sections 4.1, 4.3, 4.4, 4.5, and 4.13 are adapted or reproduced from Ref. [1]. The methods described in sections 4.6, 4.7, 4.8, 4.9, 4.10, 4.11, and 4.12 are adapted or reproduced from Ref. [2]. Method sections from Ref. [2], which were written by other authors of the publication, are provided in the appendix in B.2.1, B.2.3, B.3.1, B.3.2, and B.3.4.

4.1 VIMENTIN PREPARATION

4.1.1 Expression and purification

Adapted from Ref. [1]

Recombinant protein expression and purification is performed by Susanne Bauch. The protocols are based on Ref. [3] and were previously described in Ref. [4]. The gene for wild type human vimentin is modified by a point mutation C328N and by the addition of three three additional amino acids, GGC, at the C-terminus. The plasmid is kindly provided by Harald Herrmann. This mutation allows for the specific labeling of the cysteine residue without disruption of the rod structure. In brief, the plasmid containing the mutated vimentin gene is cloned into *E.coli* cells. The bacteria are harvested and the protein extracted from inclusion bodies and purified by subsequent anion exchange chromatography with elution by a salt concentration gradient and cation exchange chromatography. The protein is dialyzed against storage buffer and stored at -80 °C. The storage buffer consists of 1 mM 2,2′,2″,2‴-(ethane-1,2-diyldinitrilo)tetraacetic acid (EDTA, Carl Roth, Karlsruhe, Germany), 0.1 mM 3,12-bis(carboxymethyl)-6,9-dioxa-3,12-diazatetradecane-1,14-dioic acid (EGTA, Carl Roth), 0.01 M methylamine hydrochloride (MAC, Sigma), 8 M urea (Carl Roth) and 5 mM 2-amino-2-(hydroxymethyl)propane-1,3-diol (TRIS, Carl Roth) at pH 7.5 with ≈200 mM residual KCl (Carl Roth) from the ion exchange chromatography.
To exclude protease contamination, sodium dodecyl sulphate gel-electophoresis is performed of i) a freshly thawed protein sample in storage buffer, ii) of a sample taken directly after dialysis against 2 mM sodium phosphate buffer (PB, Carl Roth), and iii) of a sample taken after incubation at room temperature for several days.

4.1.2 Fluorescent labeling

Adapted from Ref. [1]

The vimentin labeling protocol is based on Refs. [5, 6]. For labeling, the protein is dialyzed (50 kDa molecular weight cut-off dialysis tubing, SpectraPor 7, Germany) against 50 mM sodium phosphate buffer (PB) containing 5 M urea (Carl Roth) at pH 7.0 at 8-10 °C over night. At this urea concentration, the

protein assembles up to the dimer state where labeling is reproducibly efficient. After dialysis, the concentration of the protein is adjusted to 1 g/L by UV-Vis absorption spectrometry (NanoDrop, ThermoFisher, Germany and peQlab, Germany). The dye ATTO647N maleimide (ATTO-Tec, Germany), 10 mM in dimethylsulfoxid (DMSO, Carl Roth), is added to 1 mL protein in four 5 µL portions for a final concentration of 0.2 mM of the dye. The maleimide group specifically binds to the free cysteine residue at the C-terminus. After incubation at room temperature for 2 h, the unreacted dye is quenched by the addition of 1 mM L-cysteine (Carl Roth) and the reaction incubated for another 60 min at room temperature. The protein and unbound dye are separated by size exclusion chromatography (Bio-gel P30, Biorad, Germany on a 1.0×30 cm Econo-column, Bio-Rad). The protein concentration and labeling ratio are determined by UV-Vis absorption spectrometry with an extinction coefficient of $\varepsilon_p(280\,\mathrm{nm})$=24.24 × $10^3\,\mathrm{M^{-1}cm^{-1}}$ [7] and a molecular mass of 53.7 kDa [8] for vimentin, and an extinction coefficient of $\varepsilon_d(647\,\mathrm{nm})$=1.5 × $10^5\,\mathrm{M^{-1}cm^{-1}}$ and correction factor $cf(280\,\mathrm{nm})$=0.05 for Atto647N [9]. The labeling ratio is calculated by the expression:

$$\text{labeling ratio} = \frac{A(647\,\mathrm{nm})\varepsilon_p(280\,\mathrm{nm})}{(A(280\,\mathrm{nm}) - A(647\,\mathrm{nm})\cdot cf)\cdot\varepsilon_d(647\,\mathrm{nm})}\,. \tag{4.1}$$

The labeled protein is dialyzed against storage buffer, 2 mM PB with 8 M urea, pH 7.5, at 8-10 °C pH over night, and subsequently stored at -80 °C.

4.1.3 Reconstitution and assembly of single filaments

Adapted from Ref. [1]

Reconstitution and assembly is performed as previously reported [4]. In brief, unlabeled and labeled monomers are mixed for the desired labeling ratio of 4% for single-filaments experiments and 0.9% for microrheology experiments. The protein is reconstituted at room temperature by dialysis (50 kDa molecular weight cut-off dialysis tubing SpectraPor 7) against 2 mM PB at pH 7.5, while decreasing the urea concentration every 30 min in steps of 6, 4, 2, 1, 0 M urea and a subsequent overnight dialysis step at 8-10 °C. Assembly is induced by one of two methods: i) For all OT experiments, the protein is dialyzed against *assembly buffer* (2 mM PB with 100 mM KCl at pH 7.5) at 36 °C for 16 h at a protein concentration of 0.2 g/L. ii) For microrheology and filament length measurements, assembly is induced by the 'kick-start-method'. Details of the microrheology sample preparation are described in section 4.8.1.

4.2 MALEIMIDE FUNCTIONALIZATION OF POLYSTYRENE BEADS

Maleimide-functionalized polystyrene beads are prepared as described in Refs. [4, 10]. The supernatant of 100 µL carboxylated polystyrene beads (Pps-4.2 COOH 4.0-4.4 µm at 5% (w/v), Kisker Biotech, Germany) is removed after cetrifugation in a table top microcentrifuge (Eppendorf miniSpin, rotor F45-12-11, Eppendorf, Hamburg, Germany) for 1-2 s at 12,000× g. The pellet is resuspended in 1 mL 100 mM 4-morpholineethanesulfonic acid (MES, Merck, Kenilworth, New Jersey, USA) buffer, mixed by shaking for 10 min, and the super-

natant decanted after centrifugation. This washing step is repeated twice. The coating solution is prepared by dissolving 8 mg NH_2-PEG-maleimide (molecular weight 5,000 g/mol, Nanocs, New York, New York, USA), 16 mg NH_2-PEG-OH, (molecular weight 5,000 g/mol, Iris-Biotech, Marktredwitz, Germany) and 40 mg 1-ethyl-3-(3-dimethylaminopropyl)carbodiimide (EDC, Merck) in 200 µL phosphate buffered saline (PBS). The bead pellet is resuspended in 100 µL PBS with 100 µL of the coating solution and thoroughly mixed by vortexing for 2 min. The mixture is subsequently sonicated for 2 h while briefly vortexing every 20 min. After this mixing step, the beads are washed with PBS containing 2% bovine serum albumin (Merck) in three centrifugation-resuspension cycles. Finally, the bead pellet is resuspended in 1 mL PBS containing 2% bovine serum albumin and stored at 4 °C.

4.3 STRETCHING SINGLE FILAMENTS BY OPTICAL TRAPPING

Reproduced from Ref. [1]

The experiments are performed using a setup that combines optical traps, confocal microscopy and microfluidics (C-Trap, Lumicks, Netherlands). A four-inlet glass microfluidic flow cell enables easy change of buffer during the experiment as the sub-channels in the flow cell are separated by laminar flow. The syringes feeding the microfluidic flow cell are driven by air pressure. Solutions are injected into the four channels (the channel geometry is shown in Fig. A1) as follows: 1: beads in measuring buffer, 2: measuring buffer, 3: assembly buffer, 4: vimentin in assembly buffer. Figure 5.1b shows a simplified sketch, excluding channel 2 that is used for calibration of the traps.
For the optical trap measurements, the filaments are diluted 150-fold in assembly buffer. Maleimide-functionalized polystyrene beads [4, 10] are diluted in measuring buffer. The optical trap is calibrated by analysis of the power spectral density of the thermal fluctuations of the trapped beads. Filaments are tethered to trapped beads in assembly buffer in flow. The flow is then stopped, the beads with the tethered filament are moved to the flow cell region that contains measuring buffer, and the filaments incubated for 30 seconds without flow. The filaments are stretched at a loading rate of 0.21 ± 0.05 µm/s. Filaments are stretched until rupture or until the force exceeds the trap potential and one of the beads is pulled out of the trap. For each condition, force-strain curves of at least seven single, stable filaments are recorded. Depending on the initial length of the filament, one measurement is completed within 30-60 s.
As measuring buffers we use 2 mM PB at varying pH (5.8 - 8.5) and concentrations of KCl (0, 50, 100, 150 mM) or $MgCl_2$ (0, 5, 10 mM) (Carl Roth). The physiological KCl concentration is up to 150 mM [11], which corresponds to the upper c(KCl) we use here. The highest $c(MgCl_2)$=10 mM used in this study is the threshold concentration observed for filament bundling and collapse of vimentin networks [12–14]. Albeit the pH in the extracellular space can be lower than 5.8, all lower values would be outside the buffer range of PB.

4.4 ANALYSIS OF SINGLE FILAMENT MECHANICS

4.4.1 Calculation of single force-strain curves

Adapted from Ref. [1]

For each filament, the initial length, L_0, is determined and used for the calculation of the strain: $\varepsilon = (L - L_0)/L_0$. To obtain L_0, the raw force-distance curve is smoothed by a moving average with a window width of 10 data points to account for fluctuations of the trap. The initial length is set as the filament length at the last data point before the smoothed curve reaches 5 pN. We choose the length at 5 pN as the reference length as this force is clearly above the thermal fluctuations of the trap as well as the filament.

4.4.2 Analysis of the filament stability

Reproduced from Ref. [1]

Force-strain curves are plotted and the curves that show a plateau and subsequent stiffening are categorized as stable filaments. All other filaments are categorized as instable. From confocal videos of the filament stretching process and the force-strain behavior of the stable filaments, bundles are identified and the force-strain curves of the bundles excluded from further analysis. Examples for confocal images of bundles and single filaments are shown in Fig. 5.5.

4.4.3 Calculation of average force-strain curves

Reproduced from Ref. [1]

For each condition, the average maximum strain of all stable filaments is calculated. Each stable force-strain curve is scaled to the average maximum strain, interpolated to 200 values, and the forces are averaged. Details of the averaging of the force-strain curves are described in Ref. [15].

4.4.4 Analysis of the slope of the plateaus

Adapted from Ref. [1]

The plateau of each single force-strain curve is analyzed for all stable filaments. A typical analysis for one single force-strain curve is shown in Fig. 4.1. The point of maximum strain, ε_{max}, of each curve is used to find the mid data point of the curve, ε_{mid} (yellow in Fig. 4.1). The data points with relatively constant slope are determined. To do so, the differential $\frac{dF}{d\varepsilon}$ of each single force-strain curve is calculated. To account for changes in length of the curve and noise of the data, each differential force-strain curve is then smoothed using a moving average with the width of $\frac{1}{20}$ of the number of data points in the curve before ε_{max}. The values $\frac{dF}{d\varepsilon}$ at the 10 data points before and after ε_{mid} are averaged to find $\frac{dF}{d\varepsilon}(\varepsilon_{mid})$. Next, the first maximum of $\frac{dF}{d\varepsilon}$, position A, is calculated (marked in Fig. 4.1). The first and last data point to fulfill

$$\frac{dF}{d\varepsilon} < \varepsilon_{mid} + 0.35 \cdot \left(\frac{dF}{d\varepsilon}(A) - \frac{dF}{d\varepsilon}(\varepsilon_{mid})\right) \tag{4.2}$$

are termed ε_I (red, solid) and ε_{II} (blue, solid), respectively. To ensure that the transition regions between I, II and III are not included in the analysis of the slope of the plateau, a linear regression (green line) of the force-strain curve is

calculated for the center 80% of the length of the plateau (between the open red and blue circles in Fig. 4.1). The mean slope and standard deviation of all force-strain curves of each measuring condition are calculated .

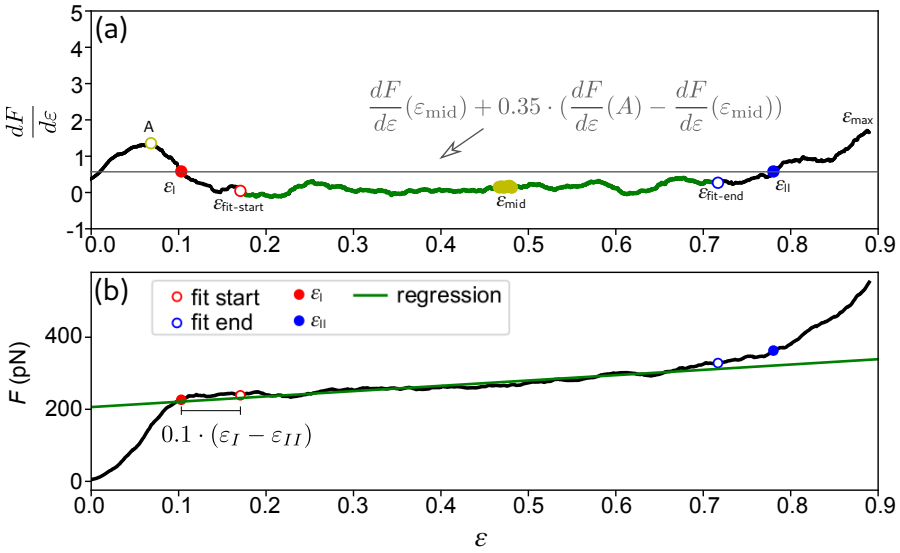

Fig. 4.1: **Analysis of the slope of the plateau for one single force-strain curve.** a) Differential force-strain curve, smoothed with a moving average with the window width of $1/20$ of number of data points in the curve before ε_{max}. The center of the curve (ε_{mid}) is marked in yellow. The peak of $\frac{dF}{d\varepsilon}$, A, is shown by the open yellow circle. The threshold for the plateau is indicated by the gray line. The values for ε_I (red, solid) and ε_{II} (blue, solid) at the threshold are shown. The open red and blue circles flank the region used for the calculation of the regression (green). b) The resulting regression, plotted together with the raw force-strain curve. Adapted from Ref. [1].

4.4.5 Analysis of the force of the plateaus

Reproduced from Ref. [1]

For the analysis of F_{plateau}, ε_{I}, determined from the average force-strain curve for each condition, is used. The force at ε_{I} for each single force-strain curve is determined and the mean value and standard deviation are calculated.

4.4.6 Determination of the end points of the elastic and plateau regions

Adapted from Ref. [1]

For the determination of the slope of the plateau, the regression is calculated over a large region of the force-strain curve. This approach compensates for noise in the data. However, the noise in each data curve limits the accurate determination of ε_{I} and ε_{II}. Therefore, for the analysis of ε_{I} and ε_{II} for each condition, the average force-strain curves are used as shown in Fig. 5.2. The average curves are treated in the same way described above for the single force-strain curves. The only difference is that here the $\frac{dF}{d\varepsilon}$ curves are smoothed with a moving average of 15 data points.

4.4.7 Analysis of the initial slope of the force-strain curves

Adapted from Ref. [1]

The initial slope is determined for all single force-strain curves by calculating linear regression for the data range between strains from 0.02 to 0.1, or from strain 0.02 to a force of 100 pN, whichever occurs earlier.

4.5 FORCE-STRAIN MONTE-CARLO SIMULATIONS

Reproduced from Ref. [1]

Simulations are performed by Charlotta Lorenz. A vimentin filament is mechanically modeled as previously described [4, 15]. The force-strain behavior of the modeled filament is determined by a Monte-Carlo simulation written in `MatLab` [15]. The simulation is run with one varied parameter while keeping the others constant as shown in Fig. 5.9a,b,e,f. The default parameters are the alpha-helical spring constant ($\kappa_\alpha = 5.5$), the number of monomers in a subunit ($N_{sub} = 32$), the free energy difference between the alpha state and unfolded state ($\Delta G = 2$), and the length by which an alpha helix can extend upon unfolding $\Delta L = 1$.

4.6 OPTICAL TRAP MEASUREMENTS OF INDIVIDUAL FILAMENT–FILAMENT INTERACTIONS

Adapted from Ref. [2]

Individual interaction measurements are performed with a high-power OTs setup (C-trap, Lumicks) in quadruple-trap mode. The OTs setup combines optical trapping with confocal microscopy with excitation lasers of wavelength 532 nm, and 638 nm, and a pressure-driven microfluidic flow cell. The four inlets of the microfluidic flow cell (I)-(IV), as shown in Fig. 6.2, are loaded with (I) maleimide-functionalized polystyrene particles [4, 10] in assembly buffer, (II) pure assembly buffer, (III) 1.3 mg/L vimentin filaments in assembly buffer, and (IV) the respective measuring buffer. The six different measuring buffers are 2 mM PB with 100 mM KCl, pH 7.5 (assembly buffer) with 1) no addition, 2) 1.6 mM (0.1% weight [w]/volume [V]) TritonX-100 (TX), 3) 0.16 mM (0.01% w/V) TX, 4) 5 mM $MgCl_2$, 5) 20 mM $MgCl_2$, or 6) 20 mM $MgCl_2$ and 1.6 mM TX. In a microfluidic flow cell (Fig. 4.2), single filaments are attached between two bead pairs, and the binding is controlled by confocal microscopy. For each measurement, four single particles are trapped at position 1, see Fig. 4.2. The trap is calibrated by recording the power spectral density caused by Brownian motion of the trapped particles at position 2 without flow. The particles are moved to the filament channel, position 3, and a weak flow is applied. The binding of the filaments to the particles is controlled with the confocal microscope with the laser power for the 638 nm laser set to 0.11 µW, and the 532 nm laser set to 0.79 µW. The pixel dwell time is 0.1 ms. When sufficiently long filaments are bound, the particles are moved back to position 2; we now have one single filament attached between particles b1 and b2, called f12 from now on, and another filament between b3 and b4, filament f34. The filaments f12 and f34 start out in a parallel conformation in the same z-plane. Filament f34 is rotated by 90° by bringing b4 closer to f12. The particle pair connected to f34 is now moved down in z by -4.7 µm. By movement of the stage, all particles and filaments are brought to the measurement position in

the respective measuring buffer, position 4 in Fig. 4.2. At position 4, filament f12 is moved upwards in z by 2.4 µm, and filament f34 is moved in the x-y-plane to cross f12. The z-position of f12 is adjusted to be in the confocal plane. The particle pair on f34 is moved along the z-axis to a position close to f12 but without bringing f12 and f34 in contact. By inspection of the forces on the particles and the confocal image, we ensure that the filaments are not stretched. The forces on all particles are now set to 0 pN in the software. The filaments are brought into contact in the confocal plane. To ensure that the filaments f12 and f34 are in contact, f34 is briefly moved to a lower z-position which leads to a slight deformation of the filaments for which a force is detected. Filament f34 is moved back upwards into the z-plane until the detected force drops to zero, which occurs in the contact plane. The filament f34 is moved across filament f12 in the confocal x-y-plane at 0.55 µm/s, and the force acting on bead b1 is recorded for further analysis.

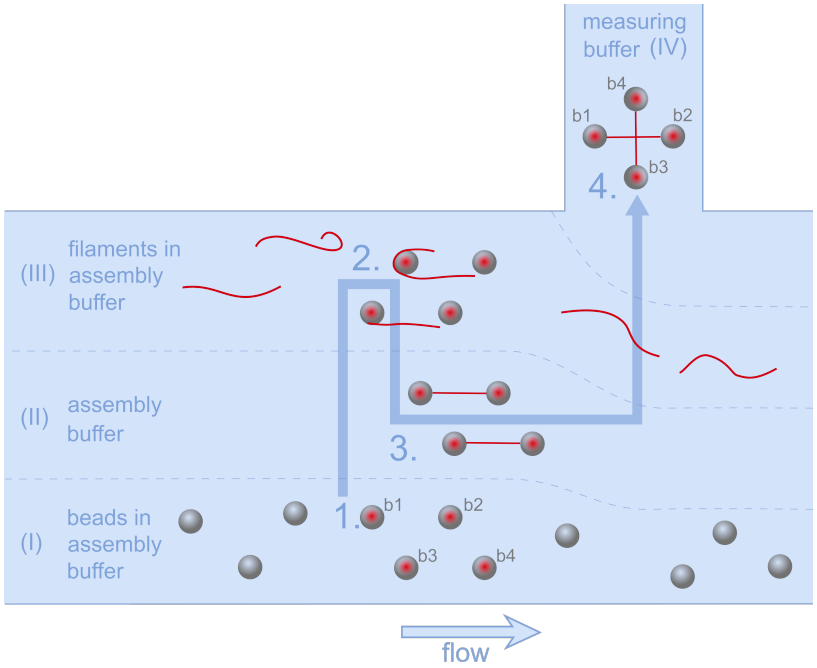

Fig. 4.2: **Schematic of the experimental protocol for single interaction measurements in the optical trap.** Laminar flow enables separation of substances in channels (I)-(IV). Four beads (b1-b4) are captured in the four OTs at position 1. in channel (I). The beads are calibrated in channel (II), and subsequently moved to position 2. in channel (III) to capture vimentin filaments. The beads are moved to position 3. in the buffer channel (II) to ensure that a single filament is connected to the beads pairs at both ends. After rotating one bead pair at position 3., the filaments are moved to position 4. in the measuring buffer in channel (IV). The filaments are brought into contact at position 4., where measurements are performed. Reproduced from Ref. [2].

During the measurements, the positions of all beads are recorded by particle tacking in bright-field images, while the filaments are observed with confocal microscopy. If possible, the movement is stopped before bead b4 comes in contact with filament f12; the particles on f34 are lifted in z, and moved back to the starting position of the measurement. Contact between the filaments is established, and another measurement is recorded. In the case of a very

strong interaction, where filament f12 is not in the initial conformation when bead b4 reaches the y-position of f12, the movement is continued until the interaction ruptures or b4 comes into contact with f12. Such interactions are typically categorized as "strong". The category of strong interactions includes all interactions with $F_{1y,\max} > 100\,\mathrm{pN}$, where the interaction is so strong that one of the beads is pulled out of the trap or one of the filaments ruptures. After failure of one of the filaments or a strong interaction, the particles are discarded.

4.7 ANALYSIS OF THE INTERACTION DATA

Adapted from Ref. [2]

The force acting on bead b1 opposing the direction of the movement of filament f34, $F_{1y,\mathrm{raw}}$, is plotted against the distance by which f34 has been moved, d, as shown in gray in Fig. 4.3a. As the particles are moved at a constant speed, the force–distance curves are equivalent to force–time curves. For each force–distance curve, regions without interaction are manually selected, as marked in blue in Fig. 4.3a. A linear regression is calculated for these regions of no interaction (gray line in Fig. 4.3a). This is necessary, as we observe a linear decrease of the force detected by trap1 over time, which can be attributed to the interaction of the trap potentials. The linear background is subtracted from the raw data (black in Fig. 4.3a).

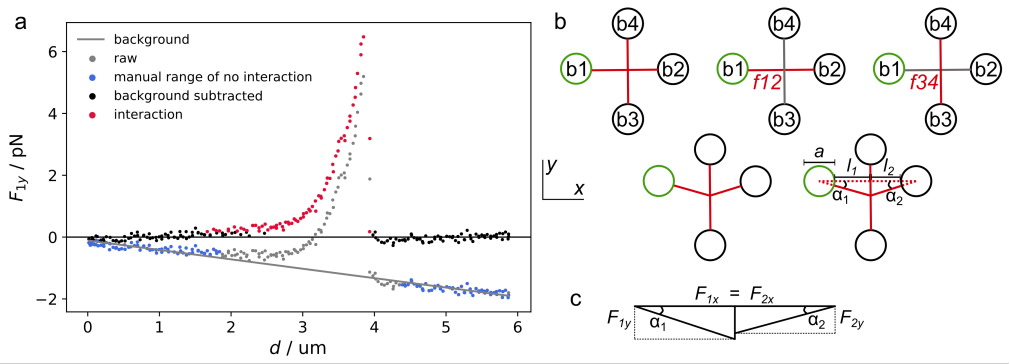

Fig. 4.3: **Analysis of single interaction experiments.** a) The force F_{1y} is plotted against the relative position change d of bead pair f34. The raw data , $F_{1y,\mathrm{raw}}$, are plotted in gray. Two regions without interaction are chosen manually (blue) and a linear regression is calculated for those data points (gray line). This line is subtracted from the raw data to obtain the corrected force F_{1y}. The standard deviation of the regions without interaction (black) is calculated and all data points exceeding the 2σ-limit of this region are classified as interactions, marked in red. b) To obtain the interaction force F, the background corrected forces are further multiplied by a geometry correction factor to account for filament f34 being off-center on filament f12 as described in Eq. 4.6. c) Force diagram for the geometry shown in b). Reproduced from Ref. [2].

4.7.1 Classification of interactions

Adapted from Ref. [2]

At this stage, the force curves are classified into two groups: (i) All background corrected $F_{1y}(d)$ curves that do not exceed 0.99 pN are considered "noninter-

acting"; and (ii) all other curves are sorted into the "interacting" class. For all curves in the interacting class, all data points exceeding the 2σ-limit of the noninteraction region (blue in Fig. 4.3a) are marked as the interaction region (red). Single data points that exceed the 2σ-limit or interaction regions that do not lead to an interaction that exceeds 0.99 pN are removed manually. The duration of interactions between filaments as well as the total time of one experiment is determined, and thereby also the experiment time without interactions. There are three different types of interactions, as shown in Fig. 6.9c-e: i) ruptures, where F_{1y} returns to 0 pN; ii) kinks, *i.e.*, ruptures where F_{1y} does not decrease to 0 pN; and iii) strong interactions, *i.e.*, cases where the experiment ends before a rupture is observed and $F_{1y,\max} > 100$ pN. Interactions where $0 < F_{1y} < 100$ pN at the end of the experiment – *i.e.*, without rupture – are excluded from further analysis, as they cannot be sorted in any of the categories i)-iii). For all interactions, the force on the interaction site, F, is calculated with the geometry factor.

4.7.2 Geometry correction

Reproduced from Ref. [2]

The force acting on the interaction site F is given by

$$F = F_{1y} + F_{2y}. \tag{4.3}$$

However, in our setup, we can only directly measure forces acting on bead b1 and not the forces acting on bead b2. We therefore calculate F from the position of filament f34 on filament f12. The forces in the x-direction have to be balanced so that $F_{1x} = F_{2x}$. With the angle α_i, $(i = [1,2])$ between the deflected and non-deflected filament section,

$$\tan\alpha_1 = \frac{F_{1y}}{F_{1x}} = \frac{\Delta y_i}{l_1 + a/2} \quad \text{and} \quad \tan\alpha_2 = \frac{F_{2y}}{F_{2x}} = \frac{\Delta y_i}{l_2 + a/2}, \tag{4.4}$$

the bead diameter a, and the distance y_i by which the interaction point is been moved, F_{2y} can be expressed in terms of F_{1y}

$$F_{2y} = F_{1y}\frac{l_1 + a/2}{l_2 + a/2}. \tag{4.5}$$

By using $l_1 + l_2 = l_{12}$ and Eq. (4.3), the interaction force F is given by the expression

$$F = F_{1y}\left(\frac{l_{12} + a}{l_2 + a/2}\right). \tag{4.6}$$

All measurements that show interactions are corrected by their respective geometry factor to obtain the actual interaction force F, shown in Figs. 6.9 and 6.12, from the measured force F_{1y}. The histogram of the maximum forces F_i, reached before a rupture or rebinding event, is plotted in Fig. 6.12.

4.7.3 Force-independent binding rates

Adapted from Ref. [2]

For each measurement, we determine the number of interactions that start at zero force and exceed 1 pN, and we extract the experiment time, during which we observe no interaction. As binding events are rare, we determine the mean binding rate by bootstrap resampling. For the resampling, we randomly draw N single measurements; N is equal to the total number of measurements, each with the corresponding number of interactions and measurement duration without interaction. A measurement is placed back into the population after each draw. The binding rate of each resampled population is calculated by summing over the number of all interactions which start at zero force, and dividing the sum by the corresponding total experimental time without interactions. This calculation results in the force-independent binding rate $r_{e,b}$, as we only take binding events at zero force into account. The resampling is repeated 10,000 times, and the mean and standard deviation of the resulting $r_{e,b}$ are determined.

4.8 MICRORHELOGY OF RECONSTITUTED VIMENTIN NETWORKS

4.8.1 Sample preparation

Adapted from Ref. [2]

Carboxylate-modified, green fluorescent microparticles of 2-µm diameter (Molecular Probes, Eugene, Oregon, USA) are added during assembly of the filaments. To prevent adsorption of the protein to the microparticles, the particles are passivated by incubation with 0.1 g/L poly-(L-lysine)(20 kDa)-g[3.5]-polyethylene glycol(2 kDa) (SuSoS AG, Dübendorf, Switzerland) at room temperature for 15 h. The microparticles are washed three times with PB before use [16].
For assembly of vimentin networks, the final protein concentration for the measurement is adjusted to 1 g/L. We prepare 6×buffers of 2 mM PB i) 600 mM KCl (assembly buffer) and ii) 600 mM KCl with 30 mM $MgCl_2$, as well as iii) 600 mM KCl with 0.96 mM TX, all at pH 7.5. Assembly is initiated by the kick-start method – *i.e.*, direct mixing of the respective assembly buffer with unpolymerized vimentin. Protein and buffer are mixed to achieve the final protein concentration of 1 g/L protein in 1× buffer, and microparticles are added at less than 0.02% solids.
Two no. 1 cover slides (24×60 mm and 18×18 mm^2, VWR, Radnor, Pennsylvania, USA) are cleaned by sonication in isopropanol for 15-20 min, and dried under a stream of $N2_2$. For the sample chamber, a rectangular hole of 9×7 mm is cut into 100- to 120-μm^2 thick doubled-sided tape. The tape is placed on a clean 24×60 mm^2 cover slide, 6 µL of the respective assembly buffer, mixed with the protein and microparticles are placed in the sample chamber, and the device is sealed with an 18×18 mm cover slide. The sample chambers are kept rotating at slow speed to avoid settling of the microparticles. After assembly in the dark at room temperature for the times given in Fig. 6.1, MPT measurements are performed.

4.8.2 Microparticle tracking

Reproduced from Ref. [2]

For passive microrheology measurements, we perform MPT using a commercial bright-field microscope with a monochromatic LED with $\lambda = 660\,\text{nm}$ and a $60\times$ objective (CFI Achromat FF, numerical aperture [NA] = 0.80, working distance = 0.3 mm, Nikon, Tokyo, Japan) with preimplemented tracking software (Lumicks). We record a time series of the two-dimensional microparticle position by tracking the diffraction-ring patterns of microparticles with a quadrant interpolation algorithm. Traces are recorded for microparticles with a minimum distance of 30 µm to all surfaces over the course of 6 min at a frame rate of $138\,\text{s}^{-1}$.

4.8.3 Active microrhelogy

Reproduced from Ref. [2]

We perform active microrheological experiments by oscillating the microparticle in the network with an OT (NanoTracker 2, JPK Instruments, Berlin, Germany) mounted on a Zeiss inverted optical microscope (AXIO Observer A1, Carl Zeiss, Jena, Germany). The setup is equipped with a water-immersion objective ($63\times$, C-Apochromat, NA = 1.2; Carl Zeiss) and an infrared laser (1,024 nm Nd:YAG, 5 W). Trap stiffness and sensitivity are calibrated in assembly buffer from the power spectrum of the thermal fluctuations of several microparticles. We oscillate each microparticle with an OT at a laser power of 20 or 50 mW. The microparticle displacement and the phase shift of the oscillation of the particle with respect to the trap center are measured by back-focal-plane interferometry with a quadrant position detector.

4.9 ANALYSIS OF MICRORHEOLOGY EXPERIMENTS

The calculation of the complex shear modulus G^* from the passive and active microrheology measurements is described in B.2.1, B.2.3. For each buffer condition and network formation time, median MPT and G^* curves are calculated. For this calculation, first, the median curve of each sample is determined. The median curves shown in Fig. 6.1, are determined by calculating the median curve of the sample-median curves.

4.9.1 Plateau modulus

Reproduced from Ref. [2]

To determine the frequency dependence of the storage modulus for each median G' curve, we fit the curve in the frequency range where $\omega > 0.005\,\text{s}^{-1}$ and $\frac{dG'}{d\omega} < 3 \times 10^{-3}\,\text{Pa s}$ by a power law $G' = C\exp(p_0\omega)$ using the least-squares method. The resulting fit curves and exponents p_0 are presented in Fig. 6.3. We evaluate the plateau modulus from the storage modulus of the sample median curves at $\omega = 1\,\text{s}^{-1}$.

4.9.2 Relaxation time

Adapted from Ref. [2]

In a network, the bending of a single filament is constrained by other filaments. The relaxation time of the bending mode with the longest wavelength that is not constrained is τ_e [17]. The relaxation time $\tau_e = 1/\omega_e$ is therefore the time scale where the mechanical response shifts from the deformation of the network $\omega < \omega_e$ to the deformation of the single filaments $\omega > \omega_e$. We extract the relaxation time from the cross-over of the median curves of G' and G'' [17].

4.9.3 Relative bundling parameter

Adapted from Ref. [2]

At high frequencies, the shear modulus of networks of semiflexible filaments is given by [18]

$$G(\omega) \approx \frac{1}{15}\rho_v \kappa l_P \left(-2i\frac{\zeta}{\kappa}\right)^{3/4} \omega^{3/4} - i\omega\eta. \tag{4.7}$$

At these high frequencies, the response depends on the total length per volume ρ_v, the persistence length l_P, the lateral drag coefficient ζ, and the bending stiffness $\kappa = k_B T l_P$. We analyze the imaginary part and fit our G'' curves at high frequencies, $\omega > 5\,\mathrm{s}^{-1}$, by

$$G'' = b\omega^{3/4} - \omega\eta. \tag{4.8}$$

We use this fit to investigate the effect of bundling on the sample mechanics. From Eq. (4.7) and $\kappa = k_B T l_P$ we obtain

$$b = \frac{1}{15}\rho_v k_B T l_P^2 \left(-2\frac{\zeta}{l_P k_B T}\right)^{3/4} * Im(i^{3/4}). \tag{4.9}$$

In Eq. (4.9), ρ_v, l_P and ζ depend on the number of filaments in a bundle, N, as described in the following. For a simplified system of a cubic mesh, the length per volume scales as $\rho_{v,b} = 1/N\rho_{v,f}$. The lateral drag coefficient is defined as

$$\zeta = \frac{4\pi\eta}{\ln(0.6\lambda/d)} \tag{4.10}$$

with the η solvent viscosity, the filament or bundle diameter d and the characteristic length scale λ, which can be the mesh size ξ [19]. The dependence of the persistence length on N in worm-like bundles depends on the coupling of the filaments within the bundle.
For comparison of the bundling parameter b (Fig. 6.1g in chapter 6) between the samples at the different time points, we calcualte a relative bundling parameter b_{rel}

$$b_{rel} = \frac{b}{b_f}\,. \tag{4.11}$$

We define a reference value for a network without bundles, b_f, and set b_f to the value obtained from $b(6\,h, \mathrm{KCl})$, which is the first time point where the networks in the control condition show confinement or the microparticles. To

determine the effect of bundling on the high frequency mechanics, we assume fully coupled bundles, [20], as discussed in chapter 6:

$$l_{pb} = N^2 l_{pf} \ . \tag{4.12}$$

By combining Eqs. 4.9, 4.12, and 4.11, we obtain

$$b_{rel} = \frac{b}{b_f} = (\frac{\zeta_b}{\zeta_f})^{3/4} N^{6/4}. \tag{4.13}$$

The lateral drag coefficients ζ_f for filaments and ζ_b for bundles have a negligible effect in this relation. In Fig. 6.4f, the relative bundling parameter is plotted against N. These calculations allow for a rough estimate of the average number of filaments per bundle.

4.10 IMAGING FILAMENT NETWORKS

Adapted from Ref. [2]

To study to overall appearance of the fluorescently labeled vimentin networks, confocal stacks of the samples used in microrheology experiments are recorded by using an IX81 confocal microscope (Olympus, Hamburg, Germany), equipped with a 100× objective with numerical aperture (NA)=1.40 (UPLANSApo100X, oil, Olympus). For each sample, the full height of the sample chamber is scanned with 5-µm z-steps. Measurements are repeated throughout the course of the week long study of the mechanics of the networks.

As fluctuations of the network strongly impede the image quality of the relatively slow confocal scans, we employ a second approach based on a fast laser scanner. Again, confocal stacks of the samples as used in microrheology experiments, shown in Fig. 6.7, are recorded. In these measurements, we determine the structure change with increasing distance from the glass surface. For these measurements, a custom, fast-laser-scanning confocal setup with a 60× objective with NA=1.20 (UPLSApo60XW, Olympus) is used to record images at a frame rate of 39 s^{-1} in steps of 1 µm z-distance. For each z-position 300 single frames are recorded and a final image is calculated as the sum of all single frames. The data is recorded by Jan Christoph Thiele and the setup is described in detail in Ref. [21].

4.11 IMAGING SINGLE FILAMENTS

Reproduced from Ref. [2]

Single filaments are imaged with wide-field fluorescence microscopy at 100× magnification (NA=1.40, UPLANSApo100X, oil, Olympus) by using an IX81 inverted microscope (Olympus). To follow the assembly speed of the filaments, vimentin protein and the respective assembly buffer are mixed at the same ratio as for microrheology experiments for a final protein concentration of 0.2 g/L and incubated for the respective duration at room temperature. The sample is diluted to a concentration of 2 mg/L for imaging. The filaments are imaged on no. 1 cover slides.

4.12 ANALYSIS OF FILAMENT LENGTHS

Adapted from Ref. [2]

We determine the lengths of the filaments in the fluorescence microscopy images (Fig. B1) by manual tracing using ImageJ. During the manual tracing, filaments are distinguished from bundles by shape and intensity, and only filaments that appear nonbundled are traced. At each time point and for each buffer condition, we plot the distribution of the filament lengths in histograms with a bin width of 3× the full width half maximum (FWHM) of the point-spread function.
The assembly of IFs occurs in two steps, combining lateral assembly to ULFs and longitudinal assembly by end-to-end annealing of the ULFs as shown in Fig. 6.2. As described in section 3.4.1, the longitudinal assembly of IFs is equivalent to a polymer step growth where the ULFs are the "monomers" of the polymerization. Following the Flory-Schulz theory [22], the probability that a single reaction, the end-to-end annealing, has occurred is equal to q, the extent of the reaction. To build a polymer from x monomers, $x-1$ reactions have to take place, which occur with the probability q^{x-1}. The probability to find an unreacted end group is $1-q$. The probability to find a polymer of length x is therefore given by:

$$P_x = (1-q)q^{x-1} = \frac{N_x}{N}, \tag{4.14}$$

where N is the total number of molecules of all sizes and N_x is the number of molecules of length x. As we fit histograms of the length distributions, Fig. B2, with a certain bin width, we use the integrated form of Eq. (4.14) and optimize the fit for the full width of the bin by the least square method. The resulting q values are shown in Fig. B3. To convert the lengths we measure here into the number of ULFs in one filament, we use $l_m = 43$ nm [23] – the repeat length of ULFs in IFs– as the "monomer size". We utilize that a ULF has a constant weight and length to calculate the length average l_M from q, in analogy to the number average:

$$l_M = \frac{l_m}{1-q}. \tag{4.15}$$

4.13 FINITE ELEMENT SIMULATION OF THE MICROFLUIDIC FLOWCELL

Reproduced from Ref. [1]

A simplified microfluidic chip design (Fig. A1) is used for finite element method (FEM) simulations with `COMSOL Multiphysics 5.3` (COMSOL GmbH, Göttingen, Germany). Flow and diffusion are simulated for an average velocity of 0.001 m/s laminar inflow for each inlet for water plus K^+ ($D_K = 1.67\,10^{-9}\,m^2/s$) [24] or Mg^{2+} ($D_{Mg} = 0.594\,10^{-9}\,m^2/s$) ions [24]. For the pH, the concentration of hydrogen ions $c(H^+)$ is calculated as

$$c(H^+) = 10^{-pH} \tag{4.16}$$

and the diffusion of H^+ is estimated by using $D_H = 8.17\,10^{-9}\,m^2/s$ [24]. First, the equilibrium ion distribution in the chip is simulated under flow. Taking this as a starting condition, a second simulation is calculated without flow, only allowing diffusion. The change of the concentrations of the cations and H^+

ions is simulated at the position of the force-strain measurement (Fig. A1a, red mark) for a duration of 5 min.
For the experiments where we measure single interactions, we use the microfluidic flow cell as shown in Figs. 4.2 and A2e. The measuring buffer is injected as indicated by the orange flow lines in Fig. A2e. During the measurement itself, no flow is applied. This leads to a slow decrease of the concentration of the species of interest (Mg^{2+} or TX) at the position of the measurement by diffusion. To approximate the concentration during the experiment, we perform finite element method (FEM) simulations using COMSOL Multiphysics 5.3. The results are shown in Fig. A2a-d, alongside the flow cell design we use for the simulation in Fig. A2e. The simulation combines two steps: first, the equilibrium concentration distribution is calculated in flow, *i.e.*, during the period where the microparticles are trapped and the filaments are tethered to the particles. Here, we use an average laminar inflow velocity of 0.001 m/s for each inlet. All channels are filled with water, in channel 4 we additionally add Mg^{2+} or TX. Because of the detergent properties of TX, the diffusion coefficient depends on the concentration. At c(TX)=0.16 mM, which is below the critical micelle concentration of TX, $D_{TX} = 8.25 \times 10^{-7}\,cm^2s^{-1}$, whereas c(TX)=1.6 mM is higher than the critical micelle concentration, therefore $D_{TX} = 6.93 \times 10^{-7}\,cm^2s^{-1}$ [25]. In the second simulation step, the inflow is stopped and we observe the decrease of the concentration by diffusion at the position of the measurement, which is marked by the black square in Fig. A2e.

4.14 STRETCHING MDCK II CELLS ON ELASTIC SUBSTRATES

4.14.1 Elastic devices for cell stretching

For cell stretching experiments, an elastic, biocompatible poly(dimethylsiloxan) (PDMS) device is fabricated. For the complete device, a thin PDMS membrane is attached to PDMS side walls. The side walls are hexagonal with a corner-to-corner diameter of 38 mm, have 5 mm diameter holes in the corners of the hexagon and a circular inner hole with 14 mm diameter (Fig. 4.4, top). Cells can be cultured in the "well" formed by the inner hole of the side walls and the thin PDMS membrane and the complete PDMS stretching device, including cell, can be mounted on our custom built cell stretcher.

PDMS device casting

The side walls of the PDMS stretching device are prepared by mixing PDMS (Sylgard 184, Dow, Midland, Michigan, USA) and the supplied crosslinker at a ratio of 20:1. Air bubbles are removed by dessication and 3.0 g of the PDMS are transferred into a 3D-printed poly(lactic acid) (PLA) casting mold. After a second step of dessication to remove air bubbles that were introduced during the filling of the mold, the PDMS is cured at 65-70 °C for 90 min. The cured side walls are carefully removed from the casting mold using isopropanol (VWR) and residual isopropanol is removed by dessication.

PDMS membrane fabrication

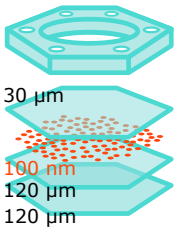

Fig. 4.4: Steps of the PDMS device fabrication.

The PDMS membrane is prepared in three layers (Fig. 4.4). In a first step, 5 g PDMS are mixed with the supplied crosslinker at a ratio of 13:1. The mixture is dessicated for 20 min. A 120 µm-thin layer of PDMS is spin coated (spin coater: KLM, IBR Spincoaterworld, Markkleeberg, Germany; distributor: Schaefer Technologie, Langen, Germany) onto a 4 inch silicon wafer (525±25 µm thickness, microchemicals, Ulm, Germany). The spin coating protocol includes a 25 s ramp to a speed of 10 rps and subsequent rotation at 10 rps for another 25 s. The mixture is cured at 65-70 °C for 45 min. A second layer of PDMS is spin coated onto the cured PDMS using the same protocol. The surface of the second layer of PDMS is treated with air-plasma (Zepto, diener electronic, Ebhausen, Germany) for 30 s 75% power (75 W). Red fluorescent beads of 100 nm diameter (FluoSpheres, Molecular Probes, Eugene, Oregon, USA) are diluted in isopropanol, 50 µL in 1 mL. The diluted beads are distributed on the activated PDMS with the same spin coating protocol as described above. A final, 30 µm-thin layer of 13:1 PDMS is spin coated onto the bead layer at higher speed: 40 s ramp to a speed of 41 rps and subsequent rotation at 41 rps for another 20 s. To attach the side walls to the PDMS membrane as sketched in Fig.4.4, 3 g of 1:13 PDMS are evenly spread in a 9 cm diameter (VWR) petri dish, dessicated, and the finished side walls are dipped into the thin layer of PDMS. The side walls are subsequently placed on the uncured top PDMS layer of the membrane. The components are gently pressed together and cured at 65-70 °C for 45 min. The devices are cut to size and are removed from the wafer using isopropanol. The regions of the membrane that cover the six holes in the corners of the device, are removed with a 3.5 mm diameter biopsy puncher (Harris Uni-core, World Precision Instruments, Sarasota, Florida, USA). The height of the final membrane is determined by measuring cross-sections of pieces of the membrane in bright field and fluorescence microscopy.

Preparation of the PDMS for cell culture

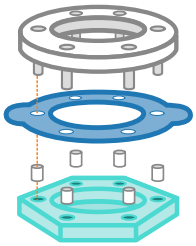

Fig. 4.5: Assembly of the device for pre-stretching. Top to bottom: pre-stretcher, transfer aid, PTFE sleeves, PDMS device.

Small poly(tetrafluoroethylene) (PTFE) sleeves are inserted into the holes of the PDMS device, see bottom of Fig. 4.5. These PTFE sleeves prevent the PDMS from sticking to the cell stretcher. The device, including the PTFE sleeves, is sterilized in boiling water for 40-60 min. This boiling step also leads to an increase of the hydrophilicity of the PDMS surface [26]. In the next step, the PDMS device is mounted onto a pre-stretcher, top in Fig. 4.5. The pre-stretcher consists of a PTFE ring with six 2.8 mm stainless-steel pins. The pre-stretcher ensures that the membrane is even and all devices are set to the same, fixed starting strain. For this step, the device and a transfer aid (blue in Fig. 4.5) are mounted onto the pre-stretcher. The 3D-printed transfer aid consists of a thin layer of PLA with holes that match the pre-stretcher and enables the transfer of the PDMS device from the pre-stretcher to the cell stretcher without distortion of the cell layer. The well of the PDMS device is subsequently incubated with 25 µg/mL of the extracellular matrix protein fibronectin from bovine plasma (F1141, Merck) in PBS for 45-60 min at room temperature. After rinsing with PBS 5 times to remove

excess fibronectin, the device is filled with culture medium and kept at 37 °C and 5 % CO_2 until cells are plated.

4.14.2 Cell culture of MDCK II cells

MDCK II cells are purchased from the European Collection of Authenticated Cell Cultures (UK) and are kindly provided by Tabea Oswald / Andreas Janshoff at passage number P33. The cells are cultured in Eagle's Minimum Essential Medium (12-125F, Lonza, Switzerland), supplemented with 10 % fetal calf serum (10270, Gibco, Thermo Fisher Scientific, Waltham, Massachusetts, USA) and 4 mM Glutamax (035050, Gibco), at 37 °C in a 5 % CO_2 and water saturated atmosphere. The cells are passaged every 3-4 days, when they are at least 80% confluent. For passaging, the cells are rinsed with PBS once and then treated with 1 mL 0.25% Trypsin with 0.02% EDTA in PBS (P10-020100, Pan-Biotech, Aidenbach, Germany) for 5-8 min at 37 °C. The detached cells are diluted with 4 mL culture medium and the cells are plated in a fresh 25 cm^2 cell culture flask at a ratio of 1:20-1:30. For experiments that require an exact cell number, the cell suspension is centrifuged at 21 °C, 270×g for 3 min, and the supernatant is carefully removed. The pellet is resuspended in 1 mL culture medium and the cell number is determined at a 1:10 dilution in a Neubauer cell counting chamber (0.1 mm, Marienfeld, Lauda Königshofen, Germany). A stock solution of the cells at the desired cell concentration of 10,000 cells/device is prepared and the cells are plated in the fibronectin-coated PDMS device. The cells are used up to passage number P60.

Madin-Darby Canine Kidney (MDCK II) cells were originally established from the kidney of an adult female cocker spaniel in 1958 by S.H. Madin and N.B. Darby Jr. [27]. The MDCK II cell line used in this thesis were isolated from a high passage number of the parental MDCK cell line in 1981 [28, 29].

4.14.3 Transfection with fluorescent proteins

The plasmid for keratin K8-EYFP is kindly provided by Nicole Schwarz / Rudolf Leube. The cells are transfected three days after plating on the PDMS. The polymer nanoparticle based transfection kit Xfect (Takara Bio, Kusatsu, Japan) is used. For each transfection, 10 µg deoxyribonucleic acid (DNA), at 2.7 µg/µL, are diluted in the Xfect reaction buffer, mixed with the supplied polymer to a final volume of 100 µL, according to the supplied instructions. The mixture is incubated at room temperature for 10 min and is subsequently added to the cells in full culture medium, which are incubated with the transfection reagents over night. The medium is replaced with fresh cell culture medium on the next day and the cells are incubated for a total of ∼48 h after transfection before the stretching experiments.

4.14.4 Fluorescent labeling with SiR-actin

For labeling of actin filaments, the jasplakenolide and silica rhodamine based SiR-actin (Spirochrome, Stein am Rhein, Switzerland) compound is used. For a better labeling efficiency, the supplied efflux inhibitor verapamil (5 µM) is added together with the SiR-actin compound (1 µM). The reagents are diluted in phenol red-free Eagle's Minimum Essential Medium (Lonza 12-668F), sup-

plemented with 10 % fetal calf serum and 4 mM Glutamax, as described in section 4.14.2. The cell medium is replaced with the dilute SiR-actin in phenol-red free medium 18-24 h before the stretching experiments.

4.14.5 Isotropic stretching of cells on an elastic substrate

The cells are stretched using a custom built cell stretcher, sketched in Fig. 7.2. The stretcher is designed and assembled by Peter Luley. In brief, the substrate is mounted on six holding arms, which are moved by a gear in an iris-like motion. The gear is actuated by tangential movement of a connecting rod which is driven by a stepper motor (Nanotec, Feldkirchen, Germany). The stepper motor of the stretcher is controlled by a Pollux Box NT (Physik Instrumente (PI), Karlsruhe, Germany) using the software `spec` (Certified Scientific Software, Cambridge, Massachusetts, USA) at intervals of 0.1 arbitrary units.
The PDMS device with transfected and stained cells is mounted into the stretcher that is set to the same size as the pre-strecher. To prevent the device from moving upwards during stretching, , nuts are fastened on top of the screws protruding from the top of the PTFE sleeves. The device is stretched in intervals of 0.1 units in the software. Devices are stretched up to 2.5-3.0 arbitrary units. Each strain is sustained for approximately 5 min while the cells and beads are imaged, and the complete stretching experiment takes up to 2 h.

4.14.6 Imaging cells during stretching

The cell stretcher is mounted on the stage of a BX63 upright microscope (Olympus) and the sample is imaged with a 60× water immersion dipping objective with a high working distance of 2 mm and NA=1.00 (LUMPLFLN60XW, Olympus). At each stretching position, z-stacks of the beads (mCherry filter set, Olympus, ET560/40x, T585LP, ET630/75m) and a two-color z-stack of the cells (for keratin: GFP filter set, Olympus, 470/40x, 495LP, 525/50m, and for actin filaments: Cy5 filter set, Olympus, 620/60x, T660LPXR, ET700/75m) are recorded with an ORCA-Flash4.0 camera (Hamamatsu, Hamamatsu City, Japan). For all fluorescence images, the fluorescence lamp (Lumencolor Sola light engine, Beaverton, Oregon, USA) intensity is set to 15%. For images of the beads and the actin, the exposure time is set to 50 ms. For images of the keratin structure, the exposure time is increased from 50 ms to 150 ms throughout the experiment due to intensity changes of the sample, likely caused by bleaching.

4.15 ANALYSIS OF IMAGES OF STRETCHED CELLS

4.15.1 Correction of membrane tilt

The free-standing PDMS membranes show varying degrees of tilt. A single image of the membrane therefore consists of regions that are in focus and other regions that are out of focus (Fig. 4.6a, top). One single image is hence not sufficient and the beads are imaged in a z-stack (Fig. 4.6a, bottom).

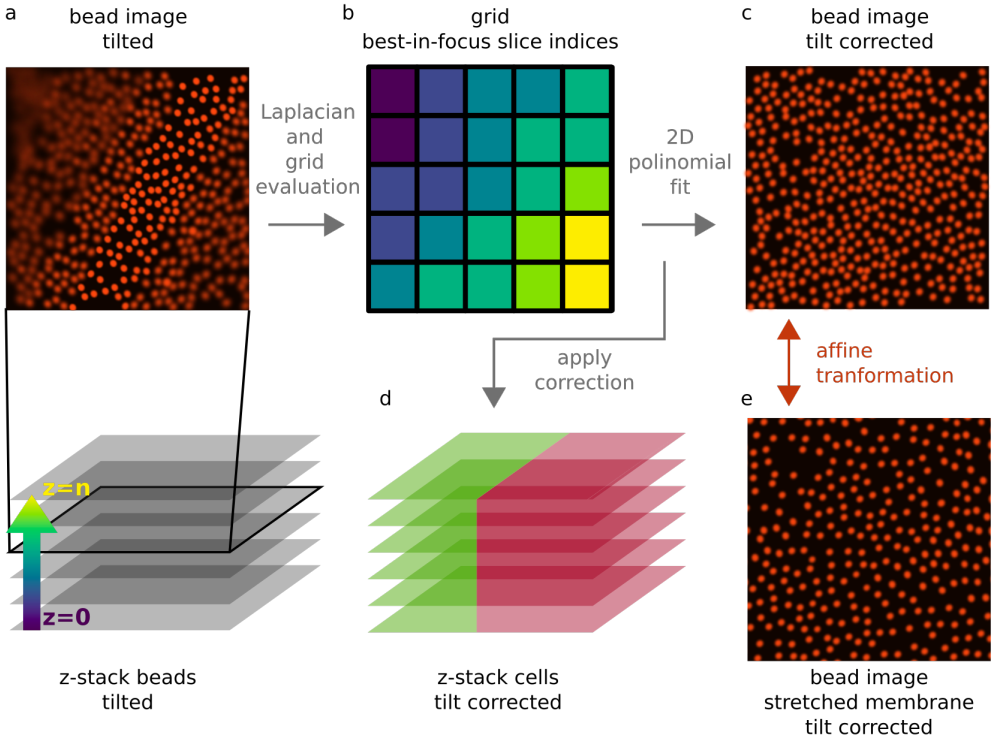

Fig. 4.6: **Correction and analysis of z-stacks from stretching experiments.** a) Bottom: z-stacks of the beads, embedded in the tilted PDMS membrane. Top: Schematic z-slice with in-focus and out-of-focus beads. b) The in-focus regions are determined by applying a spatial Laplacian to the images. The indices of the in-focus slices are determined for a coarse grid. c) A tilt-corrected image is calculated based on a second order 2D-polynomial fit to the grid data. d) The resulting parameters are applied to the z-stacks of the cells. Strain calculation: c,e) Tilt corrected bead images at different strains are registered with an affine transformation to determine the scaling of the membrane.

For the correction of the tilt, we exploit that the beads are in one layer and are therefore a 2D-structure in the PDMS. There is consequently only one z-position for each pixel of the z-stack where the sample is in focus. In the first step of the tilt correction, we define a local measure of sharpness. The sharpness is determined by calculating a spatial Laplacian of each image over a kernel size of 5 pixels. In the second step, we compare the local sharpness along the z-axis of the stack. To directly compare the sharpness, the results of the Laplacian, *i.e.*, the gradient, are normalized along the z-axis in in the second step. This normalization is performed with respect to the maximum of the absolute value along the z-axis in a pixelwise fashion. These steps of the algorithm are inspired by Ref. [30]. In a third step, we determine which slice is in focus for each region of the stack. We determine the 'best-in-focus" slice for a coarse grid, as a coarse evaluation of the sharpness improves the robustness of the analysis. The coarse grid is generated, for example, with 128×128 pixels per grid block for an original image of 2048×2048 pixels. For each z-slice and grid block, the sum of the normalized, absolute gradient values is calculated. The index of the z-slice with the highest sum is saved in a 2D matrix which then contains the indices of the "best-in-focus" slices at each grid block (Fig. 4.6b). In the fourth step, a 2D

polynomial of the second order is fitted into this coarse best-in-focus matrix. A tilt-corrected image is calculated by interpolation of the original z-stack to the result of the polynomial fit (Fig. 4.6c,e). The result of the polynomial fit is applied to calculate a tilt-corrected stack of the cell images, in Fig. 4.6d.

4.15.2 Calculating membrane expansion

Before the membrane deformation is calculated, all tilt-corrected images of the stretching series are centered with respect to the image taken at the highest strain position. The alignment is performed semi-automatically with a custom "point and click"-python code. The membrane expansion is subsequently calculated using the software `elastix` [31, 32] with the python implementation `itk-elastix`. Bead images are registered with respect to the previous image one-by-one with an affine transformation, as depicted on the right in Fig. 4.6. The images are alternatively registered with a similarity transformation and a non-rigid transformation based on B-splines.

4.15.3 Processing cell images

The tilt corrected z-stacks are used for further image analysis. To determine the cell area, the slices of the z-stack where the cell contour is visible are combined in `Fiji` by maximum intensity projections. The projections are segmented with the software `CellPose` [33] using the cyto2 model. The cell probability threshold and model match threshold are adjusted for each image to achieve the most accurate segmentation. The segmentation is manually inspected, and partially or wrongly segmented cells are removed using a semi automatic python code. For the single cell images shown in Figs. 7.4 and 7.6, the z-slice where the structure of interest is best in focus is smoothed by a median filter of 1 pixel in `Fiji`.

REFERENCES

[1] A. V. Schepers, C. Lorenz, and S. Köster. "Tuning Intermediate Filament Mechanics by Variation of pH and Ion Charges." *Nanoscale* 12 (2020), pp. 15236–15245. DOI: 10.1039/D0NR02778B.

[2] A. V. Schepers et al. "Multiscale mechanics and temporal evolution of vimentin intermediate filament networks." *Proc. Natl. Acad. Sci.* 118 (2021), e2102026118. DOI: 10.1073/pnas.2102026118.

[3] H. Herrmann, L. Kreplak, and U. Aebi. "Isolation, Characterization, and In Vitro Assembly of Intermediate Filaments." *Methods in Cell Biology*. Vol. 78. Academic Press, 2004, pp. 3–24. DOI: 10.1016/S0091-679X(04)78001-2.

[4] J. Block et al. "Viscoelastic Properties of Vimentin Originate from Nonequilibrium Conformational Changes." *Sci. Adv.* 4 (2018), eaat1161. DOI: 10.1126/sciadv.aat1161.

[5] S. Winheim et al. "Deconstructing the Late Phase of Vimentin Assembly by Total Internal Reflection Fluorescence Microscopy (TIRFM)." *PLoS ONE* 6 (2011), e19202. DOI: 10.1371/journal.pone.0019202.

[6] B. Nöding, H. Herrmann, and S. Köster. "Direct Observation of Subunit Exchange Along Mature Vimentin Intermediate Filaments." *Biophys. J.* 107 (2014), pp. 2923–2931. DOI: 10.1016/j.bpj.2014.09.050.

[7] M. Kooijman et al. "Transient Electric Birefringence Study of Intermediate Filament Formation from Vimentin and Glial Fibrillary Acidic Protein." *J. Biol. Chem.* 272 (1997), pp. 22548–22555. DOI: 10.1074/jbc.272.36.22548.

[8] I. Szeverenyi et al. "The Human Intermediate Filament Database: Comprehensive Information on a Gene Family Involved in Many Human Diseases." *Hum. Mutat.* 29 (2008), pp. 351–360. DOI: 10.1002/humu.20652.

[9] ATTO-TEC GmbH. *Product Information: ATTO 647N*. URL: https://www.atto-tec.com/fileadmin/user_upload/Katalog_Flyer_Support/ATTO_647N.pdf (visited on 06/01/2021).

[10] R. Janissen et al. "Invincible DNA Tethers: Covalent DNA Anchoring for Enhanced Temporal and Force Stability in Magnetic Tweezers Experiments." *Nucleic Acids Res.* 42 (2014), e137. DOI: 10.1093/nar/gku677.

[11] M. Zacchia et al. "Potassium: From Physiology to Clinical Implications." *Kidney Dis.* 2 (2016), pp. 72–79. DOI: 10.1159/000446268.

[12] C. Dammann, B. Nöding, and S. Köster. "Vimentin networks at tunable ion-concentration in microfluidic drops." *Biomicrofluidics* 6 (2012), p. 022009. DOI: 10.1063/1.4705103.

[13] C. Dammann and S. Köster. "Dynamics of Counterion-Induced Attraction between Vimentin Filaments Followed in Microfluidic Drops." *Lab Chip* 14 (2014), pp. 2681–2687. DOI: 10.1039/c3lc51418h.

[14] C. Dammann, H. Herrmann, and S. Köster. "Competitive Counterion Binding Regulates the Aggregation Onset of Vimentin Intermediate Filaments." *Isr. J. Chem.* 56 (2016), pp. 614–621. DOI: 10.1002/ijch.201400153.

[15] C. Lorenz et al. "Lateral Subunit Coupling Determines Intermediate Filament Mechanics." *Phys. Rev. Lett.* 123 (2019), p. 188102. DOI: 10.1103/PhysRevLett.123.188102.

[16] S. Köster et al. "Nanomechanics of vimentin intermediate filament networks." *Soft Matter* 6 (2010), p. 1910. DOI: 10.1039/c000113a.

[17] M. Keller et al. "Slow Filament Dynamics and Viscoelasticity in Entangled and Active Actin Networks." *Philos. Trans. R. Soc. A* 361 (2003), pp. 699–712. DOI: 10.1098/rsta.2002.1158.

[18] F. Gittes and F. C. MacKintosh. "Dynamic Shear Modulus of a Semiflexible Polymer Network." *Phys. Rev. E* 58 (1998). DOI: 10.1103/PhysRevE.58.R1241.

[19] M. Schopferer et al. "Desmin and Vimentin Intermediate Filament Networks: Their Viscoelastic Properties Investigated by Mechanical Rheometry." *J. Mol. Biol.* 388 (2009), pp. 133–143. DOI: 10.1016/j.jmb.2009.03.005.

[20] B. Nöding and S. Köster. "Intermediate Filaments in Small Configuration Spaces." *Phys. Rev. Lett.* 108 (2012), p. 088101. DOI: 10.1103/PhysRevLett.108.088101.

[21] J. C. Thiele et al. "Confocal Fluorescence-Lifetime Single-Molecule Localization Microscopy." *ACS Nano* 14 (2020), pp. 14190–14200. DOI: 10.1021/acsnano.0c07322.

[22] P. J. Flory. "Molecular Size Distribution in Linear Condensation Polymers." *J. Am. Chem. Soc.* 58 (1936), pp. 1877–1885. DOI: 10.1021/ja01301a016.

[23] P. M. Steinert, L. N. Marekov, and D. A. D. Parry. "Diversity of intermediate filament structure. Evidence that the alignment of coiled-coil molecules in vimentin is different from that in keratin intermediate filaments." *J. Biol. Chem.* 268 (1993), pp. 24916–24925. DOI: 10.1016/S0021-9258(19)74552-9.

[24] Y.-H. Li and S. Gregory. "Diffusion of Ions in Sea Water and in Deep-Sea Sediments." *Geochim. Cosmochim. Ac.* 38 (1974), pp. 703–714. DOI: 10.1016/0016-7037(74)90145-8.

[25] R. M. Weinheimer, D. F. Evans, and E. L. Cussler. "Diffusion in surfactant solutions." *J. Colloid Interface Sci.* 80 (1981), pp. 357–368. DOI: 10.1016/0021-9797(81)90194-6.

[26] J. Y. Park et al. "Surface chemistry modification of PDMS elastomers with boiling water improves cellular adhesion." *Sens. Actuators, B* 173 (2012), pp. 765–771. DOI: 10.1016/j.snb.2012.06.096.

[27] *Cell line profile-MDCK (ECACC catalogue number 85011435)*. Tech. rep. (visited on 05/15/2021). URL: https://www.phe-culturecollections.org.uk/media/137096/mcdk-cell-line-profile.pdf.

[28] G. Barker and N. L. Simmons. "Identification of two strains of cultured canine renal epithelial cells (MDCK cells) which display entirely different physiological properties." *Q. J. Exp. Physiol.* 66 (1981), pp. 61–72. DOI: 10.1113/expphysiol.1981.sp002529.

[29] J. D. Dukes, P. Whitley, and A. D. Chalmers. "The MDCK variety pack: Choosing the right strain." *BMC Cell Biol.* 12 (2011), p. 43. DOI: 10.1186/1471-2121-12-43.

[30] Github user: momonala. *Github focusstack for python*. 2020. URL: https://github.com/momonala/focus-stack (visited on 06/01/2021).

[31] S. Klein et al. "elastix: A Toolbox for Intensity-Based Medical Image Registration." *IEEE Trans. Med. Imaging* 29 (2010), pp. 196–205. DOI: 10.1109/TMI.2009.2035616.

[32] D. Shamonin et al. "Fast parallel image registration on CPU and GPU for diagnostic classification of Alzheimer's disease." *Front. Neuroinform.* 7 (2014), pp. 1–15. DOI: 10.3389/fninf.2013.00050.

[33] C. Stringer et al. "Cellpose: a generalist algorithm for cellular segmentation." *Nat. Methods* 18 (2021), pp. 100–106. DOI: 10.1038/s41592-020-01018-x.

5 TUNING INTERMEDIATE FILAMENT MECHANICS BY VARIATION OF PH AND ION CHARGES

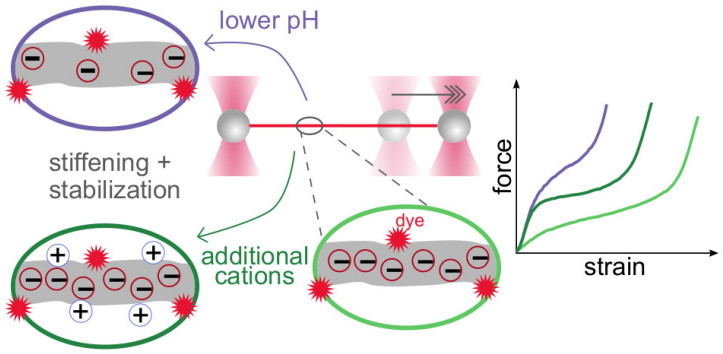

This chapter is published as *A. V. Schepers, C. Lorenz and S. Köster, "Tuning intermediate filament mechanics by variation of pH and ion charges" Nanoscale, 2020, 12, 15236-15245*, Ref. [1]. Text and figures are reproduced with permission by The Royal Society of Chemistry. Where appropriate, figures from the supporting information of the original publication are incorporated in the main text of this chapter. The additional section 5.2.2 is not included in the original publication and the original Fig. S2 is replaced by the extended Fig. 5.5 in this chapter.

Contributions: S. K. conceived the project. A. V. S. performed the experiments and the data analysis. C. L. developed the method for force-strain data averaging and performed the simulations. A. V. S. and S. K. wrote the manuscript.

ABSTRACT

The cytoskeleton is formed by three types of filamentous proteins – microtubules, actin filaments, and intermediate filaments (IFs) – and enables cells to withstand external and internal forces. Vimentin is the most abundant IF protein in humans and assembles into ~10 nm diameter filaments with remarkable mechanical properties, such as high extensibility and stability. It is, however, unclear to which extent these properties are influenced by the electrostatic environment. Here, we study the mechanical properties of single vimentin filaments by employing optical trapping combined with microfluidics. Force-strain curves, recorded at varying ion concentrations and pH values, reveal that the mechanical properties of single vimentin IFs are influenced by pH and ion concentration. By combination with Monte-Carlo simulations, we relate these altered mechanics to electrostatic interactions of subunits within the filaments. We thus suggest possible mechanisms that allow cells to locally tune their stiffness without remodeling the entire cytoskeleton.

5.1 INTRODUCTION

Biological cells are constantly exposed to varying intra- and extracellular forces, thus their mechanical properties are challenged. It is meanwhile well accepted that the mechanical properties of cells are, to a large extent, governed by the cytoskeleton, a stabilizing, yet flexible framework, which is composed of microtubules, actin filaments, and intermediate filaments (IFs), together with motor proteins and crosslinkers. While microtubules and actin filaments are conserved in eukaryotic cell types, there are around 70 different genes encoding IFs in man that are expressed according to the cell's specific requirements [2, 3]. Despite differences in their amino acid sequence, all cytoskeletal IF proteins share their secondary structure with a tripartite alpha-helical rod and disordered head and tail domains [4, 5]. During the hierarchical assembly, two monomers form a parallel coiled coil and these dimers organize into anti-parallel tetramers in a half-staggered arrangement. The tetramers rapidly assemble laterally to form unit length filaments (ULFs) within 100 ms [6], which in turn elongate to filaments by end-to-end annealing [4]. The resulting biopolymer comprises a complex high-order arrangement of coiled coils [4], which allows IFs to be extended up to at least 4.5-fold their initial length [7, 8], including a strong loading-rate dependence [9]. This enormous extensibility is in stark contrast to microtubules and F-actin [10].

Vimentin is the IF typically expressed in mesenchymal cells [3], and up-regulated during the epithelial-to-mesenchymal transition in wound healing, early embryogenesis, and cancer metastasis [11]. In addition to being highly extensible [9, 12, 13], vimentin is flexible [14–16] and stable [17]. While the extensibility describes how much a filament can be elongated before rupture, it does not explain the mechanisms underlying the extension and therefore the response of the filament to an applied strain, *i.e.* the relative elongation of the filament. By analyzing force-strain curves, fundamental properties of the material are determined. For example, the elasticity and the Young's modulus can be derived from a linear force increase. During stretching, three regimes are observed in the force-strain data [9, 12, 13, 18, 19]: an initial linear increase, a plateau of relatively constant force, and a subsequent stiffening regime. These regimes have been linked to structural changes in the protein [18]. The initial linear increase is described as the elastic stretching of the filament consisting of the alpha helices, the plateau as the unfolding of alpha-helical structures, and the stiffening as the further stretching of the unfolded structures. Once the filament is stretched beyond the linear regime, the deformation becomes inelastic. The three-regime behavior is, among the cytoskeletal filaments, unique for IFs, as F-actin and microtubles rupture at much lower strains [10]. The IFs show a pronounced softening upon re-stretching, while, at the same time, the elongation itself is fully reversible and the noise threshold of 2 pN is reached at residual strains of 0.05 ± 0.02 (mean, standard deviation) [13, 20].

A similar three-regime force-distance behavior has been found for single coiled coils [21, 22], which are a common theme in protein structures. The overall structural stability of coiled coils depends on the buffer conditions, however, the results are partially conflicting. Some studies show an increased stability at

low pH compared to neutral pH [23, 24], whereas others find higher stability in neutral pH conditions [25, 26]. It has been discussed that the response of a coiled coil to altered pH conditions depends on the concentration of salt ions in the buffer but also on the sequence of the peptide [27]. Molecular dynamics simulations of the isolated vimentin coiled-coil dimer [19] agree qualitatively with experimental force-strain curves of single coiled coils [21, 22, 28] and vimentin filaments [9, 13]. These results indicate that coiled coils play a pivotal role in the force-strain response of mature IFs.
Here we address the open question of how strongly the variability of the mechanical response observed for coiled coils in different measurement conditions is conserved in fully assembled vimentin IFs. We study the response of mature vimentin IFs to tuning of the ionic conditions of the buffer and to the internal charge distribution in the protein by adjusting the pH of the buffer, and find that both factors strongly influence the mechanics of single vimentin IFs. Monte-Carlo simulations enable us to link electrostatic interactions within the filament and modifications of the free energy landscape of the unfolding reaction to the observed force-strain behavior. These results extend the list of remarkable mechanical properties of IFs by adding a responsiveness to pH and ionic environment to the established loading rate sensitivity [9] and tensile memory [13]. The possibility to tune filament mechanics fast and locally may have important implications within living cells.

5.2 RESULTS AND DISCUSSION

5.2.1 Cations stiffen single vimentin IFs

To investigate the effect of the ionic environment on the mechanical behavior of single vimentin filaments, we stretch the filaments after incubation in different buffers. For comparability, all filaments are assembled in standard assembly buffer (2 mM phosphate buffer (PB) with 100 mM KCl, pH 7.5, see Fig. 5.1a for a schematic representation of the hierarchical assembly pathway) before the stretching experiment. A single filament is then tethered to optically trapped beads and incubated in the respective measuring buffer for 30 s before stretching. A graphical protocol of the experiment is shown in Fig. 5.1b. Fig. 5.1c shows a typical resulting force-strain curve, where the strain is defined as $\varepsilon = (L - L_0)/L_0$ with the original filament length L_0 measured at 5 pN force. The mechanical response of single filaments to stretching shows a clear dependence on the experimental conditions, as shown in Fig. 5.2. All panels show average data and the individual curves are omitted here for clarity, but are shown in Figs. A3 and A4. The three regimes that have been previously reported [9, 12, 13, 18, 19] are evident in the force-strain data recorded under standard assembly conditions as shown in Fig. 5.2a (100 mM KCl, see legend for color code): The initial linear increase (I in Fig. 5.1c), the plateau (II) and the subsequent stiffening at high strains (III) can be clearly distinguished. Note that what we describe as "plateau" here does not necessarily have a slope of zero, but a considerably decreased slope compared to the rest of the curve. The curves recorded at high salt concentrations, *i.e.* c(KCl) = 100 mM or 150 mM and

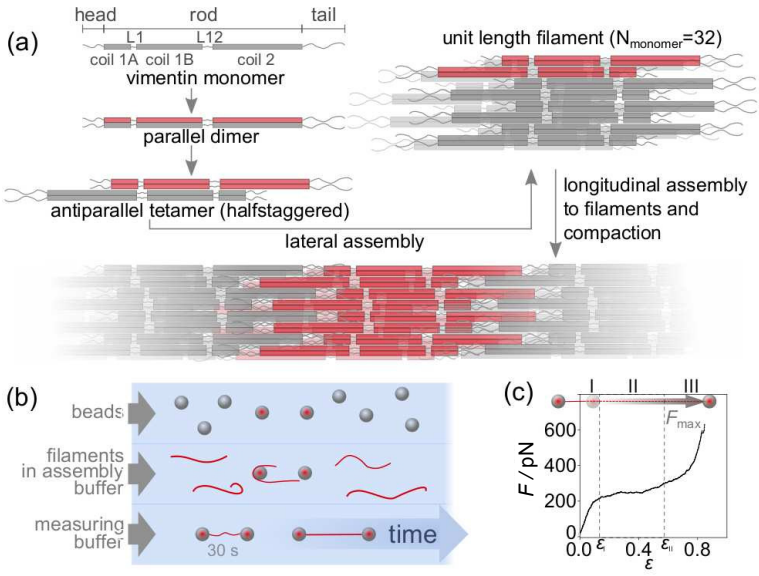

Fig. 5.1: **Stretching experiments on fully assembled vimentin filaments.** a) Schematic of the hierarchical assembly of vimentin monomers into filaments. In each step, the respective precursor subunit is highlighted in red. b) Simplified measurement protocol of the optical trap experiment in microfluidic flow channels: Two beads are captured and calibrated (1), a single filament is covalently attached to both beads (2) and stretched after a 30 s incubation period in the measuring buffer (3). c) Typical force-strain curve for a vimentin filament showing the elastic (I), plateau (II) and stiffening (III) regime. The strain at the transition of region I to II is ε_I, from II to III it is ε_{II}. Figure reproduced from Ref. [1].

$c(MgCl_2)$ = 5 mM or 10 mM, are consistent with this mechanical behavior. In particular, the initial slopes, which describe the initial elasticity of the filament, agree well between these four salt conditions, as shown in detail by the solid circles in Fig. 5.3a. These values are determined by fitting the initial slopes of the individual force-strain curves (Figs. A3 and A4).
When the filaments are incubated in low salt buffer (PB, pH 7.5), where tetramers are known to be stable [29], before stretching, the mechanics change significantly. Fig. 5.2a shows that the complete curve is shifted to lower forces, the initial slope is lower and the plateau is less pronounced. The decreased initial slope is indicative of a softer material. As a consequence of this softening, the filament can be stretched to higher strains as compared to high salt buffers before the maximum force of the optical trap is reached. The curve measured at 50 mM KCl lies between the data for low salt buffer and the standard assembly buffer curve, as does the maximum strain for this condition. Independent of the measuring conditions, the strain at which the initial linear increase ends is at $\varepsilon_I = 0.15 \pm 0.04$ (see Fig. 5.2a), showing that the elastic extensibilty of the filament is not affected by the salt ions. It is remarkable that the slope of the plateau is constant for all buffers, as shown in Fig. 5.3a by the open circles.
Amino acids, the building blocks of proteins, may be either hydrophobic, polar or charged. Ions in the buffer interact with those polar and charged amino acids that are accessible within a supramolecular structure, thus mediating interactions within the assembled filament. Such electrostatic interactions caused by ions in the buffer can be regarded as *indirect* charge effects. The similarity be-

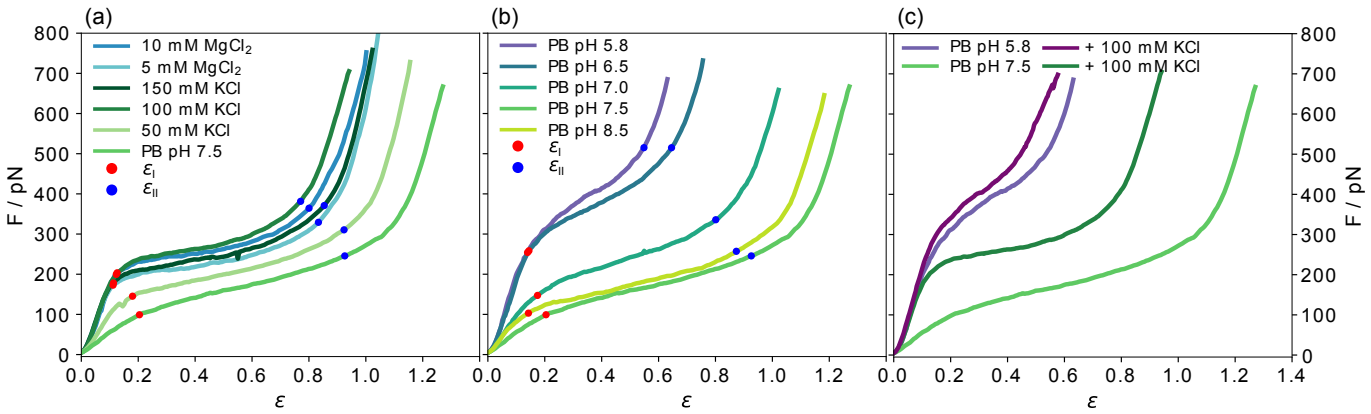

Fig. 5.2: **Force-strain behavior of single vimentin filaments.** All curves shown are averages of the individual measurements shown in Figs. A3 and A4. The strain values at the end of the initial linear regime ε_I (red) and the plateau regime ε_{II} (blue) for all average curves are indicated. a) Effect of indirect charge shifts caused by salt ions in the measurement buffer at pH 7.5. b) Effect of direct charge shifts by varying pH conditions without any additional salt. While ε_I is similar in all measurements, ε_{II} increases for lower c(KCl) and for increasing pH. c) Comparison of the effect of an addition of 100 mM K^+ ions at pH 7.5 and 5.8. Figure reproduced from Ref. [1].

tween the curves at $c(KCl) = 100$ mM or 150 mM and $c(MgCl_2) = 5$ mM or 10 mM indicates that predominantly the cations are causing the different behavior and not the Cl^- anions. In contrast, if it were mainly the Cl^- ions that caused the stiffening of the filaments, we would expect the curve at $c(KCl) = 50$ mM to lie above both $MgCl_2$ curves since $c_{KCl}(Cl^-) > c_{MgCl_2}(Cl^-)$ for all measured buffers. The cations do not only stiffen but also stabilize the single filaments as shown in Fig. 5.3b by the relative count of stable filaments (solid bars) and instable filaments (open bars). The stability is determined from the shape of the force-strain curve. Filaments that break before the stiffening regime (III in Fig. 5.1) is reached, are classified as instable. The fraction of stable filaments increases from 0.45 for the measurements in low salt buffer to 0.88 ± 0.02 (average and standard deviation from data at $c(KCl) = 100$ mM and 150 mM, and $c(MgCl_2) = 5$ mM and 10 mM) at higher salt concentrations. The cations additionally promote bundling (see Fig. 5.4a and Fig. 5.5). In particular, at $c(MgCl_2) = 10$ mM, the amount of bundling limits the number of measurable single filaments [30, 31]. This observation agrees well with the reported behavior of vimentin networks where – with increasing concentrations of multivalent ions – freely fluctuating networks collapse to dense aggregates [32]. It has further been reported that reconstituted vimentin networks stiffen upon addition of divalent ions [15, 33, 34], and that the network stiffness increases with increasing concentration of divalent ions until total collapse of the network [35]. Combined with these findings from literature, our results show that the divalent ion dependent stiffening of vimentin networks is solely due to stronger interactions between filaments and not to additional stiffening of single filaments in the network. The small number of instable filament we observe at physiologically relevant c(KCl) [36] as well as all measured $c(MgCl_2)$ probably do not contribute considerably to cell mechanics. In line with the known high stability under large applied strains of IF networks [10], and cell experiments that identify IFs as the load

bearing elements at high strains [37], our data thus suggest that the stable filaments determine IF mechanics in cells.

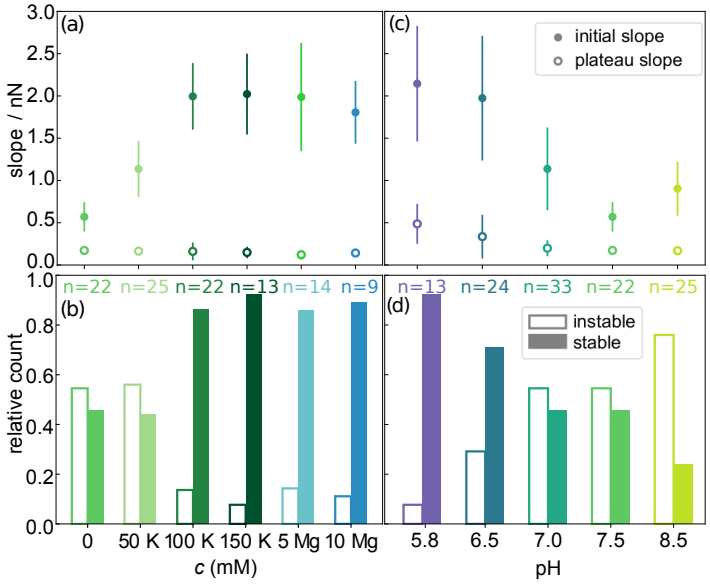

Fig. 5.3: **Mechanical properties of single vimentin filaments.** a),c) Analysis of the initial slopes (solid circles) and slopes of the plateau regions (open circles) of all stable filaments. The error bars indicate the standard deviation. b),d) The stability of the measured filaments is presented as fractions of instable and stable filaments. Figure reproduced from Ref. [1].

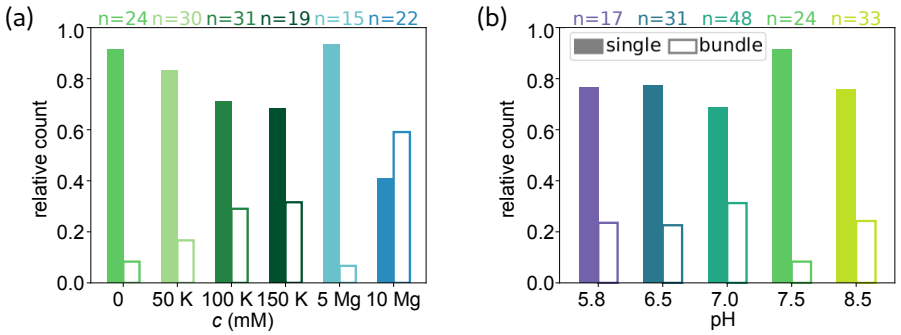

Fig. 5.4: **Relative count of single filaments and bundles for each condition.** The bundles were identified from the confocal images and from the force data. Only single filaments were used in further analysis. a) The increased fraction of bundles at higher salt concentrations indicates that the ions promote filament bundling. b) The fraction of bundles does not show a trend at different pH conditions. Figure reproduced from Ref. [1].

5.2.2 Stretching vimentin filament bundles

The increased bundling propensity of vimentin filaments at high $MgCl_2$ concentrations allows for the evaluation of the bundle mechanics. In Fig. 5.5a, force-strain curves for vimentin filament bundles, measured in 10 mM $MgCl_2$, are plotted. The variation between the curves is larger than for single filaments as shown in Fig. A3. The average force-strain curve of all single filaments is indicated in blue in all panels of Fig. 5.5, and a typical force-strain curve for a single filament shown in Fig. 5.5c. Besides the large variability of the force-strain curves, two main features indicate a bundle: Firstly, the forces reached in the initial linear regime (Fig. 5.5a, d-f) are often higher than for single filaments, and, in some cases, also the slope of the initial regime is higher (Fig. 5.5b). Secondly, "kinks" in the force-strain curve indicate that part of a bundle either ruptures or detaches. Examples for such kinks are shown in Figs. 5.5e,f. Whereas these features facilitate the distinction between single filaments and bundles, quantitative analysis of, for example, the number of filaments per bundle, is not possible.

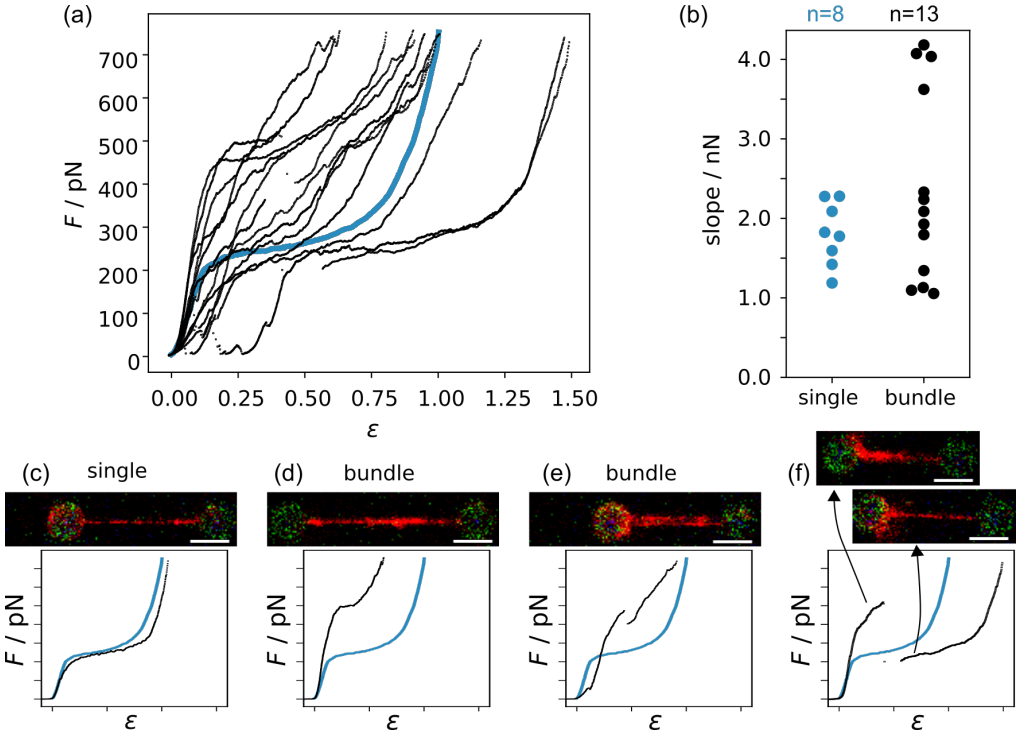

Fig. 5.5: **Force-strain behavior of vimentin filament bundles.** a) Force-strain curves for all bundles in the presence of 10 mM $MgCl_2$. The average curve for single filaments in the same buffer condition is shown in blue. b) Slope of the initial, linear regime. c)-f) Examples of confocal and force-strain data of c) a single vimentin IF and d)-f) bundles. The heterogeneity along the length of the bundle complicates the quantification of the bundle properties. f) In some cases, individual filaments in the bundle rupture during the experiment, leading to one single filament left between the beads. The scale bars are 5 µm.

For a perfect bundle of filaments that all reach from bead to bead, and where all filaments have the same spring constant, the bundle spring constant is the filament spring constant times the number of filaments. The number of filaments

can therefore be calculated from the spring constant of the bundle. However, as visible in the confocal images in Fig. 5.5d-f, bundles are highly heterogeneous along their length. Comparison of the slope of the linear regime, shown in Fig. 5.5b, reveals that stretching of most bundles leads to a slope similar to the single filaments. However, few bundles have a slope approximately twice as high as determined for the single filaments. This increased slope indicates that more than one filament is contributing to the stretching response. For bundles that have a similar initial slope as the single filaments, the elastic stretching response seems to be dominated by a single filament. It is also possible that part the bundle has detached and only a single filament is stretched.
Besides the high forces reached at low strains, the plateau regime of the force-strain curves of bundles is often very short if it is visible at all. Such a short plateau is, for example, shown in Fig. 5.5d. This shortening of the plateau might indicate that the unfolding of alpha helices and coiled coils is restricted by internal interactions in bundles.
In future experiments, it would be interesting to prepare controlled bundles to quantify the stretching and bending properties of vimentin bundles. For such controlled bundles, the coupling between filaments may be tuned. By such an approach, situations as shown in Fig. 5.5e might be prevented where spatially separate filaments or multiple, separated bundles are stretched.

5.2.3 IF mechanics adapt to pH changes

Whereas the interactions of ions with the protein described in the previous sections represent an indirect charge effect on the filament, we can also *directly* manipulate the charge of specific amino acids, *e.g.* by varying the pH of the buffer. To keep the two effects separate, at first, we use the curve recorded in the low salt buffer (2 mM PB, pH 7.5) as a starting point and do not add any additional salt ions. As the cytoplasmic pH in eukaryotic cells is reported to lie between 7.0 and 7.5 [38, 39], we lower the pH to 7.0. The resulting curves are shifted to higher forces and the plateau region is shorter compared to the low salt buffer at pH 7.5 (see Fig. 5.2b and Fig. A4c,d). The stiffening effect is amplified at even lower pH as shown by data for pH 6.5 and pH 5.8. The curves recorded in these low pH conditions are remarkably similar to each other and the filaments are considerably stiffer than in all previous measurement conditions with the plateau almost disappearing. If we, in contrast, increase the pH from 7.5 to 8.5, the mechanics of the filament do not change. Thus, the adaption of the filament occurs between pH 6.5 to 7.5 and it assumes an intermediate state at pH 7.0.
In line with the observations for varying salt concentrations reported above, the strain reached with the initial, linear increase (ε_I =0.16±0.03) is not strongly influenced by the pH of the measurement buffer. This result shows that the elastic extensibility of the filament is neither strongly affected by pH or ionic charge variation. Additionally, the initial slope at low pH is the same as for the standard assembly buffer or high salt concentrations (Fig. 5.3a,c), indicating that low pH and high salt have a similar effect on the initial stiffness of the filament. The decrease of the initial slope with increasing pH is plotted by

solid circles in Fig. 5.3c and is evident in the force-strain curves at low strains in Fig. 5.2b. In contrast to the cations, the pH clearly affects the unfolding mechanism responsible for the plateau formation and the increased slope of the plateau region at low pH suggests that the force needed for unfolding events increases with decreasing pH. Because the onset of the stiffening moves to lower strains for low pH, the strain range of the plateau becomes very short. Unlike for filaments in varying salt conditions (Fig. 5.6a), the ratio of the initial slope and slope of the plateau does not change with the pH (Fig. 5.6b).

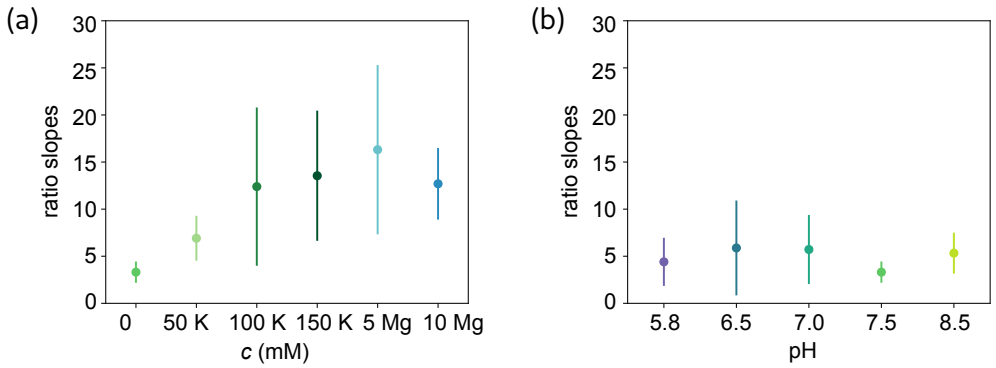

Fig. 5.6: **The ratio of the initial slope and the slope of the plateau for each measuring condition.** The respective slopes are presented in Fig. 3 in the main text. a) The ratio changes at different salt conditions as the plateaus have the same slope, whereas the initial increase changes at different salt conditions. b) The ratio of the slopes in buffers of increasing pH stays relatively constant. Figure reproduced from Ref. [1].

Taken together, our force-strain data on vimentin IFs at different pH values show that the overall stiffness of the filament and the unfolding are altered considerably when the charge of a few specific amino acids is varied. This assumption is further supported by the stability behavior of the filaments (see Fig. 5.3d). Here, the fraction of stable filaments, represented by solid bars, decreases with increasing pH, from 0.92 at pH 5.8 to 0.24 at pH 8.5, while the force-strain curves do not change between pH 7.5 and 8.5 or between 5.8 and 6.5. A stabilization or destabilization therefore still continues even if the force-strain behavior of the stable filaments is not affected. While the measuring condition clearly affects the stability of the filaments, there is no correlation of the stability, *i.e.* the maximum force reached during the experiment, and the initial length of the filament, as shown in Fig. 5.7.

5.2.4 IF stiffening saturates at low pH

We observe an overall weaker stiffening by cationic (indirect) charge shifts compared to pH (direct) charge shifts on single vimentin filaments. This phenomenon is especially prominent in the plateau regions. To understand the interplay of the two effects, we compare two sets of data recorded at different pH (7.5 and 5.8) without additional salt and with 100 mM KCl each. The four average curves are shown in Fig. 5.2c. At pH 5.8, 100 mM KCl does not have a strong effect, and the curves with and without additional salt are strikingly similar (purple), especially when compared to the pronounced effect of 100 mM

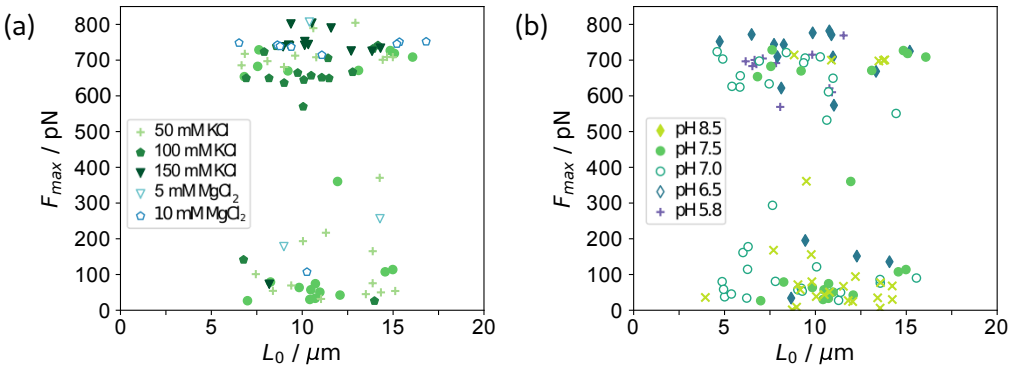

Fig. 5.7: **Maximum force plotted against initial filament length for each filament.** There is no correlation between the initial filament length and the maximum force reached during stretching. The data cluster at forces around 700 pN because beads are pulled out of the traps. a) For varying salt concentrations, b) for varying pH conditions. Figure reproduced from Ref. [1].

KCl at pH 7.5 (green). This observation suggests that the maximum stiffness has already been reached at low pH without salt and the ions only have a negligible effect. To ensure that the saturation of the stiffening effect we observe at low pH is constant on the time scales accessible here, we further investigate the temporal evolution of the adaptation of the mechanics of the filament at low pH. The negligible difference between curves (Fig. 5.8) recorded at incubation times of 15 s, 30 s, and 60 s shows that the additional interactions within the filaments have developed already after a few seconds.

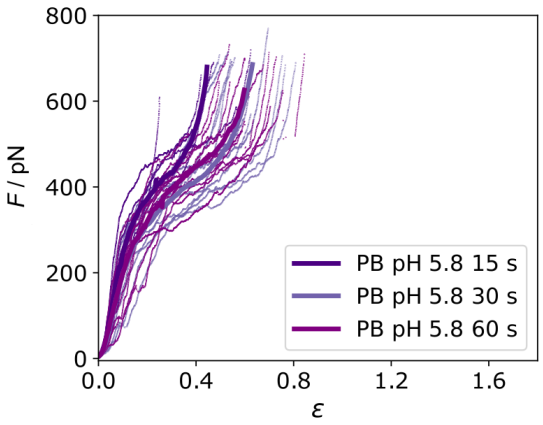

Fig. 5.8: **Force-strain curves for filaments stretched in phosphate buffer (PB), pH 5.8 with varying incubation times.** All single measurements are plotted by thin lines, the average curves are shown by bold lines. Within the variation of the single curves in each condition there is no difference apparent between the incubation times. Figure reproduced from Ref. [1].

5.2.5 Variations in the free energy landscapes influence filament mechanics

The observed filament softening in low salt buffer and the stiffening at low pH raises the question of how these mechanical properties are governed by molecular charge interactions within the filament. To answer this question, we first regard the initial slope of the force-strain curves in Fig. 5.2. The initial slope decreases when fewer monovalent cations are present and increases with decreasing pH.

We model force-strain curves by Monte-Carlo simulations that are based on the hierarchical structure of the filaments [9, 40]. In the model, monomers consist of a spring and an extendable element that can either be open or closed. The spring accounts for the elastic contribution of the alpha helices. Lateral arrangement of 32 such monomers represents one ULF. The filament is simulated as a series of 100 ULFs that are connected by springs. In the model, we can define the elastic properties of the springs κ_α, the strength of the coupling between lateral monomers in each ULF, the free energy difference of the closed (alpha) and unfolded state ΔG, and the length that is added by stretching a monomer ΔL. In our 1D experimental setting, we can interpret the initial slope as a measure of the filament stiffness, which for the sake of modeling we describe by the spring constant of the filament, κ_f. We expect an increase with the number of monomers, N, per cross-section of the filament [41]. We can, however, exclude the possibility of a reorganization of mature filaments *in vitro* by addition or loss of subunits as it only occurs on timescales of tens of minutes [42] which is much slower than the time scales of our experiments. We can therefore safely assume that the number of monomers is constant during our experiments. Instead, stiffening of the filament may originate from an increase of the spring constant of an individual alpha helix, κ_α, as shown in the Monte-Carlo simulated force-strain curves in Fig. 5.9a.

An increased stiffness can furthermore be explained if we regard the filament as a bundle of protofilaments. If these protofilaments are fully coupled to each other, the persistence length of the bundle increases as N^2 instead of linearly in N in the uncoupled case [41]. An increase in coupling strength and thus an increased initial slope may be caused by higher salt concentration or lower pH and is thus in line with our experimental results. It should be noted, however, that we do not include this effect in our simulations. Instead, we simulate 'subunit coupling', see Fig. 5.9b, that describes the size of fully coupled lateral subunits into which the monomers are organized [40]. Thus, in higher order subunits, more elements have to unfold simultaneously to achieve the length change, ΔL, of the filament. This effect already plays a role for the initial stretching and leads to a slightly increased slope (see inset of Fig. 5.9b).

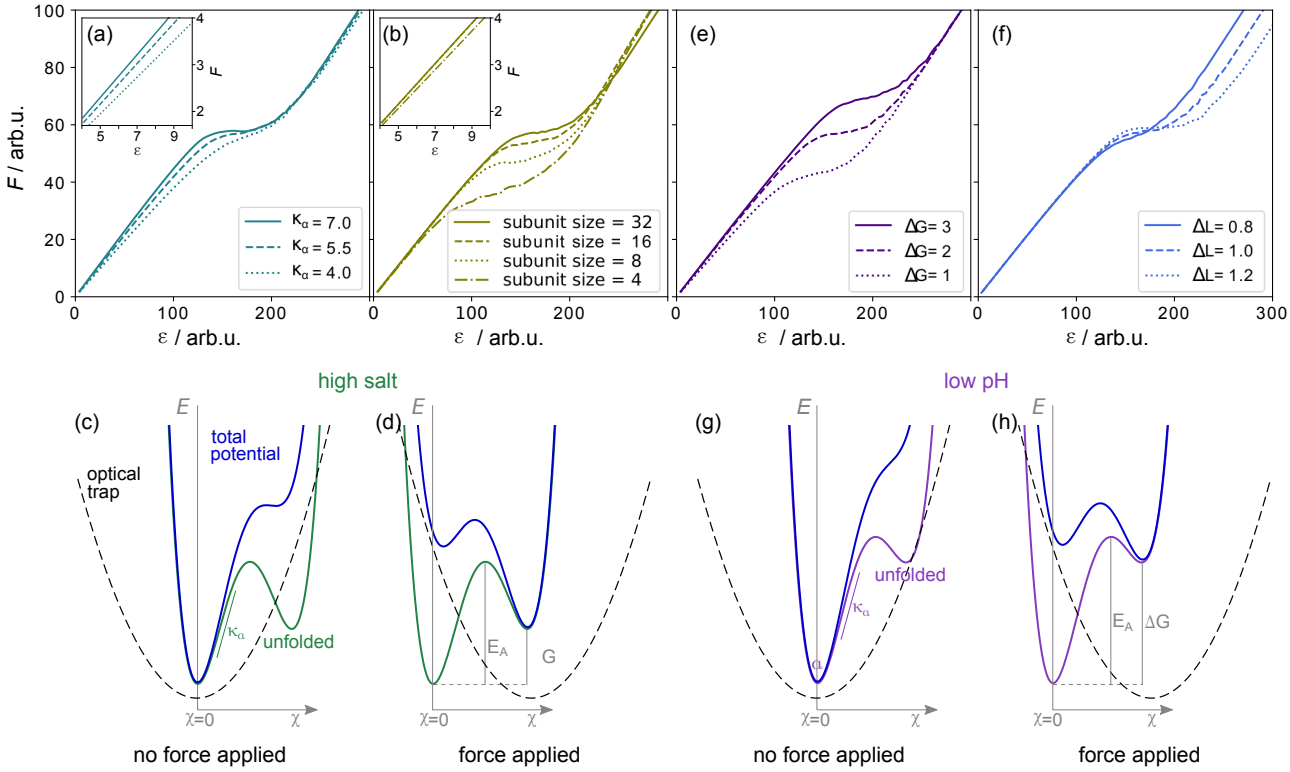

Fig. 5.9: **Monte-Carlo simulations of force-strain curves and schematics of energy landscapes.** a) An increased κ_α causes an increase of the initial slope. b) A stronger coupling into larger subunits moves the plateau to higher forces, decreases the slope of the plateau and weakly influences the initial slope. The insets in a and b show the initial slope for each parameter set. c) Energy landscape E plotted against the reaction coordinate χ with minima for the alpha and unfolded state at high salt conditions (green) within the harmonic potential corresponding to the optical trap (dashed line). The resulting total potential is shown in blue. Without applied load, the alpha state is stable. d) By moving the optical trap, and thereby the harmonic potential, the energy barrier is reduced and the unfolded state becomes more probable. e) A higher free energy difference ΔG between the alpha and unfolded state increases F_{plateau} without affecting the slope of the plateau. f) Increasing the length of the unfolded monomer increases $\varepsilon_{||}$. g) The suggested energy landscape at low pH, which leads to an increased energy barrier ΔG, shows a higher E_A making the transition to the unfolded state less probable, h) even after applying the same trap load as in f). Figure reproduced from Ref. [1].

The origin of intra-filament coupling is found in the structure of vimentin. Each vimentin monomer has an excess of -19 e negative charges. A representation of the charge distribution in the vimentin monomer is shown in Fig. 5.10a. The excess negative charges are mostly found in coil 1B, coil 2, and the tail domain. As most polar and charged amino acids are not buried within the alpha helix [43], the excess negative charges of neighboring monomers within the filaments are likely to be in close proximity. The resulting repulsion presumably destabilizes the filament structure. The decreased initial slope and reduced stability we observe in low salt conditions therefore indicates that cations screen or – in case of multivalent ions – cross-bridge these repulsions. This is supported by the fact that vimentin is known to assemble in the presence of a sufficiently high concentration of cations and to disassemble in low salt buffer [29].

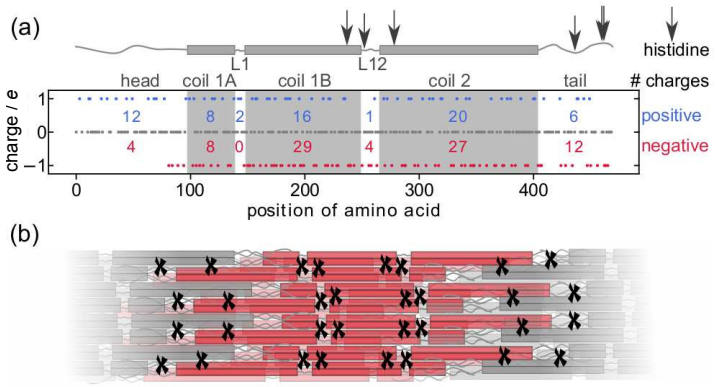

Fig. 5.10: **Charged amino acids in vimentin.** a) Top: Schematic representation of the vimentin monomer. The positions of histidines in one vimentin monomer are marked with arrows. Bottom: The charges of the amino acids are plotted versus their position in the sequence. The number of amino acids that carry a positive (lysine and arginine, blue) or negative charge (aspartic acid and glutamic acid, red) at pH 7.4 are shown for the head, coils, linkers and tail. b) The possible additional intra-filament interaction sites upon charge changes in the histidines are marked by 'x' for the visible front half of the red ULF. Figure reproduced from Ref. [1].

In contrast to the ion mediated, indirect, electrostatic effect, a pH change directly influences the charge pattern of the protein sequence. To be specific, in the pH range used here, we switch histidines from being uncharged to positively charged in an acidic environment [44, 45]. In vimentin there are six histidines at various positions, indicated by the arrows in Fig. 5.10a. These additional positive charges increase the number of possible electrostatic interaction sites between monomers in the filament (Fig. 5.10b), and therefore in our case decrease the repulsion, increase attraction, and promote coupling in the filament, similar to added ions.

Whereas the change of the initial slope is well explained by variations of κ_α, other experimentally observed changes in the force-strain curves, such as the plateau slope and length are not reproduced by this variation. To be able to compare the mechanisms that affect the plateau, we first examine the unfolding reaction that leads to the plateau formation. The force level of the plateau F_{plateau} (Fig. 5.11), the force reached at strain ε_I, is a measure of the energy necessary for unfolding. Fig. 5.9c shows a schematic and simplified energy landscape for the transition from the alpha to the unfolded state (green). The energy barrier E_A between the two states is indicated in Fig. 5.9d. The optical trap is approximated by a harmonic potential (dashed line). By applying a force (Fig. 5.9d), the harmonic potential is moved to the right, thereby decreasing the energy barrier in the total potential (blue) and the unfolded state becomes more probable.

The simulated force-strain curves in Fig. 5.9b reveal a strong dependence of F_{plateau} on the subunit size. By choosing a small subunit size such as $N_{sub} = 4$ we are able to reproduce the observed decrease of F_{plateau} in low salt buffer. At low pH, F_{plateau} is even higher than in high salt buffer. Thus, E_A is apparently even further increased at low pH. This behavior may be explained by an increased free energy difference, ΔG, between the alpha and unfolded state (purple

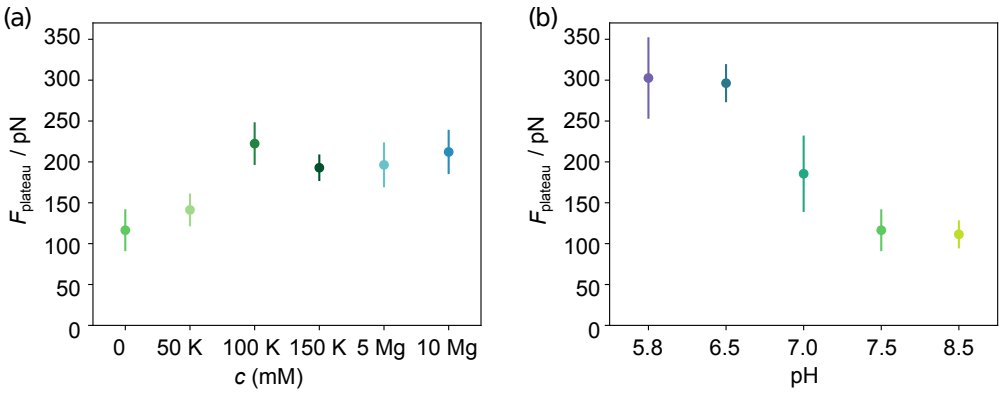

Fig. 5.11: **Plateau force of the force-strain curves.** The force at ε_I is shown for all single force-strain curves for each condition. The error bars correspond to the standard deviation. a) F_{plateau} from curves recorded at pH 7.5 with varying salt concentrations. The plateau is shifted to higher forces for higher KCl concentrations or in the presence of $MgCl_2$. b) F_{plateau} extracted from the force-strain curves measured at varying pH values. The plateau appears at higher forces for lower pH conditions. Figure reproduced from Ref. [1].

curve in Fig. 5.9h as compared to green curve in Fig. 5.9d), thus rendering the transition from the alpha to the unfolded state less probable at the same applied force (Fig. 5.9g,h), effectively increasing F_{plateau}. Fig. 5.9e shows how ΔG influences the force-strain curve.

In addition to an increased F_{plateau}, we also observe a shortening of the plateau at low pH (Fig. 5.2b). The length of the plateau, $\varepsilon_{\text{II}} - \varepsilon_{\text{I}}$, depends on the number of unfolding events and the length increase during unfolding, ΔL. Here, by the 'number of unfolding events' we summarize (i) fully unfolded ULFs and (ii) partially unfolded ULFs, as each of them consists of 32 monomers with three coils each, which can unfold fully or in parts. As ε_{I} is relatively constant in all measuring conditions, ε_{II} is a measure for the length of the plateau. Fig. 5.9f demonstrates how a decrease of ΔL shortens the plateau.

Earlier interpretations of the plateau being a transition from the alpha helices to beta sheets would allow for an elongation to strain 0.77 [9, 19] in the plateau. This value agrees with ε_{II} at high salt concentrations, but is exceeded at low salt conditions and not reached at low pH values (Fig. 5.2). Recent results indicate that the unfolding is in fact not a two-state process but that alpha helices first unfold to a random coil structure [20]. These random coils could be either longer or shorter than the beta-sheet conformation and thereby explain the variations in ΔL. The remarkably short plateaus we observe at low pH indicate a strong influence of the pH on ΔL. From the simulation in Fig. 5.9f we learn that decreasing ΔL furthermore increases the slope of the plateau, which agrees well with the increase of the slope we observe at low pH (Fig. 5.3c). The additional positive charges located at the sites of the histidines might act as crosslinkers in the filament, 'locking' the monomers in place and thereby decreasing ΔL.

Combining the simulations and the experimental results, we are now able to explain the observed increase of the initial slope, shortening of the plateau, shift to higher forces F_{plateau} at low pH or high salt conditions by increased subunit coupling and decreased ΔL. Additionally, for the low pH conditions, a

more pronounced ΔG comes into play, whereas for high salt, κ_α is increased. The slope of the plateau can be modeled by a decrease of the subunit size or of ΔL. As we observe no change of the slope of the plateau throughout all salt conditions at pH 7.5, these effects seem to be balance out during the plateau formation.

Previous studies of the stability of single coiled coils at varying pH and ionic strength showed seemingly conflicting results [23, 25, 27]. These opposing observations can be understood in the light of different primary sequences that lead to coiled coils of varying stability, based on the length of the coils [22], the hydrophobic packing or helix propensity, *i.e.* how prone an amino acid is to form alpha-helical structures [28], and electrostatic interactions in the coil [23, 25, 27]. It is, however, remarkable that even for coiled-coils, which have a very defined amino acid pattern, the response to external charge cues can vary to the reported extent. The effect of the electrostatic environment we report here is valid for vimentin but might be considerably weaker or stronger for other types of IFs. As the charge patterns in different types of IFs vary, we expect the extent of the effect of salt ions to scale according to the strength of the repulsion between subunits in the different IFs. For example, similar IFs, such as desmin and glial fibrillary acidic protein (GFAP) have an excess charge of -15 e and -13 e, respectively. We therefore anticipate the effect of ions to be weaker in these filaments. For the nuclear IF lamin A, which has an excess charge of -3 e [2], the dependence of the mechanical properties on ion concentrations is likely negligible. For the pH dependence, we expect the impact to scale with the number of histidines per monomer rather than the excess charge of the protein sequence. Whereas vimentin and desmin posses six histidines ($N_H = 6$), GFAP ($N_H = 8$) contains more potential additional interaction sites at low pH [2]. The effect in GFAP may therefore be even stronger than observed here for vimentin. For lamin A, $N_H = 13$, which leads us to the hypothesis that lamin A is more sensitive to pH variation than vimentin but less prone the mechanical changes by variations of salt concentration. The exact pH values the different IFs are sensitive to depend on the pKa of each single histindine.

As the cytoplasmic pH typically lies between 7.0-7.5 [38], the mechanical properties of vimentin are susceptible to pH changes in this range. Thus, cells are equipped with a "tool" to rapidly and locally tune their stiffness without remodeling the whole cytoskeleton. However, it remains unclear, how relevant the adaptability of the IF mechanics is in living cells. One intriguing phenomenon, where considerable pH changes and the up-regulation of vimentin in epithelial cells coincide, is wound healing. In epithelial wounds, mesenchymal cells expressing vimentin promote healing of the skin. During the restoration of the tissue, these cells might be exposed to pH milieus reaching from the healthy skin pH (4.0-6.0) to the body's internal pH (7.0-7.4) [39, 46]. Vimentin is not only up-regulated in the cells but also excreted into the extracellular space [47]. The result of our studies suggest that the mechanical changes vimentin undergoes in this pH range are considerable and might play a role within cells as well as the extracellular space during skin repair. Direct studies of the mechanical properties of cells and the corresponding structure of the IF network after exposure to varying pH milieus are necessary to make a more substantiated statement

about the role of pH milieus for IF mechanics. Intracellular and extracellular pH gradients have furthermore been found to be a feature of migrating tumor cells. A decrease of the pH along the axis of migration as well as local pH variations, such as nanodomains of high pH close to focal adhesions, have been reported [48]. An influence of the pH on the actin cytoskeleton is known [48], however, the role of IFs in this scenario is so far, to our knowledge, unexplored.
IFs have been shown to provide a "rescue mechanism" for cells that are subject to large areal strains [37]. At high strains, the actin network cannot compensate the applied force and IFs become load bearing. The extensibility of IFs therefore seems to be a crucial filament property, allowing them support the cell at these high strains. In the case of decreased pH, IFs are extended less at equal force, potentially leading to network stiffening. According to the strong effect we observe, we speculate, that local, intracellular pH changes may influence the role the IFs play under strain considerably. Studies of the strain response of single cells and multi-cellular ensembles at varying cell internal pH may shed light onto the role of IFs for cell mechanics in general. As a change of the pH milieu is often correlated with stress, the results for single filaments presented here, together with future experiments in cells may improve our understanding of biological stress response.

5.3 CONCLUSIONS

To conclude, we directly relate the mechanical response of single vimentin filaments to stretching in different buffer conditions to variations in the molecular electrostatic interactions in the filament. Our results show that the strong response to the electrostatic environment reported for coiled coils is preserved in mature vimentin filaments. A likely interpretation is that salt ions in the buffer screen or bridge electrostatic repulsion in the hierarchical structure and thereby stabilize the filaments. Additional positive charges in the amino acid sequence, caused by a lowered pH, stabilize and stiffen vimentin filaments as well. Thus, our results indicate that the mechanical role of IFs in cells can adapt to local pH and ion concentrations. Both effects, salt and pH, may allow cells to locally tune their stiffness without having to rebuild the entire cytoskeleton and thereby adapt their mechanics to varying requirements. In this context, we show that the stiffening of vimentin networks that was previously reported upon the addition of Mg^{2+} relies on increased inter-filament interactions and does not originate from stiffening of single filaments. Thus, by ensuring a relatively constant stiffness, extensibility, force-strain behavior, and stability of the filaments at physiological potassium concentrations and in conditions that are known to affect the bundling behavior of vimentin, we suggest that network mechanics can be tuned independent of the single filament properties. Consequently, the next step is to study, how the variability of single filament mechanics translates to network properties. This will allow for relating the intra-filament interactions studied here and inter-filament interaction in networks.

CONFLICTS OF INTEREST

There are no conflicts to declare.

ACKNOWLEDGEMENTS

We thank J. Forsting, J. Kraxner, H. Herrmann and J. C. Thiele for helpful discussions, S. Bauch and K. Sabagh for technical support, U. Rölleke and H. Somsel for critical reading of the manuscript.
This project was funded by the European Research Council (ERC) under the European Union's Horizon 2020 research and innovation program (Consolidator Grant Agreement no. 724932). This research was conducted within the Max Planck School Matter to Life supported by the German Federal Ministry of Education and Research (BMBF) in collaboration with the Max Planck Society. The work further received financial support via an Excellence Fellowship of the International Max Planck Research School for Physics of Biological and Complex Systems (IMPRS PBCS) and the Studienstiftung des deutschen Volkes e.V..

[1] A. V. Schepers, C. Lorenz, and S. Köster. "Tuning Intermediate Filament Mechanics by Variation of pH and Ion Charges." *Nanoscale* 12 (2020), pp. 15236–15245. DOI: 10.1039/D0NR02778B.

[2] I. Szeverenyi et al. "The Human Intermediate Filament Database: Comprehensive Information on a Gene Family Involved in Many Human Diseases." *Hum. Mutat.* 29 (2008), pp. 351–360. DOI: 10.1002/humu.20652.

[3] J. E. Eriksson et al. "Introducing Intermediate Filaments : From Discovery to Disease." *J. Clin. Invest.* 119 (2009), pp. 1763–1771. DOI: 10.1172/JCI38339.cells.

[4] H. Herrmann et al. "Structure and Assembly Properties of the Intermediate Filament Protein Vimentin: The Role of its Head, Rod and Tail Domains." *J. Mol. Biol.* 264 (1996), pp. 933–953. DOI: 10.1006/jmbi.1996.0688.

[5] A. A. Chernyatina, D. Guzenko, and S. V. Strelkov. "Intermediate Filament Structure: The Bottom-Up Approach." *Curr. Opin. Cell Biol.* 32 (2015), pp. 65–72. DOI: 10.1016/j.ceb.2014.12.007.

[6] N. Mücke et al. "Assembly Kinetics of Vimentin Tetramers to Unit-Length Filaments: A Stopped-Flow Study." *Biophys. J.* 114 (2018), pp. 2408–2418. DOI: 10.1016/j.bpj.2018.04.032.

[7] L. Kreplak et al. "Exploring the Mechanical Behavior of Single Intermediate Filaments." *J. Mol. Biol.* 354 (2005), pp. 569–577. DOI: 10.1016/j.jmb.2005.09.092.

[8] L. Kreplak, H. Herrmann, and U. Aebi. "Tensile Properties of Single Desmin Intermediate Filaments." *Biophys. J.* 94 (2008), pp. 2790–2799. DOI: 10.1529/biophysj.107.119826.

[9] J. Block et al. "Nonlinear Loading-Rate-Dependent Force Response of Individual Vimentin Intermediate Filaments to Applied Strain." *Phys. Rev. Lett.* 118 (2017), p. 048101. DOI: 10.1103/PhysRevLett.118.048101.

[10] P. A. Janmey et al. "Viscoelastic Properties of Vimentin Compared with Other Filamentous Biopolymer Networks." *J. Cell Biol.* 113 (1991), pp. 155–160. DOI: 10.1083/jcb.113.1.155.

[11] M. Zeisberg and E. G. Neilson. "Biomarkers for Epithelial-Mesenchymal Transitions." *J. Clin. Invest.* 119 (2009), pp. 1429–1437. DOI: 10.1172/JCI36183.protected.

[12] N. Pinto et al. "Self-Assembly Enhances the Strength of Fibers Made from Vimentin Intermediate Filament Proteins." *Biomacromolecules* 15 (2014), pp. 574–581. DOI: 10.1021/bm401600a.

[13] J. Block et al. "Viscoelastic Properties of Vimentin Originate from Nonequilibrium Conformational Changes." *Sci. Adv.* 4 (2018), eaat1161. DOI: 10.1126/sciadv.aat1161.

[14] N. Mücke et al. "Assessing the Flexibility of Intermediate Filaments by Atomic Force Microscopy." *J. Mol. Biol.* 335 (2004), pp. 1241–1250. DOI: 10.1016/j.jmb.2003.11.038.

[15] Y.-C. Lin et al. "Divalent Cations Crosslink Vimentin Intermediate Filament Tail Domains to Regulate Network Mechanics." *J. Mol. Biol.* 399 (2010), pp. 637–644. DOI: 10.1016/j.jmb.2010.04.054.

[16] B. Nöding and S. Köster. "Intermediate Filaments in Small Configuration Spaces." *Phys. Rev. Lett.* 108 (2012), p. 088101. DOI: 10.1103/PhysRevLett.108.088101.

[17] C. Guzmán et al. "Exploring the Mechanical Properties of Single Vimentin Intermediate Filaments by Atomic Force Microscopy." *J. Mol. Biol.* 360 (2006), pp. 623–630. DOI: 10.1016/j.jmb.2006.05.030.

[18] T. Ackbarow and M. J. Buehler. "Superelasticity, Energy Dissipation and Strain Hardening of Vimentin Coiled-Coil Intermediate Filaments: Atomistic and Continuum Studies." *J. Mater. Sci.* 42 (2007), pp. 8771–8787. DOI: 10.1007/s10853-007-1719-2.

[19] Z. Qin, L. Kreplak, and M. J. Buehler. "Hierarchical Structure Controls Nanomechanical Properties of Vimentin Intermediate Filaments." *PLoS ONE* 4 (2009), e7249. DOI: 10.1371/journal.pone.0007294.

[20] J. Forsting et al. "Vimentin Intermediate Filaments Undergo Irreversible Conformational Changes During Cyclic Loading." *Nano Lett.* 19 (2019), pp. 7349–7356. DOI: 10.1021/acs.nanolett.9b02972.

[21] D. D. Root et al. "Coiled-Coil Nanomechanics and Uncoiling and Unfolding of the Superhelix and α-Helices of Myosin." *Biophys. J.* 90 (2006), pp. 2852–2866. DOI: 10.1529/biophysj.105.071597.

[22] M. Goktas et al. "Molecular Mechanics of Coiled Coils Loaded in the Shear Geometry." *Chem. Sci.* 9 (2018), pp. 4610–4621. DOI: 10.1039/c8sc01037d.

[23] K. Dutta et al. "pH-Induced Folding of an Apoptotic Coiled Coil." *Protein Sci.* 10 (2001), pp. 2531–2540. DOI: 10.1110/ps.ps.28801.

[24] M. M. Stevens et al. "pH-Dependent Behavior of Surface-Immobilized Artificial Leucine Zipper Proteins." *Langmuir* 20 (2004), pp. 7747–7752. DOI: 10.1021/la030440e.

[25] K. Pagel et al. "Random Coils, β-Sheet Ribbons, and α-Helical Fibers: One Peptide Adopting Three Different secondary Structures at Will." *J. Am. Chem. Soc.* 128 (2006), pp. 2196–2197. DOI: 10.1021/ja057450h.

[26] R. M. Reja et al. "pH Sensitive Coiled Coils: A Strategy for Enhanced Liposomal Drug Delivery." *Nanoscale* 8 (2016), pp. 5139–5145. DOI: 10.1039/c5nr07734f.

[27] Y. Yu et al. "Ion Pairs Significantly Stabilize Coiled-Coils in the Absence of Electrolyte." *J. Mol. Biol.* 255 (1996), pp. 367–372. DOI: 10.1006/jmbi.1996.0030.

[28] P. López-García et al. "Structural Determinants of Coiled Coil Mechanics." *Phys. Chem. Chem. Phys.* 21 (2019), pp. 9145–9149. DOI: 10.1039/C9CP00665F.

[29] H. Herrmann and U. Aebi. "Intermediate filament assembly: fibrillogenesis is driven by decisive dimer-dimer interactions." *Curr. Opin. Struc. Biol.* 8 (1998), pp. 177–185. DOI: 10.1016/S0959-440X(98)80035-3.

[30] C. Dammann, B. Nöding, and S. Köster. "Vimentin networks at tunable ion-concentration in microfluidic drops." *Biomicrofluidics* 6 (2012), p. 022009. DOI: 10.1063/1.4705103.

[31] C. Dammann, H. Herrmann, and S. Köster. "Competitive Counterion Binding Regulates the Aggregation Onset of Vimentin Intermediate Filaments." *Isr. J. Chem.* 56 (2016), pp. 614–621. DOI: 10.1002/ijch.201400153.

[32] C. Dammann and S. Köster. "Dynamics of Counterion-Induced Attraction between Vimentin Filaments Followed in Microfluidic Drops." *Lab Chip* 14 (2014), pp. 2681–2687. DOI: 10.1039/c3lc51418h.

[33] Y.-C. Lin et al. "Origins of elasticity in intermediate filament networks." *Phys. Rev. Lett.* 104 (2010), p. 058101. DOI: 10.1103/PhysRevLett.104.058101.

[34] S. Köster et al. "Nanomechanics of vimentin intermediate filament networks." *Soft Matter* 6 (2010), p. 1910. DOI: 10.1039/c000113a.

[35] H. Wu et al. "Effect of divalent cations on the structure and mechanics of vimentin intermediate filaments." *Biophys. J.* 119 (2020), pp. 55–64. DOI: 10.1016/j.bpj.2020.05.016.

[36] M. Zacchia et al. "Potassium: From Physiology to Clinical Implications." *Kidney Dis.* 2 (2016), pp. 72–79. DOI: 10.1159/000446268.

[37] E. Latorre et al. "Active superelasticity in three-dimensional epithelia of controlled shape." *Nature* 7730 (2018), pp. 6481–6487. DOI: 10.1021/ac8009643.

[38] W. H. Moolenaar, L. G. J. Tertoolen, and S. W. De Laat. "The Regulation of Cytoplasmic pH in Human Fibroblasts." *J. Biol. Chem.* 259 (1984), pp. 7563–7569. DOI: 10.1016/S0021-9258(17)42827-4.

[39] G. R. Bright et al. "Fluorescence Ratio Imaging Microscopy: Temporal and Spatial Measurements of Cytoplasmic pH." *J. Cell Biol.* 104 (1987), pp. 1019–1033. DOI: 10.1083/jcb.104.4.1019.

[40] C. Lorenz et al. "Lateral Subunit Coupling Determines Intermediate Filament Mechanics." *Phys. Rev. Lett.* 123 (2019), p. 188102. DOI: 10.1103/PhysRevLett.123.188102.

[41] J. F. Nolting, W. Möbius, and S. Köster. "Mechanics of Individual Keratin Bundles in Living Cells." *Biophys. J.* 107 (2014), pp. 2693–2699. DOI: 10.1016/j.bpj.2014.10.039.

[42] B. Nöding, H. Herrmann, and S. Köster. "Direct Observation of Subunit Exchange Along Mature Vimentin Intermediate Filaments." *Biophys. J.* 107 (2014), pp. 2923–2931. DOI: 10.1016/j.bpj.2014.09.050.

[43] J. M. Mason and K. M. Arndt. "Coiled Coil Domains: Stability, Specificity, and Biological Implications." *ChemBioChem* 5 (2004), pp. 170–176. DOI: 10.1002/cbic.200300781.

[44] M. Miyagi and T. Nakazawa. "Determination of pKa values of individual histidine residues in proteins using mass spectrometry." *Anal. Chem.* 17 (2008), pp. 6481–6487. DOI: 10.1021/ac8009643.

[45] S. P. Edgcomb and K. P. Murphy. "Variability in the pKa of histidine side-chains correlates with burial within proteins." *Proteins: Struct., Funct., Genet.* 1 (2002), pp. 1–6. DOI: 10.1002/prot.10177.

[46] L. A. Schneider et al. "Influence of pH on Wound-Healing: A New Perspective for Wound-Therapy?" *Arch. Dermatol. Res.* 298 (2007), pp. 413–420. DOI: 10.1007/s00403-006-0713-x.

[47] J. L. Walker et al. "In Wound Repair Vimentin Mediates the Transition of Mesenchymal Leader Cells to a Myofibroblast Phenotype." *Mol. Biol. Cell* 29 (2018), pp. 1555–1570. DOI: 10.1091/mbc.e17-06-0364.

[48] F. T. Ludwig, A. Schwab, and C. Stock. "The Na+/H+-Exchanger (NHE1) Generates pH Nanodomains at Focal Adhesions." *J. Cell. Physiol.* 228 (2012), pp. 1351–1358. DOI: 10.1002/jcp.24293.

6 MULTISCALE MECHANICS AND TEMPORAL EVOLUTION OF VIMENTIN INTERMEDIATE FILAMENT NETWORKS

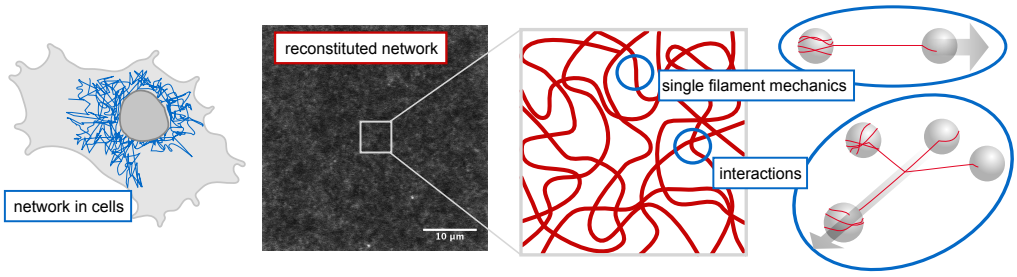

This chapter is published as *A. V. Schepers, C. Lorenz, P. Nietmann, A. Janshoff, S. Klumpp, and S. Köster, "Multiscale mechanics and temporal evolution of vimentin intermediate filament networks" Proc. Natl. Acad. Sci., 2021, 118, 15236-15245* [1]. Text and figures are reproduced with permission. Where appropriate, figures from the supporting information of the original publication are incorporated in the main text of this chapter. The original manuscript is extended by the additional sections 6.2.4, 6.2.5, 6.2.8, and 6.4 for this thesis.

Contributions: S. Kö. conceived and supervised the project. A. V. S. performed and analyzed the single filament mechanics, elongation, and interaction experiments. P. N. performed and analyzed active microrheology measurements. A. V. S. performed MPT measurements and P. N. and A. V. S. analyzed MPT experiments. C. L. and S. Kl. designed, and C. L. performed numerical simulations. All authors contributed to writing the manuscript.

ABSTRACT

The cytoskeleton, an intricate network of protein filaments, motor proteins, and cross-linkers, largely determines the mechanical properties of cells. Among the three filamentous components, F-actin, microtubules, and intermediate filaments (IFs), the IF network is by far the most extensible and resilient to stress. We present a multiscale approach to disentangle the three main contributions to vimentin IF network mechanics – single-filament mechanics, filament length, and interactions between filaments – including their temporal evolution. Combining particle tracking, quadruple optical trapping, and computational modeling, we derive quantitative information on the strength and kinetics of filament interactions. Specifically, we find that hydrophobic contributions to network mechanics enter mostly via filament-elongation kinetics, whereas electrostatics have a direct influence on filament–filament interactions.

6.1 INTRODUCTION

Cells have remarkably diverse and dynamic mechanical properties that are largely determined by the cytoskeleton [2]. The adaptability of the cytoskeleton relies on the unique and distinct mechanical properties of the different biopolymers that form this composite network [3]. Intermediate filaments (IFs) are particularly interesting from a mechanical point of view. By contrast to F-actin and microtubules, both single IFs and networks thereof display an enormous extensibility and stability at high strains. These properties have been impressively shown for vimentin IFs, which are found in cells of mesenchymal origin [3–5]. Rheological studies reveal that vimentin networks are soft at small strains, but show pronounced strain stiffening up to a critical strain, at which the networks soften [3, 6–9], unless they are covalently cross-linked [9]. Furthermore, vimentin networks stiffen in the presence of divalent ions, which has been attributed to transient interactions between filaments, specifically between the negatively charged, disordered tail domains [7–11]. Whereas these previous studies provide a rich pool of information on network mechanics, they cannot unravel the effects of filament-elongation kinetics, single filament mechanics and filament–filament interactions, which are all superimposed. For instance, an influence of divalent cations for IF network mechanics is indisputable, but the exact mechanism by which they alter the network properties remains elusive. Here, we present a targeted experimental and computational approach that enables us to disentangle the contributions of single-filament properties and filament–filament interactions to network mechanics. With our multiscale approach we extract binding and unbinding rates for single interactions, and thereby directly quantify the transient nature of direct interactions between vimentin filaments.

6.2 RESULTS AND DISCUSSION

6.2.1 Vimentin filament networks mature and stiffen on time scales of days

Previous studies of vimentin network mechanics have typically focused on time points of about 1 to 2 h after initiation of filament assembly and network formation, which in most experimental protocols occur simultaneously [6–8, 10, 11]. We extend this work and study the formation of vimentin IF networks and the evolution of the network mechanics over a broad time range, from 3 h to 144 h after initiation of assembly, and at standard conditions, *i.e.*, in the presence of 100 mM KCl [12]. We record tracks of microparticles embedded in the networks, as shown in Fig. 6.1a (Middle), and calculate the mean squared displacement (MSD) for each assembly duration; see Fig. 6.1b (Middle). At 3 h (black line), microparticle tracking (MPT) reveals subdiffusive behavior. For comparison, the MSD for diffusive motion is shown as the purple dashed line. For longer network-formation times, we observe a decrease of the mobility of the particles. This stiffening of the vimentin network leads to a flattening of the MSDs at long lag times; as expected, after very long network-formation times, the beads are confined and the MSDs approach a plateau.

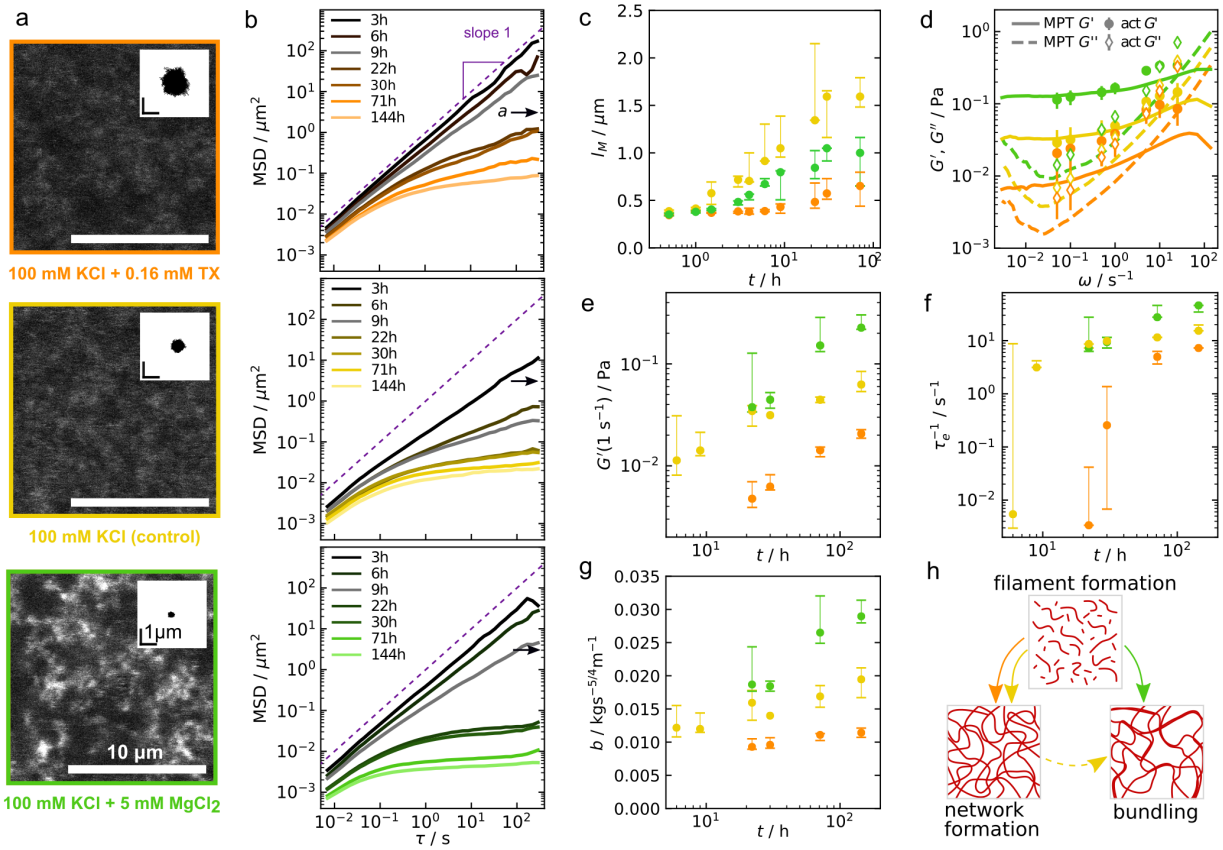

Fig. 6.1: **Formation and mechanics of vimentin networks.** a) Microscopy images of vimentin networks after 3 days (74 h-80 h) of network-formation time, buffer conditions indicated below each image. The insets show representative traces from MPT, recorded over the course of 6 min after three days (71 h) of network-formation. b) Median MSD for each condition for increasing network-formation times (for color code, see legend); the cross section of particles with diameter $a = 2\,\mu\text{m}$ is indicated by arrows. Individual curves are shown in Figs. B4-B6. c) Elongation of the filaments; shown is the length average l_M. The corresponding cumulative length histograms from three interdependent datasets are provided in Fig. B2, and the extent of reaction q as determined from step-growth polymerization is shown in Fig. B3. d) Comparison of active (symbols) and passive (lines) microrheology measurements after 3 days. The error bars denote the standard deviation of the active measurements. e) Temporal evolution of G' at $\omega = 1\,\text{s}^{-1}$. f) Temporal evolution of the relaxation times of single filaments in the network. g) Temporal evolution of the bundling parameters, calculated from the shift of $G'' = b\omega^{3/4} - \eta\omega$ [13] at high frequencies. For c, e, f, and g, the median values of the results, analyzed sample by sample, are shown, along with the minimum and maximum, indicated by the error bars. For each time point and condition, between one and five samples are measured; see Figs. B4-B6 for the numbers of samples and particles. h) Schematic of the filament and network formation process with the competition between lateral arrangement – *i*.e., bundling – and filament elongation that leads to an entangled network. Reproduced from Ref. [1].

The stiffening of the network continues over the whole assembly duration probed. From 6 h on, the particles are confined, as the movement does not exceed the particle cross section of particles with a diameter of $a = 2\,\mu m$ after the total measuring time. This behavior is in accordance with Ref. [10] where 2-µm beads were reliably confined in a vimentin network at 1 g/L protein concentration as well as the theoretical mesh size of 0.45 µm calculated for a homogeneous, cubic vimentin network at 1 g/L. The transition from subdiffusive to confined motion is caused by the network formation of the slowly growing filaments. The hierarchical assembly pathway of vimentin filaments and the corresponding time scales are shown in Fig. 6.2.

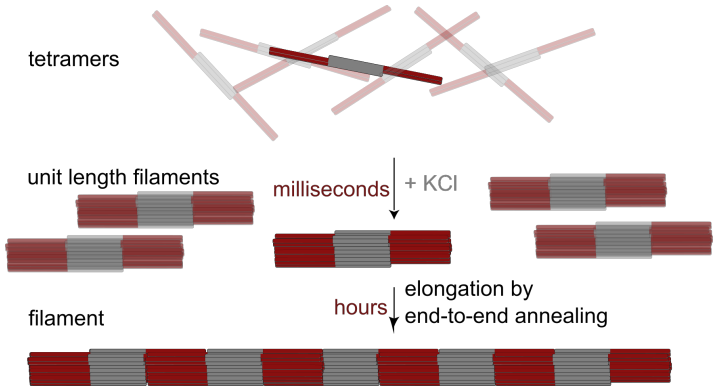

Fig. 6.2: **Filament assembly.** Sketch of the assembly process of vimentin IFs. unit length filaments (ULFs) form by lateral arrangement of eight tetramers. Filaments form by end-to-end annealing of the ULFs. Based on Ref. [14]. Reproduced from Ref. [1].

6.2.2 The filament length depends on elongation and lateral association

To investigate the cause of the network stiffening, we analyze the temporal evolution of the filament length. Vimentin filament assembly strongly depends on the ionic strength of the utilized buffer [15–18], and the type and concentration of the ions influence the filament structure [15, 19–23]. Specifically, the formation kinetics, architecture, and mechanics of the networks depend on a careful balance between the slow longitudinal assembly of single filaments and the lateral association of filaments – *i.e.*, bundling. This balance is influenced by lateral interactions between the filaments [24] which we examine by varying the interaction strength, specifically hydrophobic and electrostatic interactions, between vimentin IFs [6, 25, 26]. For keratin IFs, in particular, it has been observed that diminishing hydrophobic interactions by detergents may cause softening of IF networks [25, 27]. By contrast, an increase of electrostatic attraction, mediated by divalent ions, leads to a stiffening of IF networks [7, 9–11]. To separate hydrophobic and electrostatic effects, we assemble vimentin filaments in the presence of additional nonionic detergent TritonX-100 (TX) at a concentration of 0.16 mM to diminish hydrophobic interactions, or 5 mM $MgCl_2$ for increased electrostatic attraction (Fig. 6.1c). We observe a slower filament elongation with overall shorter filaments in both cases. In the presence of TX, decreased hydrophobic interactions severely impair the elongation (Fig. B2).

We therefore conclude that hydrophobic interactions within filaments – *i.e.*, between subunits – play a pivotal role during vimentin IFs assembly, including elongation. This phenomenon has, to our knowledge, so far only been studied for the first steps of assembly, up to the unit-length filament stage [20, 28, 29]. For added $MgCl_2$, we follow the line of arguments of Ref. [24] and assume that the balance is shifted toward increased attraction between filaments, leading to lateral association of short filaments, rather than longitudinal annealing. For vimentin IFs, such bundling events have been directly observed in the presence of sufficiently high concentrations of $MgCl_2$ [30, 31].

6.2.3 Electrostatic and hydrophobic interactions lead to mechanically distinct networks

The bundle formation caused by the addition of $MgCl_2$ not only influences elongation kinetics, but also network mechanics. We extend previous studies of vimentin network mechanics in the presence of divalent ions [7, 9–11] to much longer assembly time scales, since we expect a saturation of the network mechanical properties after days rather than hours, as shown above for the control condition. We assemble the networks in the same buffer conditions as the single filaments, with 0.16 mM TX for reduced hydrophobic interactions (Fig. 6.1a, Top) or 5 mM $MgCl_2$ for increased electrostatic attraction (Fig. 6.1, Bottom). Confocal images of the respective networks reveal no apparent difference between the control condition and in the presence of TX, whereas the networks are more heterogeneous in the presence of $MgCl_2$.
As expected from the filament-elongation studies, the corresponding MPT data in Fig. 6.1b, Top and Bottom, show that the network formation, in particular the transition from subdiffusive to confined motion, is delayed for both conditions compared to the control. As we eventually observe confinement, we reason that the relevant length scales of the networks – which can, for example, be the mesh size, entanglement length or filament length – are comparable. We transfer the MSDs that show confinement into the complex shear modulus $G^* = G' + iG''$ with the storage G' and loss G'' moduli, as shown in Figs. B8-B10 [32]. Analysis of the plateau modulus $G'(1\,s^{-1})$ illustrates the continuous stiffening that all samples undergo with advancing time (Fig. 6.1e). From 22 h on, the network with $MgCl_2$ is the stiffest; the network in the control sample shows intermediate stiffness; and the sample with detergent stays the softest throughout. As an example, the comparison of G' and G'' of the networks after 71 h in Fig. 6.1d illustrates this difference clearly. Active microrheology by optical trapping of microparticles embedded in the respective samples (Fig. 6.1d and Fig. B11) validates the passive microrheology results from MPT with remarkable agreement. The moduli we obtain from MPT are lower than those reported from macrorheological measurements [6–9], however, they are on the same order of magnitude as reported for other microrheological studies of vimentin networks [10, 11].

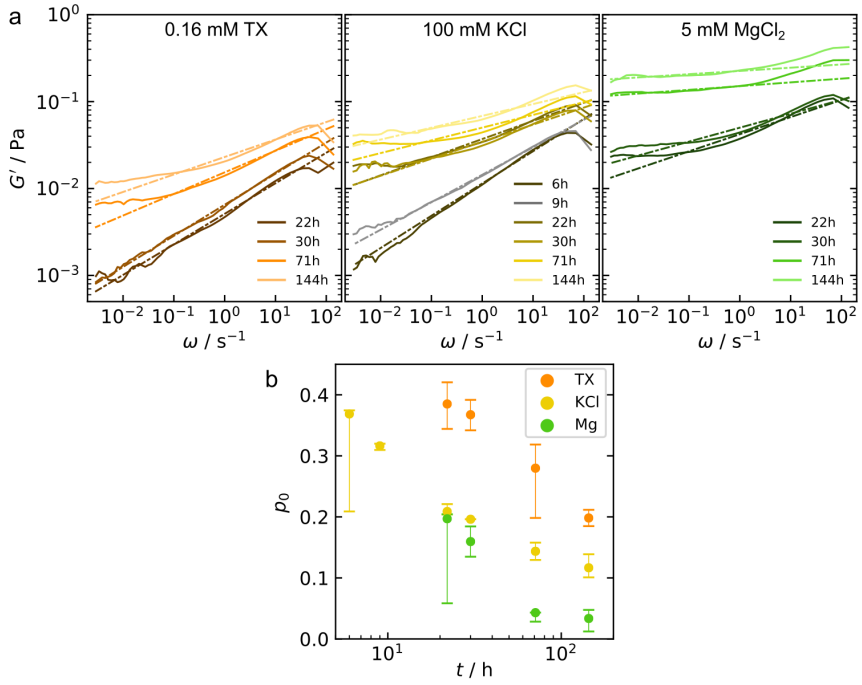

Fig. 6.3: **Frequency dependence of the storage modulus.** a) The exponent p_0 of a power law fit to the storage modulus G' describes the frequency dependence of the storage modulus. For clarity, the median G' curve of all samples (solid line) and the resulting fit (dashed line) are shown. b) Comparison of the exponents of the power law fits over the network assembly duration. The median values of the results, analyzed sample-by-sample, are shown, along with the minimum and maximum indicated by the error bars. The number of samples and particles per measurement are provided in Figs. B4-B6. Reproduced from Ref. [1].

The connectivity of the networks influences the frequency dependence of the plateau. In presence of $MgCl_2$ (Fig. 6.3), the plateau is the least frequency-dependent, indicating a more pronounced contribution of cross-linking rather than entanglement to the network mechanics [11]. This is in agreement with the established hypothesis that divalent ions serve as transient cross-linkers in IF networks [7, 9, 10]. The binding and unbinding rates of these transient cross-links, however, cannot be inferred from our measurements. The increased connectivity of the networks as well as stiffening due to bundle formation further cause an increase of the inverse relaxation time τ_e^{-1}, as determined from the cross-over frequency of G' and G'' (Fig. 6.1f) [33]. Above τ_e^{-1}, single-filament or bundle mechanics dominate over the network properties (Fig. 3.13).
As we expect an influence of bundling on the network mechanics, we analyze the coupling of filaments in bundles by investigating the slope of G^* at high frequencies. At $\omega > 5\,s^{-1}$, G'' follows a power law with exponent $3/4$ for all samples (Eq. (4.7) and Fig. 6.4), as theoretically predicted for networks consisting of single filaments or of bundles that are coupled so strongly that they behave like single filaments [34].

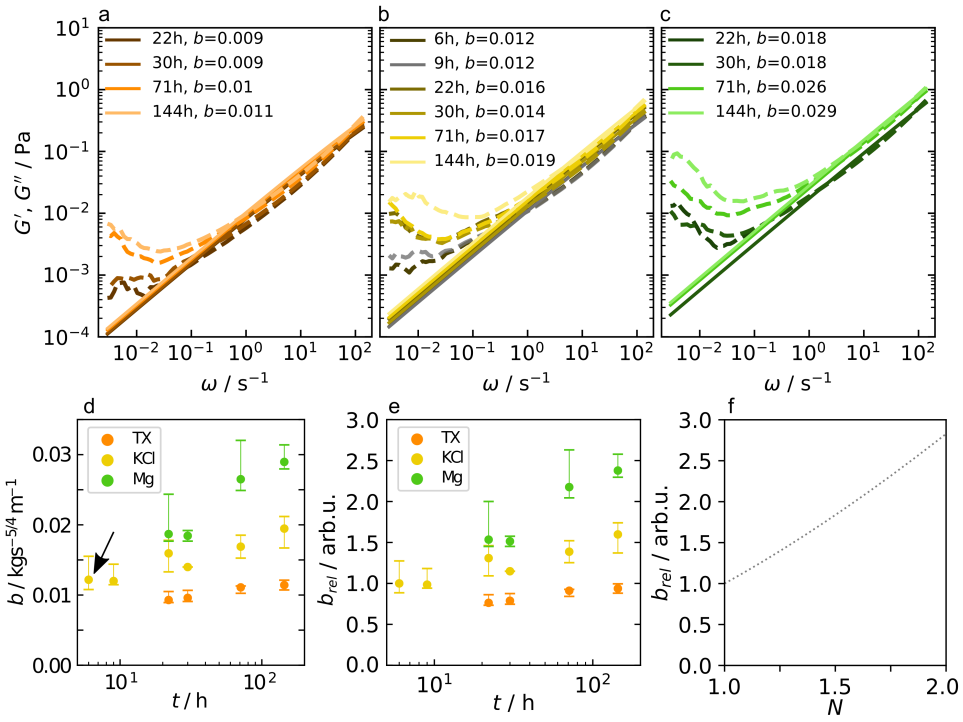

Fig. 6.4: **Relative bundling parameter.** a) Fit of $G'' \propto b\omega^{3/4} - \eta\omega$ to the data involving TX, b) only KCl, and c) $MgCl_2$. The dashed line corresponds to the median G'' of the samples and the solid line is the fit curve, the fit result is provided in the legend. For clarity, we here show the fit of the median of the samples, the result of the sample-by-sample analysis is provided in d) and e). d) The median of the fit parameters b, calculated on a sample-by-sample basis, plotted against the assembly time of the network. The error bars indicate the minimum and maximum values. e) The median bundling parameter b_{rel} calculated on a sample-by-sample basis, relative to the median value obtained for the KCl sample after 6 h, marked with the arrow in d). The error bars indicate the minimum and maximum values. The number of samples and particles per measurement are provided in Figs. B4-B6. f) The simple approximation described in section 4.9.3 gives an estimate of the dependence of b_{rel} on the average number of filaments per bundle. For fully coupled bundles this estimation leads to $b_{rel} \propto N^{6/4}$. The ratio of the lateral drag coefficients $(\zeta_b/\zeta_f)^{3/4}$ only weakly influences b_{rel} and is neglected here. Reproduced from Ref. [1].

Furthermore, in a simple approximation of the experimental networks, the offset of the power-law regime of G'', b (Eq. (4.8)) indicates trends in the degree of bundling, as it strongly depends on the persistence length of the filaments l_P or bundles $l_{P(bundle)} = N^{\alpha} l_{P(filament)}$, where α denotes the coupling strength of the filaments within the bundle and lies between 1 (uncoupled) and 2 (fully coupled) [35]. Fig. 6.1g shows a strong increase of b over the network-formation times in the presence of Mg^{2+} and a much weaker increase for the control condition or in the presence of TX, suggesting that in the presence of Mg^{2+}, there are, on average, more filaments per bundle (see also Fig. 6.4). All processes described above are shown schematically in Fig. 6.1h.

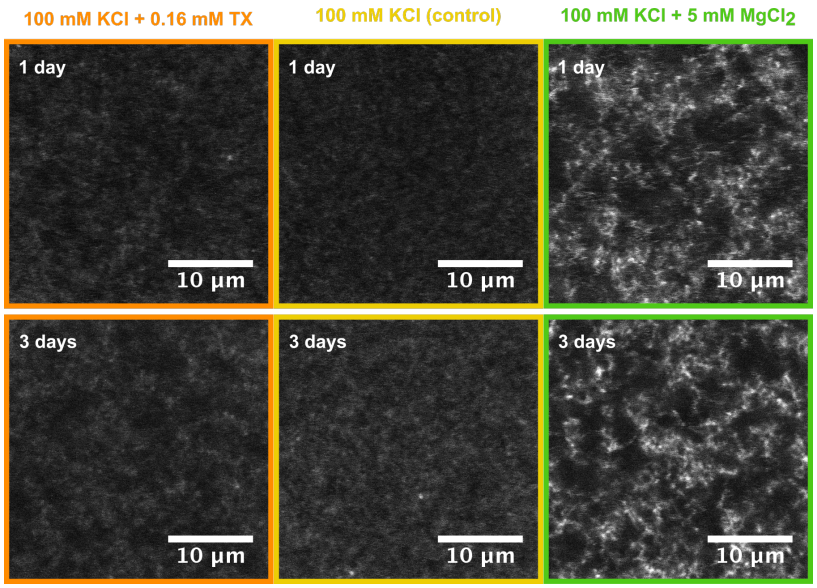

Fig. 6.5: **Confocal images of networks after one day and three days of assembly.** The images recorded after three days show the same sample as in Fig. 6.1a. No apparent difference between the different times for one sample are visible. Reproduced from Ref. [1].

While we see a clear effect of the network maturation on the mechanical properties, we cannot resolve any structural changes in confocal images recorded after one day and three days of assembly (Fig. 6.5). Here, the high flexibility of the filaments strongly impeded the achievable resolution and we do not expect to resolve single bundling events. These images, however, nicely demonstrate the differences between samples in different buffer conditions.

6.2.4 Maturation of networks is concentration dependent

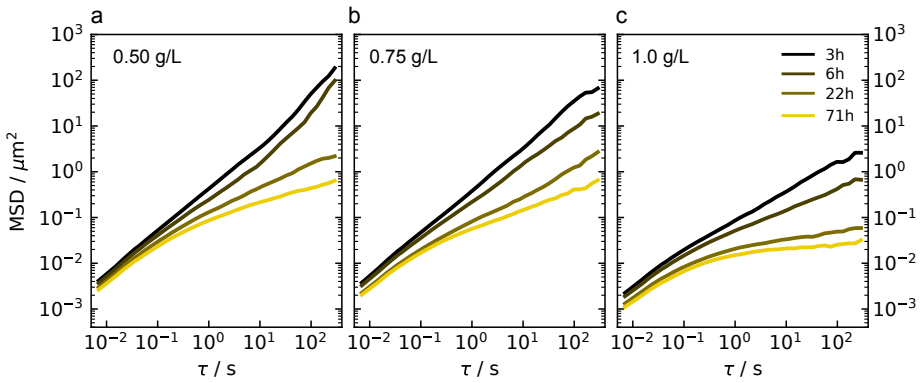

Fig. 6.6: **Concentration dependent evolution of the MSD.** Median MSD for each condition for increasing network-formation times at a) 0.50 g/L, b) 0.75 g/L, and c) 1.0 g/L. Data are recorded for one sample at each concentration. Individual curves are shown in Fig. B7.

To verify that the slower filament assembly leads to a slower maturation of the networks, we assemble networks in the control buffer conditions at lower initial vimentin protein concentrations than used in section 6.2.1. The speed of the assembly of vimentin filaments has been shown to decrease at lower protein

concentrations [36–38]. At the lower initial protein concentrations, we observe mostly diffusive motion for a longer assembly duration, *i.e.*, the time point, at which the network forms, is delayed, see Fig. 6.6. This delay indicates that slower filament assembly leads to slower maturation, which strengthens our hypothesis that in the presence of Mg^{2+} or TX, the slower filament assembly causes the observed delay. However, the lower protein concentration leads to overall softer networks as the network structure is also influenced by the protein concentration. The exact contributions of the filament elongation to the network mechanics cannot be quantified solely by MPT.

6.2.5 **Surface effects modify network structures**

Besides the protein concentration, interactions with the surface of the measuring chamber additionally influence the network structure. To analyze such surface effects, we record z-stacks of the networks with confocal microscopy (Fig. 6.7a). The average intensity decreases with increasing distance to the glass surface (Fig. 6.7b) in all samples, and reaches a relatively constant value at $z \approx 4\,\mu m$ in the chambers of $\approx 100\,\mu m$ height.
In the z-stacks shown in Fig. 6.7a, the inhomogeneity of the network in presence of Mg^{2+} becomes evident. These results are interesting when comparing the moduli we obtain from MPT to those reported from macrorheological measurements, which are typically higher than our results [6–9]. However, our results are on the same order of magnitude as reported for other microrheological studies of vimentin networks [10, 11]. The discrepancy between the mechanics determined by microrheology and macrorheology, *i.e.*, shear rheometry, might arise from the density gradient of the network, caused by surface interactions. As it it crucial for shear rheometry that the network is attached to the rheometer plates, we expect a similar density gradient to occur in shear rheometry setups, which might lead to a stiffer result. In the MPT experiments, we take care to measure at 30-40 µm distance to the surface to reduce such stiffening from surface interactions. Moreover, the discrepancy between G' and G'', measured by microrheology and bulk rheology [25], has additionally been attributed to interfacial elasticity at the air-sample interface [27].

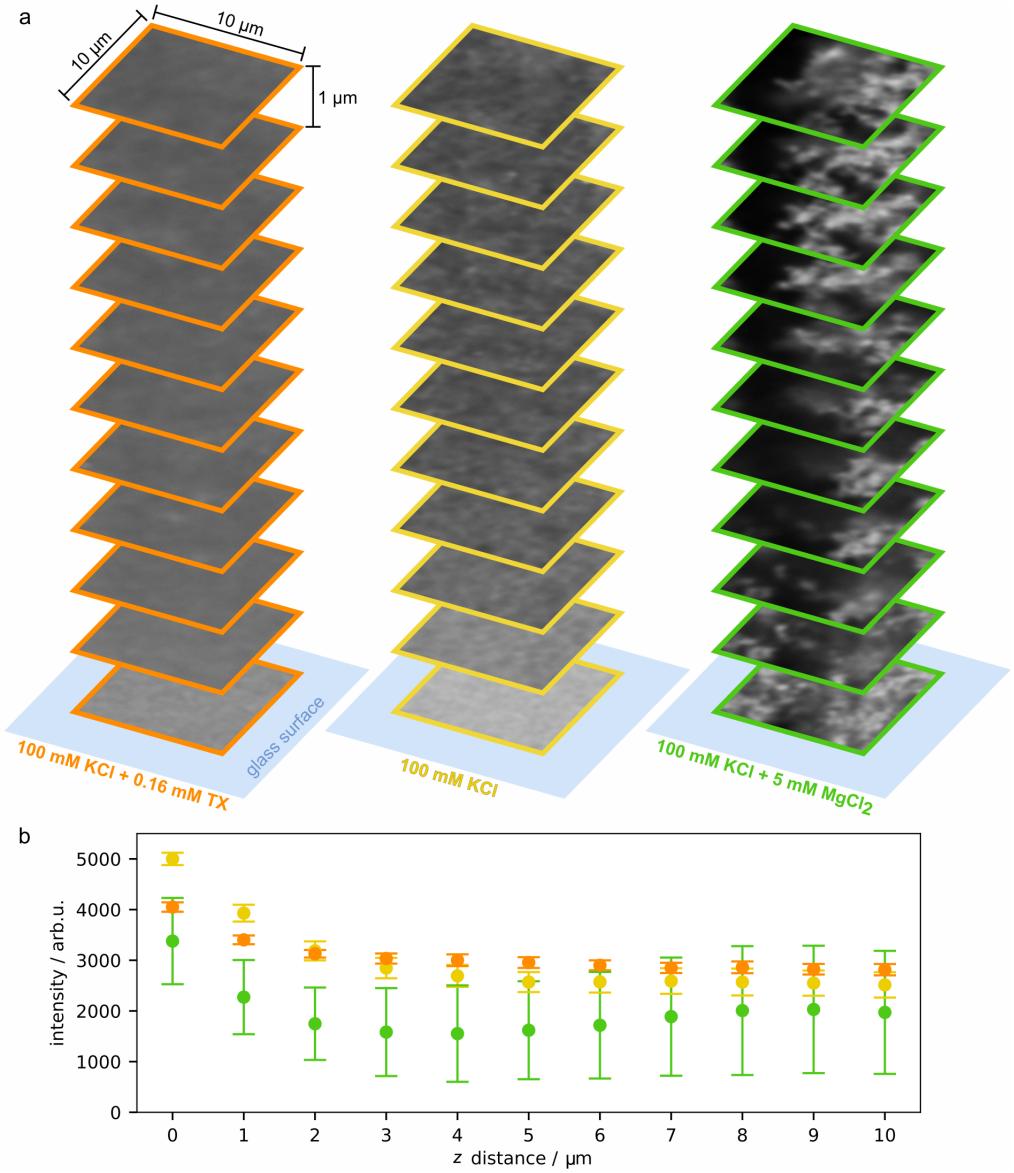

Fig. 6.7: **Surface effects on network structure.** a) Confocal z-stacks of vimentin networks in the different buffer conditions. The distance between the slices is 1 µm. Each image shown here is the sum of 300 frames in the respective z-plane recorded at a frame rate of 39 s^{-1}. Images recorded by Jan Christoph Thiele. b) The average intensity (mean, standard deviation) of each image shown in a) over the distance to the glass surface.

6.2.6 Single filament mechanics are unaffected by detergents or divalent ions

Apart from filament-elongation kinetics, single-filament mechanics and filament–filament interactions may be influenced by the addition of cations or detergent. Indeed, MPT probes all of these effects in a combined fashion. To disentangle these effects, we focus on single-filament mechanics next. The mechanical properties of single vimentin IFs are well established [5, 39–41], and it has been shown that they sensitively depend on the surrounding charges [42]. We find that divalent ions do not stiffen single filaments and TX only slightly softens filaments, as shown in Fig. 6.8. We can therefore safely exclude single-filament mechanics as the main cause for the marked differences found for the networks in the three buffer conditions.

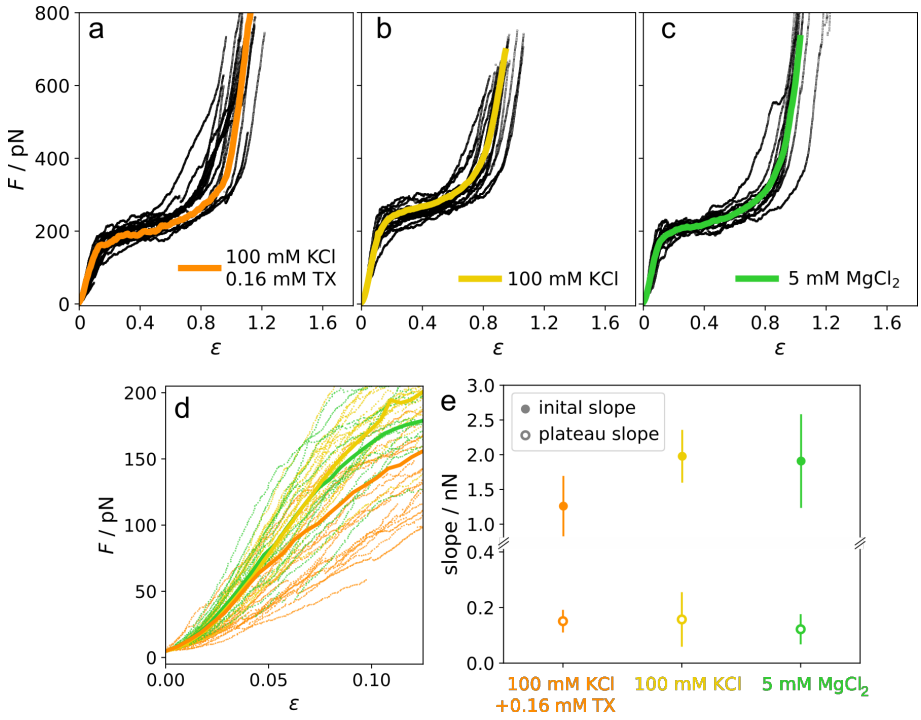

Fig. 6.8: **Stretching single filaments.** a) Force strain curves recorded for single vimentin filament stretching in the optical trap. The filaments are assembled in assembly buffer and measured after 30 s incubation in assembly buffer + 0.16 mM TX, b) assembly buffer, c) 2 mM phosphate buffer + 5 mM $MgCl_2$ at pH 7.5. The data shown in b) and c) are published in Ref. [42]. The single curves are shown in black and the average curve in the respective color. The numbers of single filaments measured are a) 18, b) 25, c) 13. d) Comparison of the initial, linear increase of the force-strain curves for all three conditions, showing the slight softening of the filaments in TX. e) Comparison of the slope of a linear regression for the initial regime and the plateau regime. We show the mean of all single curves and the standard deviation (error bars). The slope of the plateau is constant for all conditions whereas the initial slope is slightly lower in TX than in assembly buffer and Mg-buffer. Reproduced from Ref. [1].

6.2.7 Electrostatics increase single filament–filament interactions

After investigating filament elongation and single-filament mechanics, in a third step, we scrutinize filament–filament interactions with single-molecule precision. To this end, we bring two filaments in contact in a perpendicular configuration using a quadruple optical trap setup (Fig. 4.2). Confocal images of the experiment are shown in Fig. 6.9a.

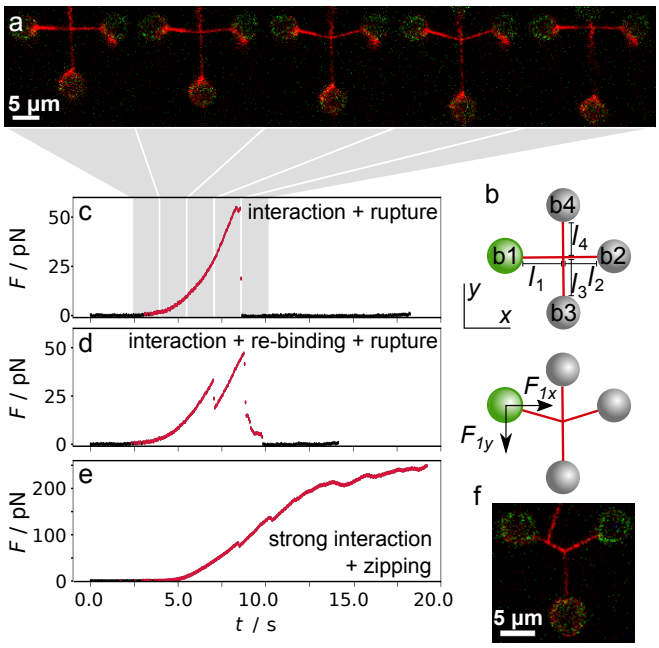

Fig. 6.9: **Interaction measurements.** a) Confocal image series of a filament pair showing deformation of the horizontal filament as a consequence of the interaction and the return to the initial conformation after rupture of the interaction. b) Schematic of the measuring geometry and nomenclature used in the experiments. We measure and analyze the force F_{1y} acting on b1 (green). c) Typical interaction force, F, plotted against time for the filament pair shown in a); rupture force F_i. d) Typical force–time curve for a measurement with interaction, rupture of the interaction with rebinding under force, and rupture of the interaction. e) Force–time curve for a strong interaction of filaments that show "zipping", as shown in the micrograph in f). Reproduced from Ref. [1].

We slide one filament perpendicularly along the other one and measure the interaction force by the deflection of the particle "b1", marked green in Fig. 6.9b. The resulting interaction force for the filament pair shown in Fig. 6.9a is plotted in Fig. 6.9c. We extract the duration of the interaction (red in Fig. 6.9c) and the strength of the interaction from the maximum interaction force, F_i, before the interaction ruptures; see also Fig. 4.3. Notably, not all filament pairs show this interaction behavior, and some pairs show no detectable interaction at all. In other cases, the filaments interact, the interaction ruptures, and the filaments start to interact again before the force has dropped to zero (Fig. 6.9d).
Lastly, filaments can interact strongly (Fig. 6.9e and Fig. 6.10), which, only in the presence of $MgCl_2$, leads to remarkable "zipping events", *i.e.*, the parallel association of two filaments [43] as shown in Fig. 6.9f and Fig. 6.11. From these events, we conclude that interactions are localized and do not slip.

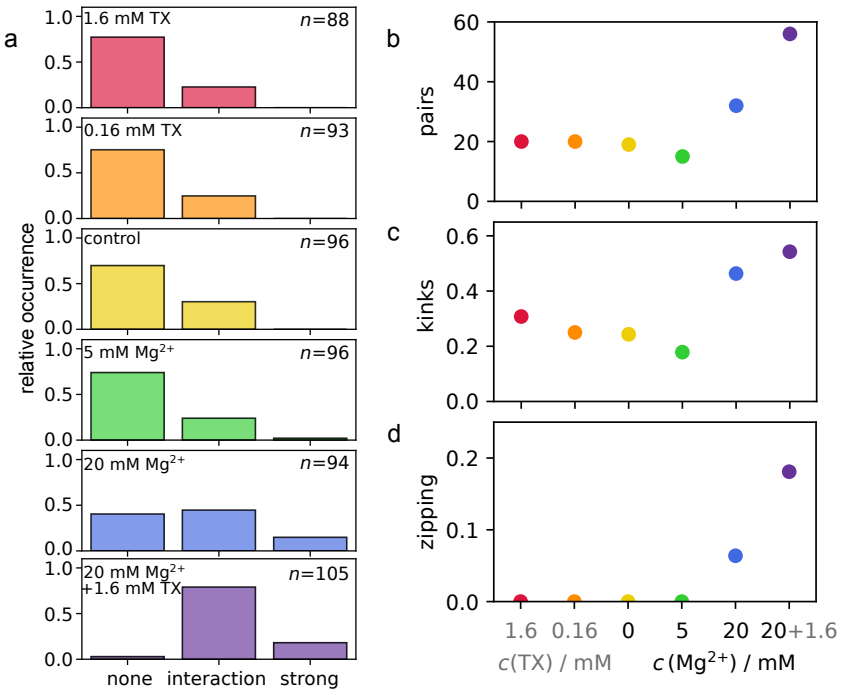

Fig. 6.10: **Interaction types.** a) The relative occurrence of measurements without any interaction, measurements with only interactions that show the characteristic force jump of a breaking interaction, and strong interactions, where the measurement ends before a force jump is observed. The strongest interaction of each measurement defines the category. n denotes the number of measurements. b) The number of filament pairs measured in each condition. Pairs, where filaments are stable and interaction strengths do not exceed the maximal trap forces can be measured multiple times. c) The relative occurrence of kinks in all, *i.e.* normal and strong, interactions. d) Fraction of zipping events in all measurements. Reproduced from Ref. [1].

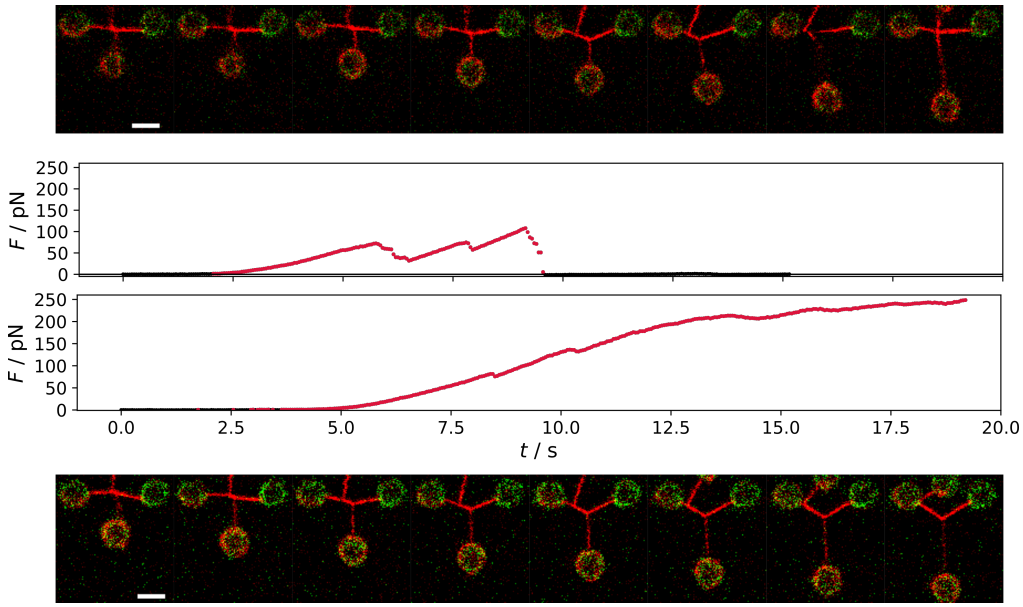

Fig. 6.11: **Zipping during interaction experiments.** Confocal scans and respective force curves for unzipping (top) and zipping (bottom). The confocal videos are available as Supplementary movies of Ref. [1]. The scale bar is 5 µm. Reproduced from Ref. [1].

As we perform the optical trapping experiments in a microfluidic flow cell, we can readily exchange the measuring buffer. A schematic of the experiment is shown in Fig. 4.2. For the interaction measurements, we always assemble filaments in standard assembly buffer and then move both filaments into measuring buffer, where we bring the filaments in contact and record a sliding assay. This allows us to measure the interactions in extreme buffer conditions, such as 20 mM $MgCl_2$, where filament networks collapse [30, 31], or high detergent concentrations $c(\mathrm{TX}) = 1.6$ mM.

The distribution of forces F_i shown in Fig. 6.12a at both TX concentrations (red, 1.6 mM; orange, 0.16 mM) are similar to the control condition (yellow). We calculate the force-independent binding rate $r_{e,b}$ as the ratio of the number of interactions that start at zero force and exceed 1 pN and the experiment time during which we observe no interaction; see methods for a detailed description. Since TX, compared to the control condition, has no effect on two parameters that largely determine network stiffness, the strength of the interactions and $r_{e,b}$ (Fig. 6.12b), we conclude that the relative softness of vimentin networks in the presence of TX is predominantly caused by impaired filament elongation. It is, however, remarkable that the filaments do interact with nonnegligible forces of up to 57 pN (1.6 mM TX), 85 pN (0.16 mM TX), and 112 pN (control). Contrary to observations for keratin networks [25, 27], decreasing the hydrophobic interactions does not affect the attraction between single vimentin filaments. Therefore, even without divalent ions present, the filaments interact with physiologically relevant forces [44–46].

By contrast, the interaction strength clearly increases for increasing $c(MgCl_2)$ (green and blue in Fig. 6.12a). This observation is in agreement with the stiffening of vimentin networks in the presence of 5 mM $MgCl_2$ at sufficiently long network-formation times as shown in Fig. 6.1b. The interactions can reach several hundred pN, as shown in Figs. 6.9e and 6.12a and Fig. 6.10a, and are oftentimes even stronger than the optical trap. While interactions are stronger at low $c(MgCl_2) = 5$ mM than for the control condition (Fig. 6.12a), the force-independent binding rate $r_{e,b}$ is not increased (Fig. 6.12b), indicating that interactions occur with the same probability. By contrast, at high $c(MgCl_2)$, interactions become more likely (see also Fig. 6.10a). The increase of F_i for both $c(MgCl_2)$ measured here and the increase of $r_{e,b}$ solely at high $c(MgCl_2)$ explains why vimentin networks form "scaffold"-like structures at $c(MgCl_2) < 10$ mM and collapse at high $c(MgCl_2)$ [30, 31]. We therefore hypothesize that it is a significant increase of the binding rate that causes the collapse of the networks, and not the increased binding strength. This hypothesis is further supported, as we only observe zipping in the presence of 20 mM $MgCl_2$ (Fig. 6.10d).

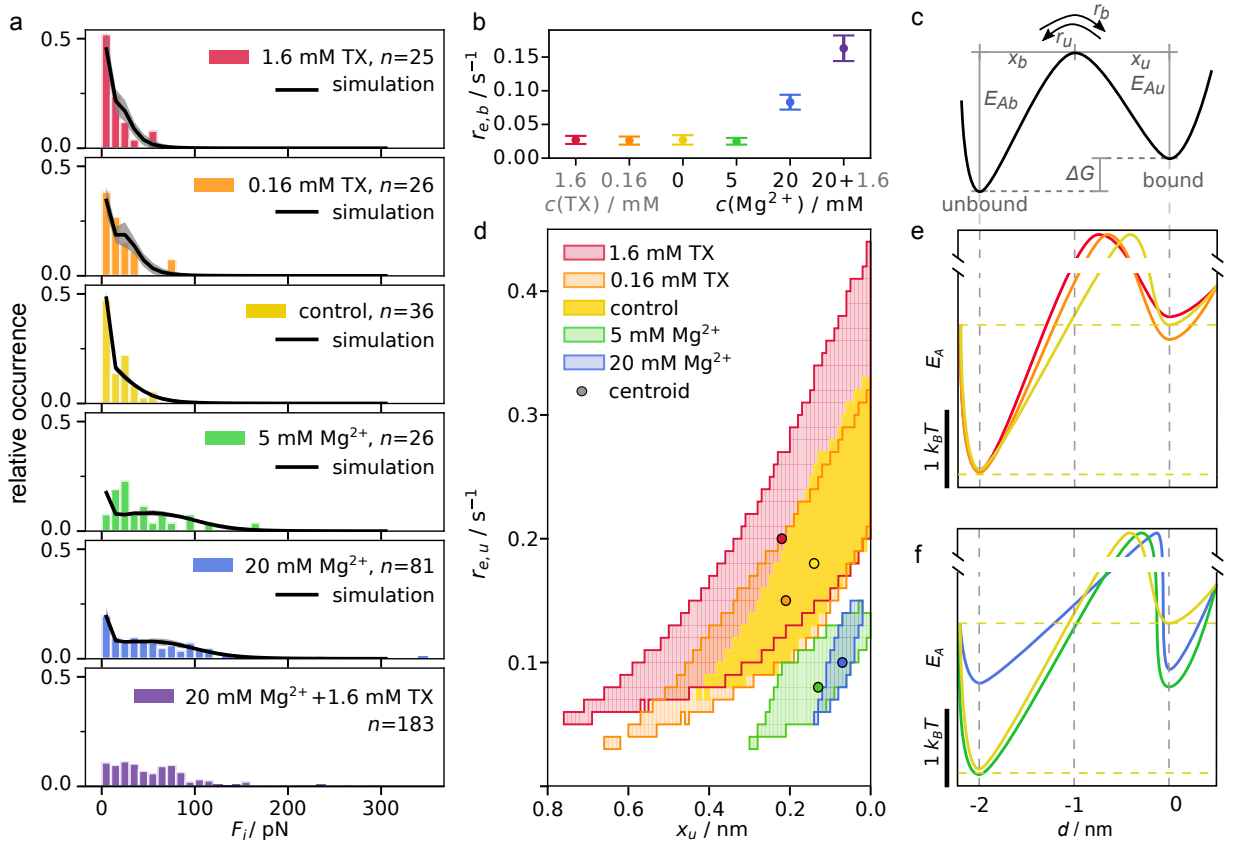

Fig. 6.12: **Results of the interaction experiments and simulation.** a) Histograms of the rupture forces from experiments (colored bars) and mean curve of the simulation results (black) with standard deviation (shaded area). With decreasing TX concentrations (red, orange, and yellow), higher forces are reached. The addition of Mg^{2+} (green, blue, and purple) causes a broadening of the force distribution and a shift toward higher forces. b) Force-independent binding rate $r_{e,b}$. The binding rate is constant, unless Mg^{2+} is present at a concentration of 20 mM. The mean and standard deviation are determined from bootstrap resampling of all single measurements. c) Schematic of the two-state model used for the simulations. d) Parameter pairs of x_u and the force-independent unbinding rate $r_{e,u}$, extracted from the simulation, that satisfy the 5% significance level in the Kolmogorov–Smirnov test. The centroid of each parameter space is marked. e) and f) Energy landscapes corresponding to the centroid of the parameter space. The relative E_A values are shown. The ordinate axis is interrupted to indicate the unknown absolute height of the transition state. Reproduced from Ref. [1].

The strongest increase of binding rate, interaction strength, and thereby also occurrence of zipping events is caused by the addition of high concentrations of $MgCl_2$ and TX in combination (purple in Fig. 6.12a,b and Fig. 6.10). This "amplifying" effect of TX on $MgCl_2$ is remarkable, as TX alone only weakly affects the interaction. It can possibly be explained by a swelling of the negatively charged and intrinsically disordered tail domains of the vimentin monomers, which decorate the filament surface, thus making them more accessible for interactions mediated by $MgCl_2$. Because of this drastic change, we refrain from fitting the interactions in this condition with our simplified model.

6.2.8 Interactions are independent of binding-site encounter rate

We compare the interaction forces and force-independent binding rates in the presence of $MgCl_2$ shown in Fig.6.12 to the results from measurements performed at a lower pulling speed, *i.e.*, slower movement of the OTs. Neither the interaction force distributions (Fig. 6.13a) nor the binding rate (Fig. 6.13b) are affected by the pulling speed at either of the two $MgCl_2$ concentrations. This independence of the encounter rate of possible binding sites indicates that interactions can form seemingly continuously along the filaments and are not limited to sparse binding sites. Assuming that interactions are mediated by the tail domains of vimentin monomers, we expect this continuous binding between two filaments at the pulling rates we use here, since tails protrude from vimentin filaments approximately every 40 nm [47]. These discrete interaction sites might be resolved by reducing the pulling speed so that the force-independent binding rate is higher than the time it takes the interaction site between the filaments to travel the distance between tail domains. However this can be only achieved by pulling speeds below 5 nm/s which is experimentally not feasible. Additionally, interacting, disordered tail regions are not point-like and likely extensible, thereby further reducing the space to the next tail region which leads to an even more continuous encounter of potential binding sites.

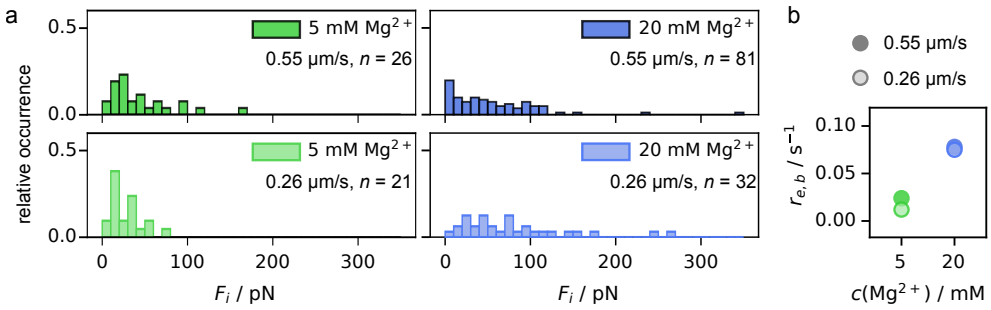

Fig. 6.13: **Results of interaction measurements at two encounter rates.** a) The distributions of the interaction forces are not influenced by the pulling speed at neither Mg^{2+} concentration. n denotes the number of interactions events. b) The force-independent binding rate does not show a clear trend between the pulling speeds.

6.2.9 A two-state model accurately describes network mechanics

Details of the model are described in B.3.

From the interaction experiments, we extract the force-independent binding rate $r_{e,b}$ (Fig. 6.12b), and the distribution of interaction forces (Fig. 6.12a). For a quantitative comparison of the bonds formed in each condition, we model the interaction as a single bond. The filaments undergo force-dependent, stochastic transitions between the bound (b) and unbound (u) state that are described by Bell-Evans kinetics [48]. The binding (r_b; see methods and Eq. (B.9)) and unbinding rates (r_u; Eq. (B.10)) consist of a force-independent term ($r_{e,b}$ and $r_{e,u}$, Eq. (B.11), Eq. (B.12)) that depends on the respective activation energy, E_{Ab} or E_{Au}, and the thermal energy k_BT, and a force-dependent term that depends on k_BT, the applied force, and the distance of the respective state to the transition

state, x_b or x_u (Fig. 6.12c) [49]. The sum $x_c = x_b + x_u$ is constant due to detailed balance [50]. We calculate the distribution of F_i for a constant x_c, the $r_{e,b}$ derived from the experiment (Fig. 6.12b), and for pairs of x_u and $r_{e,u}$, by simulating 1,000 $F(t)$ curves. Equivalent results are achieved by numerical solutions, as discussed in detail in Ref. [49]. Comparison of the experimental distribution and each simulated distribution based on the Kolmogorov-Smirnov test [51] with a 5% acceptance threshold, provides valid x_u and $r_{e,u}$ pairs. The means and standard deviations of the resulting distributions are shown in Fig. 6.12a. All parameter pairs for which the two-state model describes the experiment well, are plotted as pixels in Fig. 6.12d. The parameter spaces derived for the control and TX conditions overlap. The representative energy landscapes, calculated for the centroid of each respective parameter space (circles in Fig. 6.12d) [$r_{e,u}$(control)=0.18 s^{-1}, $r_{e,u}$(0.16 mM TX)=0.15 s^{-1}, $r_{e,u}$(1.6 mM TX)=0.20 s^{-1}], shown in Fig. 6.12e, show no distinct differences. In the presence of $MgCl_2$, $r_{e,u}$ decreases compared to the control [$r_{e,u}$(5 mM $MgCl_2$)=0.08 s^{-1}, $r_{e,u}$(20 mM $MgCl_2$)=0.10 s^{-1}], which becomes apparent in a larger $E_{A,u}$ in Fig. 6.12f. These results are similar to values determined from rheometry on actin networks (0.43 $\pm$0.06 s^{-1} [52]) but significantly larger than reported for vimentin networks ($>$ 0.001 s^{-1} [9]) which is likely caused by surface effects in the macrorheology experiments.
The distance of the transition state to the bound state, x_u, enters r_u (Eq. (B.10)) in the factor that describes the force-dependent unbinding. Therefore, the decrease of both, x_u and $r_{e,u}$ in the presence of $MgCl_2$, leads to a mostly force-independent opening of the bond and thereby to high interaction forces. The presence of TX has the opposite effect: The parameter space reaches larger values of x_u, indicating a more force-sensitive bond between the filaments. The broader distribution of the parameters represented by the shaded areas in Fig. 6.12d, for the control condition and in the presence of TX are mostly due to the lower number of interactions.
These results support the assumptions we made during the analysis of the MPT experiments: As the filaments interact in all conditions, the resulting networks are not purely entangled, but are connected by transient cross-links. However, in the control condition and in the presence of TX, the binding rate between filaments is low, and interactions are weak; thus, entanglements govern the network properties. In the presence of $MgCl_2$, however, the unbinding rate is low, leading to stronger interactions, which, in turn, cause a more cross-linked network. As a low $c(MgCl_2)$ mostly affects the unbinding rate and not x_u, $E_{A,u}$ can be increased without necessarily decreasing $E_{A,b}$.

6.3 CONCLUSIONS

By combining experimental and modeling approaches, we are able to quantify three important contributions to biopolymer network properties and their temporal evolution, *i.e.*, filament-elongation kinetics, single-filament mechanics and filament–filament interactions. We further determine which kinds of interactions – *i.e.*, hydrophobic or Mg^{2+}-mediated, electrostatic – are relevant for different processes involved in network formation and mechanics. We identify altered individual interactions between filaments as the cause of the network

stiffening, where Mg^{2+}-mediated, electrostatic effects play a key role and, consequently, promote bundling. An increased interaction strength, caused by a less force-dependent unbinding, causes the stiffening of the networks that was reported in literature [7, 9–11]. For neurofilaments, another type of IF, a similar Mg^{2+}-mediated stiffening, has been reported [7]. Based on these findings and the fact that also other cytoskeletal filament networks such as F-actin – for example, in Ref. [33] – show a stiffening behavior in the presence of divalent ions, we expect a similar response from other IFs.

We find that hydrophobic interactions only play a minor role for filament interactions but are, in the case of vimentin IFs, important during filament elongation. The head domain of IFs has been shown to be crucial for the assembly of filaments [16, 53–55] and we hypothesize that decreasing the hydrophobic interactions slows down the assembly. However, the effect might not be as pronounced for other IF types that generally assemble faster. These results show that vimentin networks, even in standard buffer conditions without divalent ions, are not purely entangled, but are connected by transient cross-links, and the kinetics and strength of these transient cross-links strongly depend on divalent ions/electrostatic interactions [9, 11]. In future work, it would now be interesting to apply our approach to filaments without the negatively charged tail domain and quantify the influence of the tail domain, as the deletion of the tail has been reported to reduce the stiffening effect of multivalent ions on vimentin networks [7, 9].

With further knowledge of the architecture of the network – in particular, the number of potential interaction partners for each filament – the binding probability in the network may be determined in future studies. Our quantitative approach allows us to disentangle the intricate viscoelastic properties of IFs from their environment in cells – for example, by contributions from other filament types, crowding, or the plasma membrane. Our results can, furthermore, be applied to the study of biopolymer networks, their rheology, and polymerization kinetics, as well as protein-based materials science and synthetic cell research.

6.4 OUTLOOK

6.4.1 Entropic and elastic stretching of single vimentin filaments

Most interactions we observe between two single filaments occur in the force regime $F < 100\,\mathrm{pN}$. So far, we have analyzed the linear force-strain relation during single filament stretching at forces below the plateau regime. However, at very low forces, entropic stretching of the filament becomes relevant which is evident in the non-linear increase at low forces. A typical example for a force-length curve is shown in Fig. 6.14a. By calculating the strain with respect to the "initial length" of the filament determined from the filament length at 5 pN, we have so far mostly excluded this entropic-stretching regime from our analysis as we have focused on the stretching response at higher forces. However, since many interactions occur in the entropic or early linear regime, we now focus on this low force regime $F < 80\,\mathrm{pN}$ of the stretching curves. As described before, entropic stretching, here approximated by the WLC model, contributes to the stretching response of IFs [5]. At low applied stretching forces, the filaments exhibit thermal fluctuations. With increasing applied forces, the degrees of freedom are reduced, and the force necessary to further straighten the filament increases. The entropic contribution therefore leads to a super-exponential force increase that approaches infinity, the closer a filament is stretched to its contour length L_C.
The WLC model does not account for extensibility of the stretched chain. However, as shown in chapters 5 and 6.2.6, IFs are extensible with a linear force-strain response before the plateau regime is reached. We therefore employ a model that describes the filament as an entropic and an elastic spring connected in series (Fig. 6.14), similar to the "molecular model" described in chapter B.3.2.
In our model, we elongate the filaments in small, constant steps of $\Delta L_{OT,i}$ which corresponds to the movement of the OT. Whereas the length of the steps is constant

$$\Delta L_{OT,i} = \Delta L_{el,i} + \Delta L_{en,i}\ , \tag{6.1}$$

the elastic $\Delta L_{el,i}$ and entropic $\Delta L_{en,i}$ contributions change with increasing total elongation of the filament. After each step, the contribution of the entropic and elastic components to the elongation is determined. After N steps, the force acting on the entropic spring is given by the sum of all incremental force increases $F_{en} = \sum_{i=1}^{N} \Delta F_{en,i}$, and the elongation of the entropic spring consequently by the sum over all elongation increments $\Delta L_{en} = \sum_{i=1}^{N} \Delta L_{en,i}$. We do not directly calculate the force but use the description of the worm-like chain from Ref. [56] to approximate the spring constant of the entropic spring after each step by the derivative

$$k_{en,N}(\Delta L_{en}) = \frac{dF_{en}}{d\Delta L_{en}} = \frac{k_B T}{L_P}\left(\frac{1}{L_C} - \frac{L_C^2}{2(L_0 + \Delta L_{en} - L_C)^3}\right) \tag{6.2}$$

with the persistence length L_P, the initial length of the filament L_0, and the contour length L_C. As the spring constant of the entropic spring $k_{en,N}(\Delta L_{en})$ continuously increases, $k_{en,N}(\Delta L_{en})$ eventually exceeds the constant elastic spring

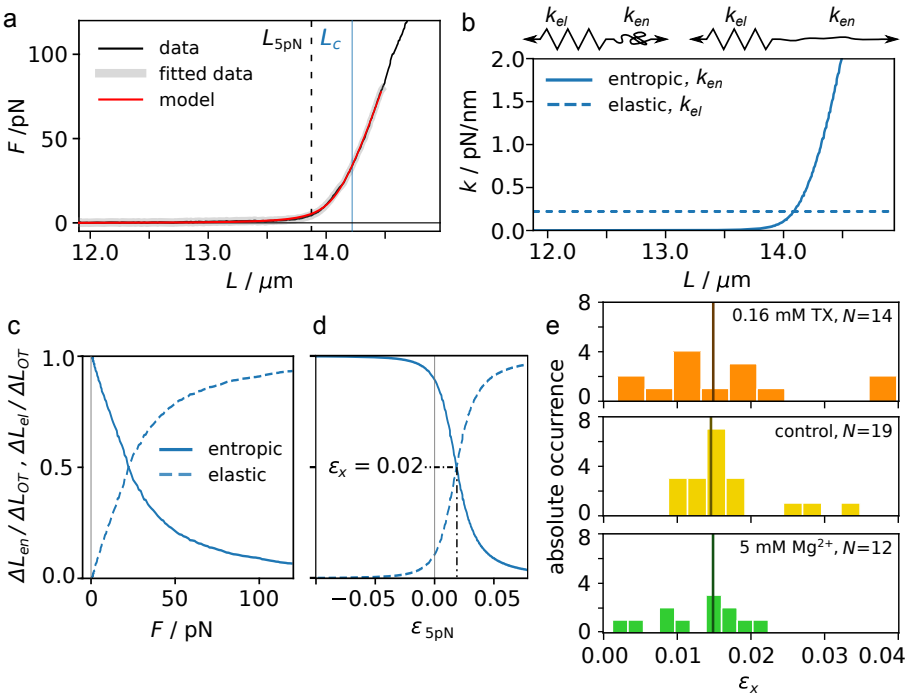

Fig. 6.14: **Low-force regime during single-filament stretching.** a) Typical force-length curve of a filament (black), modeled by an elastic and an entropic spring in series (red). For this fit, the parameters are $k_{el} = 0.22\,\text{pN/nm}$, $L_P = 0.28\,\mu\text{m}$. The resulting contour length L_C is indicated in blue. The length at 5 pN is indicated by the dashed line. b) The entropic spring constant k_{en} increases with increasing length of the filament whereas the elastic spring constant k_{el} remains unchanged. c) At low forces, the entropic spring extends more than the elastic spring and the entropic spring dictates the stretching response. d) Above the crossover strain ε_x, the elastic stretching dominates over the entropic stretching. The strain ε_{5pN} is calculated with the filament length at 5 pN as reference. e) The distribution of ε_x determined for the stretching data shown in Fig. 6.8. The median of ε_x (dark line) is similar across the three buffer conditions.

constant k_{el} (Fig. 6.14b), and the majority of the force is used to elongate the elastic spring (Fig. 6.14c). At strains larger than the cross-over strain ε_x, the elastic spring dominates the stretching response of the complete filament (Fig. 6.14d). In the limit of high extension of the entropic spring, $\lim_{L_0+\Delta L_{en}\to L_C}$, the spring constant of the entropic spring spring approaches infinity. Based on the momentary entropic spring constant $k_{en,N}$ and the constant elastic spring constant k_{el}, we calculate the corresponding force increment with the expression

$$\Delta F_i = \Delta L_{OT,i}\left(\frac{1}{k_{el}} + \frac{1}{k_{en,i}(\Delta L_{en})}\right)^{-1}. \tag{6.3}$$

The total force after N steps is determined by $\sum_{i=0}^{N}\Delta F_i$. We fit this numerical model to the low force regime of single-filament force-length curves, as shown for a typical curve in Fig. 6.14a. The model (red) describes the low-force regime (black) remarkably well. From the model, we can extract the contribution of the entropic and elastic spring at each force (Fig. 6.14c) and for each strain (Fig. 6.14d). The strain shown here is calculated with respect to the length at 5 pN as in the previous results in chapters 5 and 6.2.6 and Refs. [5, 39, 41, 57]. We find the crossover strain ε_x, where the elastic contribution starts to

exceed the entropic contribution, to be nearly identical for different buffer conditions (Fig. 6.14e). From these results, we determine that at strains $\varepsilon > 0.02$, for most filaments, the elastic contribution to elongation dominates the entropic contribution. As this crossover strain is relatively small, the strain used for the analysis of the filament stretching experiments is a good approximation. The mean persistence length determined from the fit of the model to the data $0.34 \pm 0.17\,\mu m$ is clearly lower than determined from freely fluctuating vimentin filaments, $2.0 \pm 0.5\,\mu m$ [58], even though both calculations are based on bending by thermal fluctuations. This discrepancy might be due to the constraints imposed by the beads attached at the ends of the filament or indicate that the model is too simple to quantitatively reflect the mechanism of the filament mechanics. Moreover, the amplitude of the bending observed by fluorescence microscopy are on the scale of $1\,\mu m$ [58], while the confinement though the OTs only allows fluctuations on the nm-scale. However, our model represents the experimental data curves remarkably well and gives an approximation of the entropic and elastic contributions to the stretching response.

6.4.2 Single interactions of pre-strained filaments

We study how the entropic and elastic stretching influence the interactions between filaments by repeating the single-interaction measurements with pre-strained filaments. Due to experimental limitations, the filaments are typically not at the same strain. At least one of the filaments is pre-strained between ε=0.03-0.14. In Fig. 6.15, preliminary results of the interaction measurements between pre-strained filaments are shown. For the buffer conditions with TX and in the control condition, we do not observe a change of the interaction force distributions (Fig. 6.15a). In the presence of $MgCl_2$, however, interactions between pre-strained filaments rupture at lower forces than between filaments without pre-strain. We here note that the number of measurements with pre-strained filaments is clearly lower than for filaments without pre-strain and that the observed trend might therefore be influenced by statistical effects. Nonetheless, the interaction forces agree well between the measurements in presence of TX and the control condition, indicating that also for pre-stretched filaments, hydrophobic interactions do not dominate the binding strength. When comparing the force-independent binding rates $r_{e,b}$, we see a clear effect of the pre-straining (Fig. 6.15b). In all buffer conditions, except for 20 mM $MgCl_2$, pre-straining leads to an increase of $r_{e,b}$ compared to measurements without pre-strain. In the presence of 20 mM $MgCl_2$, $r_{e,b}$ is slightly decreased within the margin of the error in comparison to experiments without pre-strain. To draw reliable conclusions, more data have to be acquired, however, these preliminary results indicate that pre-straining increases the binding rate. This increase is probably due to the filaments being in more constant contact as thermal fluctuations are diminished. Two typical force-time interaction curves shown in Fig. 6.15c,d verify that the characteristic entropic stretching regime is lost through pre-straining in Fig. 6.15d.
The reduction of thermal fluctuations might have two effects: On the one hand, the filaments might be in contact for a longer time as they cannot detach by

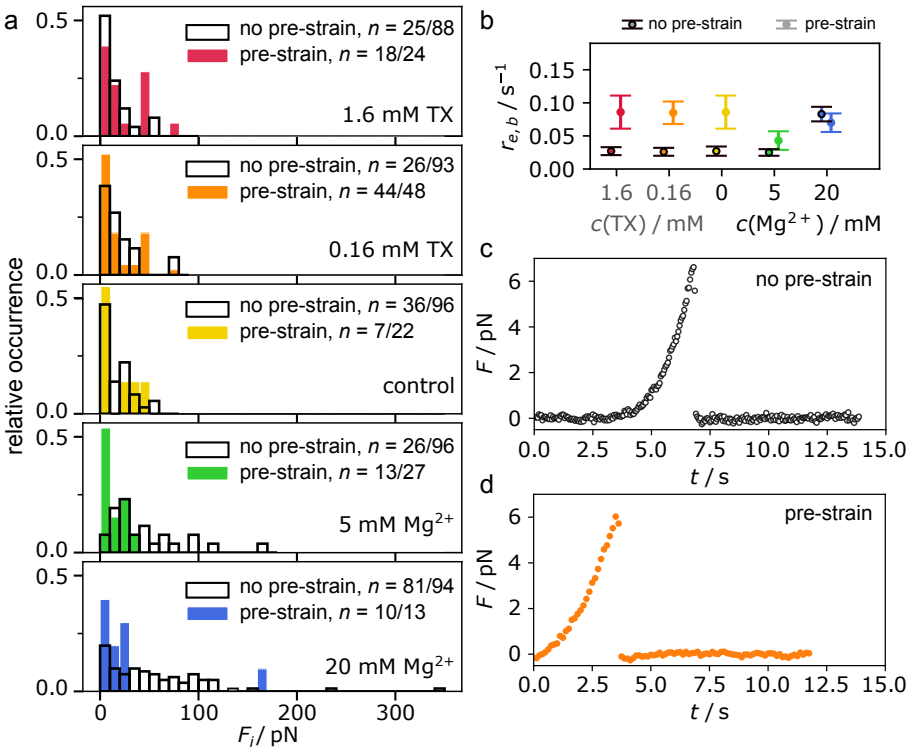

Fig. 6.15: **Interactions of pre-strained filaments.** a) Interaction force histograms of unstrained (black outline) and pre-strained filaments (solid). n denotes the number of interactions / number of measurements. b) Force-independent binding rates. The mean and standard deviation are determined from bootstrap resampling of all single measurements as described in section 4.7.3. c) Typical force-time curve of a pair of unstrained filaments, measured in the presence of 0.16 mM TX. d) Force-time curve of a filament pair, measured in the presence of 0.16 mM TX, with one filaments pre-strained to $\varepsilon = 0.03$ and the other filament to $\varepsilon = 0.02$.

diffusive motion. On the other hand, for unstrained filaments, the fluctuations might allow the filaments to be in contact at more than one interaction site, effectively forming very short bundled regions, similar to the zipping discussed above. If the bundled region is smaller than we can resolve with the confocal microscope, we might not be able to detect such multiple interaction sites in the contact region. Such multiple interaction sites might then decrease the unbinding probability, effectively increasing the interaction forces. This second effect might explain the decrease of interaction forces we observe in the presence of $MgCl_2$ when comparing pre-strained to unstrained filaments. This hypothesis can be corroborated by reducing the speed of the trap movement during the interaction measurement. In the case that the unbinding rate is changed by the pre-strain whereas the force-dependence of the interaction is unaltered, these changes should affect the resulting interaction force histograms.

All interactions described here are between filaments stretched to strains within the linear regime of single filament stretching curves. As the unfolding of alpha helices mostly occurs in the plateau regime, it will be interesting to study how this drastic structural change affects the interactions. By unfolding, other residues become exposed and, in contrast to all results presented her, hydrophobic interactions might become relevant.

The transient interactions between IFs we observe in the interaction experiments lead to fluidization of networks at high strains and on longer time scales [9]. Comparison of interactions in different pre-strain regimes might shed light on the role of the structure of the filaments for the interactions in the network and thereby the emerging network response. As IFs become especially mechanically relevant during high cellular deformations [59], interactions at these high pre-strain interactions might play an important role for cell integrity.

CONFLICTS OF INTEREST

The authors declare no competing interest.

DATA AVAILABILITY

Simulation code for filament–filament interactions, length distributions from fluorescence images, and original data on optical trap interaction experiments have been deposited in Göttingen Research Online (`https://data.goettingen-research-online.de/`; `https://doi.org/10.25625/OINLIY`; `https://doi.org/10.25625/AFERDB`; `https://doi.org/10.25625/4ISIQ9`).

ACKNOWLEDGEMENTS

We thank J. Kraxner and J. C. Thiele for helpful discussions; A. Blob for help with experiments; and S. Bauch for technical support. This project was funded by the European Research Council under the European Union's Horizon 2020 research and innovation program (Consolidator Grant Agreement 724932). This research was conducted within the Max Planck School Matter to Life supported by the German Federal Ministry of Education and Research in collaboration with the Max Planck Society. The work further received support via an Excellence Fellowship of the International Max Planck Research School for Physics of Biological and Complex Systems

REFERENCES

[1] A. V. Schepers et al. "Multiscale mechanics and temporal evolution of vimentin intermediate filament networks." *Proc. Natl. Acad. Sci.* 118 (2021), e2102026118. DOI: 10.1073/pnas.2102026118.

[2] D. A. Fletcher and R. D. Mullins. "Cell Mechanics and the Cytoskeleton." *Nature* 463 (2010), pp. 485–92. DOI: 10.1038/nature08908.

[3] P. A. Janmey et al. "Viscoelastic Properties of Vimentin Compared with Other Filamentous Biopolymer Networks." *J. Cell Biol.* 113 (1991), pp. 155–160. DOI: 10.1083/jcb.113.1.155.

[4] Z. Qin, L. Kreplak, and M. J. Buehler. "Hierarchical Structure Controls Nanomechanical Properties of Vimentin Intermediate Filaments." *PLoS ONE* 4 (2009), e7249. DOI: 10.1371/journal.pone.0007294.

[5] J. Block et al. "Nonlinear Loading-Rate-Dependent Force Response of Individual Vimentin Intermediate Filaments to Applied Strain." *Phys. Rev. Lett.* 118 (2017), p. 048101. DOI: 10.1103/PhysRevLett.118.048101.

[6] M. Schopferer et al. "Desmin and Vimentin Intermediate Filament Networks: Their Viscoelastic Properties Investigated by Mechanical Rheometry." *J. Mol. Biol.* 388 (2009), pp. 133–143. DOI: 10.1016/j.jmb.2009.03.005.

[7] Y.-C. Lin et al. "Divalent Cations Crosslink Vimentin Intermediate Filament Tail Domains to Regulate Network Mechanics." *J. Mol. Biol.* 399 (2010), pp. 637–644. DOI: 10.1016/j.jmb.2010.04.054.

[8] Y.-C. Lin et al. "Origins of elasticity in intermediate filament networks." *Phys. Rev. Lett.* 104 (2010), p. 058101. DOI: 10.1103/PhysRevLett.104.058101.

[9] A. Aufderhorst-Roberts and G. H. Koenderink. "Stiffening and Inelastic Fluidization in Vimentin Intermediate Filament Networks." *Soft Matter* 15 (2019), pp. 7127–7136. DOI: 10.1039/C9SM00590K.

[10] S. Köster et al. "Nanomechanics of vimentin intermediate filament networks." *Soft Matter* 6 (2010), p. 1910. DOI: 10.1039/c000113a.

[11] H. Wu et al. "Effect of divalent cations on the structure and mechanics of vimentin intermediate filaments." *Biophys. J.* 119 (2020), pp. 55–64. DOI: 10.1016/j.bpj.2020.05.016.

[12] N. Mücke et al. "Assessing the Flexibility of Intermediate Filaments by Atomic Force Microscopy." *J. Mol. Biol.* 335 (2004), pp. 1241–1250. DOI: 10.1016/j.jmb.2003.11.038.

[13] F. Gittes and F. C. MacKintosh. "Dynamic Shear Modulus of a Semiflexible Polymer Network." *Phys. Rev. E* 58 (1998). DOI: 10.1103/PhysRevE.58.R1241.

[14] J. Block et al. "Physical Properties of Cytoplasmic Intermediate Filaments." *Biochim. Biophys. Acta, Mol. Cell Res.* 1853 (2015), pp. 3053–3064. DOI: 10.1016/j.bbamcr.2015.05.009.

[15] I. Hofmann, H. Herrmann, and W. W. Franke. "Assembly and structure of calcium-induced thick vimentin filaments." *Eur. J. Cell Biol.* 56 (1991), pp. 328–341.

[16] H. Herrmann et al. "Structure and Assembly Properties of the Intermediate Filament Protein Vimentin: The Role of its Head, Rod and Tail Domains." *J. Mol. Biol.* 264 (1996), pp. 933–953. DOI: 10.1006/jmbi.1996.0688.

[17] M. Kooijman et al. "Transient Electric Birefringence Study of Intermediate Filament Formation from Vimentin and Glial Fibrillary Acidic Protein." *J. Biol. Chem.* 272 (1997), pp. 22548–22555. DOI: 10.1074/jbc.272.36.22548.

[18] C. G. Lopez et al. "Effect of ionic strength on the structure and elongational kinetics of vimentin filaments." *Soft Matter* 14 (2018), pp. 8445–8454. DOI: 10.1039/C8SM01007B.

[19] M. E. Brennich et al. "Impact of ion valency on the assembly of vimentin studied by quantitative small angle X-ray scattering." *Soft Matter* 10 (2014), pp. 2059–2068. DOI: 10.1039/C3SM52532E.

[20] A. Premchandar et al. "Structural dynamics of the vimentin coiled-coil contact regions involved in filament assembly as revealed by hydrogen-deuterium exchange." *J. Biol. Chem.* 291 (2016), pp. 24931–24950. DOI: 10.1074/jbc.M116.748145.

[21] M. E. Brennich et al. "Mutation-induced alterations of intra-filament subunit organization in vimentin filaments revealed by SAXS." *Soft Matter* 15 (2019), pp. 1999–2008. DOI: 10.1039/c8sm02281j.

[22] A. Mónico et al. "Zinc Differentially Modulates the Assembly of Soluble and Polymerized Vimentin." *Int. J. Mol. Sci.* 21 (2020), pp. 1–20. DOI: 10.3390/ijms21072426.

[23] M. Denz et al. "Ion type and valency differentially drive vimentin tetramers into intermediate filaments or higher order assemblies." *Soft Matter* 17 (2021), pp. 870–878. DOI: 10.1039/d0sm01659d.

[24] J. Kayser et al. "Assembly Kinetics Determine the Structure of Keratin Networks." *Soft Matter* 8 (2012), p. 8873. DOI: 10.1039/C2SM26032H.

[25] P. Pawelzyk et al. "Attractive Interactions Among Intermediate Filaments Determine Network Mechanics In Vitro." *PLoS ONE* 9 (2014), e93194. DOI: 10.1371/journal.pone.0093194.

[26] C. Y. J. Hémonnot et al. "Assembly of Simple Epithelial Keratin Filaments: Deciphering the Ion Dependence in Filament Organization." *Biomacromolecules* 16 (2015), pp. 3313–3321. DOI: 10.1021/acs.biomac.5b00965.

[27] S. Yamada, D. Wirtz, and P. A. Coulombe. "The Mechanical Properties of Simple Epithelial Keratins 8 and 18: Discriminating Between Interfacial and Bulk Elasticities." *J. Struct. Biol.* 143 (2003), pp. 45–55. DOI: 10.1016/S1047-8477(03)00101-1.

[28] A. A. Chernyatina, D. Guzenko, and S. V. Strelkov. "Intermediate Filament Structure: The Bottom-Up Approach." *Curr. Opin. Cell Biol.* 32 (2015), pp. 65–72. DOI: 10.1016/j.ceb.2014.12.007.

[29] H. Herrmann and U. Aebi. "Intermediate Filaments : Structure and Assembly." *Cold Spring Harbor Perspect. Biol.* 8 (2016), a018242. DOI: 10.1101/cshperspect.a018242.

[30] C. Dammann, B. Nöding, and S. Köster. "Vimentin networks at tunable ion-concentration in microfluidic drops." *Biomicrofluidics* 6 (2012), p. 022009. DOI: 10.1063/1.4705103.

[31] C. Dammann and S. Köster. "Dynamics of Counterion-Induced Attraction between Vimentin Filaments Followed in Microfluidic Drops." *Lab Chip* 14 (2014), pp. 2681–2687. DOI: 10.1039/c3lc51418h.

[32] J. C. Crocker et al. "Two-Point Microrheology of Inhomogeneous Soft Materials." *Phys. Rev. Lett.* 85 (2000), pp. 888–891. DOI: 10.1103/PhysRevLett.85.888.

[33] B. Gurmessa et al. "Counterion Crossbridges Enable Robust Multiscale Elasticity in Actin Networks." *Phys. Rev. Res.* 1 (2019), p. 013016. DOI: 10.1103/PhysRevResearch.1.013016.

[34] C. Heussinger, F. Schüller, and E. Frey. "Statics and Dynamics of the Wormlike Bundle Model." *Phys. Rev. E* 81 (2010), p. 021904. DOI: 10.1103/PhysRevE.81.021904.

[35] C. Heussinger, M. Bathe, and E. Frey. "Statistical mechanics of semiflexible bundles of wormlike polymer chains." *Phys. Rev. Lett.* 99 (2007), p. 048101. DOI: 10.1103/PhysRevLett.99.048101.

[36] N. Mücke et al. "Molecular and biophysical characterization of assembly-starter units of human vimentin." *J. Mol. Biol.* 340 (2004), pp. 97–114. DOI: 10.1016/j.jmb.2004.04.039.

[37] C. G. Lopez et al. "Lateral association and elongation of vimentin intermediate filament proteins: A time-resolved light-scattering study." *Proc. Natl. Acad. Sci.* 113 (2016), pp. 11152–11157. DOI: 10.1073/pnas.1606372113.

[38] N. Mücke et al. "Assembly Kinetics of Vimentin Tetramers to Unit-Length Filaments: A Stopped-Flow Study." *Biophys. J.* 114 (2018), pp. 2408–2418. DOI: 10.1016/j.bpj.2018.04.032.

[39] J. Block et al. "Viscoelastic Properties of Vimentin Originate from Nonequilibrium Conformational Changes." *Sci. Adv.* 4 (2018), eaat1161. DOI: 10.1126/sciadv.aat1161.

[40] J. Forsting et al. "Vimentin Intermediate Filaments Undergo Irreversible Conformational Changes During Cyclic Loading." *Nano Lett.* 19 (2019), pp. 7349–7356. DOI: 10.1021/acs.nanolett.9b02972.

[41] C. Lorenz et al. "Lateral Subunit Coupling Determines Intermediate Filament Mechanics." *Phys. Rev. Lett.* 123 (2019), p. 188102. DOI: 10.1103/PhysRevLett.123.188102.

[42] A. V. Schepers, C. Lorenz, and S. Köster. "Tuning Intermediate Filament Mechanics by Variation of pH and Ion Charges." *Nanoscale* 12 (2020), pp. 15236–15245. DOI: 10.1039/D0NR02778B.

[43] C. Dammann, H. Herrmann, and S. Köster. "Competitive Counterion Binding Regulates the Aggregation Onset of Vimentin Intermediate Filaments." *Isr. J. Chem.* 56 (2016), pp. 614–621. DOI: 10.1002/ijch.201400153.

[44] B. H. Blehm et al. "In Vivo Optical Trapping Indicates Kinesin's Stall Force is Reduced by Dynein During Intracellular Transport." *Proc. Natl. Acad. Sci.* 110 (2013), pp. 3381–3386. DOI: 10.1073/pnas.1219961110.

[45] M. Vleugel, M. Kok, and M. Dogterom. "Understanding Force-generating Microtubule Systems Through In Vitro Reconstitution." *Cell Adh. Migr.* 10 (2016), pp. 475–494. DOI: 10.1080/19336918.2016.1241923.

[46] M. S. Woody et al. "Single Molecule Mechanics Resolves the Earliest Events in Force Generation by Cardiac Myosin." *eLife* 8 (2019), e49266. DOI: 10.7554/eLife.49266.

[47] P. M. Steinert, L. N. Marekov, and D. A. D. Parry. "Diversity of intermediate filament structure. Evidence that the alignment of coiled-coil molecules in vimentin is different from that in keratin intermediate filaments." *J. Biol. Chem.* 268 (1993), pp. 24916–24925. DOI: 10.1016/S0021-9258(19)74552-9.

[48] G. I. Bell. "Models for the Specific Adhesion of Cells to Cells." *Science* 200 (1978), pp. 618–627. DOI: 10.1126/science.347575.

[49] L. Schaedel et al. "Vimentin intermediate filaments stabilize dynamic microtubules by direct interactions." *Nat. Commun.* 12 (2021), p. 3799. DOI: 10.1038/s41467-021-23523-z.

[50] A. Kolomeisky. *Motor Proteins and Molecular Motors*. CRC press, 2015.

[51] G. W. Corder and Dale I. Foreman. *Nonparametric Statistics: A Step-By-Step Approach*. John Wiley & Sons, 2014.

[52] Y. Mulla et al. "Frustrated Binding of Biopolymer Crosslinkers." *Soft Matter* 15 (2019), pp. 3036–3042. DOI: 10.1039/c8sm02429d.

[53] E. Kaufmann, K. Weber, and N. Geisler. "Intermediate filament forming ability of desmin derivatives lacking either the amino-terminal 67 or the carboxy-terminal 27 residues." *J. Mol. Biol.* 185.4 (1985), pp. 733–742. DOI: 10.1016/0022-2836(85)90058-0.

[54] M. Hatzfeld and M. Burba. "Function of type I and type II keratin head domains: Their role in dimer, tetramer and filament formation." *J. Cell Sci.* 107.7 (1994), pp. 1959–1972. DOI: 10.1242/jcs.107.7.1959.

[55] H. Herrmann, I. Hofmann, and W. W. Franke. "Identification of a nonapeptide motif in the vimentin head domain involved in intermediate filament assembly." *J. Mol. Biol.* 223 (1992), pp. 637–650. DOI: 10.1016/0022-2836(92)90980-X.

[56] J. F. Marko and E. D. Siggia. "Stretching DNA." *Macromolecules* 28 (1995), pp. 8759–8770. DOI: 10.1021/ma00130a008.

[57] J. Kraxner et al. "Post-translational modifications soften vimentin intermediate filaments." *Nanoscale* 13 (2021), pp. 380–387. DOI: 10.1039/d0nr07322a.

[58] B. Nöding and S. Köster. "Intermediate Filaments in Small Configuration Spaces." *Phys. Rev. Lett.* 108 (2012), p. 088101. DOI: 10.1103/PhysRevLett.108.088101.

[59] E. Latorre et al. "Active superelasticity in three-dimensional epithelia of controlled shape." *Nature* 7730 (2018), pp. 6481–6487. DOI: 10.1021/ac8009643.

7 RESPONSE OF ACTIN AND KERATIN STRUCTURES TO ISOTROPIC CELL STRETCHING

In this section, I describe the design of an isotropic cell stretching setup and the development of the characterization on the instrument. The cell stretcher was designed by Peter Luley and built by Peter Luley in collaboration with the machine shop. I present preliminary results of cell-stretching experiments.

7.1 INTRODUCTION

The three main filamentous components of the cytoskeleton, microtubules, filamentous actin and intermediate filaments, all contribute unique mechanical properties to the integrity, resilience and flexibility of cells. It is well established that the filamentous actin and acto-myosin structures are a major determinant of the mechanical properties of cells as well as their ability to generate mechanical forces [1]. Actin forms several distinct structural features in cells. For example, actin stress fibers, contractile acto-myosin bundles which connect to the extracellular matrix *via* focal adhesions, are involved in the generation of forces [1]. Actin filaments further form the actin cortex, a thin network just below the cell membrane which provides stability to the membrane, determines the shape of the cell surface, and strongly contributes to the cell stiffness [1].
Whereas actin is highly conserved along cell types and organisms, different IF proteins are expressed cell-type specifically. It is therefore not surprising that IFs form a plethora of different structures in different cells [2]. In many cells expressing vimentin and keratin IF proteins, a dense IF network is observed close to the nucleus, often described as a "nuclear cage" [3, 4]. Keratin, the IF protein found in epithelial cells, typically forms bundles that connect the nuclear cage to the cell periphery in a radial arrangement [5]. Keratin bundles connect to desomosomes at cell–cell contacts and hemidesmosomes at contacts between cells and the extracellular matrix [5]. Recently, another structural entity formed by keratin filaments was described, where the IFs arrange in a layer beneath the plasma membrane. This subplasmalemmal keratin layer, called keratin cortex in the following, together with the radial bundles, produces a 'rim-and-spoke' IF structure [5]. The keratin cortex has been hypothesized to contribute additional mechanical support to the plasma membrane. This hypothesis has, so far, not been proven on mechanically stressed cells. In contrast to actin fibers and networks, IFs are highly extensible as shown in chapters 5 and 6, and might contribute complementary mechanical properties to the layer structure consisting of plasma membrane, actin cortex, and keratin cortex.
We here study the effect of isotropic cell stretching on the actin and keratin structures in epithelial cells. We design an isotropic stretching device which increases the circumference of the cell more than a uniaxial stretching at the

same nominal strain. We characterized the stretching device and show how the actin an keratin structures in Madin-Darby Canine Kidney II (MDCK II) cells react to isotropic stretching.

7.2 RESULTS AND DISCUSSION

7.2.1 Equibiaxial stretching of PDMS devices

For cell stretching, we design and construct a custom cell stretcher. The cells are plated on a PDMS device that consists of hexagonal side walls with a circular hole that are attached to a thin PDMS membrane. The corners of the hexagon are pulled outwards. A photograph of a stretched device, mounted on an upright microscope, is shown in Fig. 7.1 and a simplified technical drawing of the PDMS device (light blue), mounted in the cell stretcher is shown in Fig.7.2a. The cell stretcher consists of a gear (blue) that, when rotated, causes an iris-like movement of the holding arms (gray). The gear is actuated by a stepper motor that is tangentially attached by a connecting rod (not sketched). The movement direction of the holding arms is indicated by arrows for the corresponding rotation of the gear (arrow in the bottom left). This design leads to rotation as well as stretching of the membrane.

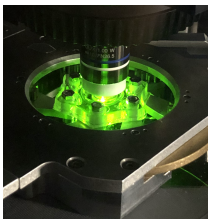

Fig. 7.1: Photograph of the stretched PDMS device during fluorescence imaging of the cells.

The resulting spiral motion is apparent when comparing fluorescence images of beads that are embedded in the membrane at increasing extension. (Fig. 7.2b). The stepper motor is controlled by the software `spec` [6] in intervals of 0.1 arbitrary units. At each strain, z-stacks of full height of the stretched cells are recorded in slices of 0.5 µm distance. Small, 100-nm fluorescent beads that are embedded in the PDMS membrane in a 2D layer serve as fiducial markers to determine the strain of the membrane. As the membrane is typically not perfectly parallel to the imaging plane of the upright microscope, the beads are further used to correct for the tilt of the membrane. The algorithm we developed for the tilt correction is described in detail in chapter 4.15.1.
After correcting for tilt of the membrane, the bead images at each extension are registered with respect to the image at the previous number of stretching units. This registration is performed with the software `elastix` [7, 8]. The registration is most reliable when images are compared to the previous or subsequent image in the stretching sequence. For larger intervals, most registration methods fail here. A comparison of the pixelwise correlation between images registered with various methods is shown in Fig. 7.2c, and the distributions are shown in Fig. 7.2d. As expected, pure translational registration leads to the lowest correlation (blue). From the three registration methods tested, the affine transformation, which includes rotation, shearing (biaxial), stretching (biaxial) and translation (biaxial), and similarity transformation which includes stretching (isotropic), rotation and translation (biaxial), lead to the highest correlation between the images. The B-spline-based transformation accounts for local deformations, it is, however, less robust for the scale of deformations we observe in our experiments. Even though the B-spline analysis can be optimized, the high correlation we achieve by affine and similarity transformations indicates that the deformation is largely homogeneous and that a local analysis is not

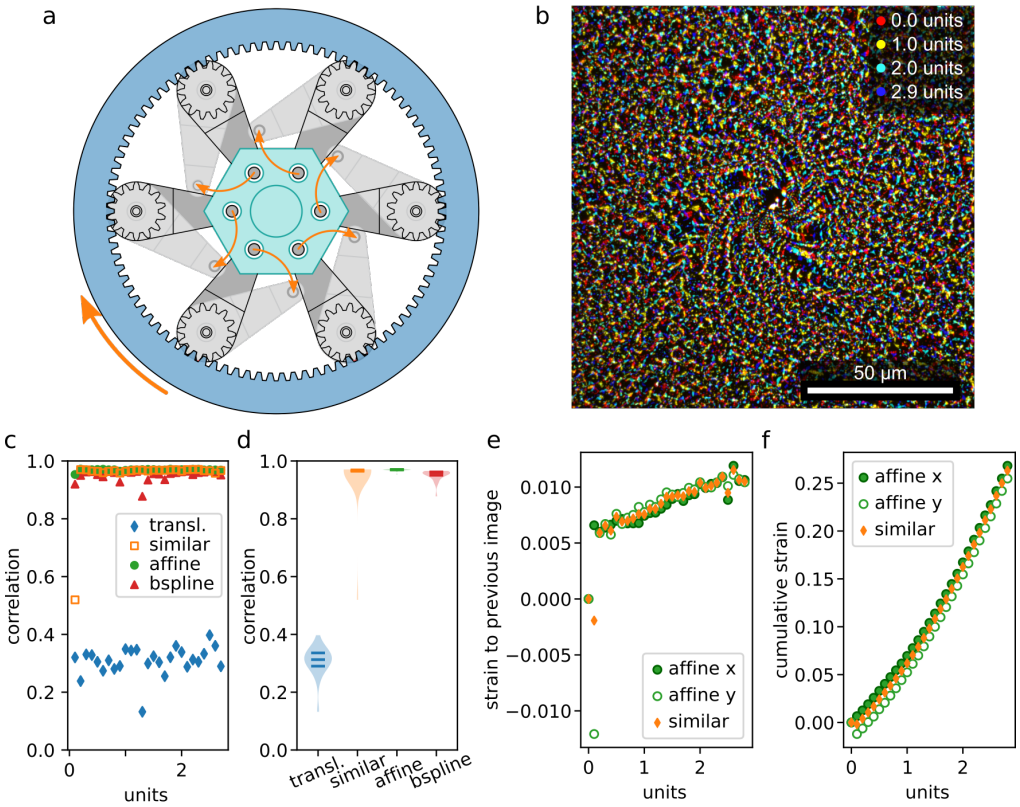

Fig. 7.2: **Cell stretching setup and characterization.** a) Simplified technical drawing of the cell stretcher. By rotation of the outer gear, the holding arms are pivoted and the PDMS device deformed. b) Overlay of typical bead images recorded at increasingly high extension. The images are aligned with a semi-automatic procedure. The rotation and stretching of the membrane is visible. c) Performance of different registration and transformation methods implemented in `elastix`. The correlation between a transformed image and the corresponding, previous image is shown. d) Distribution of the correlation results. e) Strain (ε) values resulting from affine and similarity transformations between each image and the respective previous image and f) corresponding cumulative product of the extension ($\varepsilon + 1$) values. The data shown in c-f is from a single, representative sample.

required. Comparison of the strains extracted from the two transformations in Fig. 7.2e and f shows that the strain is equibiaxial and therefore isotropic in the field of view of the camera of the microscope. Due to the isotropic strain, the substrate is deformed equally at each position, independent of the orientation of, for example, structures in the cells. As the strain determined from similarity and affine transformations agree well, we use the results from the similarity transform as the reference strain of the sample and for the correction of the rotation of the images of the cells. While other approaches to equibiaxial cell stretching have been reported [9–13], most designs are not compatible with AFM measurements as they require space above or around the sample. Even tough AFM measurements are not included in this chapter, it is the aim of this project to combine structural observations with mechanical characterizations with AFM. Our cell stretcher therefore provides reliable stretching with isotropic strains of up to at least 0.25 and compatibility with AFM setups.

7.2.2 The cell area increases during isotropic stretching

After establishing the stretching device, we study the effect of isotropic stretching on the cytoskeleton. We focus on the structural investigations first. To this end, MDCK II cells are transfected with keratin K8-enhanced yellow fluorescent protein (EYFP) and stained with SiR-actin before the stretching measurements. Widefield fluorescence images of the actin structures are shown in Fig. 7.3a. In the images, it is apparent that the cell area increases with the isotropic strain indicated in the figure. We analyze the cell area A_{cell} from the actin images with the segmentation software `CellPose` [14]. The cell area distribution of all correctly segmented cells at representative strains is shown in Fig. 7.3b. The median value is marked with a blue line in each distribution and the ratio of the median value with respect to the median of the initial cell area $A_{cell,0}$ is indicated by orange circles. The cell area increases throughout the experiment up to 1.55-fold. The area increase of the substrate as calculated from the bead images (dashed line in Fig. 7.3b) agrees remarkably well with the increase of the cell size, see also Fig. C1 for a second example. This complete transmission of the stretching indicates that the cells are well adhered to the PDMS membrane and do not detach or reduce their cell size on the time scales of the stretching experiment, where the cells are kept at each strain for approximately 5 min.

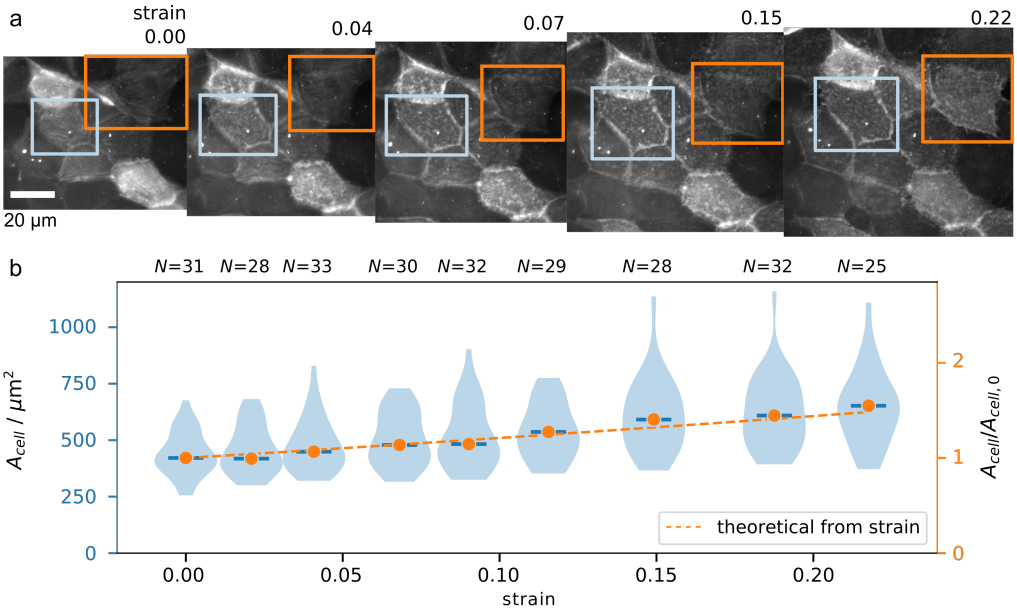

Fig. 7.3: **The cell area increases with the isotropic strain.** a) SiR-actin staining of cells shows how the cell area increases with the isotropic strain. Magnifications of the marked cells are shown in Fig. 7.4. b) The actin images are segmented using `CellPose` to extract the cell area distribution and median (blue line). The ratios of the median cell areas with respect to the median of the initial cell area distribution are indicated by orange circles. The expected area increase, calculated from the isotropic strain of the bead images, is shown by the dashed line.

A stretching-induced increase of the cell proliferation has been observed for MDCK II cells and we expect the cell areas to decrease when the extension is

maintained at strains $\varepsilon > 0$ for longer times than in our experiments due to cells undergoing mitosis [15].
It is well established that MDCK II cells form strong cell–cell junctions through tight junctions, adherens junctions and desmosomes, which all provide connections between cells and from cell–cell contacts to the cytoskeleton [16, 17]. Since the cells are in a confluent layer at the start of the experiment, any reduction of the cell size of single cells leads to an increase of the cell area for other cells, *i.e.*, an increase of the heterogeneity of the cell size, unless cell–cell junctions are released. Such a heterogeneous response of MDCK II cells to stretching has been observed [13]. We do not observe a marked increase of the width of the cell area distribution, however, these results are from a single measurement and more data is necessary to draw any statistically significant conclusions.

7.2.3 Actin stress fibers disassemble at increasing cell extension

Magnified images of single cells, shown in Fig. 7.4, shows stress fibers. During stretching, these stress fibers seem less continuous at low strains than before strain is applied, and are not recognizable at strains above 0.15.
The low staining efficiency limits the number of cells in which any actin structures, including stress fibers, are visible and we refrain from quantification here. Nonetheless, we observe an overall loss of stress fibers in the cells during isotropic stretching. Such a disassembly of stress fibers in response to stretching stimuli has been observed previously as the first step in stress fiber reorientation during uniaxial stretching [18]. The remodeling of stress fibers during cell stretching has been shown to be sensitive to the frequency of cyclic stretching stimuli [19] where repeated stretching at frequencies of 1 Hz prevents the assembly of stress fibers due to fluidization of the actin cytoskeleton. Each extension increment is applied instantly in our measurements and we sustain each strain for approximately 5 min. The short incubation duration is likely not sufficient for the cells to form new stress fibers. For future measurements, it will be interesting to include longer incubation times at each strain to further study a more dynamic response of the cells.
To image the actin structures, we stain the cells with the jasplakinolide-based label SiR-actin. We use the SiR-compound as it allows for a much higher labeling efficiency than, for example, transfection of the MDCK II cells with Lifeact [20]. To determine the cell size and observe the actin structure we require a high labeling efficiency. A new, also jasplakinolide-based, labeling compound has been reported [21] that provides a better labeling for cells with high efflux activity such as MDCK II cells. The higher staining efficiency would benefit the structural analysis, however, the labeling compound is not yet commercially available. However, jasplakinolide is known to stabilize stress fibers by preventing the depolymerization of F-actin also during cell stretching [19] and will therefore bias the observations in our experiments. Comparison of the response of cells stained with a jasplakinolide-based label and cells transfected with Lifeact for actin visualization will give insight into which processes are affected by the labeling procedure.

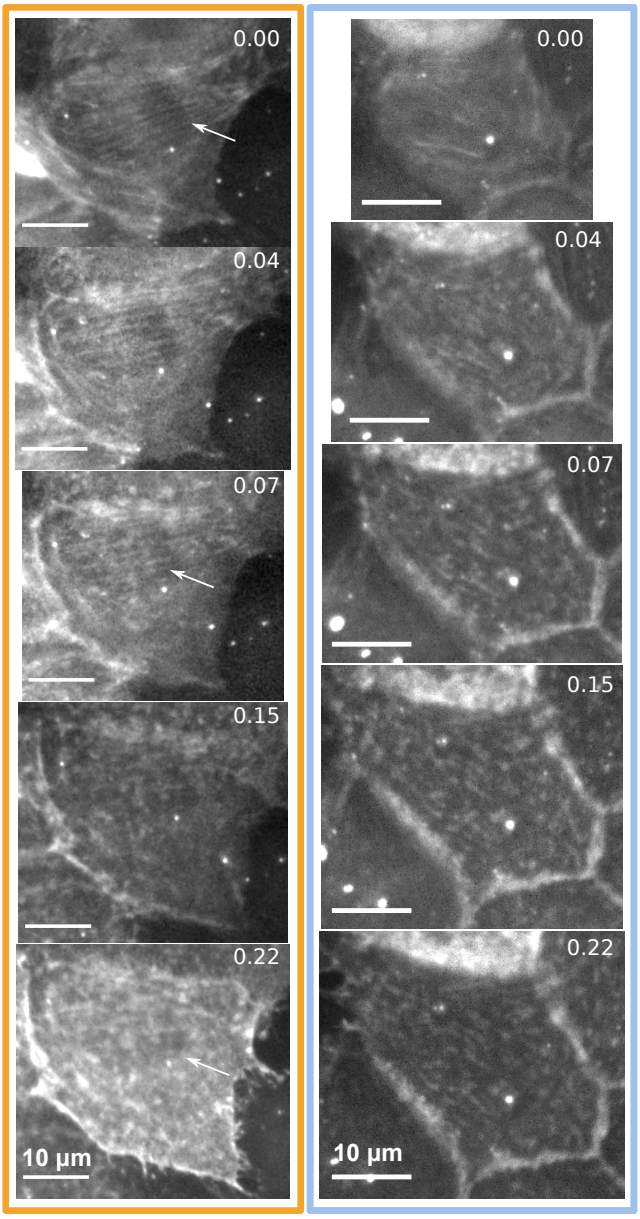

Fig. 7.4: **Stress fibers disassemble during the stretching experiment.** Two typical cells, stained with SiR-actin, are shown. Cells exhibit stress fibers at low strains that become less pronounced at increasing isotropic strains. At the highest strain, the cell shown in the left column start to retract. One example of a disappearing stress fiber is indicated by white arrows in the left column.

As we eventually want to study the effect of the keratin cortex on the strain response of the actin cortex, we compare actin cortex regions. In Fig. 7.5a,c, we show typical cortex regions. Overall, the cortex seems less homogeneous in the stretched cells than before stretching. Intensity profiles perpendicular to the actin cortex before and at maximum strain show a widening of the cortex: the FWHM of a Gaussian fit to the data increases by 0.4-0.5 µm in both cortex areas as shown in Fig. 7.5b,d. Surprisingly, we do not observe a clear decrease of the intensity of the cortex fluorescence. We expect such a decrease as the cortex has to adapt to the increased circumference of the cells and a decrease of the actin density in the cortex region has been observed for isotropically stretched

cells [13]. However, in the published experiments, the cells were observed over longer times than we allow the cells to adapt to the increased strain. Probably, the internal, contractile forces "pulling" the cortex towards the cell center lead to a widening of the cortex. Moreover, we observe that stressed or dying cells accumulate more of the SiR-actin label, thereby increasing the intensity. Even though a similar reduction of cortex density was studied with SiR-actin and phalloidin staining [13], this increased susceptibility might affect our results. Comparison of our results to cells without a keratin cortex will elucidate the influence of the keratin cortex in the actin cortex stability.

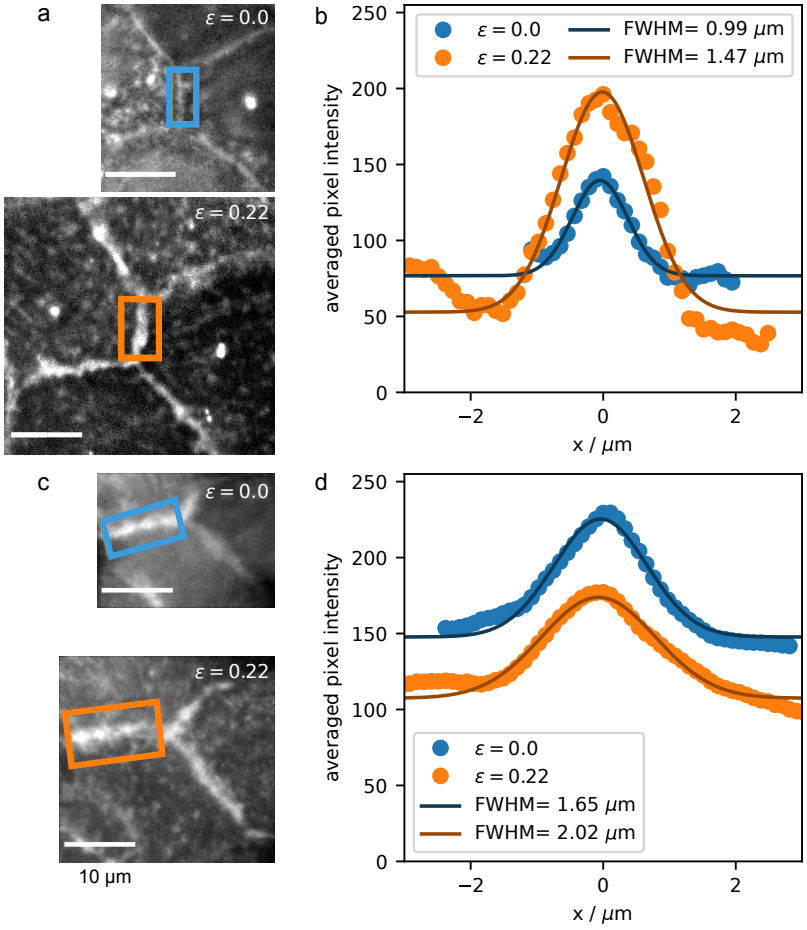

Fig. 7.5: **Comparison of the actin cortex before stretching and at maximum strain.** a,c) Fluorescence images of the actin cortex before (top, blue) and at maximum strain $\varepsilon = 0.22$ (bottom, orange). b,d) Intensity profiles of the regions marked in a,c), respectively. The intensity is averaged along the long axis of the rectangles. The FWHM of each Gaussian fit is indicated. All fluorescence images are shown to scale.

7.2.4 The keratin structure adapts to increasing strains

In contrast to the actin structures that change drastically, the keratin structure is much more robust. Keratin structures are known for their resilience even at high cellular deformations [13, 22]. In Fig. 7.6, examples for MDCK II cells, transiently transfected with keratin K8-EYFP, are shown. The transfection rate

is low so that only few cells are visible despite them being part of a confluent cell layer. The spoke-like keratin bundles are clearly visible in all cells while the subplasmalemmal keratin cortex is mostly visible at cell–cell contacts between labeled cells. In agreement with published results [13, 22–25], we observe a straightening of the spoke-like keratin bundles upon stretching, an example is indicated by white arrows in the left cell, top and bottom in Fig. 7.6. This straightening, *i.e.*, the keratin becoming load bearing, at strains where the actin cytoskeleten fluidizes has been hypothesized to be a rescue mechanism against cell rupture [13].

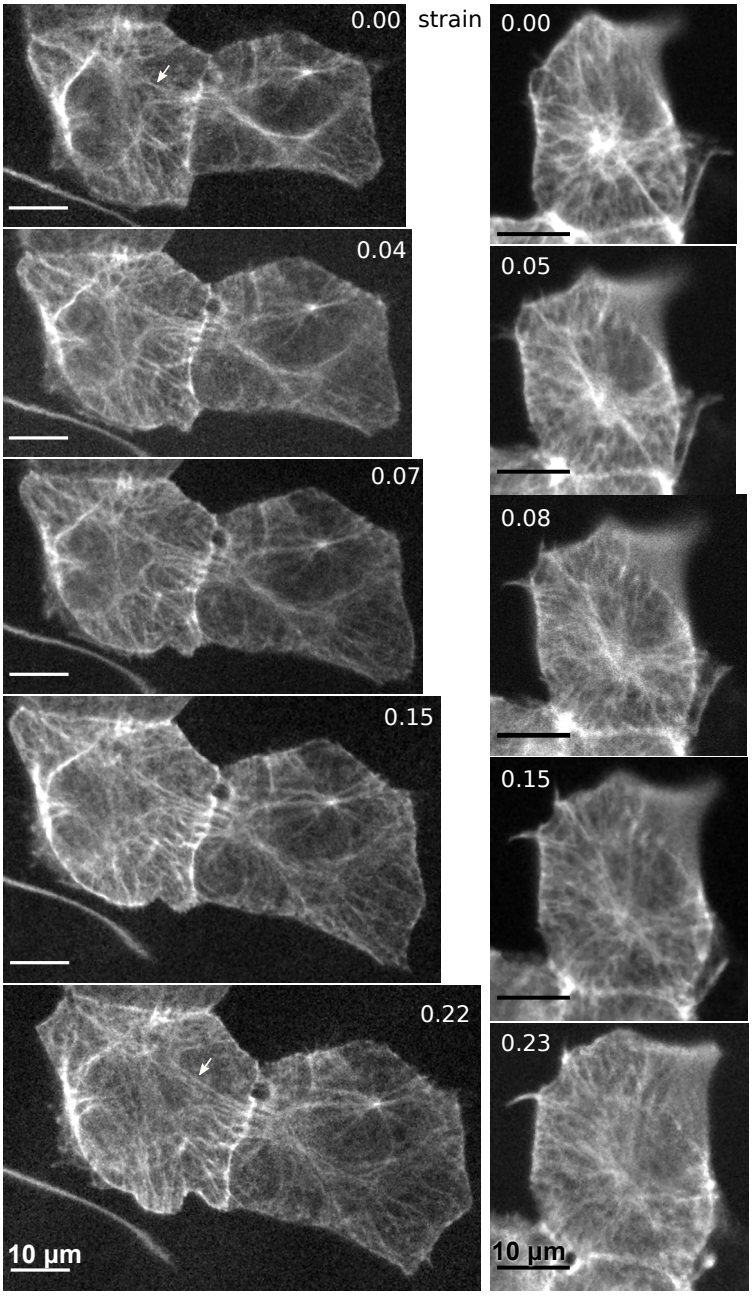

Fig. 7.6: **The keratin network during stretching.** Transiently transfected cells from two samples are shown. The isotropic strain is indicated in each image. Keratin bundles straighten at increasing strains, one example is indicated by white arrows in the left column.

We further observe that the spoke keratin bundles become less distinct at increasing strains, see Fig. 7.6, right column. Such a decrease of the contrast between spoke keratin bundles and cytosol in response to stretching has been reported for other cell lines, where a decrease of the bundle diameter was determined by fluorescence and electron microscopy [25]. The decrease of the bundle diameter is followed by an increase of keratin phosphorylation [23, 24] which has been hypothesized to be a mechanism for the cell to reduce the mechanical stress that keratin bundles exert on desmosomes to maintain the integrity of tissues [25]. In our experiments, bleaching is likely also a cause for the decreasing contrast and the exposure time for the imaging of the keratin structures had to be increased from 50 to 150 ms throughout the experiment for the cells shown in the left column in Fig. 7.6. The extent of the bleaching can be tested by imaging unstrained cells with the same imaging protocol used here and comparing any loss of intensity to the data recorded for the strained cells. We detect no quantifiable change of the keratin cortex structures. However, these observations are based on the three cells presented in Fig. 7.6 and the experiments have to be repeated for any meaningful conclusions to be drawn. Ideally, experiments will be repeated with cells with a higher transfection rate, for example by establishing a stable transfection. Nonetheless, the observations we make here are in good agreement with published results.

7.3 CONCLUSION

Our measurements clearly show a drastic difference between the response of the actin and keratin networks to isotropic cell stretching. We already observe a disassembly of the actin stress fibers and an increasing heterogeneity and broadening of the actin cortex. Whereas the response of the stress fibers is in agreement with other published observations [18], we expect a dilution and decrease of the actin cortex [13] that is not apparent from our data. As our images are recorded with widefield fluorescence microscopy, measurements with higher resolution will be beneficial to accurately determine structural changes. Higher resolution is further relevant to image the keratin cortex, as we do not observe an effect of the stretching on the keratin cortex here. In combination with a higher labeling efficiency of both the actin and keratin filaments, high resolution imaging will allow for the analysis of the interplay of the actin and keratin cortices. Comparison of the structural observation from these experiments with measurements of cells lacking the keratin cortex will give insight into the role of the subplasmalemmal keratin structure for the overall cell response and the effect on the actin structure under stretching conditions. In future experiments, we plan to combine the stretching device we have developed here with AFM measurements to quantify the mechanical properties of the cortex regions under strain for wt cells and cells lacking the keratin cortex. The combination of the cell stretching device with widefield fluorescence microscopy provides insight into the response of MDCK II cells and their cytoskeletal structures to isotropic stretching which provides the basis for many future measurements. This long list of unstudied questions shows the potential of the cell stretching device we have developed.

REFERENCES

[1] B. Alberts et al. *Molecular biology of the cell*. Vol. 6. W. W. Norton & Company, 2014.

[2] G. Dutour-Provenzano and S. Etienne-Manneville. "Intermediate filaments." *Curr. Biol.* 31 (2021), R522–R529. DOI: 10.1016/j.cub.2021.04.011.

[3] S. Karsch et al. "An intact keratin network is crucial for mechanical integrity and barrier function in keratinocyte cell sheets." *Cell. Mol. Life Sci.* 77 (2020), pp. 4397–4411. DOI: 10.1007/s00018-019-03424-7.

[4] A. E. Patteson et al. "The vimentin cytoskeleton: when polymer physics meets cell biology." *Phys. Biol.* 18 (2021), p. 011001. DOI: 10.1088/1478-3975/abbcc2.

[5] R. A. Quinlan et al. "A rim-and-spoke hypothesis to explain the biomechanical roles for cytoplasmic intermediate filament networks." *J. Cell Sci.* 130 (2017), pp. 3437–3445. DOI: 10.1242/jcs.202168.

[6] Certified Scientific Software. "Spec^{TM} X-Ray Diffraction Software User Manual" (2017). URL: http://www.certif.com.

[7] S. Klein et al. "elastix: A Toolbox for Intensity-Based Medical Image Registration." *IEEE Trans. Med. Imaging* 29 (2010), pp. 196–205. DOI: 10.1109/TMI.2009.2035616.

[8] D. Shamonin et al. "Fast parallel image registration on CPU and GPU for diagnostic classification of Alzheimer's disease." *Front. Neuroinform.* 7 (2014), pp. 1–15. DOI: 10.3389/fninf.2013.00050.

[9] A. Quaglino et al. "Mechanical strain induces involution-associated events in mammary epithelial cells." *BMC Cell Biol.* 10 (2009), p. 55. DOI: 10.1186/1471-2121-10-55.

[10] H. Majd et al. "A Novel Method of Dynamic Culture Surface Expansion Improves Mesenchymal Stem Cell Proliferation and Phenotype." *Stem Cells* 27 (2009), pp. 200–209. DOI: 10.1634/stemcells.2008-0674.

[11] C. P. Ursekar et al. "Design and construction of an equibiaxial cell stretching system that is improved for biochemical analysis." *PLoS ONE* 9 (2014), e90665. DOI: 10.1371/journal.pone.0090665.

[12] S. Schürmann et al. "The IsoStretcher: An isotropic cell stretch device to study mechanical biosensor pathways in living cells." *Biosens. Bioelectron.* 81 (2016), pp. 363–372. DOI: 10.1016/j.bios.2016.03.015.

[13] E. Latorre et al. "Active superelasticity in three-dimensional epithelia of controlled shape." *Nature* 7730 (2018), pp. 6481–6487. DOI: 10.1021/ac8009643.

[14] C. Stringer et al. "Cellpose: a generalist algorithm for cellular segmentation." *Nat. Methods* 18 (2021), pp. 100–106. DOI: 10.1038/s41592-020-01018-x.

[15] S. A. Gudipaty et al. "Mechanical stretch triggers rapid epithelial cell division through Piezo1." *Nature* 543 (2017), pp. 118–121. DOI: 10.1038/nature21407.

[16] J. D. Dukes, P. Whitley, and A. D. Chalmers. "The MDCK variety pack: Choosing the right strain." *BMC Cell Biol.* 12 (2011), p. 43. DOI: 10.1186/1471-2121-12-43.

[17] B. R. Brückner and A. Janshoff. "Importance of integrity of cell-cell junctions for the mechanics of confluent MDCK II cells." *Sci. Rep.* 8 (2018), p. 14117. DOI: 10.1038/s41598-018-32421-2.

[18] K. Hayakawa, N. Sato, and T. Obinata. "Dynamic reorientation of cultured cells and stress fibers under mechanical stress from periodic stretching." *Exp. Cell Res.* 268 (2001), pp. 104–114. DOI: 10.1006/excr.2001.5270.

[19] I. Andreu et al. "The force loading rate drives cell mechanosensing through both reinforcement and cytoskeletal softening." *Nat. Commun.* 12 (2021), p. 4229. DOI: 10.1038/s41467-021-24383-3.

[20] J. Riedl et al. "Lifeact: A versatile marker to visualize F-actin." *Nat. Methods* 5 (2008), pp. 605–607. DOI: 10.1038/nmeth.1220.

[21] R. Gerasimaitė et al. "Efflux pump insensitive rhodamine–jasplakinolide conjugates for G- and F-actin imaging in living cells." *Org. Biomol. Chem.,* 18 (2020), pp. 2929–2937. DOI: 10.1039/D0OB00369G.

[22] D. Fudge et al. "The intermediate filament network in cultured human keratinocytes is remarkably extensible and resilient." *PLoS ONE* 3 (2008), e2327. DOI: 10.1371/journal.pone.0002327.

[23] E. Felder et al. "Mechanical strain of alveolar type II cells in culture: changes in the transcellular cytokeratin network and adaptations." *Am. J. Physiol. Lung Cell Mol. Physiol.* 295 (2008), pp. L849–L857. DOI: 10.1152/ajplung.00503.2007.

[24] G. Fois et al. "Effects of keratin phosphorylation on the mechanical properties of keratin filaments in living cells." *FASEB J.* 27 (2013), pp. 1322–1329. DOI: 10.1096/fj.12-215632.

[25] A. Lutz et al. "Acute effects of cell stretch on keratin filaments in A549 lung cells." *FASEB J.* 34 (2020), pp. 11227–11242. DOI: 10.1096/fj.201903160RR.

8 DISCUSSION AND CONCLUSION

Cells can regulate their mechanical response to stress through the versatile IF cytoskeleton. For example, on long time scales of hours and days [1], differential expression of IF proteins can lead to a definite change in the motility and stiffness of cells [2]. One prominent example is the decrease of the keratin expression levels during the epithelial to mesenchymal transition, which is accompanied by an increased vimentin expression [3]. This pathway to changing the mechanical properties is highly complex and relatively slow.
On shorter time scales, for example, during mechanical stimulation by stretching, cells can alter IF mechanics through post-translational modifications. An increase of phosphorylation, the most studied post-translational modification [4], of keratin filaments is observed within 10-30 s of stretching of lung epithelial cells [5, 6]. As it has been shown that phosphorylations at specific positions in the IF sequence soften single filaments [7], the increase of phosphorylation during cell stretching might be a mechanism to maintain a constant load on cell-to-cell contacts [6] and thereby sustain tissue integrity. This modification of the existing IFs is less time and energy consuming than the exchange of the protein type by differential expression [8].
These two examples show how cells can exploit the tunability of IF cytoskeleton mechanics on multiple scales. We show that on time scales of seconds, networks of one type of IF also possess plenty of potential to directly, *i.e.*, without enzymatic modification, and possibly locally, tune their mechanical properties. In chapter 5, we show with OT measurements that by small changes in the environment, *i.e.*, the pH and the ion concentrations in the buffer, the mechanical properties of single vimentin IFs are drastically altered (Fig. 8.1). In particular, the pH of the environment sensitively tunes the mechanical response of vimentin filaments within seconds. Interestingly, the stretching behavior of single filaments is mostly unaltered at physiological concentrations of KCl [9] and at all $MgCl_2$ concentrations we measure here, whereas sub-physiological KCl concentrations clearly lead to a softening and destabilization of the filaments. Vimentin IFs therefore not only show force-strain curves that are reminiscent of the stretching response of coiled coils [10, 11], the building blocks of all IFs [12], but also that the responsiveness of coiled-coils to pH and ion concentrations [11, 13–16] is preserved in the filaments. This ion dependence, and especially the pH sensitivity, might allow cells to tune the mechanics of their IF network without having to express a different protein or chemically modify the protein. We therefore hypothesize that the tunability of single vimentin filaments we have uncovered here represents a fast mechanism to alter IF mechanics of relatively low complexity.
We have so far reduced the system to one single filament and quantified single filament mechanics. The IF cytoskeleton is, however, formed by more than one single filament so that interactions between IFs become relevant. Therefore, in

Fig. 8.1: OT measurements reveal that single vimentin filament mechanics are tuneable by environmental charge shifts.

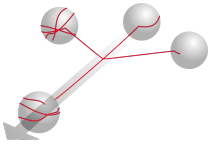

Fig. 8.2: OT measurements of direct interactions between single filaments reveal that hydrophobic interactions are not relevant for the interaction forces and kinetics and that Mg^{2+}-mediated interactions increase interaction forces and alter interaction kinetics.

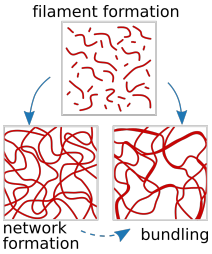

Fig. 8.3: Filament elongation and bundling influence the maturation of networks. Interactions between filaments can lead to bundling. Adapted from Ref. [29].

the next step of our multiscale approach to study the tunability of IF mechanics, we increase the complexity of the system from one filament to two filaments. We directly measure interactions between two single vimentin filaments with four OTs (Fig. 8.2), and complement the measurements by Monte-Carlo simulations in chapter 6. Through the addition of a detergent, we determine that hydrophobic interactions play no measurable role for vimentin-vimentin interactions. In contrast, we ascertain that transient, Mg^{2+}-mediated interactions between vimentin filaments decrease the rates of force-independent unbinding, compared to interactions between filaments solely in presence of monovalent ions. The decreased force-independent unbinding rates effectively lead to a stabilization of the interactions. Such binding kinetics could so far only be indirectly inferred from rheological studies [17, 18].

The next level of complexity is a full network, where many filaments interact. The stabilization of the interactions by Mg^{2+} ions leads to a stiffening of the network structure. A continuous stiffening of IF networks at increasing concentrations of multivalent ions has been reported [18–21]. Above a threshold ion concentration that varies with the ion type and charge, IF networks [21–27] collapse to dense structures. With the results of the quadruple OTs interaction experiments, we can attribute this collapse to an increased force-independent binding rate, which we only observe at a high Mg^{2+}-concentration which is well above the collapse-threshold concentration.

Any of the buffer variations, which effectively disturb the environment of the IFs, always affect multiple processes on multiple scales, and it is often necessary to investigate the temporal evolution of the mechanical properties. For example, by combining the results from the multiscale approach with filament elongation studies, we show that introducing Mg^{2+} ions during network formation slows down vimentin filament elongation and stabilizes the interactions between filaments, whereas single filament mechanics remain mostly unchanged. The altered elongation kinetics, in turn, translate to a delayed network maturation. Similar effects were also observed for keratin networks [28]. All of these processes contribute to the network mechanics and their evolution over time. Through an extended measurement period of six days, we show that vimentin networks continue to stiffen over the complete duration of the experiments.

By disentangling these effects in separate measurements and subsequently increasing the complexity of the system, we can quantify the influence of the ion mediated, electrostatic as well as hydrophobic interactions on elongation, filament mechanics, and interactions. By studying vimentin filament networks by active and passive microrheology, we show in chapter 6 that all three properties – elongation, stretching response, and filament-filament interactions – as well as bundling affect the final network mechanics (Fig. 8.3). We conclude that single IF properties and their role in the final network mechanics can only be determined with such a multiscale approach.

As cells seem to rely on the unique mechanical resilience of IFs, the stretching response of single IFs and the underlying structural changes have been discussed in detail in this thesis (chapters 2.2.2 and 5) and in literature [7, 30–37]. However, the structural changes IFs undergo in the cellular environment might differ from these changes observed for single filaments. Recent nonlinear Raman imaging

studies of the secondary structure of vimentin in cells that were subjected to different mechanical environments, show the coexistence of alpha-helical and beta sheet structures [38]. Similar studies of IFs in mechanically stressed cells, for example by employing the isotropic cell stretcher developed in chapter 7, will shed light on the structural changes IFs undergo in the complex environment of the cytosol of living cells. The persistence length determined from fluctuations of vimentin filaments in small confined microfluidic channels [39] or from fluctuations of vimentin filaments in cells [40] are remarkably similar. The single filament mechanics we measure with the OTs setup might be transferable to vimentin properties in cells. This hypothesis can be tested by studying the response of single, fluorescently labeled vimentin filaments as in Ref. [40] in cells during stretching.

In contrast to the relatively loose network structure of vimentin in the periphery of cells, keratin filaments are known to form bundles in cells [41]. To transfer the mechanical properties of keratin filaments [36] to their mechanical role in the cell environment, it will be interesting to measure the mechanical response of keratin bundles. The comparison of different types of IFs can reveal the mechanisms underlying their mechanical properties. Additionally, the measurement of single interactions between different types of IFs, for example keratin and vimentin filaments, is highly relevant, as some cells [6] express both types of IF proteins. Moreover, during the epithelial to mesenchymal transition, both proteins are present. Biochemical assays of cells coexpressing vimentin and keratin proteins have shown a direct interaction between the two IFs and the coexistence of both IF networks has been observed to be crucial for the healthy migration of these cells [42].

So far in our studies, we have focused on the direct tunability of the IF properties, interactions, and the resulting network properties. The IF cytoskeleton might, however, furthermore, contribute to the tunability of cell mechanics through interactions with other cytoskeletal components. As demonstrated in Ref. [43], interaction forces and kinetics between vimentin filaments and microtubules can be quantified. Since observations in cells indicate some degree of interplay between the two cytoskeletal networks [44], such direct measurements of interactions are indispensable to understanding the mechanism behind the cytoskeletal crosstalk. Very recently, observations of interpenetrating networks of actin filaments and vimentin filaments in the cell cortex region of fibroblasts were reported [45]. From electron microscopy studies, the authors of Ref. [45] hypothesize that the filaments either directly interact or that interactions are mediated by small proteins. These hypotheses can be tested using the quadruple OTs approach. Moreover, the effect of soluble globular actin on the stretching response of vimentin filaments may give additional insight to the mechanisms of the interactions and the question, which subunits interact. As the actin filaments in cells are constantly under tension [45], it will be enlightening to study the effect of pre-straining of both filaments individually on the actin-vimentin crosstalk. As different types of IFs have now been observed in close proximity to the actin cortex [45, 46], extending the multiscale approach by the study of the response of these actin-IF cortex structures in mechanically deformed, living cells with our isotropic cell stretcher becomes even more relevant (Fig. 8.4).

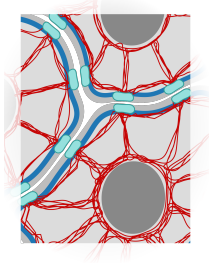

Fig. 8.4: Cell stretching gives insight into the properties of IF (red) and actin (blue) networks, their interplay, and their role for cell mechanics.

Comparison of the reaction of the actin cortex to stretching in the presence and absence of different types of IFs might reveal the differences and similarities between the roles of the specific IF proteins in cell cortex mechanics.
Moreover, the changes IFs undergo through altered environment conditions will likely affect the interactions with other cellular, non-cytoskeletal components. For example the molecular chaperone (αB-crystallin) is known to preferentially bind to desmin IFs at low pH rather than slightly basic pH conditions [47]. The bound small proteins likely affect the mechanical response of the single filaments as well as network interactions, which may both be quantified by our multiscale approach. The altered interactions with binding factors further increase the number of ways in which IFs are involved in the tunability of cellular responses.

CONCLUSION

In essence, we have characterized various mechanisms by which the mechanics of the IF cytoskeleton can be tuned. We reveal different ways in which cells may be able to tune their stiffness on multiple time scales and levels of complexity: i) Filament elongation is impeded through the inhibition of hydrophobic interactions or introducing Mg^{2+}-mediated electrostatic interactions. This deceleration of the elongation consequently slows down the maturation of networks. ii) We observe a softening of single filaments by reducing the concentration of KCl. iii) By contrast, single filaments stiffen through the reduction of the pH-value. iv) Stabilization of the interactions between filaments by the addition of Mg^{2+} ions leads to a stiffening of networks. Network stiffening is further promoted by Mg^{2+}-induced bundling. The IF cytoskeleton therefore presents a system through which cells might be able to quickly and locally adapt to altered mechanical requirements without having to rebuild the entire cytoskeleton. In combination with simulations, we determine the mechanisms by which charge shifts alter single vimentin filament mechanics and we extract energy landscapes for interactions between single filaments. The multiscale approach we implement here, including single filament elongation studies, dual and quadruple OTs measurements, microrheology, and the cell stretcher, thereby allows for the study of a plethora of mechanics-defining processes within the cytoskeleton. Such insights will provide a deeper understanding of the mechanisms by which cells can maintain their integrity and adapt to the mechanical requirements set by their environment.

[1] G. Greenburg and E. D. Hay. "Epithelia suspended in collagen gels can lose polarity and express characteristics of migrating mesenchymal cells." *J. Cell Biol.* 95 (1982), 333–339. DOI: 10.1083/jcb.95.1.333.

[2] M. G. Mendez, S.-I. Kojima, and R. D. Goldman. "Vimentin induces changes in cell shape, motility, and adhesion during the epithelial to mesenchymal transition." *FASEB J.* 24 (), pp. 1838–1851. DOI: 10.1096/fj.09-151639.

[3] E. D. Hay. "The mesenchymal cell, its role in the embryo, and the remarkable signaling mechanisms that create it." *Dev. Dyn.* 233.3 (2005), pp. 706–720. DOI: 10.1002/dvdy.20345.

[4] N. T. Snider and M. B. Omary. "Post-translational modifications of intermediate filament proteins: mechanisms and functions." *Nat. Rev. Mol. Cell Biol.* 15 (2014), pp. 163–177. DOI: 10.1038/nrm3753.

[5] E. Felder et al. "Mechanical strain of alveolar type II cells in culture: changes in the transcellular cytokeratin network and adaptations." *Am. J. Physiol. Lung Cell Mol. Physiol.* 295 (2008), pp. L849–L857. DOI: 10.1152/ajplung.00503.2007.

[6] A. Lutz et al. "Acute effects of cell stretch on keratin filaments in A549 lung cells." *FASEB J.* 34 (2020), pp. 11227–11242. DOI: 10.1096/fj.201903160RR.

[7] J. Kraxner et al. "Post-translational modifications soften vimentin intermediate filaments." *Nanoscale* 13 (2021), pp. 380–387. DOI: 10.1039/d0nr07322a.

[8] J. Amthor. "The McCree–de Wit–Penning de Vries–Thornley Respiration Paradigms: 30 Years Later." *Ann. Bot.* 86 (2000), pp. 1–20. DOI: 10.1006/anbo.2000.1175.

[9] M. Zacchia et al. "Potassium: From Physiology to Clinical Implications." *Kidney Dis.* 2 (2016), pp. 72–79. DOI: 10.1159/000446268.

[10] D. D. Root et al. "Coiled-Coil Nanomechanics and Uncoiling and Unfolding of the Superhelix and α-Helices of Myosin." *Biophys. J.* 90 (2006), pp. 2852–2866. DOI: 10.1529/biophysj.105.071597.

[11] M. Goktas et al. "Molecular Mechanics of Coiled Coils Loaded in the Shear Geometry." *Chem. Sci.* 9 (2018), pp. 4610–4621. DOI: 10.1039/c8sc01037d.

[12] N. Geisler and K. Weber. "The amino acid sequence of chicken muscle desmin provides a common structural model for intermediate filament proteins." *EMBO J.* 1 (1982), pp. 1649–1656. DOI: 10.1002/j.1460-2075.1982.tb01368.x.

[13] Y. Yu et al. "Ion Pairs Significantly Stabilize Coiled-Coils in the Absence of Electrolyte." *J. Mol. Biol.* 255 (1996), pp. 367–372. DOI: 10.1006/jmbi.1996.0030.

[14] K. Dutta et al. "pH-Induced Folding of an Apoptotic Coiled Coil." *Protein Sci.* 10 (2001), pp. 2531–2540. DOI: 10.1110/ps.ps.28801.

[15] K. Pagel et al. "Random Coils, β-Sheet Ribbons, and α-Helical Fibers: One Peptide Adopting Three Different secondary Structures at Will." *J. Am. Chem. Soc.* 128 (2006), pp. 2196–2197. DOI: 10.1021/ja057450h.

[16] P. López-García et al. "Structural Determinants of Coiled Coil Mechanics." *Phys. Chem. Chem. Phys.* 21 (2019), pp. 9145–9149. DOI: 10.1039/C9CP00665F.

[17] B. Gurmessa et al. "Counterion Crossbridges Enable Robust Multiscale Elasticity in Actin Networks." *Phys. Rev. Res.* 1 (2019), p. 013016. DOI: 10.1103/PhysRevResearch.1.013016.

[18] A. Aufderhorst-Roberts and G. H. Koenderink. "Stiffening and Inelastic Fluidization in Vimentin Intermediate Filament Networks." *Soft Matter* 15 (2019), pp. 7127–7136. DOI: 10.1039/C9SM00590K.

[19] Y.-C. Lin et al. "Divalent Cations Crosslink Vimentin Intermediate Filament Tail Domains to Regulate Network Mechanics." *J. Mol. Biol.* 399 (2010), pp. 637–644. DOI: 10.1016/j.jmb.2010.04.054.

[20] S. Köster et al. "Nanomechanics of vimentin intermediate filament networks." *Soft Matter* 6 (2010), p. 1910. DOI: 10.1039/c000113a.

[21] H. Wu et al. "Effect of divalent cations on the structure and mechanics of vimentin intermediate filaments." *Biophys. J.* 119 (2020), pp. 55–64. DOI: 10.1016/j.bpj.2020.05.016.

[22] C. Dammann, B. Nöding, and S. Köster. "Vimentin networks at tunable ion-concentration in microfluidic drops." *Biomicrofluidics* 6 (2012), p. 022009. DOI: 10.1063/1.4705103.

[23] C. Dammann and S. Köster. "Dynamics of Counterion-Induced Attraction between Vimentin Filaments Followed in Microfluidic Drops." *Lab Chip* 14 (2014), pp. 2681–2687. DOI: 10.1039/c3lc51418h.

[24] M. E. Brennich et al. "Impact of ion valency on the assembly of vimentin studied by quantitative small angle X-ray scattering." *Soft Matter* 10 (2014), pp. 2059–2068. DOI: 10.1039/C3SM52532E.

[25] C. Dammann, H. Herrmann, and S. Köster. "Competitive Counterion Binding Regulates the Aggregation Onset of Vimentin Intermediate Filaments." *Isr. J. Chem.* 56 (2016), pp. 614–621. DOI: 10.1002/ijch.201400153.

[26] M. Denz et al. "Ion type and valency differentially drive vimentin tetramers into intermediate filaments or higher order assemblies." *Soft Matter* 17 (2021), pp. 870–878. DOI: 10.1039/d0sm01659d.

[27] K. Cruz et al. "Polyelectrolyte Gels Formed by Filamentous Biopolymers: Dependence of Crosslinking Efficiency on the Chemical Softness of Divalent Cations." *Gels* 7 (2021), p. 41. DOI: 10.3390/gels7020041.

[28] J. Kayser et al. "Assembly Kinetics Determine the Structure of Keratin Networks." *Soft Matter* 8 (2012), p. 8873. DOI: 10.1039/C2SM26032H.

[29] A. V. Schepers et al. "Multiscale mechanics and temporal evolution of vimentin intermediate filament networks." *Proc. Natl. Acad. Sci.* 118 (2021), e2102026118. DOI: 10.1073/pnas.2102026118.

[30] Z. Qin, L. Kreplak, and M. J. Buehler. "Hierarchical Structure Controls Nanomechanical Properties of Vimentin Intermediate Filaments." *PLoS ONE* 4 (2009), e7249. DOI: 10.1371/journal.pone.0007294.

[31] Z. Qin, L. Kreplak, and M. J. Buehler. "Nanomechanical properties of vimentin intermediate filament dimers." *Nanotechnology* 20 (2009), p. 425101. DOI: 10.1088/0957-4484/20/42/425101.

[32] C. Guzmán et al. "Exploring the Mechanical Properties of Single Vimentin Intermediate Filaments by Atomic Force Microscopy." *J. Mol. Biol.* 360 (2006), pp. 623–630. DOI: 10.1016/j.jmb.2006.05.030.

[33] J. Block et al. "Nonlinear Loading-Rate-Dependent Force Response of Individual Vimentin Intermediate Filaments to Applied Strain." *Phys. Rev. Lett.* 118 (2017), p. 048101. DOI: 10.1103/PhysRevLett.118.048101.

[34] J. Block et al. "Viscoelastic Properties of Vimentin Originate from Nonequilibrium Conformational Changes." *Sci. Adv.* 4 (2018), eaat1161. DOI: 10.1126/sciadv.aat1161.

[35] J. Forsting et al. "Vimentin Intermediate Filaments Undergo Irreversible Conformational Changes During Cyclic Loading." *Nano Lett.* 19 (2019), pp. 7349–7356. DOI: 10.1021/acs.nanolett.9b02972.

[36] C. Lorenz et al. "Lateral Subunit Coupling Determines Intermediate Filament Mechanics." *Phys. Rev. Lett.* 123 (2019), p. 188102. DOI: 10.1103/PhysRevLett.123.188102.

[37] K. T. Sapra et al. "Nonlinear mechanics of lamin filaments and the meshwork topology build an emergent nuclear lamina." *Nat. Commun.* 11 (2020), p. 6205. DOI: 10.1038/s41467-020-20049-8.

[38] F. Fleissner et al. "Tension Causes Unfolding of Intracellular Vimentin Intermediate Filaments." *Adv. Biosyst.* 4 (2020), p. 2000111. DOI: 10.1002/adbi.202000111.

[39] B. Nöding and S. Köster. "Intermediate Filaments in Small Configuration Spaces." *Phys. Rev. Lett.* 108 (2012), p. 088101. DOI: 10.1103/PhysRevLett.108.088101.

[40] M. Smoler et al. "Apparent stiffness of vimentin intermediate filaments in living cells and its relation with other cytoskeletal polymers." *Biochim. Biophys. Acta, Mol. Cell Res.* 1867 (2020), p. 118726. DOI: 10.1016/j.bbamcr.2020.118726.

[41] J. F. Nolting, W. Möbius, and S. Köster. "Mechanics of Individual Keratin Bundles in Living Cells." *Biophys. J.* 107 (2014), pp. 2693–2699. DOI: 10.1016/j.bpj.2014.10.039.

[42] C. Velez-delValle et al. "Epithelial cell migration requires the interaction between the vimentin and keratin intermediate filaments." *Sci. Rep.* 6.1 (2016), p. 24389. DOI: 10.1038/srep24389.

[43] L. Schaedel et al. "Vimentin intermediate filaments stabilize dynamic microtubules by direct interactions." *Nat. Commun.* 12 (2021), p. 3799. DOI: 10.1038/s41467-021-23523-z.

[44] Z. Gan et al. "Vimentin Intermediate Filaments Template Microtubule Networks to Enhance Persistence in Cell Polarity and Directed Migration." *Cell Syst.* 3.3 (2016), 252–263.e8. DOI: 10.1016/j.cels.2016.08.007.

[45] H. Wu et al. "Vimentin Intermediate Filaments and Filamentous Actin Form Unexpected Interpenetrating Networks That Redefine the Cell Cortex." *BioRxiv* (2021). (visited on 08/04/2021). DOI: 10.1101/2021.07.29.454155.

[46] R. A. Quinlan et al. "A rim-and-spoke hypothesis to explain the biomechanical roles for cytoplasmic intermediate filament networks." *J. Cell Sci.* 130 (2017), pp. 3437–3445. DOI: 10.1242/jcs.202168.

[47] J. L. Elliott et al. "The specificity of the interaction between αB-crystallin and desmin filaments and its impact on filament aggregation and cell viability." *Phil. Trans. R. Soc. B* 368 (2013), p. 20120375. DOI: 10.1098/rstb.2012.0375.

SUPPORTING INFORMATION: TUNING INTERMEDIATE FILAMENT MECHANICS BY VARIATION OF PH AND ION CHARGES

A

A.1 FLOW SIMULATIONS

Reproduced from Ref. [1]

The concentrations and pH conditions given are the buffers that were injected into the microfluidic chip. Because the flow was stopped during incubation and stretching of the filaments, diffusion of the cations between the assembly and measuring buffers, and the assimilation of the pH have to be considered. This means that the conditions in proximity to the filament during the measurement were slightly different to the injected buffer. The temporal evolution of the salt concentrations and the pH at the measurement position was simulated and is described in the following.

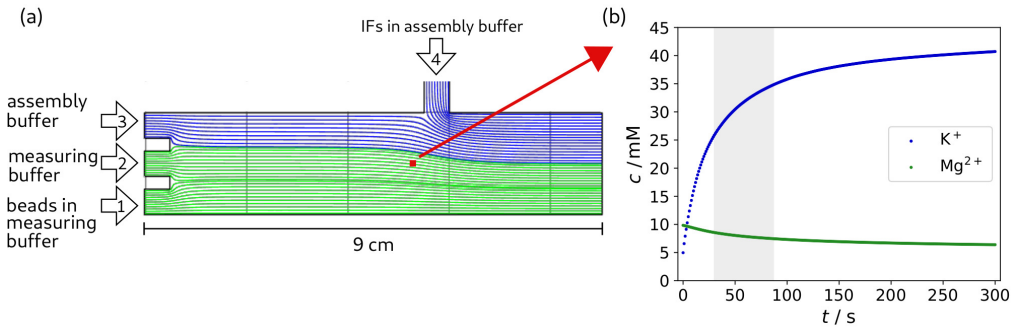

Fig. A1: **Results of FEM simulations.** a) Schematic of the flow cell including simulated stream lines of the in-flowing buffers. In the experiment, beads in measuring buffer are injected in channel 1, measuring buffer in channel 2, assembly buffer in channel 3 and vimentin in assembly buffer in channel 4. In Fig 5.1b in the main text, we omit channel 2, as it is solely used for calibration of the traps and not crucial for the understanding of the measurement procedure. It is, however, relevant for the flow properties presented here. The colors correspond to the cation species of the buffer (blue: K^+, green: Mg^{2+}). For this simulation, the measuring buffer contained 10 mM Mg^{2+} and the assembly buffer 100 mM K^+. IFs and beads were not included in the simulation. The position of the measurement is marked in red and corresponds to the position for which the development of the cation concentrations after stopping the flow was calculated. b) Plot of the temporal evolution of the concentrations of Mg^{2+} and K^+ ions at the measurement position after stopping the flow. The time window of the measurement is indicated. Reproduced from Ref.[1].

First, the equilibrium ion distribution in the chip is simulated under flow. Taking this as a starting condition, a second simulation is calculated without flow, only allowing diffusion. The change of the concentrations of the cations and H^+ ions is simulated at the position of the force-strain measurement (Fig. A1a, red mark) for a duration of 5 min. The equilibrium pH is reached within the first minute and then stays relatively constant over time and in the flow cell. This resulting equilibrium pH was clearly distinguishable for the different measuring buffers.

The change of cation concentrations (Mg^{2+} from the measuring buffer, K^+ from the adjacent assembly buffer) is shown in Fig. A1b for the example of the 10 mM $MgCl_2$ measuring buffer.
For the experiments where we measure single interactions, we use the microfluidic flow cell as shown in Fig. A2. The decrease of the concentration by diffusion is plotted in Fig. A2a-d. The position of the measurement is marked by the black square in Fig. A2e.

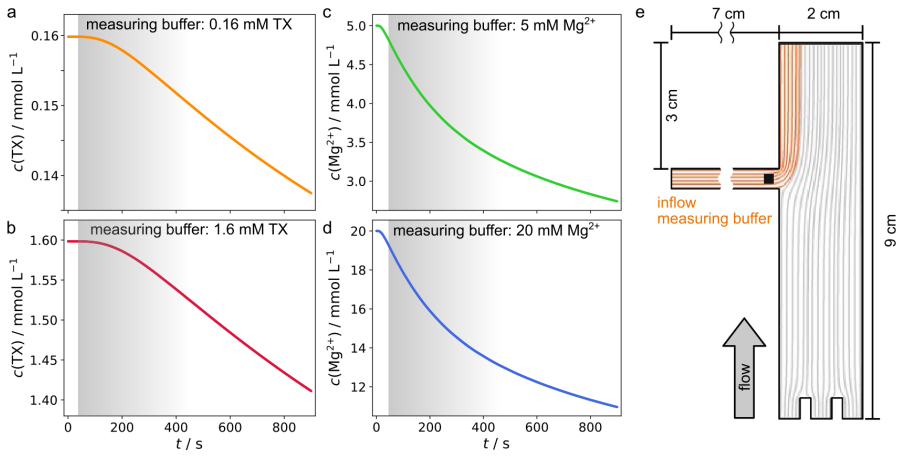

Fig. A2: **Temporal evolution of the concentration of TX and Mg^{2+} at the measurement position for the interaction measurements.** a) Concentration of TX with the starting condition 0.16 mM. Because of the detergent properties of TX, the diffusion coefficient depends on the concentration. For this concentration $D_{TX} = 8.25 \times 10^{-7}\,cm^2\,s^{-1}$ is used [2]. b) Concentration of TX with the starting condition 1.6 mM. For this condition, $D_{TX} = 6.93 \times 10^{-7}\,cm^2\,s^{-1}$ is used [2]. c), d) Concentration of Mg^{2+} for 5 mM and 20 mM $MgCl_2$ measuring buffer with $D_{Mg^{2+}} = 0.594 \times 10^{-9}\,cm^2\,s^{-1}$ [3]. The duration of the experiments is marked in gray. e) Flow cell used for finite element simulations. The flow lines for the measuring buffer are highlighted in orange. The measuring position is marked with a black square and the flow direction is indicated by the gray arrow.

A.2 SINGLE FORCE-STRAIN CURVES

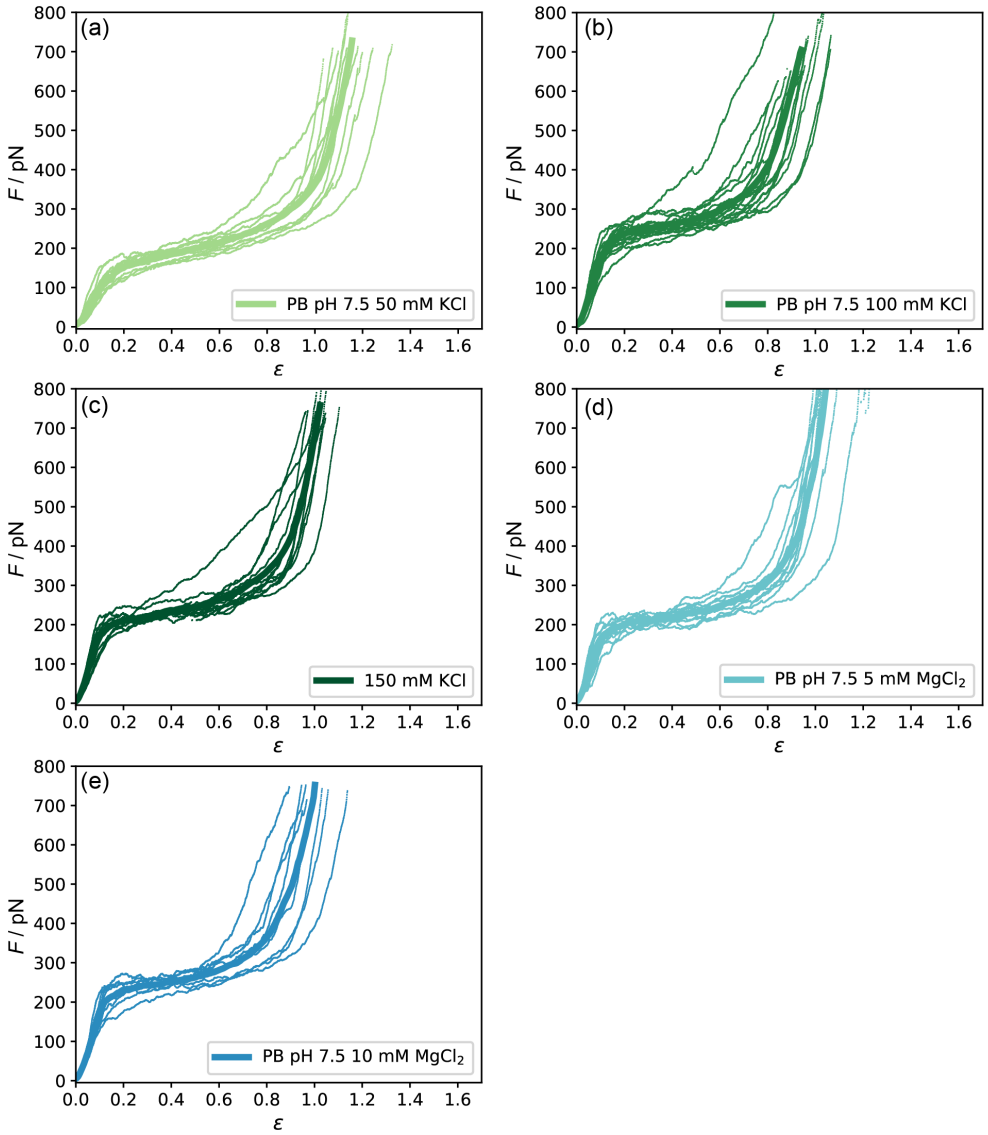

Fig. A3: **Force-strain curves for each measured salt condition.** a)-e) All single measurements of stable filaments are plotted (thin lines) along with the average curves (bold lines, as shown in Fig. 5.2a in the main text). Reproduced from Ref. [1].

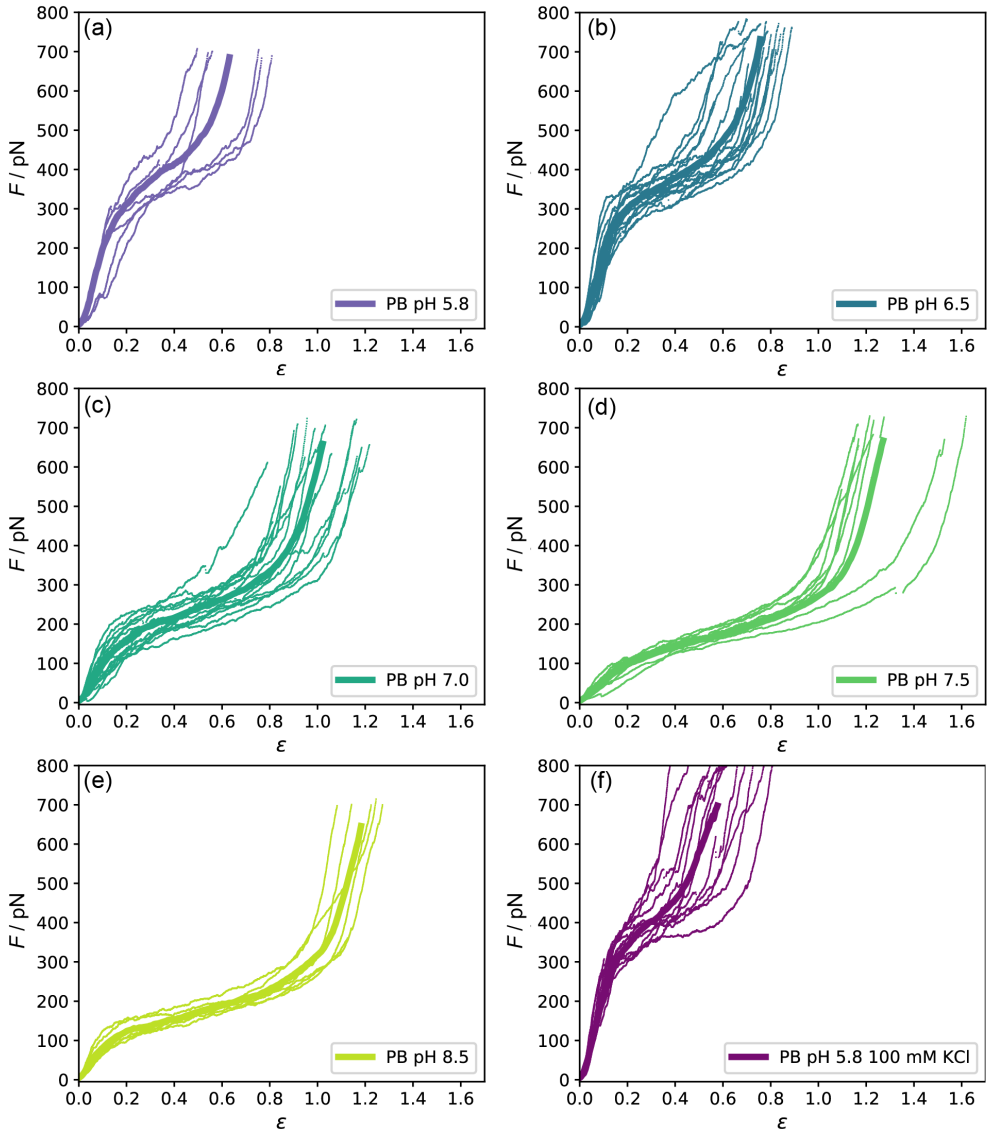

Fig. A4: **Force-strain curves for each pH condition measured.** All single measurements of stable filaments are plotted (thin lines) along with the average curve (bold lines, as shown in Fig. 5.2b). a)-e) Show data recorded at increasing pH values and f) measurements at pH 5.8 with 100 mM KCl. Reproduced from Ref. [1].

SUPPORTING INFORMATION: MULTISCALE MECHANICS AND TEMPORAL EVOLUTION OF VIMENTIN INTERMEDIATE FILAMENT NETWORKS

B

B.1 ADDITIONAL INFORMATION FOR ELONGATION MEASUREMENTS

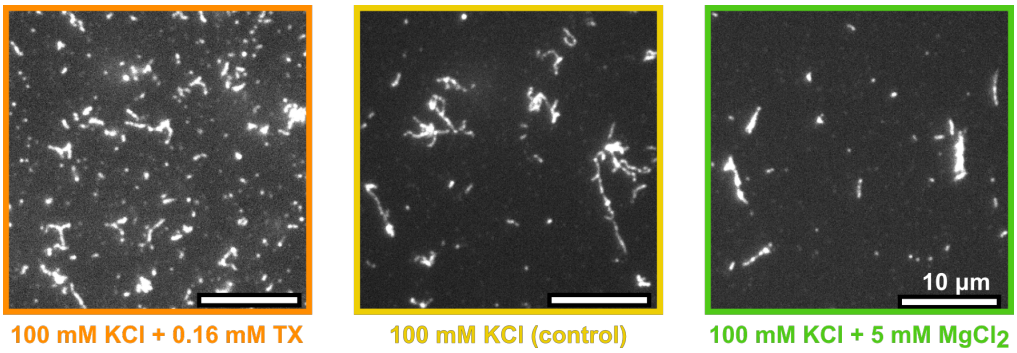

Fig. B1: **Example fluorescence microscopy images after 71 h assembly duration.** The filaments are assembled at 0.2 g/L in the respective buffer and diluted 100-fold for imaging. The corresponding length distributions of several of such images are shown in Fig. B2. Reproduced from Ref. [4].

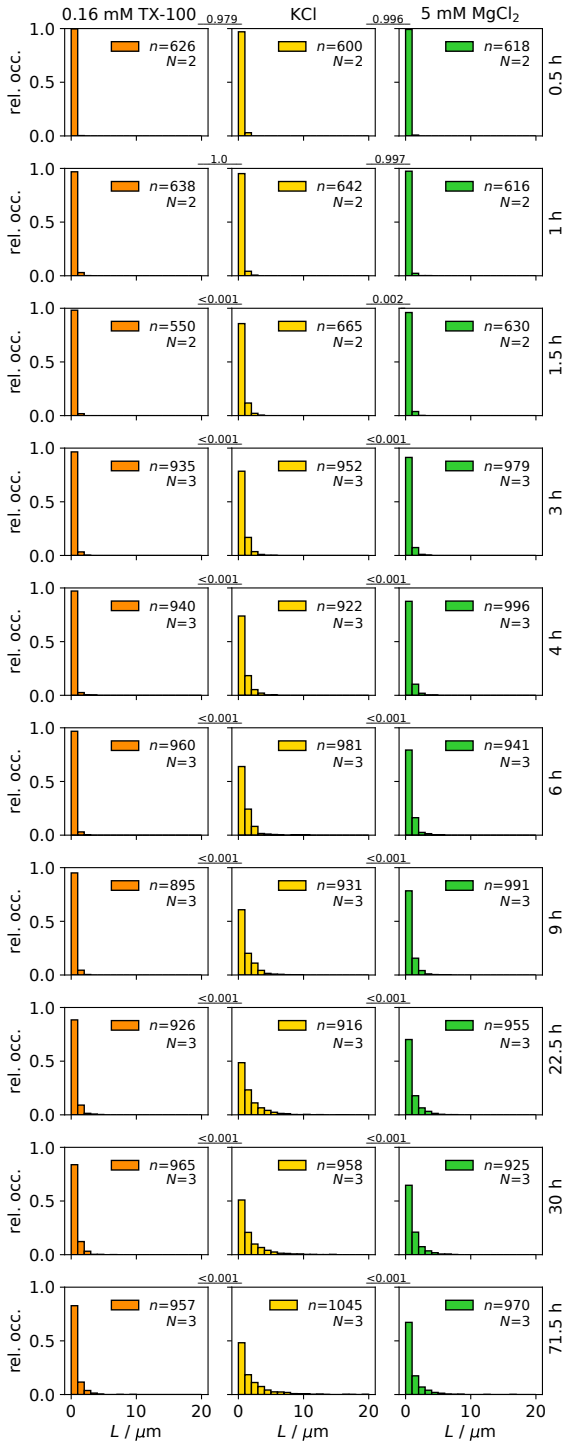

Fig. B2: **Histograms of filaments lengths measured by fluorescence microscopy images after the given assembly duration.** The filaments are assembled at 0.2 g/L and diluted 100-fold for imaging. N denotes the number of independent data sets and n the cumulative number of measured filaments from all experiments. For each experimental repeat, about 300 filaments were traced at each time point and condition. The statistical p-value corresponding to the comparison of the TX/$MgCl_2$-data to the control condition at each time point is indicated above each plot. We use the Kolmogorov-Smirnov test to compare the distributions. Reproduced from Ref. [4].

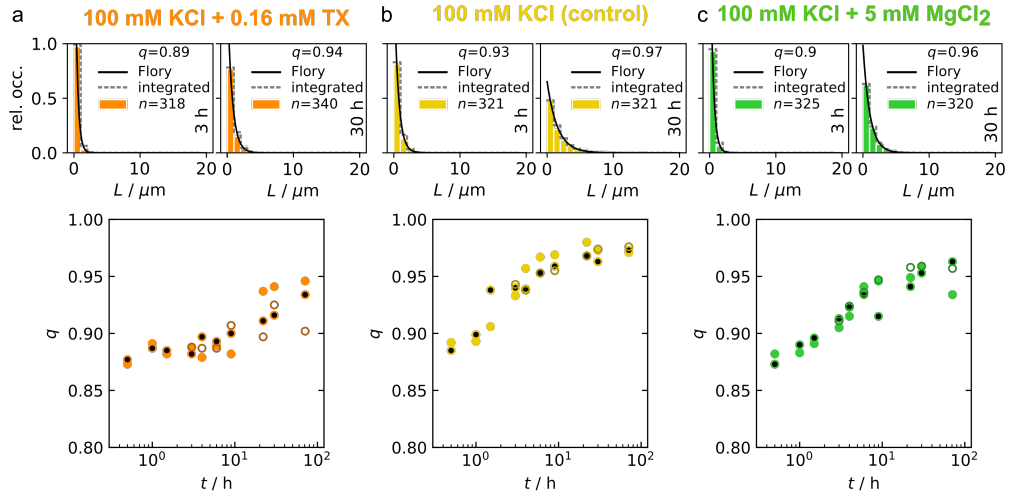

Fig. B3: **Extent of the filament elongation reaction.** Top: Example length histograms. The extent of the reaction, q, results from fits of the length histograms with the integrated version of the Flory-Schulz distribution (dashed line) and the corresponding distribution (solid line). The data are shown for one experiment after 3 h and 30 h of assembly for protein concentrations of 0.2 g/L. Bottom: Fit results for the extent of reaction q for vimentin assembled in a) assembly buffer + 0.16 mM TX, b) pure assembly buffer and c) in assembly buffer + 5 mM $MgCl_2$. The different shades of each color indicate independent repeats of the experiment. Reproduced from Ref. [4].

B.2 DATA ANALYSIS OF MICRORHEOLOGY MEASUREMENTS

Sections B.2.1 and B.2.3 were written by Peter Nietmann for publication in Ref. [4].

B.2.1 Passive microrheology

Reproduced from Ref. [4]

The fluctuation-dissipation theorem can be applied to the recorded thermal motion of microparticles embedded in a viscoelastic medium that is in equilibrium on the time scale of the measurement. By utilizing the fluctuation-dissipation theorem, we imply that the medium, here the filament network, reacts to small, time-dependent external disturbances the same way it reacts to internal thermal fluctuations. The viscoelastic properties of a medium are characterized by the shear modulus $G^*(\omega)$, which is connected to the thermal fluctuations of the microparticles via a generalized Stokes-Einstein equation. A Laplace unilateral transformation – denoted by the tilde symbol – of the generalized Stokes-Einstein equation results in

$$\tilde{G}(s) = \frac{k_B T}{\pi a s \langle \Delta \tilde{r}^2(s) \rangle} \tag{B.1}$$

with the particle diameter a and the Laplace frequency s. The MSD $\langle \Delta r^2(\tau) \rangle$ is directly calculated from the thermal fluctuations of the microparticles for the lag time τ. The difficulty lies in the Laplace transformation of the data over a limited frequency range, which can distort the result. To simplify the fitting process, a limited frequency range is described by a local power law and $G^*(\omega)$ determined analytically [5, 6]. The local power law is extracted from the logarithmic time derivative of the MSD.

$$|G^*| \approx \frac{k_B T}{\pi a \langle \Delta r^2(1/\omega) \rangle \Gamma[1 + \alpha(1/\omega)]} \tag{B.2}$$

$$\alpha(\tau) = \frac{d \ln \langle \Delta r^2(\tau) \rangle}{d \ln \tau} \tag{B.3}$$

Here, Γ is the gamma function and α the local power-law exponent. Using the second order for this step improves performance of the algorithm [7]. We use a custom Matlab code based on this method to calculate G^* [8]. Finally, the complex shear modulus G^* is separated into the real part, the storage modulus $G'(\omega)$, and the imaginary part, the loss modulus $G''(\omega)$.
Interestingly, the heterogeneity observed in the confocal image of the network in Fig.6.1a (bottom) is not obvious in the single MSD curves in Figs. B4-B6. We attribute this observation to the fact that only microparticles that are embedded in sufficiently dense network regions are accessible by our method and thus conclude that the regions where particles are embedded are homogeneous.

B.2.2 Single curves from passive microrheology measurements

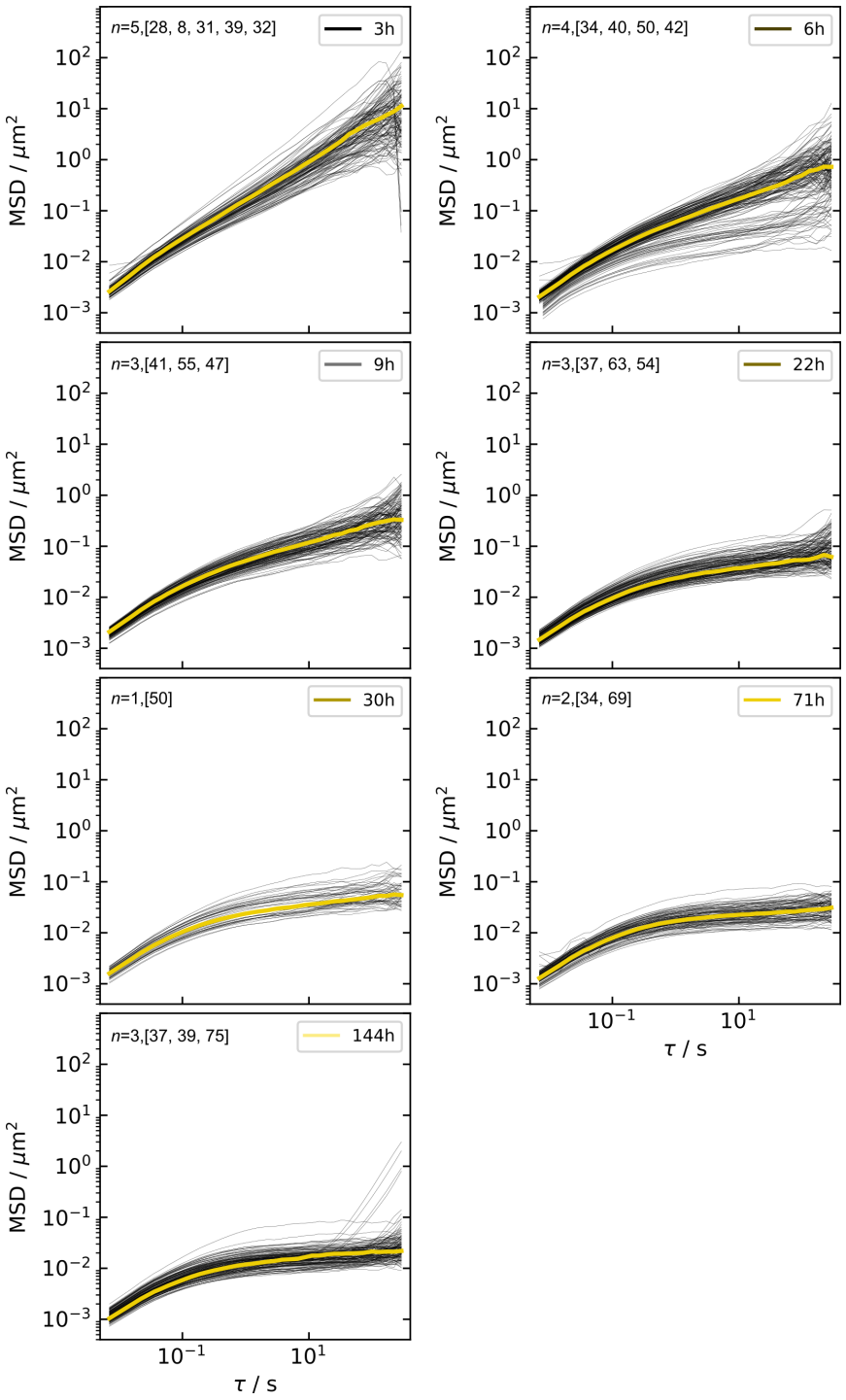

Fig. B4: **All single MSDs recorded for each assembly duration in KCl buffer.** The median curves are highlighted. n denotes the number of samples measured, followed by the number of particles per measurement. Reproduced from Ref. [4].

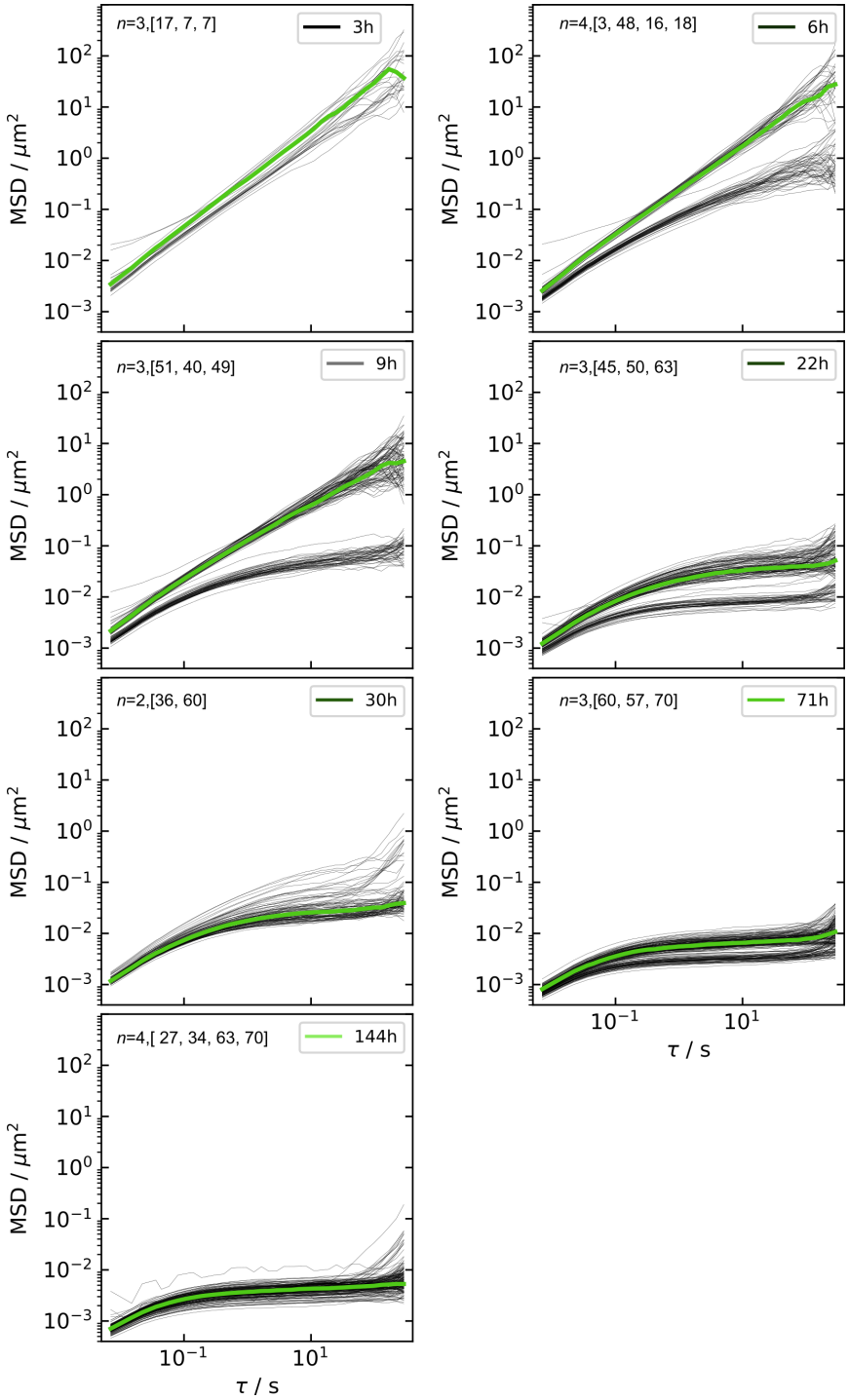

Fig. B5: **All single MSDs recorded for each assembly duration in 5 mM $MgCl_2$ buffer.** The median curves are highlighted. n denotes the number of samples measured, followed by the number of particles per measurement. We observe variation between different samples prepared with the same concentration of $MgCl_2$, in particular at early time points. However, for each individual sample we obtain consistent MSD curves. Reproduced from Ref. [4].

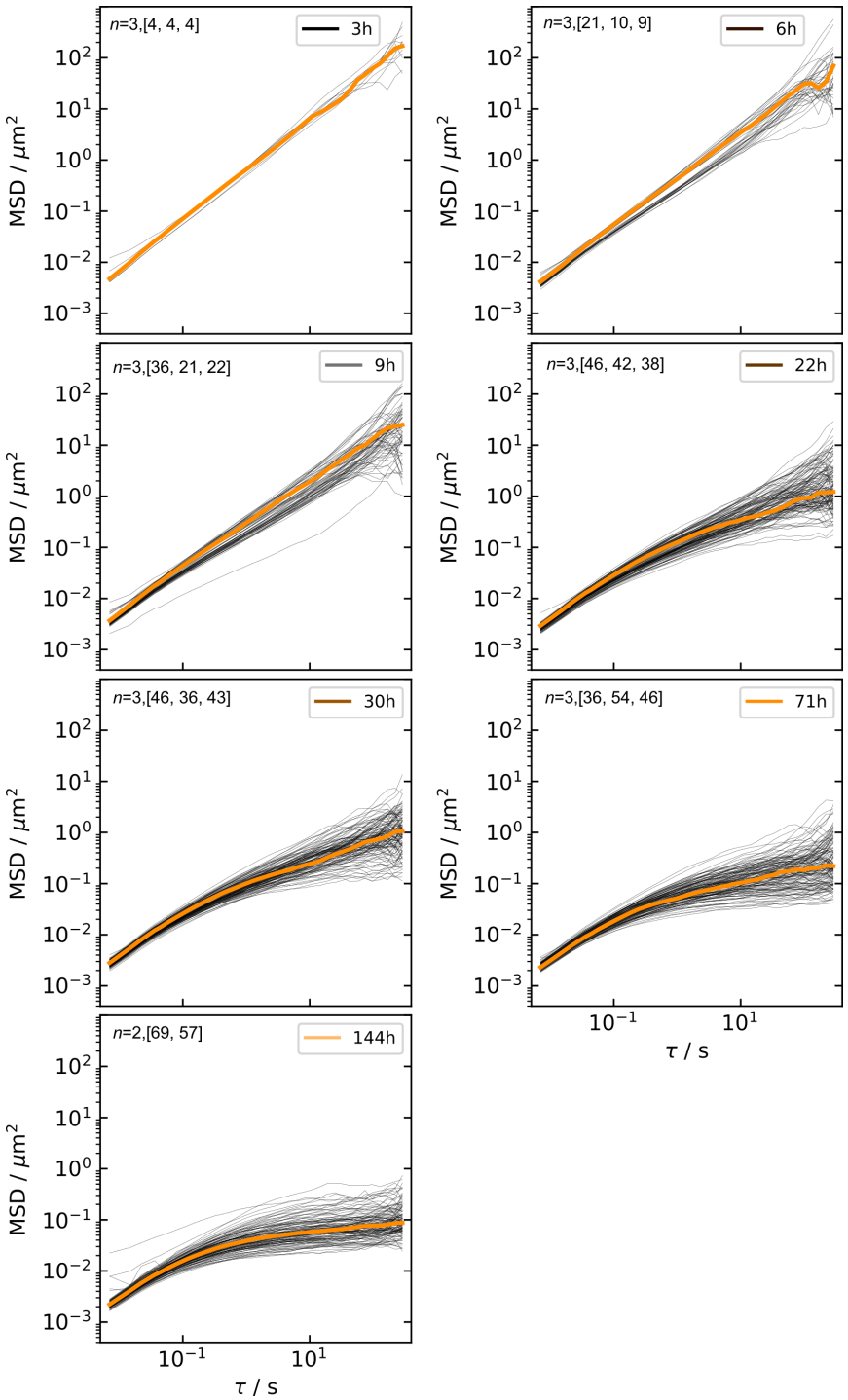

Fig. B6: **All single MSDs recorded for each assembly duration in 0.16 mM TX buffer.** The median curves are highlighted. n denotes the number of samples measured, followed by the number of particles per measurement. Reproduced from Ref. [4].

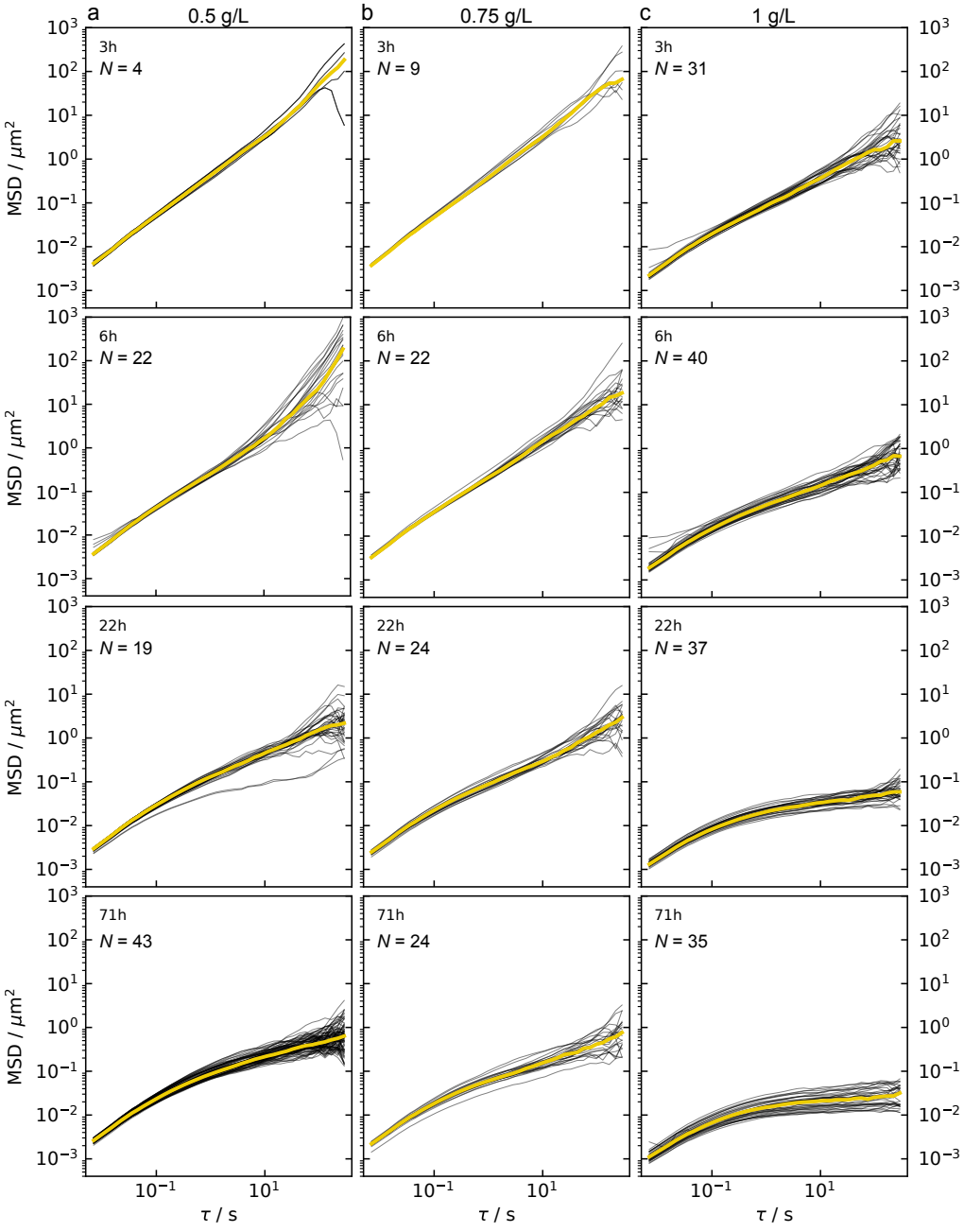

Fig. B7: **All single MSDs recorded at varying vimentin concentrations for each assembly duration in KCl buffer.** The median curves are highlighted. N denotes the number of particles for each measurement. The data are from one sample per concentration.

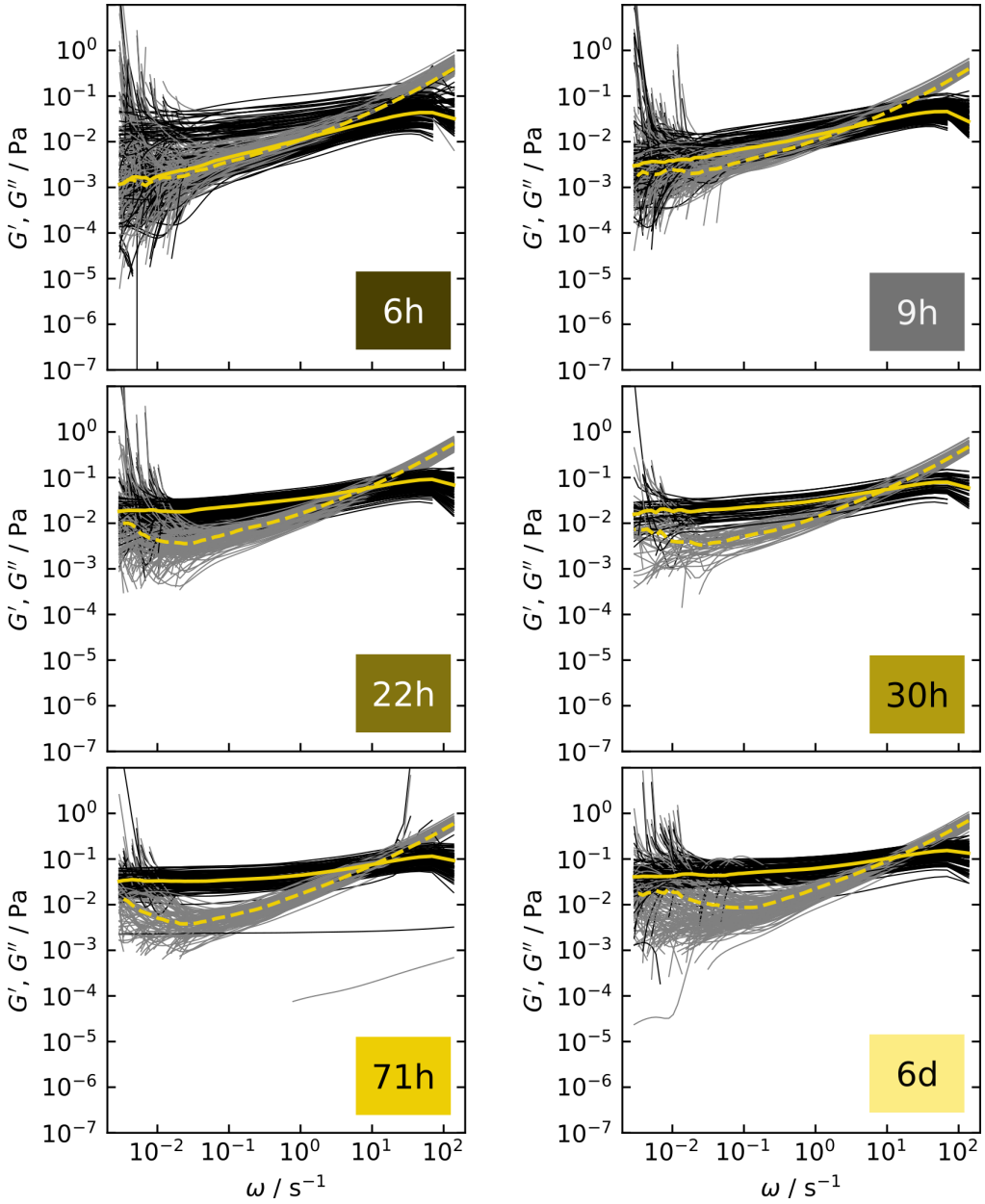

Fig. B8: **All single storage (black) and loss (gray) moduli recorded for each assembly duration in KCl buffer.** The median curves are highlighted, the solid line corresponds to G' and the dashed line G''. The number of samples and particles per measurement are provided in Fig. B4. Reproduced from Ref. [4].

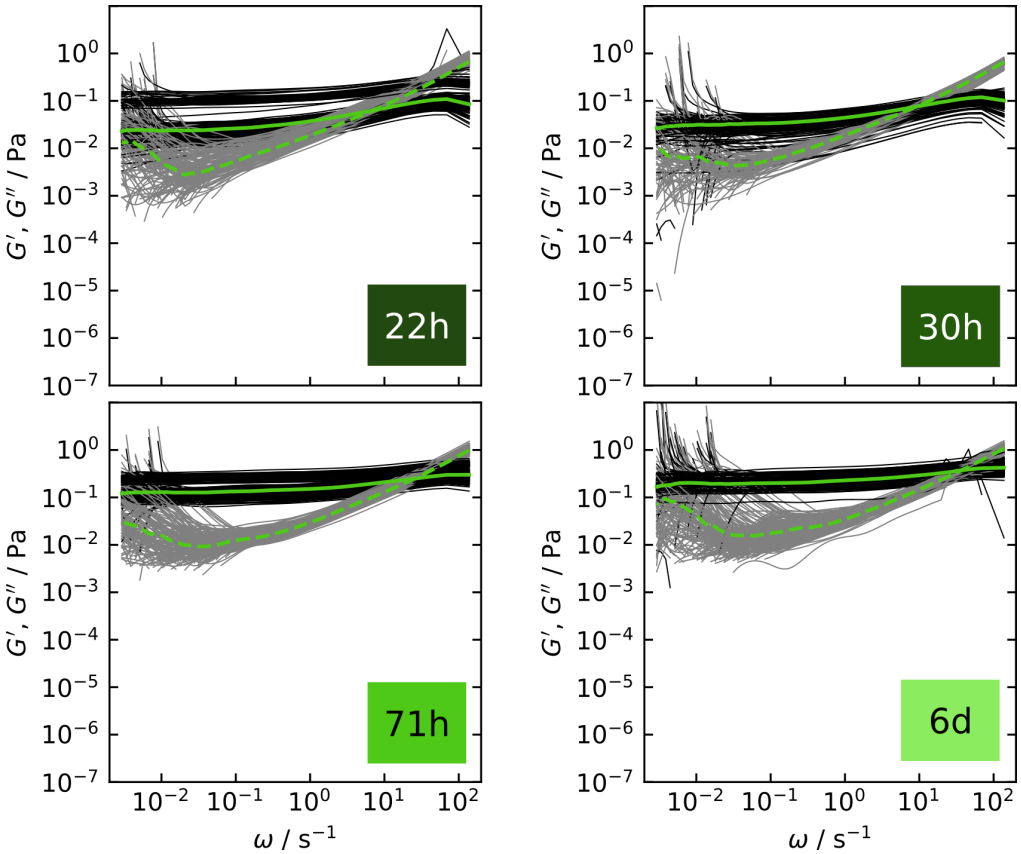

Fig. B9: **All single storage (black) and loss (gray) moduli recorded for each assembly duration in 5 mM $MgCl_2$ buffer.** The median curves are highlighted, the solid line corresponds to G' and the dashed line G''. The number of samples and particles per measurement are provided in Fig. B5. Reproduced from Ref. [4].

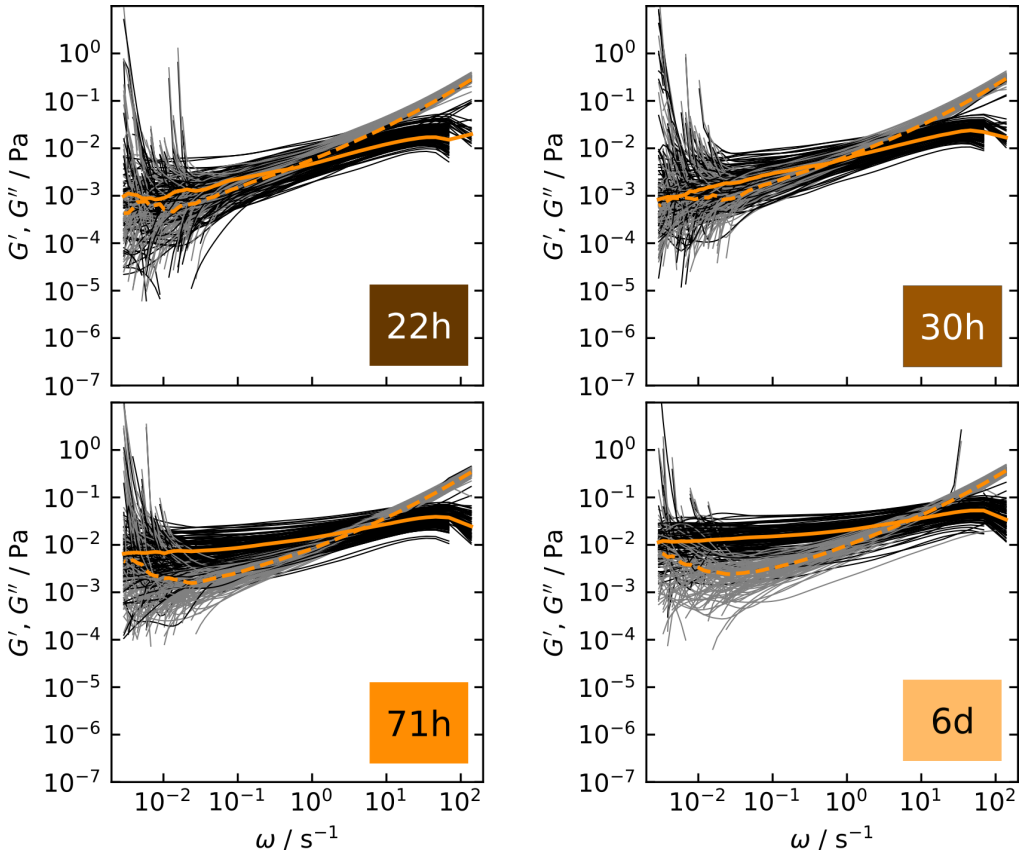

Fig. B10: **All single storage (black) and loss (gray) moduli recorded for each assembly duration in 0.16 mM TX buffer.** The median curves are highlighted, the solid line corresponds to G' and the dashed line G''. The number of samples and particles per measurement are provided in Fig. B6. Reproduced from Ref. [4].

B.2.3 Active microrheology

Reproduced from Ref. [4]

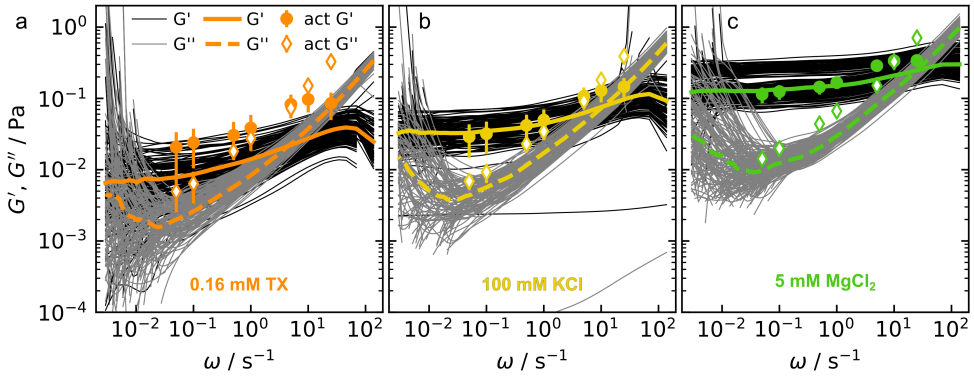

Fig. B11: **Comparison of active and passive rheology.** The single G' and G'' curves from passive measurements after 71 h assembly time are shown by thin black and gray lines, respectively. The median of the samples is plotted with a bold line (G') and bold, dashed line (G''). The active measurements are recorded on the same day. Rheological properties for measurements in 100 mM KCl plus a) 0.16 mM TX, b) nothing or c) 5 mM $MgCl_2$. Reproduced from Ref. [4].

The amplitude-phase shift data are analyzed with a custom Matlab code. The particle is oscillated in the potential of an optical trap with the trap stiffness κ and the amplitude A. The equation of motion for the particle is modeled with statistical random forces $f_R(t)$ acting on the particle and a drag force with the complex viscosity $\eta^*(\omega)$ as response of the surrounding medium:

$$m\ddot{x} = -6\pi a\eta^*(\omega)\dot{x} - f_R(t) + \kappa x + \kappa A e^{i\omega t}. \tag{B.4}$$

The equation is solved with a dampened and phase shifted sinusoidal motion:

$$x(t) = D(\omega)e^{i(\omega t - \delta(\omega))}, \tag{B.5}$$

where D is the amplitude of the particle motion and δ its phase shift with regards to the driving force [9].

By neglecting the comparably small random forces and the inertial term for low oscillation frequencies, we can use a generalized Stokes-Einstein equation to connect the complex shear modulus $G^*(\omega)$ with $\eta^*(\omega)$, $\eta^*(\omega) = \frac{G^*(\omega)}{\omega i}$. We arrive at an expression for G^* with D and δ as only remaining unknowns, which are determined by a sinusoidal fit to the trap motion as well as to the particle motion.

$$G^*(\omega) = \frac{\kappa}{6\pi a}\left(\frac{A}{D}\left(\cos(\delta(\omega) + i\sin(\delta(\omega)))\right) - 1\right) \tag{B.6}$$

This complex term is separated into the real part, the storage modulus $G'(\omega)$, and the imaginary part, the loss modulus $G''(\omega)$ [10].

$$G'(\omega) = \frac{\kappa}{6\pi a}\left(\frac{A}{D}(\cos(\delta(\omega))) - 1\right) \tag{B.7}$$

$$G''(\omega) = \frac{\kappa}{6\pi a}\left(\frac{A}{D}(\sin(\delta(\omega)))\right) \tag{B.8}$$

B.3 MODELING SINGLE INTERACTIONS

Sections B.3.1, B.3.2 and B.3.4 were written by Charlotta Lorenz for publication in Ref. [4].

B.3.1 Reaction rates

Reproduced from Ref. [4]

We model single interactions between two vimentin intermediate filaments with a two-state model since the filaments can be either in a bound (b) or an unbound (u) state. We describe the transition between the two states, *i.e.* the binding and unbinding rate, r_b and r_u, respectively, with Bell-Evans kinetics [11]. The reaction rates, with the force $F(t)$, the activation energy E_{Ab} or E_{Au}, the constant prefactor attempt rate $r_{0,b}$ or $r_{0,u}$, the potential width x_b or x_u and the thermal energy k_BT at time t are

$$r_b(t) = r_{0,b} \exp\left(\frac{-E_{Ab}}{k_BT}\right) \cdot \exp\left(\frac{-F(t)x_b}{k_BT}\right), \tag{B.9}$$

$$r_u(t) = r_{0,u} \exp\left(\frac{-E_{Au}}{k_BT}\right) \cdot \exp\left(\frac{F(t)x_u}{k_BT}\right). \tag{B.10}$$

The transition rates have a force-independent contribution, $r_{e,b}$ or $r_{e,u}$

$$r_{e,b} = r_{0,b} \exp\left(\frac{-E_{Ab}}{k_BT}\right), \tag{B.11}$$

$$r_{e,u} = r_{0,u} \exp\left(\frac{-E_{Au}}{k_BT}\right), \tag{B.12}$$

and a force-dependent term, scaling with the distance to transition state x_b or x_u. The sum of x_b and x_u has a constant value x_c to ensure detailed balance [12]. The rate equations may be either solved by simulating many single interaction events or numerically, as described in detail in Ref. [13].

B.3.2 Microscopic model of the filament interaction

Reproduced from Ref. [4]

To solve Eq. B.9 and Eq. B.10, we derive the functional shape of the force increase $F(t)$ with a microscopic modeling approach. To this end, we describe the filaments as a combination of springs. Two factors contribute to the force increase at the interaction site: 1. The elastic stretching and the entropic stiffening of the vimentin filaments, and 2. the variation of the deflection angle between the filament sections of filament f12 and the direction of motion of beads b3 and b4.

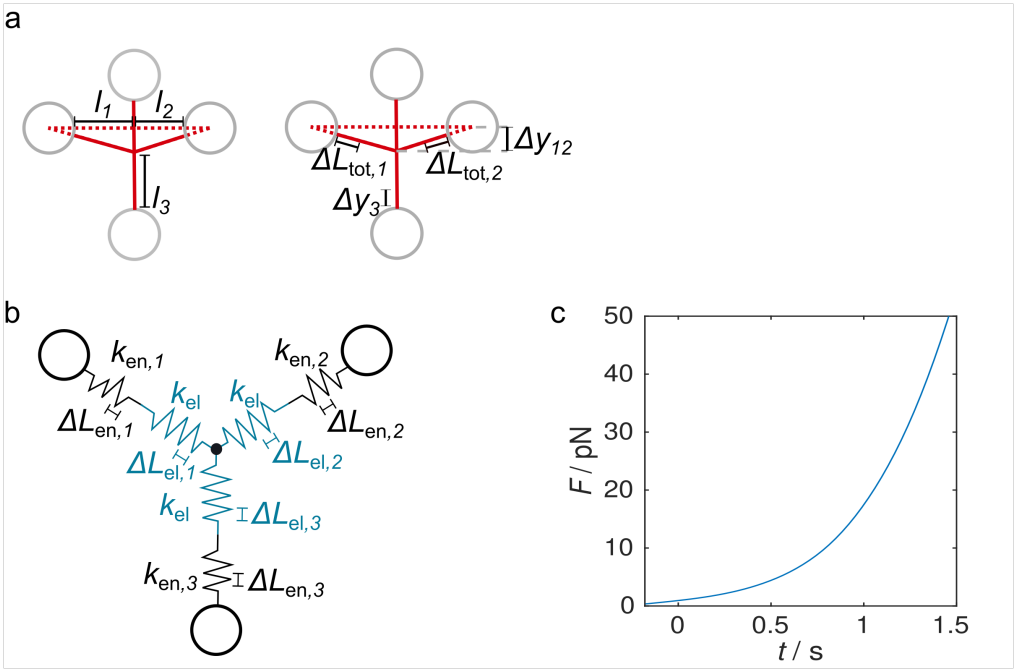

Fig. B12: **Parameters required for the microscopic model qualitatively describing the force increase in the quadruple optical tweezers experiment.** a) Lengths and extensions of the filaments. b) Microscopic model of two interacting filaments with the spring constants required to calculate the force increase on the interaction. c) Theoretically expected force increase resulting from the microscopic model. Reproduced from Ref. [4].

1. Elastic and entropic filament stretching

We model vimentin filaments with a spring constant $k_{f,i}$ as consisting of an elastic (k_{el}), and an extension-dependent, entropic ($k_{\mathrm{en},i}$) spring that are connected in series, as sketched in Fig. B12b, where i is the index for the i^{th} filament section as marked in Fig. B12a:

$$k_{f,i} = \left(\frac{1}{k_{\mathrm{el}}} + \frac{1}{k_{\mathrm{en},i}} \right)^{-1} . \tag{B.13}$$

The elastic spring constant of the of vimentin filaments is set to $k_{\mathrm{el}} = (0.22 \pm 0.06)\,\mathrm{pN/nm}$ [14]. To calculate the entropic spring constant, we assume a worm-like chain model to describe the end-to-end extension $l_{ee,i}$ of the i^{th} filament section, with the entropic force F_e, the persistence length l_P, $k_B T$ and the contour length of the i^{th} filament section $l_{c,i}$ [15]:

$$\frac{F_e l_P}{k_B T} = \frac{l_{ee,i}}{l_{c,i}} + \frac{1}{4\left(1 - \frac{l_{ee,i}}{l_{c,i}}\right)^2} - \frac{1}{4} . \tag{B.14}$$

We set the initial stretch c_s of the filament to $c_s = l_{ees,i}/l_{c,i}$, where $l_{ees,i}$ is the initial end-to-end extension. With the extension of the entropic spring $L_{\mathrm{en},i}$, the end-to-end distance is $l_{ee,i} = l_{ees,i} + L_{\mathrm{en},i}$. We approximate the entropic spring

constant of a filament section by the derivative of the entropic force with respect to the extension of the entropic spring:

$$k_{\mathrm{en},i} = \frac{\mathrm{d}F_e}{\mathrm{d}L_{\mathrm{en},i}} = \frac{\mathrm{d}}{\mathrm{d}L_{\mathrm{en},i}} \left(\frac{k_B T}{l_P} \left(\frac{L_{\mathrm{en},i}}{l_{c,i}} + c_s + \frac{1}{4\left(1 - \frac{L_{\mathrm{en},i}}{l_{c,i}} - c_s\right)^2} - \frac{1}{4} \right) \right)$$
$$= \frac{k_B T}{l_P} \left(\frac{1}{l_{c,i}} - \frac{l_{c,i}^2}{2((c_s - 1) l_{c,i} + L_{\mathrm{en},i})^3} \right) . \tag{B.15}$$

The extension of the entropic spring depends on the total extension $\Delta L_{\mathrm{tot},i}$ of the filament section and the elastic spring in the filament model, assuming that the force acting on the entropic and elastic spring is the same:

$$L_{\mathrm{en},i} = \frac{k_{\mathrm{el}}}{k_{\mathrm{en},i} + k_{\mathrm{el}}} \Delta L_{\mathrm{tot},i} . \tag{B.16}$$

We rewrite the total extension of the filament section in terms of the angle α_i by which the i^{th} filament section is deflected while it is moved down, the bead diameter a, the distance Δy_{12} by which the point of interaction moves and the length l_i of the i^{th} ($i = [1,2]$) filament section when the filaments start to interact:

$$\Delta L_{\mathrm{tot},i} = \frac{\Delta y_{12}}{\sin \alpha_i} - \frac{a}{2} - l_i . \tag{B.17}$$

Substituting Eq. B.16 and Eq. B.17 into Eq. B.15 results in:

$$k_{\mathrm{en},i}(\Delta y_{12}) = \frac{k_B T}{l_P} \left(\frac{1}{l_{c,i}} - \frac{l_{c,i}^2}{2\left[(c_S - 1) l_{c,i} + \frac{k_{\mathrm{el}}}{k_{\mathrm{en},i} + k_{\mathrm{el}}} \left(\frac{\Delta y_{12}}{\sin \alpha_i} - \frac{a}{2} - l_i \right) \right]^3} \right) , \; i = [1,2] . \tag{B.18}$$

We solve this equation for $k_{\mathrm{en},i}$ with the Matlab function `vpasolve`. A maximum of three solutions are possible and we assume the one with solely a real part is the physically feasible solution.
In analogy to the spring constants of filament sections 1 and 2, we calculate the spring constant of filament section 3. However, the distance Δy_3 by which filament section 3 is extended is set by the distance that beads b3 and b4 are moved and by Δy_{12}. v is the speed with which the beads are moved and t is the time after the interaction starts:

$$vt = \Delta y_3 + \Delta y_{12} . \tag{B.19}$$

Thus, the entropic spring constant of filament section 3 is:

$$k_{\mathrm{en},3}(\Delta y_{12}) = \frac{k_B T}{l_P} \left(\frac{1}{l_{c,3}} - \frac{l_{c,3}^2}{2\left[(c_s - 1) l_{c,3} + \frac{k_{\mathrm{el}}}{k_{\mathrm{en},3} + k_{\mathrm{el}}} (vt - \Delta y_{12}) \right]^3} \right) . \tag{B.20}$$

2. Deflection of the filaments
The filament sections 1 and 2 are deflected when an interaction forms and beads b3 and b4 are moved, leading to an increased contribution to the force in the y direction. We calculate the projection of the forces on the y axis with the factor $c_{g,i}$:

$$c_{g,i}(\Delta y_{12}) = \sin\alpha_i(\Delta y_{12}) = \sin\left(\arctan\left(\frac{\Delta y_{12}}{l_i + a/2}\right)\right) = \frac{\frac{\Delta y_{12}}{l_i+a/2}}{\sqrt{\left(\frac{\Delta y_{12}}{l_i+a/2}\right)^2 + 1}}, \tag{B.21}$$

see Figs. 4.3 and B12 for definition of the parameters. The total force acting on the interaction site in the y direction therefore is:

$$F = \left(c_{g,1}(\Delta y_{12})k_{f,1}(\Delta y_{12}) + c_{g,2}(\Delta y_{12})k_{f,2}(\Delta y_{12})\right) \cdot \Delta y_{12}\,. \tag{B.22}$$

The forces in the y direction are balanced, $F = F_3$, and by using Eqs. B.19 and B.22 we thus obtain:

$$(c_{g,1}(\Delta y_{12})k_{f,1}(\Delta y_{12}) + c_{g,2}(\Delta y_{12})k_{f,2}(\Delta y_{12})) \cdot \Delta y_{12} = (vt - \Delta y_{12}) \cdot k_3(vt - \Delta y_{12})\,. \tag{B.23}$$

We solve Eq. B.23 with the Matlab function `fminsearch`. A typical, calculated force increase is shown in Fig. B12c, and it qualitatively resembles the experimental data. The calculated force increase is well-described by an exponential function for small forces and a subsequent linear increase.

B.3.3 Experimental force increase

Reproduced from Ref. [4]

The results of the microscopic model as well as the experimental force-time curves are well represented by a simplified description consisting of an exponential increase at low forces and a linear increase at times $t \geq t_c$. Therefore, this simplified description is used to fit the experimental data, curves that reach forces $> 10\,\mathrm{pN}$ are fitted by:

$$F(t) = \begin{cases} f(t) = A\exp(Bt) & t \leq t_c \\ g(t) = f(t_c)\,(1 + B(t - t_c)) & t \geq t_c\,, \end{cases}$$

utilizing that $F(t_c)$ is continuous and differentiable. The parameters A and B are constants. Experiments where the interaction ruptures at $< 10\,\mathrm{pN}$ are fitted by $f(t)$. We perform this analysis for all initial increases that start at zero force. For rebinding events under force (kinks), the increase is assumed to be equal to the initial increase in the same measurement.

B.3.4 Comparison of simulated and experimental data

Reproduced from Ref. [4]

To determine $r_{e,u}$ and x_u, Eq. B.9 and Eq. B.10 are solved for different pairs of $r_{e,u}$ and x_u with the force increase $F(t)$ derived from the experimental data. $r_{e,u}$ is varied from 0.01 s^{-1} to 0.5 s^{-1} in steps of 0.01 s^{-1}, and x_u is varied from 0 nm to 0.8 nm in steps of 0.01 nm. The resulting force distributions for all experimental force increases and a specific $r_{e,u}$–x_u pair are averaged and compared to the experimental force histogram with the Kolmogorov-Smirnov test [16]. If the simulated and experimental histograms differ less than allowed by the 5% significance level of the Kolmogorov-Smirnov test, the $r_{e,u}$–x_u pair is accepted. We start with the evaluation of $r_{e,u}$-x_u pairs around $r_{e,u} = 0.1$ s^{-1} and $x_u = 0.1$ nm, and evaluate only $r_{e,u}$–x_u pairs around previously accepted $r_{e,u}$-x_u pairs. We determine the values of $r_{e,u}$ and x_u at the centroid of the valid parameter space, $\overline{r_{e,u}}$ and $\overline{x_u}$, shown in Fig. 6.12d.

B.3.5 Calculation of the energy landscape

Reproduced from Ref. [4]

To calculate the energy landscapes in Fig. 6.12e,f, we calculate the equilibrium free energy difference ΔG from the force-independent binding $r_{e,b}$, and unbinding rates at the centroid of the valid parameter space, $\overline{r_{e,u}}$:

$$\Delta G = -k_B T \ln\left(\frac{\overline{r_{e,u}}}{r_{e,b}}\right) . \tag{B.24}$$

The absolute values of the activation energies cannot be determined from our experiments. However, we can calculate the differences between activation energies between different conditions, *e.g.* condition M ($c(MgCl_2)$=5 mM) and condition T c(TX)=0.16 mM):

$$\frac{r_{e,b,M}}{r_{e,b,T}} = \frac{\exp\left(\frac{-E_{Ab,M}}{k_B T}\right)}{\exp\left(\frac{-E_{Ab,T}}{k_B T}\right)} \Rightarrow k_B T \ln\left(\frac{r_{e,b,M}}{r_{e,b,T}}\right) = E_{Ab,T} - E_{Ab,M} . \tag{B.25}$$

We set the sum x_c of x_b and x_u to $x_c = 2$ nm as shown in Fig. 6.12e,f. The exact value of x_b in the range of $0.4 - 2$ nm does not change the resulting force histograms, since $r_{e,b}$ dominates the force-dependent term of Eq. B.9. From $\overline{x_u}$ and x_c, we calculate x_b. We directly plot x_b and x_u in the energy landscape as the distances from the bound or unbound state to the transition state.

C

SUPPORTING INFORMATION: RESPONSE OF ACTIN AND KERATIN STRUCTURES TO ISOTROPIC CELL STRETCHING

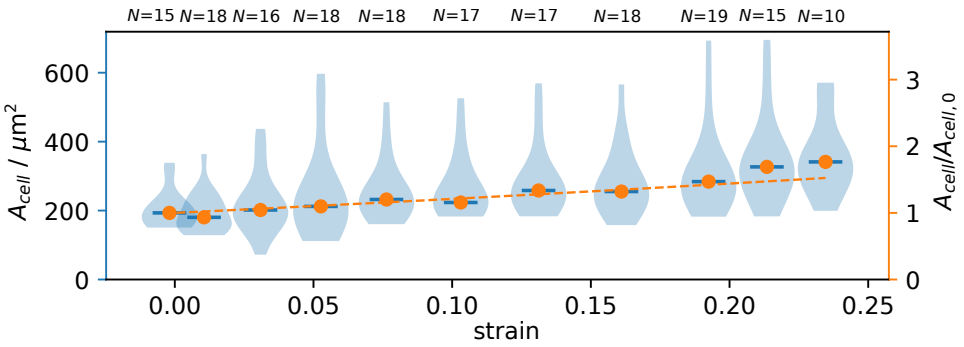

Fig. C1: **The cell area increases with the radial strain.** In a second set of measurements, the observed cell area increase also matches the area increase calculated from the bead images (dashed line). The median values of the distributions are indicated by a bold line, the ratios of the median cell areas with respect to the median of the first analyzed cell area distributions are marked with a circle.

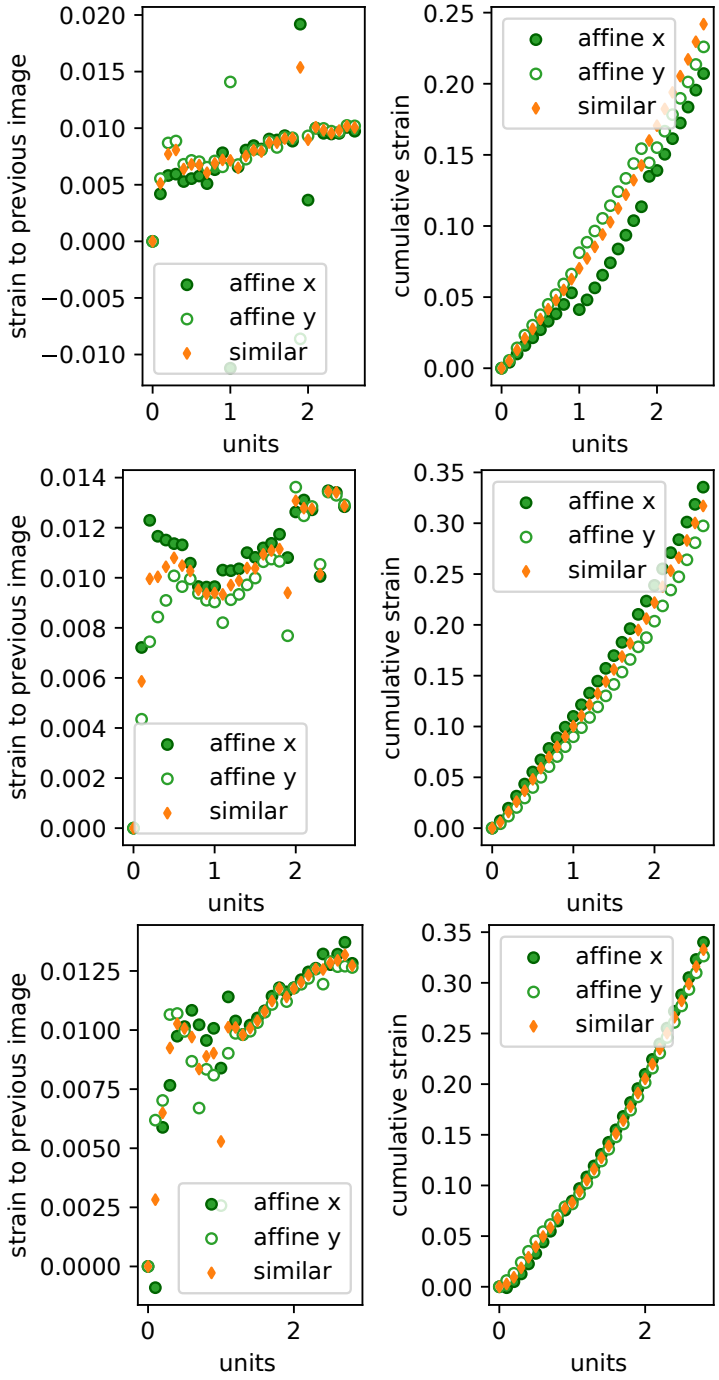

Fig. C2: **Strain calculated from bead images.** The strain, calculated from the results of affine and similarity transform from three separate stretching experiments.

[1] A. V. Schepers, C. Lorenz, and S. Köster. "Tuning Intermediate Filament Mechanics by Variation of pH and Ion Charges." *Nanoscale* 12 (2020), pp. 15236–15245. DOI: 10.1039/D0NR02778B.

[2] R. M. Weinheimer, D. F. Evans, and E. L. Cussler. "Diffusion in surfactant solutions." *J. Colloid Interface Sci.* 80 (1981), pp. 357–368. DOI: 10.1016/0021-9797(81)90194-6.

[3] Y.-H. Li and S. Gregory. "Diffusion of Ions in Sea Water and in Deep-Sea Sediments." *Geochim. Cosmochim. Ac.* 38 (1974), pp. 703–714. DOI: 10.1016/0016-7037(74)90145-8.

[4] A. V. Schepers et al. "Multiscale mechanics and temporal evolution of vimentin intermediate filament networks." *Proc. Natl. Acad. Sci.* 118 (2021), e2102026118. DOI: 10.1073/pnas.2102026118.

[5] T. G. Mason et al. "Particle Tracking Microrheology of Complex Fluids." *Phys. Rev. Lett.* 79 (1997), pp. 3282–3285. DOI: 10.1103/PhysRevLett.79.3282.

[6] T. G. Mason et al. "Rheology of F-actin solutions determined from thermally driven tracer motion." *J. Rheol.* 44 (2000), pp. 917–928. DOI: 10.1122/1.551113.

[7] B. R. Dasgupta et al. "Microrheology of Polyethylene Oxide Using Diffusing Wave Spectroscopy and Single Scattering." *Phys. Rev. E* 65 (2002), p. 051505. DOI: 10.1103/PhysRevE.65.051505.

[8] J. C. Crocker et al. "Two-Point Microrheology of Inhomogeneous Soft Materials." *Phys. Rev. Lett.* 85 (2000), pp. 888–891. DOI: 10.1103/PhysRevLett.85.888.

[9] M. T. Valentine, L. E. Dewalt, and H. D. Ou-Yang. "Forces on a colloidal particle in a polymer solution: A study using optical tweezers." *J. Phys.: Condens. Matter* 8 (1996), pp. 9477–9482. DOI: 10.1088/0953-8984/8/47/048.

[10] L. A. Hough and H. D. Ou-Yang. "A New Probe for Mechanical Testing of Nanostructures in Soft Materials." *J. Nanopart. Res.* 1 (1999), pp. 495–499. DOI: 10.1023/A:1010075223642.

[11] G. I. Bell. "Models for the Specific Adhesion of Cells to Cells." *Science* 200 (1978), pp. 618–627. DOI: 10.1126/science.347575.

[12] A. Kolomeisky. *Motor Proteins and Molecular Motors*. CRC press, 2015.

[13] L. Schaedel et al. "Vimentin intermediate filaments stabilize dynamic microtubules by direct interactions." *Nat. Commun.* 12 (2021), p. 3799. DOI: 10.1038/s41467-021-23523-z.

[14] J. Block et al. “Nonlinear Loading-Rate-Dependent Force Response of Individual Vimentin Intermediate Filaments to Applied Strain.” *Phys. Rev. Lett.* 118 (2017), p. 048101. DOI: 10.1103/PhysRevLett.118.048101.

[15] J. F. Marko and E. D. Siggia. “Stretching DNA.” *Macromolecules* 28 (1995), pp. 8759–8770. DOI: 10.1021/ma00130a008.

[16] G. W. Corder and Dale I. Foreman. *Nonparametric Statistics: A Step-By-Step Approach*. John Wiley & Sons, 2014.

ACKNOWLEDGMENTS

This thesis would not exist without the help and support of a lot of people.
First and foremost, I want to thank Sarah Köster for introducing me to intermediate filaments and their mechanics. It is a pleasure to be part of your group and I am grateful for many exciting discussions and for your constant support. I very much appreciate that you created a lot of fantastic opportunities for me.
I thank Andreas Janshoff for many interesting discussions about rheology, cell mechanics and research in general. Thank you for supporting me by being my MtL mentor, a member of my TAC, and the second examiner for this thesis. Jörg Enderlein, thank you for your helpful feedback during TAC meetings. I want to thank Stefan Klumpp for informative discussions about models and simulations. I am happy that Timo Betz, and Michael Meinecke agreed to being part of the examination board.
I want to thank Harald Herrmann for his always helpful and interesting input. I am grateful to Harald and Norbert Mücke for inviting Lotta and me to Heidelberg to discuss our assembly problems and showing us how to image filaments with AFM. There would be no electron microscopy images of our filaments without Wiebke Möbius. I am grateful to Nicole Schwarz and Sonja Lehmann for providing us with cells, plasmids, and being incredibly nice while being bombarded with questions. Thank you to Tabea Oswald for your help with general cell-related questions. I also want to thank Andreas' group for their support whenever I used their labs. I especially want to mention Peter Nietmann. Measuring and particularly discussing more or less crazy experiment ideas with you has been extremely motivating. Thank you, Jonathan, for teaching me how to make cell-stretching devices, and for many interesting discussions. Thank you also to Fereshteh and Michael, it's fascinating to lean about a completely different system, and I look forward to more tether-tests.
I thank Jochen and Mike for their help during my brief excursion to the clean room. Thank you to Jan for fixing every minor or major IT issue and installing tedious python packages. Markus, thank you for producing a fantastic video about filament interactions/noodle soup. I thank Christine, Kerstin, and Michaela for their help with a lot of confusing paper work. My thanks also extends to Antje and Frauke from the PBCS office, and the MtL offices. Thank you, Anne, for some really enjoyable chats.

I am grateful for the hands-on support of many people. Peter Luley, designing and building the isotropic stretcher, together with Peter Nieschalk and the machine shop, has been a lot of fun! Thanks for implementing so many of my extra and add-on wishes. I learnt a lot about the development of such an instrument.
I want to thank everyone in the lab. You are such an amazing and lovely group, I couldn't have wished for a better bunch of people to spend my time here with. A big thank you to the people without whom the lab would not run: Susanne Bauch, thank you for preparing so many vimentin batches! Being in the lab with you is a lot of fun, although there is always the "danger" of getting lost in long conversations. I also want to thank Susanne Hengst for taking care of

the cell lab and organising the labs. Ulrike, working with you is just amazing. Thanks for countless discussions, help with cell culture questions, and just generally being lovely. Thanks, Kamila, for your help in the lab. I want to thank you, Ruth, for choosing to work with me for the last three years. Your curiosity helped to bringing the project forward! Thanks for taking over the cell culture countless times. Anička, thank you for a lot of fun! I would have never known about the wonders of the Titanenwurz without you. Andrew, I enjoyed the late afternoon chats in our old office, when refilling the nitrogen or during walks. Heidi, I admire your enthusiasm about everything fun, especially (bad?) puns. Thank you for your patience with all of my strange language questions. Thank you, Heidi and Andrew, for inviting us all to a wonderful Thanksgiving dinner! Jan-Philipp, thank you for making late night office surprisingly fun by suddenly starting to sing. Magdalena, you brighten up any conversation. Thank you for your help with comsol and in the clean room. I was great to work with you, Laura. Thank you to Michelle, Eric, Kim for working with me on more or less doable projects over the last years. Thanks, Charlotte, for always having an open ear. I thank Johanna for getting me started with the project and introducing me to the group/ how everything works. Thanks to Hannes for diving deep into IF mechanics discussions right away. Thank you, Manuela and Gerrit, for welcoming me in the group when I started. Thank you, Anna, for your thorough and incredibly helpful proof reading of most of this thesis. You always ask exactly the right questions. I love that every "short" chat somehow always ends up much longer. You're an amazing Friday Pizza partner! While talking about pizza, I have to credit Chiara. It is amazing that you spent hours and hours making the most delicious pizza parties. You always find the right (sarcastic) words. We make a great kids-book team! Eleonora, you're an awesome motivator. Talking to you is always reassuring and your enthusiasm about everything can be so catching. I love that we got to share the excitement about Korean food and series. Julia, our painting, paint making, jewellery making (I think I can't list everything here) journey was one of the unexpected but fantastic parts of the last years. I'm so glad we could share many, many crazy and not so crazy ideas. One day, all the filaments will wear hats! Lotta, you amaze me how fast you understand everything. Discussing any scientific idea with you is fun, interesting and motivating. Talking to you about life and stuff during endless rounds around the building is always helpful. Thank you for the motivation and all of the chocolate!

I thank all the people in my life who have supported me in the last years. I am especially grateful to my family. Thank you, Elisabeth, Aloys, Judith, Waltraud for endless phone calls, motivation packages, and always being there for me. Finally, I thank Christoph. I don't have the right words to properly thank you for your support throughout everything.

LIST OF ACRONYMS

AFM atomic force microscopy

BFP back focal plane

DLS dynamic light scattering

DMSO dimethylsulfoxid

DNA deoxyribonucleic acid

DWS dynamic wave spectroscopy

EDC 1-ethyl-3-(3-dimethylaminopropyl)carbodiimide

EDTA 2,2′,2″,2‴-(ethane-1,2-diyldinitrilo)tetraacetic acid

EGTA 3,12-bis(carboxymethyl)-6,9-dioxa-3,12-diazatetradecane-1,14-dioic acid

EYFP enhanced yellow fluorescent protein

FWHM full width half maximum

IF intermediate filament

KO knock-out

MAC methylamine hydrochloride

MDCK II Madin-Darby Canine Kidney II

MDCK Madin-Darby Canine Kidney

MES 4-morpholineethanesulfonic acid

MPT microparticle tracking

MSD mean squared displacement

NA numerical aperture

OTs optical traps or optical tweezers

OT optical trap

PB sodium phosphate buffer

PBS phosphate buffered saline

PDMS poly(dimethylsiloxan)

PLA poly(lactic acid)

PSD position sensitive detector

PTFE poly(tetrafluoroethylene)

QPD quadrant photo diode

TRIS 2-amino-2-(hydroxymethyl)propane-1,3-diol

TX TritonX-100

ULF unit length filament

WAXS wide-angle X-ray scattering

WLB worm-like bundle

WLC worm-like chain

wt wild-type

PUBLICATIONS

1. A. V. Schepers*, J. Kraxner*, C. Lorenz*, S. Köster, Optical Tweezers: Methods and Protocols, Second Edition, in press 2021, Springer.
2. C. Lorenz*, A. V. Schepers*, S. Köster, Optical Tweezers: Methods and Protocols, Second Edition, in press 2021, Springer.
3. A.V. Schepers, C. Lorenz, P. Nietmann, A. Janshoff, S. Klumpp, S. Köster, 2021, Proc. Natl. Acad. Sci. 118, e2102026118.
4. L. Schaedel*, C. Lorenz*, A.V. Schepers, S.Klumpp, S.Köster, 2021, Nat. Commun., 12, 3799.
5. A.V. Schepers, C. Lorenz, S. Köster, Nanoscale, 2020, 12, 15236-15245.
6. C. Lorenz, J. Forsting, A.V. Schepers, J. Kraxner, S. Bauch, H. Witt, S. Klumpp, S. Köster, 2019, Phys. Rev. Lett. 123, 188102.

* These authors contributed equally.